



UNIVERSITÀ  
DEGLI STUDI  
FIRENZE

PhD in  
Physics and Astronomy

CYCLE XXXV

COORDINATOR Prof. Giovanni Modugno

## FIRST STARS AND DWARF GALAXIES

Academic Discipline (SSD) FIS/05

**Doctoral Candidate**

Dr. Rossi Martina



**Supervisors**

Prof. Salvadori Stefania

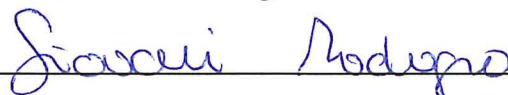


Prof. Skúladóttir Ása



**Coordinator**

Prof. Modugno Giovanni



---

*The consultation of the thesis is free. Unless a specific authorization is obtained from the author, the thesis can be, however, downloaded and printed only for strictly personal purposes related to study, research and teaching, with the explicit exclusion of any use that has – even indirectly – a commercial nature.*

---

*Ad astra*





---

# Contents

<b>Introduction</b>	<b>1</b>
<b>1 The First Stars</b>	<b>5</b>
1.1 Cosmological context - the $\Lambda$ CDM model	5
1.1.1 Linear Regime	6
1.1.2 Non-linear regime	9
1.1.3 Mass distribution of dark matter halos	10
1.2 Which halos can form stars?	12
1.3 Formation of the first stars	14
1.4 Primordial stellar IMF	18
1.5 Evolution of the first stars	20
1.6 Feedback processes	22
1.6.1 Radiative feedback	22
1.6.2 Mechanical feedback	23
1.6.3 Chemical feedback	23
<b>2 Stellar Archaeology and Dwarf galaxies</b>	<b>25</b>
2.1 Stellar Archaeology	25
2.2 Searching for metal-poor stars	26
2.2.1 Techniques	26
2.2.2 Milky Way Metal-Poor stars	28
2.2.3 Carbon-Enhanced Metal Poor (CEMP) stars	29
2.2.4 Stellar chemical abundances	30
2.3 Primordial IMF from Stellar Archaeology	33
2.4 Dwarf Galaxies	34
2.4.1 Ultra-Faint Dwarf Galaxies	38
2.4.2 Boötes I	39
<b>3 Modelling Ultra-Faint Dwarf Galaxies</b>	<b>41</b>
3.1 Model Description	41

---

3.1.1	Initial Conditions: . . . . .	41
3.1.2	Infall rate: . . . . .	43
3.1.3	Star formation rate: . . . . .	43
3.1.4	Pop III and Pop II/I stars: . . . . .	43
3.1.5	Stellar initial mass function: . . . . .	43
3.1.6	Stellar evolution: . . . . .	44
3.1.7	Mechanical feedback: . . . . .	45
3.1.8	Galaxy evolution: . . . . .	47
3.2	Model Calibration . . . . .	47
3.3	Modelling the IMF random sampling . . . . .	51
3.3.1	Stochastic IMF sampling procedure . . . . .	51
3.3.2	Model validation . . . . .	52
3.4	The evolution of UFDs with IMF random sampling . . . . .	53
3.4.1	Impact of the IMF random sampling . . . . .	56
<b>4</b>	<b>Unveiling the minimum mass of the first stars</b>	<b>61</b>
4.1	Impact of the Pop III IMF . . . . .	62
4.1.1	Pop III star survivors . . . . .	62
4.2	Constraining the low-mass end of Pop III stars . . . . .	65
4.2.1	Stronger Pop III IMF constraints . . . . .	67
4.3	Simulating the Boötes I CMD . . . . .	67
4.3.1	Can we really catch zero-metallicity stars? . . . . .	68
4.3.2	How to get tighter Pop III IMF constraints . . . . .	69
4.3.3	How deep should we go? . . . . .	72
4.3.4	Deeper or wider? . . . . .	75
4.4	Discussion and conclusions . . . . .	76
<b>5</b>	<b>Understanding the origin of CEMP-no stars through UFDs</b>	<b>81</b>
5.1	The debate origin of CEMP stars . . . . .	81
5.2	New Features of the model . . . . .	82
5.3	The Carbon Enrichment in Boötes I . . . . .	82
5.4	The different CEMP-no populations . . . . .	84
5.4.1	Moderate CEMP-s stars . . . . .	86
5.4.2	Testing our predictions: [C/Mg] . . . . .	87
5.5	Discussion and conclusions . . . . .	89
<b>6</b>	<b>Deciphering the signatures of first Pop III SNe</b>	<b>91</b>
6.1	The energy distribution function of Pop III SNe . . . . .	91
6.2	Testing different Pop III SNe energies . . . . .	93

---

6.3	The chemical signatures of Pop III SNe . . . . .	96
6.4	Looking for first stars descendants . . . . .	98
6.4.1	CEMP stars . . . . .	102
6.4.2	C-normal stars . . . . .	103
6.4.3	Testing our predictions . . . . .	104
6.4.4	Mono-enriched stars . . . . .	108
6.5	Discussion and conclusions . . . . .	112
<b>7</b>	<b>Beyond Ultra-Faint Dwarfs: the Galactic Bulge</b>	<b>115</b>
7.1	The Galactic Bulge . . . . .	115
7.2	Model . . . . .	117
7.2.1	The progenitor halos of the Bulge . . . . .	120
7.2.2	Pop III enrichment . . . . .	120
7.2.3	Discussion and conclusions . . . . .	123
<b>8</b>	<b>Beyond Ultra Faint Dwarfs: Galactic Halo</b>	<b>127</b>
8.1	Milky Way's Halo . . . . .	127
8.2	Model implementations . . . . .	127
8.3	Results . . . . .	128
8.3.1	Pop III stars: Energy Distribution Function vs IMF . . . . .	129
8.3.2	Metal contribution from Pop III stars . . . . .	133
8.3.3	Discussion and conclusions . . . . .	135
8.4	A general parametric model . . . . .	136
8.4.1	The model . . . . .	136
8.4.2	Birth environments of Pop III descendants . . . . .	137
8.4.3	Other chemical elements . . . . .	140
8.4.4	The complete abundance pattern . . . . .	140
8.4.5	The star-to-star scatter . . . . .	143
8.4.6	Conclusions . . . . .	144
<b>9</b>	<b>Conclusions</b>	<b>147</b>
9.1	Results of my work . . . . .	147
9.2	A look to the future . . . . .	152



---

# Introduction

The first stars played a crucial role in the evolution of the primordial Universe since they represented the first sources of ionising photons, dust, and chemical elements heavier than helium, i.e. metals. The amount of ionizing photons, dust, and different chemical species produced by the first stars strongly depends on their mass and on the explosion energy of the very first supernovae (SNe). Thus, understanding the Initial Mass Function (IMF) of the first stars and their Energy Distribution Function (EDF) is a fundamental problem in Cosmology. Yet, these functions are very difficult to infer both from an observational and a theoretical prospective, and they are still unknown.

First stars, also known as Population III (Pop III) stars, are predicted to form at  $z \sim 15 - 30$ , in so-called minihaloes with masses  $M_h \approx 10^6 M_\odot$  and virial temperature  $T_{\text{vir}} \leq 10^4 \text{K}$ . Since they form out of gas with primordial composition, they are expected to be completely metal-free. These metal-free stars should produce key emission lines that might allow us to easily identify their host galaxies. However, the detection of individual Pop III stars in the high-redshift Universe poses a significant challenge, even with the employ of the newly launched James Webb Space Telescope. Thus, our current knowledge of Pop III stars arises from theoretical studies and *indirect* observations. Different theoretical studies and cosmological simulations agree that Pop III stars are likely more massive than present-day stars, with mass likely extending up to  $\sim 1000 M_\odot$ . On the other hand, 3D simulations that study the cooling of primordial gas reveal that the proto-stellar gas clouds can experience strong fragmentation and Pop III stars could have masses lower than  $1 M_\odot$ . Indeed, if Pop III stars with masses below  $0.8 M_\odot$  were able to form, they should be alive today, and they should dwell in the oldest and most metal-poor systems of the Local Group. Despite long searches, zero-metallicity stars have never been found among the ancient stars in our Milky Way, supporting the idea that first stars are more massive than present-day stars. If so, most of Pop III stars would evolve and explode as SNe, rapidly disappearing from the Universe in few Myrs. However, the chemical signatures of these pristine SNe could be retained in the photospheres of low-mass (Pop II) stars that formed from the ashes of massive Pop III stars. These low-mass long-lived stars imprinted by Pop III SNe, the so-called first stars “descendants”, can survive until today and they can be individually observed in the oldest

and metal-poor environments of our Galaxy and its dwarf galaxies satellites. This is indeed the key idea behind “Stellar Archaeology”: to indirectly study the first stars by exploiting the stellar chemical abundances measured in the Local Group.

Among all environments hosting ancient stars, Ultra-Faint Dwarf (UFD) galaxies ( $L_{\text{bol}} < 10^5 L_{\odot}$ ) are the best places to look for Pop III star descendants. UFD galaxies are the most common dwarf galaxies in the Local Group, representing more than 50% of the total number of dwarf satellites. They are the oldest, most dark matter-dominated, most metal-poor, least luminous, and least chemically evolved stellar systems known. Most UFD galaxies formed more than 75% of their stars in the first Gyr of evolution and hence have old stellar populations,  $> 10$  Gyr. Furthermore they contain the highest fraction of extremely metal-poor stars,  $[\text{Fe}/\text{H}] < -3$ . Finally, these low-mass dwarf galaxies are predicted to be the building blocks of the Galactic stellar halo, and the first star-forming systems that hosted Pop III stars.

The main goal of this Thesis is to unveil the properties of the first stars by exploiting the observed chemical properties of stars in Ultra-Faint Dwarf galaxies. To achieve this goal, we develop a novel theoretical model that follows the formation and chemical evolution of Boötes I, the best studied UFD galaxy. For the first time, we present a theoretical model that accounts for the incomplete sampling of the IMF for both Pop III stars and subsequent normal Pop II, and that is able to follow the chemical enrichment star-by-star and from different sources: SNe and AGB<sup>1</sup> stars both from Pop III and Pop II stars. First, we investigate the frequency of long-living first star relics in UFDs to limit the minimum mass of the first stars. By comparing our model results with the current number of observed stars in Boötes I, and other UFDs, we can put limits on the shape and on the low-mass end of the Pop III IMF. Then, by studying the chemical signatures left by the Pop III SNe we determine the key chemical features to uniquely identify true first star descendants and we provide predictions to discover them. Finally, by exploring other ancient and metal-poor environments in our Milky Way, such as the Galactic halo and the bulge, we show how to further derive constraints on the masses and the nature of first SNe.

<sup>1</sup> Asymptotic Giant Branch

The results illustrated in this Thesis appear in the following publications in peer reviewed journals:

- ✧ **Rossi M.**, Salvadori S. and Skúladóttir Á., *Ultra-faint dwarf galaxies: unveiling the minimum mass of the first stars*, (Rossi et al. 2021);
- ✧ **Rossi M.**, Salvadori S., Skúladóttir Á., Vanni I., *Understanding the origin of CEMP - no stars through ultra-faint dwarfs*, (Rossi et al. 2023);
- ✧ **Rossi M.**, Salvadori S., Skúladóttir Á., Vanni I., Koutsouridou I., *Deciphering the signatures of first Pop III supernovae* (to be submitted to MNRAS);
- ✧ Pagnini, G., Salvadori, S., **Rossi, M.**, Aguado, D., Koutsouridou, I., Skúladóttir, Á., *On the dearth of C-enhanced metal-poor stars in the galactic bulge*, (Pagnini et al. 2023);
- ✧ Vanni I., Salvadori, S., Skúladóttir, Á., **Rossi, M.**, Koutsouridou, I., *Characterising the true descendants of the first stars*, (submitted to MNRAS);
- ✧ Koutsouridou, I., Salvadori, S., Skúladóttir, Á., **Rossi, M.**, Vanni I., Pagnini, G., *The energy distribution of the first supernovae*, (Koutsouridou et al. 2023).





---

---

# The First Stars

The first stars are expected to play a crucial role in the evolution of the primordial Universe since they are the first source of light and chemical elements heavier than helium after the Big Bang. In fact, with their formation and evolution, the Universe rapidly transformed from a simple state, i.e. gas made of neutral hydrogen and helium, into an increasingly complex one, characterised by a great variety of chemical elements. To comprehend the formation of the first stars within the initial star-forming structures, we must consider the cosmological context. Therefore in this Chapter we briefly illustrate the underlying cosmological model to understand when and where the first stars formed and what their impact on chemical enrichment of the Universe. Furthermore, we emphasize the many open questions concerning the first stars.

## 1.1 Cosmological context - the $\Lambda$ CDM model

Modern cosmology is based on two main hypotheses: i) the cosmological principle, stating that the Universe is uniform and isotropic on sufficiently large scales, and ii) Einstein's general relativity, which allow us to infer the structure of space-time based on the mass distribution contained in it. The most popular cosmological model is the so called  $\Lambda$  Cold Dark Matter ( $\Lambda$ CDM), according to which dark matter (DM) is composed by cold, weakly interacting, massive particles. The  $\Lambda$  represents the cosmological constant, which is currently associated with dark energy that is used to explain the accelerating expansion of the Universe. In  $\Lambda$ CDM Universe, about 70% of the energy is due to dark energy, 25% due to the cold dark matter and only 5% due to baryonic matter. The main phases of the evolution of the Universe are shown in Fig.1.1.

According to the  $\Lambda$ CDM model, the Universe began with the Big Bang roughly 13.8 Gyr ago and since it has been expanding and cooling down its temperature. The first light nuclei formed about 5 minutes after the Big Bang when the temperature was about  $T \sim 10^9$  K. At the Recombination epoch, i.e.  $\sim 380,000$  yr after the Big Bang when

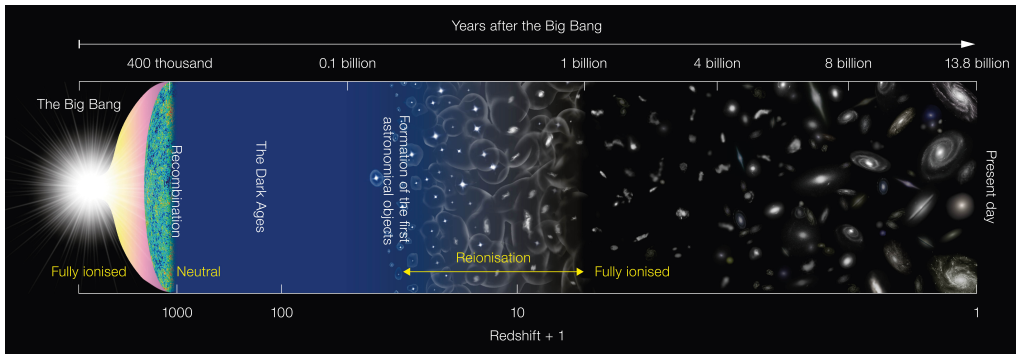


Figure 1.1: The illustration summarises the almost 14 Gyr history of our Universe, showing the main events that occurred from the initial phases of simplicity to the rich variety of cosmic structure that we observe today. From <https://astro.uni-bonn.de>.

$T \sim 10^3$  K, the radiation decoupled from matter and continued to expand through space and electrons combined with protons to form hydrogen. This radiation is now known to be what constitutes the Cosmic Microwave Background (CMB), which today is the oldest light in the Universe. Recent observations of the CMB with the Planck instrument have enabled to constrain the cosmological parameters with extreme accuracy:  $H_0 = 71$  km/Mpc s,  $\Omega_b = 0.044$ ,  $\Omega_m = 0.27$ ,  $\Omega_\Lambda = 0.73$ ,  $h = H_0/100$ ,  $t_0 = 13.7$  Gyr,  $\rho_0 = 9.21 \cdot 10^{-30}$  gr (Planck Collaboration et al. 2018). These are the parameters that we adopt in this Thesis.

### 1.1.1 Linear Regime

The CMB shows that the Universe at Recombination (i.e. at redshift<sup>1</sup>  $z \sim 1500$ ) was extremely uniform but with spatial fluctuations in the energy density of roughly one part in  $10^5$ . Such small fluctuations, generated in the early Universe, grow over time due to gravitational instability, and eventually lead to the formation of galaxies and the large-scale structure observed in the present Universe. The small density fluctuations can be described by the density contrast defined as  $\delta(\mathbf{x}, t) = (\rho(\mathbf{x}, t) - \bar{\rho}(t))/\bar{\rho}(t)$  where  $\bar{\rho}(t)$  is the average background density,  $\rho(\mathbf{x}, t)$  is the density perturbation and  $\mathbf{x}$  is the comoving distance. Initially the small fluctuations are well in the linear regime since the density contrast is small  $\delta \sim 10^{-5} \ll 1$ . The spatial form of the initial density fluctuations can be described in Fourier space, in terms of Fourier components as:

$$\delta_{\mathbf{k}} = \int d^3\mathbf{x} \delta(\mathbf{x}) e^{-i\mathbf{k}\cdot\mathbf{x}} \quad (1.1)$$

<sup>1</sup>  $z$  is the cosmological redshift defined as the relative difference between the wavelength observed,  $\lambda_o$ , and emitted,  $\lambda_e$ , by an object:  $z = \frac{\lambda_o - \lambda_e}{\lambda_e}$

Inflation generates perturbations given by a Gaussian random field, in which different  $k$ -modes are statistically independent. In the linear regime ( $\delta \ll 1$ ) the temporal evolution of the density contrast can be described as (Longair 2004):

$$\frac{d^2\delta(t)}{dt^2} + 2\left(\frac{\dot{a}}{a}\right)\frac{d\delta(t)}{dt} = \delta(4\pi G\rho - k^2 c_s^2) \quad (1.2)$$

where  $c_s$  is the sound speed,  $a = (1+z)^{-1}$  is the scale factor describing the expansion of the Universe,  $G$  is the gravitational constant, and  $k$  is the wavenumber that describe the spatial-scale of the perturbation. The second term on the left is the *Hubble drag* term that describes how expansion suppresses perturbation growth, the third component is the *gravitational term* that promotes perturbation growth and the last term is the *pressure term*. If we ignore the expansion of the Universe in Eq.1.2, the linearised fluid equations reduce to a wave equation:

$$\frac{d^2\delta(t)}{dt^2} = \delta(4\pi G\rho - k^2 c_s^2) \quad (1.3)$$

with the following dispersion relation:

$$\omega^2 = (k^2 c_s^2 - 4\pi G\rho) \quad (1.4)$$

The case  $\omega^2 = 0$  identifies a characteristic mode,  $k_J$ , which translates into a characteristic scale,  $\lambda_J = 2\pi/k_J$ , the Jeans length:

$$\lambda_J = c_s \left(\frac{\pi}{G\rho}\right)^{1/2} \quad (1.5)$$

For  $\lambda < \lambda_J$  the pressure force opposes the gravity and the density contrast oscillates as a sound wave. If  $\lambda > \lambda_J$  the oscillations are unstable and grow exponentially with time. We can associate a characteristic mass to the Jeans length, i.e. the Jeans mass,  $M_J$ , which represents the mass of the structure that will form in an over-dense region with diameter  $\lambda_J/2$  (Longair 2004):

$$M_J = \left(\frac{\pi}{48}\lambda_J^3\rho\right) \quad (1.6)$$

In perturbations with mass  $\gg M_J$  the pressure force is not counteracted by gravity hence they grow. The Jeans length and the Jeans mass depend on the sound speed, which varies through cosmic epochs, so  $\lambda_J$  and  $M_J$  evolve.

After Recombination and assuming  $\lambda \gg \lambda_J$ , we can ignore the pressure term in the linearised equation (Eq.1.2) and solve:

$$\frac{d^2\delta(t)}{dt^2} + 2\left(\frac{\dot{a}}{a}\right)\frac{d\delta(t)}{dt} = \delta(4\pi G\rho) \quad (1.7)$$

For the Einstein de Sitter Universe, which is valid for  $z \gg 1$  and  $\Omega_m \gg 1$ , we find the solution:

$$\delta(t) \propto t^{3/2} \propto a \propto \frac{1}{1+z} \quad (1.8)$$

The general solution in the linear regime for the density perturbations growth is  $\delta = \delta_0 D(z)$  where  $\delta_0$  is the density field linearly extrapolated to  $t = t_0$  and  $D(z)$  is (Carroll 2001):

$$D(z) = \frac{5\Omega_m(z)}{2(1+z)} \left( \frac{1}{70} + \frac{209}{140}\Omega_m(z) - \frac{\Omega_m^2(z)}{140}\Omega_m^{4/7}(z) \right)^{-1} \quad (1.9)$$

where

$$\Omega_m(z) = \frac{\Omega_m(1+z)^3}{\Omega_m(1+z)^3 + \Omega_\Lambda} \quad (1.10)$$

The equations that describe the growth of density perturbations in the linear regime can be divided into the dark matter and the baryonic component. Since the dark matter particles interact very weakly with the other particles, the dark matter perturbations began to grow in earlier epoch than the baryonic ones. However after Recombination the baryons fall into the dark matter potential well and their density contrast rapidly reaches the one of the dark matter (e.g. Longair 2004).

Density perturbations continue to grow until to  $\delta \gtrsim 1$  where the linear perturbation theory is not longer valid and the density perturbations enter in the non-linear regime.

### 1.1.2 Non-linear regime

The small density fluctuations grow over time as described in the previous section, until the perturbation  $\delta$  becomes of order unity, and the full non-linear gravitational problem must be considered. The model used to describe the growth of perturbations in the non-linear regime is the top-hat spherical collapse model that assumes a highly idealised system (e.g. Padmanabhan 1993). Since after Recombination the Universe is dark matter dominated, the top-hat model assumes that the Universe is homogeneous except for a single “top-hat” spherical dark matter perturbation with constant  $\delta$ . In the spherical top-hat model, the evolution of each spherical shell can be described by the equation:

$$\frac{1}{2} \left( \frac{dr}{dt} \right)^2 - \frac{GM}{r} = E \quad (1.11)$$

where  $M$  is the mass enclosed by a shell of radius  $r$ , which is defined as  $M(< r) = \frac{4}{3}\pi r^3 \bar{\rho}(1 + \delta(t))$ . The mass shell is able to collapse if  $E < 0$ , in this case the parametric solutions are:

$$r = A(1 - \cos \theta) \quad t = B(\theta - \sin \theta) \quad (1.12)$$

with

$$A = \frac{GM}{2|E|} \quad B = \frac{GM}{(2|E|)^{3/2}} \quad (1.13)$$

The maximal expansion radius of the shell,  $r_{max}$ , is reached when  $\theta = \pi$ . After this “turn-around” radius the shell starts to contract. By using the energy conservation and assuming the Einstein de Sitter Universe, we get that the turn-around radius only depends on the initial overdensity, i.e.,  $r_{max} = r_i/\delta_i$  and we can see that smaller perturbations collapse first, which directly leads to the hierarchical formation scenario. The collapse occurs when  $\theta \rightarrow 2\pi$  which correspond to  $r(t) \rightarrow 0$  at the time  $t_{coll} = 2 t_{max}$  where  $t_{max} = t(\pi)$ . This assumption breaks down for a real system because it corresponds to  $\delta(t = t_{coll}) \rightarrow \infty$ . However, N-body simulations show that in a real systems with no uniform over-density, during the collapse, the shells start to oscillate and cross each other finally reaching a virial equilibrium (e.g. Mo et al. 2010). The process results in a virialized dark matter halo, whose properties can be described as a function of its mass,  $M$ , and the virialization redshift  $z = z_{vir}$  (Barkana & Loeb 2001). For the virial radius,  $r_{vir}$  we have:

$$r_{vir} = 0.784 \left( \frac{M}{10^8 h^{-1} M_\odot} \right)^{1/3} \left( \frac{\Omega_m}{\Omega_m(z)} \frac{\Delta_c}{18\pi^2} \right)^{-1/3} \left( \frac{1+z}{10} \right)^{-1} h^{-1} \text{kpc} \quad (1.14)$$

and the corresponding velocity,  $v_{vir} = \left(\frac{GM}{r_{vir}}\right)^{1/2}$  :

$$v_{vir} = 23.4 \left(\frac{M}{10^8 h^{-1} M_\odot}\right)^{1/3} \left(\frac{\Omega_m}{\Omega_m(z)} \frac{\Delta_c}{18\pi^2}\right)^{1/6} \left(\frac{1+z}{10}\right)^{1/2} \text{ km s}^{-1} \quad (1.15)$$

Finally the binding energy of the halo,  $E_b = \frac{1}{2} \frac{GM^2}{r_{vir}}$  is:

$$E_b = 5.45 \cdot 10^{53} \left(\frac{M}{10^8 h^{-1} M_\odot}\right)^{5/3} \left(\frac{\Omega_m}{\Omega_m(z)} \frac{\Delta_c}{18\pi^2}\right)^{1/3} \left(\frac{1+z}{10}\right) h^{-1} \text{ erg}. \quad (1.16)$$

Assuming that at turn-around, all the energy is potential energy,  $U$ , and applying the scalar virial theorem,  $U = -2K$ , where  $K$  the kinetic energy, one finds that the virial radius  $r_{vir}$  is half of  $r_{max}$ , while the density  $\rho_{vir} = 8 \rho_{max} = 8 \rho(t_{max}) \sim 178 \bar{\rho}(t_{coll})$ . Therefore, the final overdensity relative to the critical density at the collapse redshift is  $\Delta_c = 18\pi^2 \approx 178$ , which is in agreement with N-body simulations.

### 1.1.3 Mass distribution of dark matter halos

To understand when and where the first stars formed we need to identify which overdensities collapse and virialize forming dark matter halos. As we have seen the top-hat theory at the time of collapse lead to  $\delta(t_{coll}) = \infty$ . However, the theory of spherical collapse is simple and approximate. By extrapolating the precise and predictive results of the linear perturbation theory, we find that  $\delta_{lin} = 1.686$  at the time of the collapse predicted by the top-hat model (Padmanabhan 1993). We can therefore use this threshold, i.e the critical density of collapse,  $\delta_{cr}$ , and see how it varies over time to identify the regions that collapse or not. Thus in top-hat model the critical density of collapse varies in time as:

$$\delta_{crit}(z) = \frac{1.686}{D(z)} \quad (1.17)$$

Therefore the regions with  $\delta > \delta_{crit}(z)$  will collapse and produce virialized dark matter halos.

To go further we need to know the statistical properties of the density perturbations that are enclosed in the spectrum  $P(k)$  that is defined as  $P(k) = \langle |\delta_{\mathbf{k}}^2| \rangle$ . According to Inflationary theories the primordial power-law spectrum  $P_{in}(k) \propto k^n$  with  $n \sim 1$  and perturbations are given by a Gaussian random field. In order to determine the formation

of objects of a given size or mass it is useful to consider the statistical distribution of the smoothed density field. Using a window function  $W(\mathbf{y})$  normalized to 1, the smoothed density perturbation field,  $\int d^3\mathbf{y} \delta(\mathbf{x} + \mathbf{y}) W(\mathbf{y})$  itself follows a Gaussian distribution with zero mean. For the spherical top-hat model the window function is (Barkana & Loeb 2001):

$$W(kR) = 4\pi R^3 \frac{(\sin(kR) - kR \cos(kR))}{(kR)^3} \quad (1.18)$$

where  $W(kR) = 1$  in the sphere of radius  $R$  and zero outside. Therefore the mass variance is defined as the root-mean square of the density fluctuation:

$$\sigma^2(M) = \delta_M^2 = \frac{1}{2\pi} \int_0^\infty P(k) W^2(kR) k^2 dk \quad (1.19)$$

As we saw, according to spherical collapse model, regions in the linear density field with  $\delta > \delta_{crit}(z)$  have collapsed to produce virialized dark matter halos. How can we associate a mass to those halos, and how can we use the statistics of the linear density field to infer the halo mass function, i.e. the comoving number density of halos as a function of halo mass?

Press & Schechter (1974), using a simple analytical model, later refined by Bond et al. (1991), determined the abundance of halos with different masses across cosmic times. To do this they postulated that “the probability that  $\delta_M > \delta_{crit}$  is twice the mass fraction that at time  $t$  is contained in halos with mass greater than  $M$ ”. Therefore for a Gaussian random field, they found that the number of halos with masses in the range  $[M, M + dM]$  per comoving volume,  $n(M, t)dM$ , is:

$$n(M, z)dM = \left(\frac{2}{\pi}\right)^{1/2} \frac{\bar{\rho}}{M^2} \frac{\delta_{crit}(z)}{\sigma(M)} \exp\left(-\frac{\delta_{crit}^2(z)}{2\sigma^2(M)}\right) \left|\frac{d \ln \sigma(M)}{d \ln M}\right| dM \quad (1.20)$$

The number density of dark matter halos as a function of redshift  $z$  and halo mass  $M$  is shown in Fig.1.2. As we can see the low mass halos form earlier than the massive ones. In particular, at  $z = 20$  halos with  $M \sim 10^7 M_\odot$  are the most common. Even if they are not shown in Fig.1.2, halos with  $M \sim 10^6 M_\odot$  are even more common ( $n > 100$  per comoving  $\text{Mpc}^3$ ) and, as we will see after, they will host the first stars. Note also that the abundance of low mass halos does not evolve substantially with redshift while the abundance of massive halos is a very strong function of redshift. This is a manifestation of hierarchical structure formation that is typical of CDM models. In this bottom-up

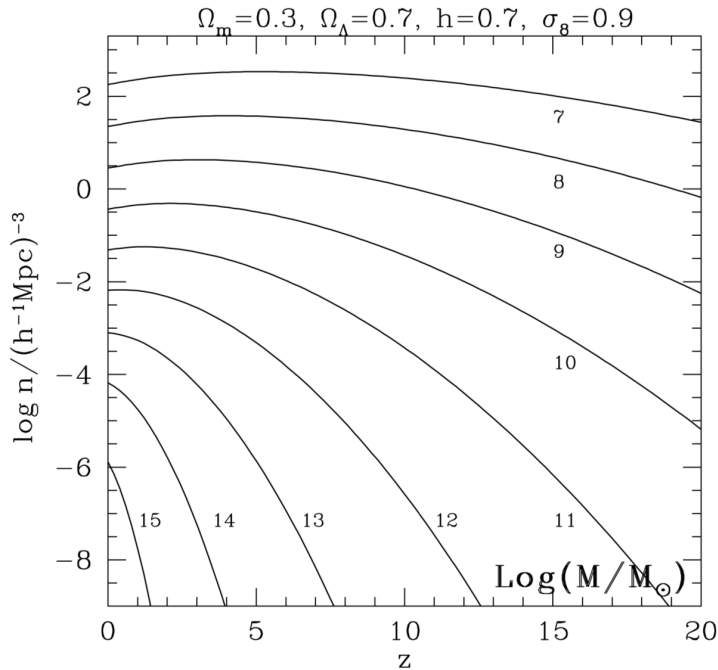


Figure 1.2: Comoving number density of dark matter halos as a function of redshift. A standard  $\Lambda$ CDM model has been assumed, with parameters indicated above the panel. The label on each curve indicates the halo mass  $\log(M/M_\odot)$  (from Mo & White 2002).

scenario, the low mass halos form early and they are quite common at every  $z$ , while larger halos form later, mainly through mergers of existing smaller objects.

## 1.2 Which halos can form stars?

As we have seen, within the framework of the  $\Lambda$ CDM model for cosmic structure formation, the first gravitationally bound structures have low masses. Once the mass of these gravitationally bound dark matter object exceeds the cosmological Jeans mass, pressure force can no longer prevent gas from falling into the potential well created by the dark matter. As already mentioned,  $M_J$  varies through cosmic time and, using a perturbative approach, the Jeans mass after Recombination can be expressed as (Peebles 1993):

$$M_J = 3.08 \cdot 10^3 \left( \frac{\Omega_m h^2}{0.13} \right)^{-1/2} \left( \frac{\Omega_b h^2}{0.022} \right)^{-3/5} \left( \frac{1+z}{10} \right)^{3/2} M_\odot \quad (1.21)$$

However, we would like to emphasise that  $M > M_J$  only represents a necessary but not sufficient condition for the gas to collapse and form stars. In fact, during the virialization process, the infalling gas, consisting in mixture of hydrogen and helium, develops shocks and gets heated to a temperature at which pressure balance prevent further collapse. The



gas reaches the virial equilibrium with the dark matter component at the temperature given by:

$$T_{vir} = 1.98 \cdot 10^4 \left( \frac{\mu}{0.6} \right) \left( \frac{M}{10^8 h^{-1} M_{\odot}} \right)^{2/3} \left( \frac{\Omega_m}{\Omega_m(z)} \frac{\Delta_c}{18\pi^2} \right)^{1/3} \left( \frac{1+z}{10} \right) \text{ K} \quad (1.22)$$

where  $\mu$  is the mean molecular weight and  $m_p$  is the proton mass. Then, the gas has to cool down to form stars. If the gas were unable to cool, there would be no further collapse, and consequently no gas fragmentation and star formation. The gas would simply persist in hydrostatic equilibrium, roughly tracing the density profile of the dark matter. The sufficient condition for efficient gas cooling is that the cooling time,  $t_{cool}$  is lower than the free-fall time,  $t_{ff}$  defined as:

$$t_{ff} = \left( \frac{3\pi}{32G\rho} \right)^{1/2} \quad (1.23)$$

$$t_{cool} = \frac{3kT}{2n\Lambda(T)} \quad (1.24)$$

where  $\Lambda(T)$  is the cooling function that is show in Fig.1.3. The main available coolant in pristine gas at low  $T < 10^4\text{K}$  is molecular hydrogen,  $H_2$  (see Fig.1.3). These are the first dark matter halos ( $T_{vir} < 10^4 \text{ K}$ ) with  $M \sim 10^6 M_{\odot}$  that virialize at  $z_{vir} \sim 20$ : the so-called *minihalos*. In the primordial Universe the dominant  $H_2$  formation process is:



where free electrons act as catalysts. The cooling of gas through  $H_2$  takes place through roto-vibrational transitions. When  $H_2$  molecule gets rotationally and vibrationally excited by collisions with another  $H_2$  molecule or with an  $H$  atom, excited  $H_2$  molecule can de-excite radiatively or collisionally. However, since  $H_2$  molecule has no permanent dipole moment, rotational transitions cannot occur via rapid electric dipole transition but only slow magnetic quadrupole radiation, therefore,  $H_2$  is a poor coolant (Bromm et al. 2002).

The ability of halos to cool and form stars depend on the abundance of  $H_2$ . In particular Tegmark et al. (1997) found that the  $H_2$  fraction,  $f_{H_2}$ , strongly depends on the halo mass. Therefore not all the halos that satisfy the condition  $M > M_J$  manage to effectively cool the gas and form stars. Tegmark et al. (1997) found that  $f_{H_2}$  needed for *minihalos* with  $T_{vir} \lesssim 10^4 \text{ K}$  to collapse in a Hubble time is almost independent to virialization redshift

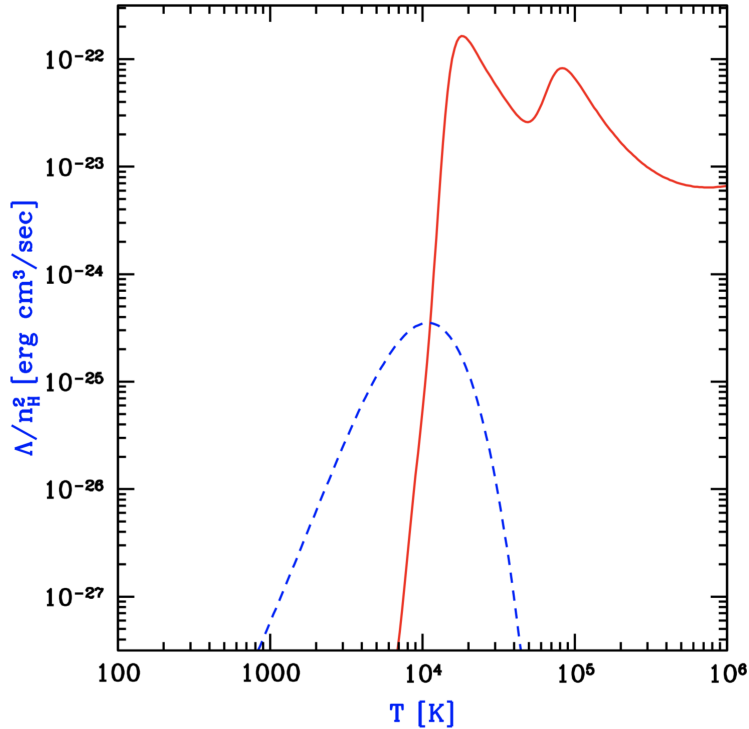


Figure 1.3: Cooling rates as a function of temperature for a primordial composition gas in the absence of any external radiation. The solid line shows the cooling curve for atomic gas, the dashed line shows the additional contribution of molecular  $H_2$  cooling (Barkana & Loeb 2001).

between  $25 \lesssim z_{vir} \lesssim 100$ : any cloud with  $f_{H_2} \gtrsim 5 \cdot 10^{-4}$  is able to cool in an Hubble time and form stars. Since the fraction of molecular hydrogen depends on the mass of the virialized halo, this translate into a minimum mass needed to cool down the gas and form stars.

This is shown in Fig.1.4 as a function of virialization redshift. The white area shows the halos in which the collapse of the gas can efficiently occur, since  $t_{cool} < t_{ff}$ : these halos will form luminous objects. The red part describes halos in which the cooling is inefficient since  $H^-$ , necessary for  $H_2$  formation, gets destroyed by CMB photons. The dashed lines correspond to halos with virial temperature of  $T_{vir} = 10^4 K$  and  $T_{vir} = 10^3 K$  (see Eq.1.22), while the solid line corresponds to  $3\sigma$  fluctuations of the density field in  $\Lambda$ CDM model. As we can see, for halos that correspond to  $3\sigma$  fluctuations of the density field the minimum mass needed to form the first stars, is  $M \gtrsim 10^6 M_\odot$  at  $z_{vir} \sim 20 - 30$ . This implies that the first star forming structures are low-mass halos with  $T_{vir} < 10^4 K$ .

### 1.3 Formation of the first stars

As discussed above, the ability of the gas in a halo to collapse and form stars depends on its ability to cool. The gas is compressionally heated to the virial temperature during the

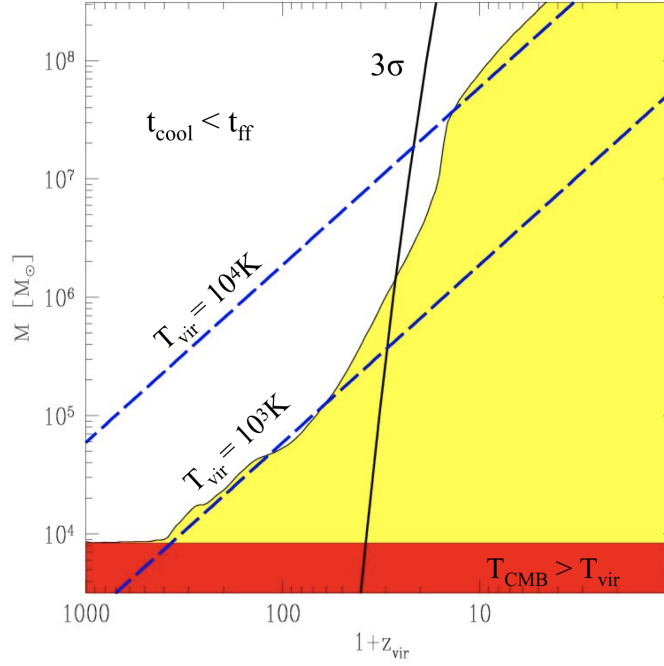


Figure 1.4: The mass of virialized dark matter halos is plotted as a function of virialization redshift for standard  $\Lambda$ CDM. Only halos that lie above the yellow area can collapse and form stars. The dashed straight lines correspond to  $T_{vir} = 10^4$  K and  $T_{vir} = 10^3$  K. In the red region no radiative cooling mechanism could help collapse, since  $T_{vir}$  would be lower than the CMB temperature. The solid line corresponds to  $3\sigma$  peaks in standard  $\Lambda$ CDM (Tegmark et al. 1997).

virialization process. Once sufficient molecular hydrogen  $H_2$ , is formed the gas goes into run-away cooling phase, which brings it down to the minimum temperature of  $T \sim 200$  K and numerical density  $n \sim 10^4 \text{ cm}^{-3}$  (see e.g. Greif 2015). In fact, the gravitational fragmentation of the gas clouds is found to be halted at a characteristic thermodynamic state that solely depends on the micro-physics of  $H_2$  molecules (e.g. Bromm 2000). The corresponding Jeans mass of this physical state is  $M_J \sim 1000 M_\odot$ . This is therefore predicted to be the typical mass of proto-stellar gas clouds formed in primordial composition gas, and it is roughly three order of magnitude larger than what is observed in local star-forming regions. This is a very solid result, which has been proven by several simulations of the first star formation in primordial *minihalos* with  $M \sim 10^6 M_\odot$ , that followed the evolution of both the dark matter and gas components, including  $H_2$  chemistry and cooling (e.g. Bromm 2000, Abel et al. 2001, Hirano et al. 2014, Klessen 2019).

After the proto-stellar gas clouds have formed on a scale of  $M_J \sim 1000 M_\odot$ , cold gas can accumulate in the center of the halo so that  $M > M_J$ . The gas becomes dynamically unstable and it starts to collapse. The collapse proceeds and the gas slowly heats up again. When the density becomes  $\gtrsim 10^8 \text{ cm}^{-3}$  the three body  $H_2$  formation becomes important and the gas turns fully molecular. Finally, a proto-star is formed in the center

of the *minihalo*. At the moment that protostar forms, its mass is less than  $0.01 M_{\odot}$ , but it is surrounded by dense, massive envelope of infalling gas with a mass of hundreds of solar masses. Accretion of this envelope is expected to occur at rapid rate. A useful estimate for protostellar accretion rate,  $\dot{M}_{acc}$ , can be derived by assuming that a Jeans mass worth of gas collapse on its free-fall timescale (Shu 1977, Omukai & Palla 2001):

$$\dot{M}_{acc} \approx \frac{M_J}{t_{ff}} \sim \frac{c_s^3}{G} \propto T^{3/2} \quad (1.26)$$

Since the temperature of the primordial gas ( $T \sim 200$  K) is larger than the one of local star-forming regions ( $T \sim 10$  K) the expected accretion rates are orders of magnitude larger. Ultimately, the first stars, given the larger proto-stellar gas clouds and the higher accretion rate, are expected to be more massive with respect to ones that form in local star-forming regions, which have  $m_{\star} = [0.1 - 100] M_{\odot}$ . This is confirmed by analytical calculations (McKee et al. 2003, Tan & McKee 2004) and cosmological simulation (e.g. Hosokawa et al. 2011, Hirano et al. 2014) that showed that the mass of the first stars is typically  $m_{\star} > 10 M_{\odot}$ , and can reach extreme values up to  $m_{\star} \approx 1000 M_{\odot}$ .

The accretion phase of primordial gas onto the proto-star and the resulting final stellar products, are substantially affected by different physical processes such as turbulence, stellar rotation and radiative feedback that are difficult to take into account all together in simulations. Current simulations of Pop III star formation (e.g. Smith et al. 2010, Clark et al. 2011, Stacy et al. 2013, Stacy et al. 2016, Hirano et al. 2014, Wollenberg et al. 2020, Sharda et al. 2021, Riaz et al. 2023, Chiaki & Yoshida 2022, Prole et al. 2022) demonstrate that primordial accretion disks are highly prone to fragmentation. Indeed, these results suggest that those primordial proto-stellar disks are ubiquitously driven towards gravitational instability and they indicate that the standard pathway of the first stars star formation leads to a stellar cluster with a wide distribution of masses, with typical masses lower than  $M_{\odot}$ , rather than the build-up of one single high-mass object (Klessen & Glover 2023). An example is illustrated in Fig.1.5, which shows the evolution of the accretion disks and the build-up of proto-stars within only about hundred years after the formation of the first object. We have to stress that these high resolution simulations follow the evolution for a very short time compared to the time scale of star formation. Hence we don't know if these fragments will eventually merge into the central object or can be thrown out and form long living first stars that may have survived until today. As a result of these highly unpredictable and stochastic events, the mass spectrum of the first stars is expected to cover a wide range of masses, possibly reaching down into the substellar regime.

---

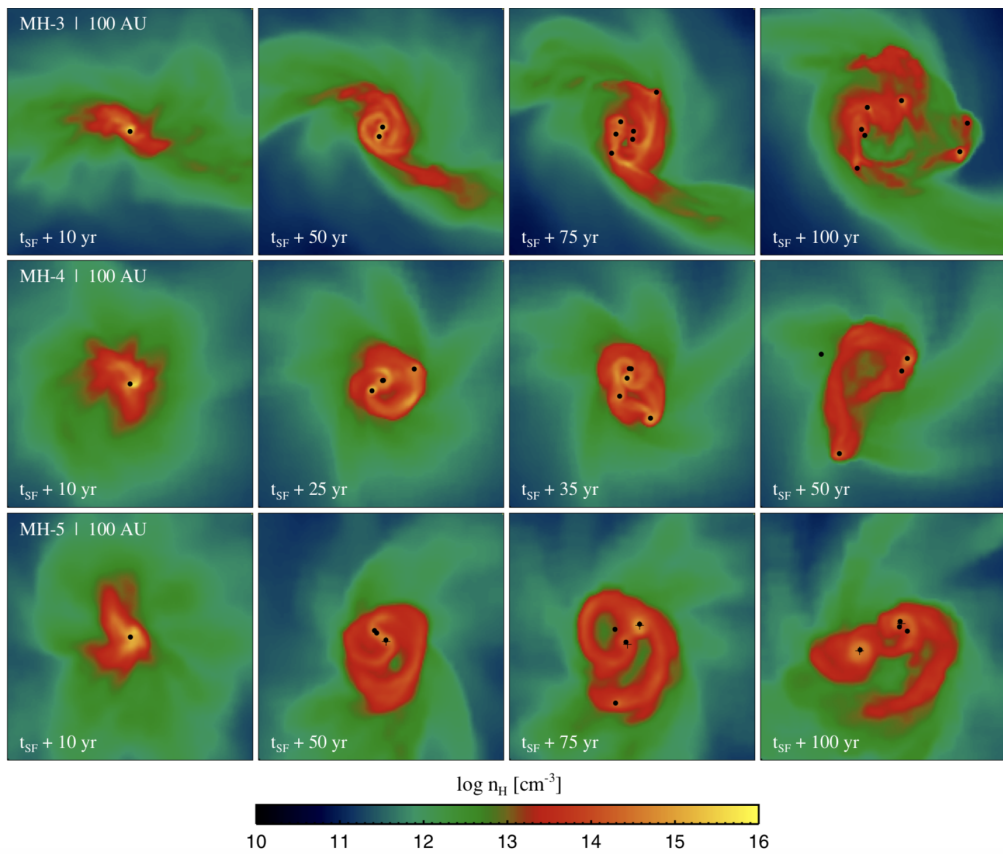


Figure 1.5: Formation of a proto-stellar cluster at the center of different *minihalos*. The panels show the density of hydrogen nuclei projected along the line of sight. Black dots and crosses denote protostars with masses below and above  $1 M_{\odot}$ , respectively (Greif et al. 2011).

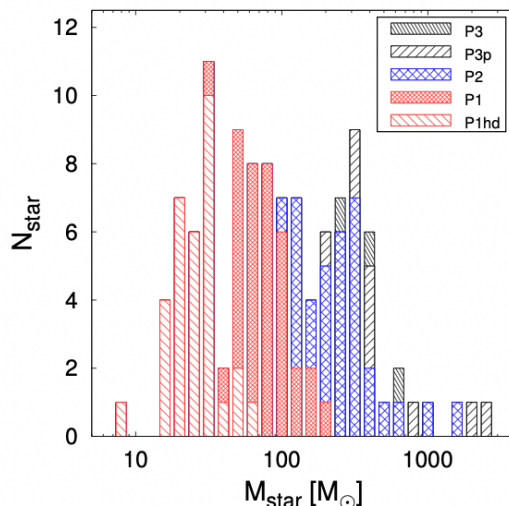


Figure 1.6: The final mass distribution of the first stars calculated 110 first stars. The red, blue, and black histograms represent the different paths of protostellar evolution; P1: KH contracting protostar (red), P2: oscillating protostar (blue), and P3: super-giant protostar (black). P1hd refers to the cases in which the gas clouds are formed by HD cooling and evolve on low-temperature tracks. P3p (predicted) indicates the same cases as P3, except that the final masses are calculated from a correlation between the properties of the cloud and the resulting stellar mass (Hirano et al. 2014).

## 1.4 Primordial stellar IMF

As we have seen the first stars formed out of a gas consisting in a mixture of hydrogen and helium only. For this reason they are expected to be metal-free and they are called Pop III stars. As discussed above, one of the puzzling questions regarding the first stars is their characteristic mass and their mass formation range, i.e. their initial mass function (IMF). The IMF is the function that describes the initial distribution of masses for a population of stars, i.e. the number of stars formed per mass bin. Due to the lack of observational constraints on the mass of the first stars, the primordial IMF of Pop III stars is very uncertain. Most of our current knowledge comes from theoretical models and numerical simulations.

For example, Hirano et al. (2014) performed 2D hydrodynamics simulations of primordial star formation in a fully cosmological context to derive the IMF of Pop III stars formed in thousands of *minihalos*. Their results are shown in Fig.1.6. As we can see, the resulting stellar masses range from  $m_* \sim [10 - 1000] M_\odot$ . Most of them are distributed around a few tens to a few hundreds solar masses. On the other hand, 3D simulations that follow the formation of the first stars for just hundred years (see Fig.1.5) found very different results (Fig.1.7): the stellar masses range of Pop III stars can vary from  $m_* = 0.1 M_\odot$  up to  $m_* = 10 M_\odot$ . Most of them are distributed around solar masses.

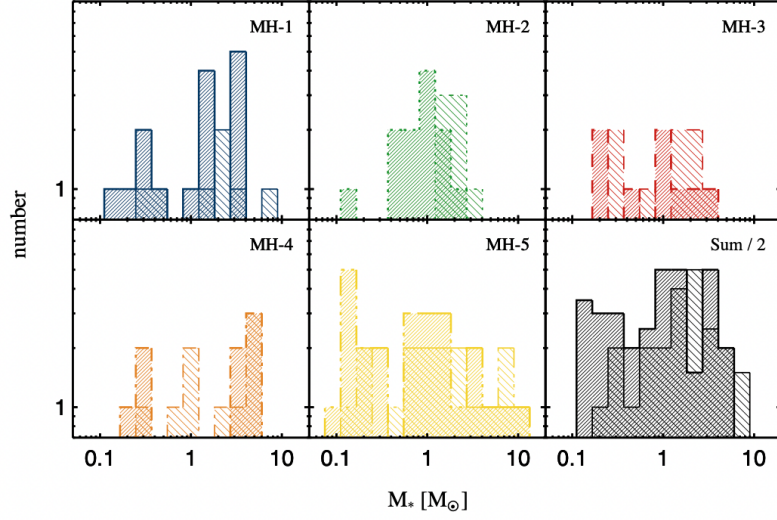


Figure 1.7: The mass distribution of the first stars derived by Greif et al. (2011) is shown after the first 1000 yr of continued accretion, for the 5 independent *minihalos* considered. The dark and light shadings distinguish the mass functions obtained for standard and adhesive sink particles, respectively. Despite very aggressive merging, a small cluster of protostars with a range of masses is formed even in the latter case. In the bottom right panel, we also show the cumulative mass functions obtained by summing up the contributions from the individual minihalos, and renormalized for better visibility. The resulting distribution is relatively flat between  $\sim 0.1 M_{\odot}$  and  $\sim 10 M_{\odot}$ , indicating that most of the mass is locked up in high-mass protostars.

To have a global picture in Fig.1.8 show the results of several simulations, giving an indication of the diversity of the current state of the art (Klessen & Glover 2023). In the Fig.1.8 has been showed the normalized (on the top) and the cumulative (on the bottom) stellar mass distribution obtained from six different studies of Pop III star formation: three high resolution without stellar feedback (Prole et al. 2022; Wollenberg et al. 2020; Stacy et al. 2013) and three simulations with radiative feedback included (Riaz et al. 2023; Hirano et al. 2015; Hirano et al. 2014). Models that include stellar feedback on average predict larger stellar masses than those without. In addition the outcome strongly depends on the spatial resolution achieved, on the time span covered, and on the details of the numerical implementation. High-resolution simulations tend to yield smaller stellar masses, because they are better able to resolve disk fragmentation but typically only cover a small fraction of the full accretion history of the halo. Similarly, simulations covering a large fraction of the halo collapse timescale do not resolve the inner accretion disk well, and therefore exhibit lower levels of fragmentation. Hence, they are biased towards higher-mass stars. Furthermore, two-dimensional simulations tend to report less fragmentation than full three-dimensional ones (Klessen & Glover 2023). Ultimately, we can assert that the IMF of Pop III stars is still largely uncertain.

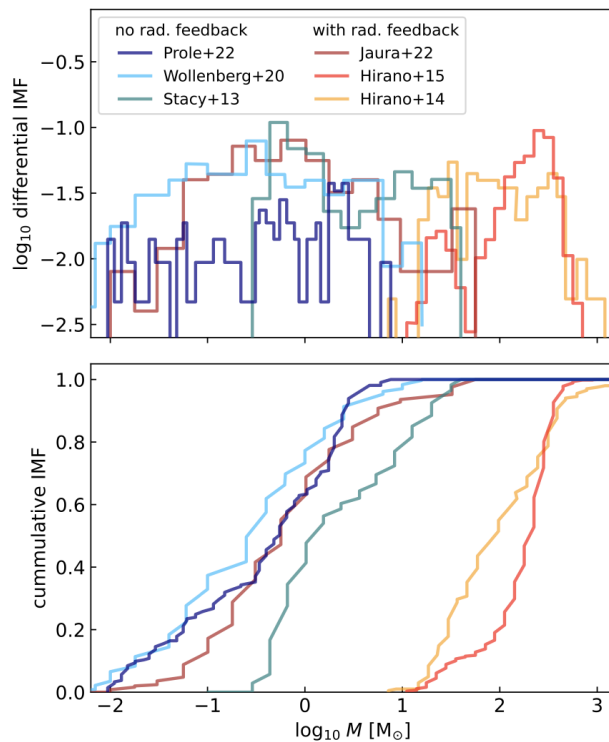


Figure 1.8: Normalized differential (top) and cumulative (bottom) stellar mass distribution obtained from six different studies of Pop III star formation (from Klessen & Glover 2023). To represent the current state-of-the art, three high-resolution models without stellar feedback have been selected (Prole et al. 2022; Wollenberg et al. 2020; Stacy et al. 2013) and three simulations with radiative feedback included (Riaz et al. 2023; Hirano et al. 2015; Hirano et al. 2014).

To a large degree, this is due to the fact that, unlike the stars that form today, no direct observations of first stars are available. This also makes it difficult to test theoretical models. Since the stellar mass determines its evolution, to understand their mass range, is important for clarifying the chemical evolution of the early Universe. Furthermore, if low-mass Pop III stars with  $m_{\star} < 0.8 M_{\odot}$  are able to form, they would have a lifetime greater than the age of the Universe and they could potentially be observed in the Local Universe.

## 1.5 Evolution of the first stars

As we have underlined in the previous section the typical mass of the first stars is very uncertain. This reflects our ignorance of the accretion phase in the primordial Universe. The result is that both the characteristic mass of the first stars and the range in mass in which they can form are still elusive. However, it is known that Pop III stars formed in a pristine environment which determines a different evolution of these metal-free stars with respect to those observed today. The major difference lies in the nuclear fusion



mechanism. The lack of carbon causes nuclear fusion to start the cycle with p-p cycle. However, the energy released by p-p chain fails to counteract the gravitational collapse. As a result of lower energy deposition, the star contracts, raising its temperature. When the central temperature reaches  $\sim 10^8$  K, some carbon has already formed and  $3\alpha$  reactions are allowed, and they release higher energy which cause the higher luminosity of the first stars. Several authors (e.g. Marigo et al. 2001; Woosley et al. 2002; Heger & Woosley 2004; Woosley 2017; Farmer et al. 2019), have investigated the evolution and the final fate of zero-metallicity stars, which is summarized in Fig.1.9.

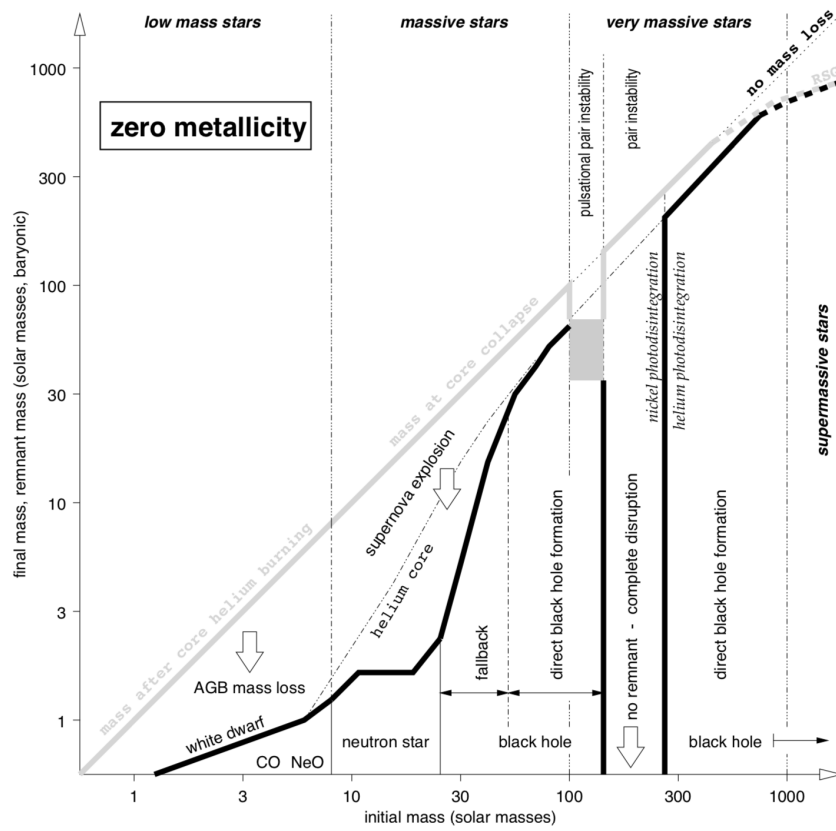


Figure 1.9: The final-fate of non-rotating primordial stars from Heger & Woosley (2002). The x-axis gives the initial stellar mass. The y-axis gives both the final stellar mass of the remnant (thick black curve) and the mass of the star when the event that produces that remnant begins.

Three regimes of initial mass can be distinguished:

- *low mass stars* ( $m_{\star} < 10 M_{\odot}$ ): they end as white dwarfs. During the asymptotic giant branch (AGB) the star loses its envelope becoming a CO or NeO white dwarf;
- *massive stars* ( $10 M_{\odot} \leq m_{\star} < 100 M_{\odot}$ ): These stars are defined as those that ignite carbon and oxygen burning non-degenerately. The hydrogen-rich envelope and parts of the helium core are ejected in a supernova (SNe) explosion. If the initial mass is  $m_{\star} \sim 25 M_{\odot}$  the remnant is a neutron star, while above black hole form.
- *very massive stars* ( $m_{\star} \geq 100 M_{\odot}$ ): these stars develop pair creation which makes them unstable after carbon burning (Woosley et al. 2002). They are called Pair Instability SNe (PISN) that have masses of  $140 M_{\odot} \leq m_{\star} \leq 260 M_{\odot}$  and they are completely disrupted in a nuclear-powered explosion, that leaves no remnants and releases all the initial stellar mass into the ISM.

## 1.6 Feedback processes

As soon as the first stars form, Pop III stars lead to dramatic change of the early Universe through production of ionizing photons and the first heavy chemical elements, synthesized during their evolution and dispersed into surrounding gas via SNe explosions and stellar winds. The feedback processes are usually divided in three classes which are not independent: radiative, mechanical and chemical feedback (e.g. Ciardi et al. 2001).

### 1.6.1 Radiative feedback

Radiative feedback is the process associated to the emission of ionizing and photo-dissociating photons produced by the first stars. This radiation can have both local and long-range effects. In particular, the radiative feedback can affect the same *minihalos* that host Pop III stars, but it can also affect the star formation in nearby objects. The ionizing radiation is produced by photons with  $h\nu > 13.6$  eV, while the photo-dissociation radiation is produced by photons in the so called Lyman-Werner (LW) band, i.e. with energy  $11.2$  eV  $< h\nu < 13.6$  eV.

The ionizing photons can have a strong effect on the subsequent star formation. In fact the UV radiation can heat the gas up to the virial temperature,  $T_{vir} \approx 10^4$  K, hence photo-evaporate the gas in *minihalos* with  $T_{vir} \lesssim 10^4$  K.

On the other hand, UV radiation increases the number of free electrons that enhances the  $H_2$  formation and hence star-formation (Johnson et al. 2007). In addition, due to

the increasing fraction of free electrons, another cooling channel becomes available: HD molecules, which form in the presence of UV radiation, can cool down the gas to lower temperature with respect to  $H_2$ .

Differently, photo-dissociating photons can easily destroy the  $H_2$  molecules. Therefore, LW radiation acts always as negative feedback reducing the gas cooling and hence the star formation. Nevertheless, several authors (e.g. Ciardi et al. 2001; Oh & Haiman 2002; Hartwig et al. 2015; Latif & Volonteri 2015; Regan & Downes 2018; Skinner & Wise 2020; Kulkarni et al. 2021), shows that the LW photons do not affect nearby star forming *minihalos* at  $z \sim 20$ . However, LW radiation will gradually arise through cosmic time, due to the increasing number of star formation events, and it will form a LW background. Ultimately, because of photo-dissociation from LW background the star formation is progressively quenched in *minihalos*.

### 1.6.2 Mechanical feedback

Not only the radiative feedback can quench the star formation in *minihalos*, also the mechanical feedback plays a crucial role. With mechanical feedback we refer to the mechanical energy injection by supernova explosions. The energy deposition associated with the first SNe explosions may induce partial or total gas removal from *minihalos* itself, thus suppressing star formation. The strength of mechanical feedback depends on the binding energy of the halo,  $E_b$ , (Eq.1.16) and on the kinetic energy released during the explosion,  $E_{kin}$ . The latter is given by (Barkana & Loeb 2001):

$$E_{kin} = f_{kin} N_{SN} \langle E_{SN} \rangle \quad (1.27)$$

where  $f_{kin}$  is the fraction of SNe explosion energy in kinetic form,  $N_{SN}$  is the number of SNe explosions in the halo, and  $\langle E_{SN} \rangle$  is the average SNe energy whose typical value is  $\sim 10^{51}$  erg for normal core-collapse SNe. If  $E_{kin} \ll E_b$  the halo can retain the products of SNe explosions (metals and gas) and the star formation can keep on going. On the other hand, if  $E_{kin} \gg E_b$  the gas is easily evacuated out of the galaxy and consequently the star formation can be halted. Low-mass halos with low binding energy such as *minihalos* can be strongly affected by mechanical feedback that suppress the subsequent star formation.

### 1.6.3 Chemical feedback

During the first SNe explosions and stellar winds, the primordial gas gets polluted with heavy elements. Once the first heavy elements are produced and dispersed by Pop III stars into the ISM, the physics and chemistry of subsequent star formation will be fundamentally changed. The presence of metals will provide efficient coolants, establishing

condition similar to the present-day Milky Way ISM in which “normal” stars form. The abundance of elements heavy than lithium present in the gas is usually described in terms of metallicity,  $Z = M_z/M_{gas}$ , where  $M_z$  is the mass of metals and  $M_{gas}$  is the mass of gas. It has been argued that there may exist a critical metallicity, governing the transition between metal-free stars, i.e. Pop III stars, and normal Population II/I (Pop II/I) stars,  $Z_{cr} = [10^{-6} - 10^{-4}] Z_{\odot}$ , where  $Z_{\odot}$  is the solar metallicity (Bromm et al., 2001). This range is determined by the fraction of metals locked in dust grains, which provide an additional cooling channel (e.g. Omukai et al. 2005; Chiaki et al. 2017). In conclusion, the chemical feedback establishes the transition between the primordial stars and “normal” Pop II/I stars. In this Thesis we will refer to Pop III stars as those formed out of  $Z \leq Z_{cr}$  gas. Those formed in an environment with  $Z > Z_{cr}$  will be considered as Pop II/I stars that form according to the present-day IMF.

---

---

## Stellar Archaeology and Dwarf galaxies

Unfortunately, Pop III stars are very hard to be individually observed in the high-redshift Universe since they formed in poorly star forming *minihalos* and they are likely too faint to be individually detected even with new-generation telescopes (Oh et al. 2001; Scannapieco et al. 2003; Riaz et al. 2022). Due to the lack of direct observations of the first stars, determining their properties is very difficult. However, ancient and metal-poor stars can be observed individually in the Local Group, from which we can *indirectly* infer their properties. In this Chapter we will describe how Stellar Archaeology can increase our knowledge about the first stars and where are the most promising places to find the most metal-poor stars and eventually long-lived Pop III stars.

### 2.1 Stellar Archaeology

Despite extensive observational searches, a truly Pop III star, i.e. with zero metallicity, has so far escaped from detection, confirming the hypothesis of a primordial IMF biased towards more massive stars than the present-day IMF (Salvadori et al. 2007; Magg et al. 2019). Massive Pop III stars explode as supernovae polluting the surrounding medium with their chemical products, whose yields depend upon the mass of the progenitor star along with the explosion energy (Nomoto et al. 2004; Heger & Woosley 2010). Hence, even if we cannot directly observe short-lived zero-metallicity stars, we can still catch their long-lived descendants (Keller et al. 2007; Starckenburg et al. 2018). Low-mass ( $m_{\star} \lesssim 0.8M_{\odot}$ ) (Pop II/I) stars, formed in environments enriched by the chemical products of the first stars to the critical metallicity value,  $Z > Z_{cr}$ , at which normal star formation is expected to proceed (Bromm et al. 2001; Schneider et al. 2003). These long-lived low-mass stars imprinted by Pop III SNe, the so-called first stars “descendants”, can survive until today and they can be individually observed in the oldest and the most metal-poor environments of our Galaxy and its dwarf galaxies satellites. In this context Stellar Archaeology operates: searching for the chemical signatures of the first stellar

Table 2.1: Denotation of metal-poor stars.

[Fe/H]	Term	Acronym
$< -1.0$	Metal-poor	MP
$< -2.0$	Very metal-poor	VMP
$< -3.0$	Extremely metal-poor	EMP
$< -4.0$	Ultra metal-poor	UMP
$< -5.0$	Hyper metal-poor	HMP
$< -6.0$	Mega metal-poor	MMP

generations in the photospheres of old ( $> 12$  Gyr) and *metal-poor* stars that dwell in our Galaxy and its ancient dwarf satellites. Since the chemical elements released in the interstellar medium by these pristine SNe, depend on their masses and on their energies, the study of the relative abundances of different chemical elements measured in the Pop III “descendants” can help to constrain the primordial IMF as well as the explosion energy of first supernovae.

## 2.2 Searching for metal-poor stars

Metallicity, i.e. the abundance of elements heavier than hydrogen and helium present in a star, is commonly used as a proxy for evolution. In particular, iron has a very distinctive nucleosynthesis channel (Woosley & Weaver, 1995), and well-traces the enrichment of the interstellar medium through the Milky Way’s evolution. Moreover, iron has numerous absorption lines that occur throughout stellar spectra, and hence can be measured very accurately at high spectral resolution. For these reasons, iron has traditionally been taken as a reference element to enable comparisons of the metallicity. Although the term metal-poor is not always synonymous with Fe-poor, a standard nomenclature of metal-poor stars has been defined by Beers & Christlieb (2005) for stars in different ranges of iron abundances<sup>1</sup> [Fe/H] as listed in Table 2.1.

### 2.2.1 Techniques

From the early 1960s to the present day, great steps forward have been made in the discovery of metal-poor stars, mainly thanks to dedicated surveys. Since metal-poor stars are rare, an important feature of these surveys is an efficient procedure to select metal-poor candidates. The process usually involves three major observational steps: (a) large-area

<sup>1</sup> [Fe/H] =  $\log(N_{\text{Fe}}/N_{\text{H}}) - \log(N_{\text{Fe}}/N_{\text{H}})_{\odot}$ , where  $N_{\text{Fe}}$  ( $N_{\text{H}}$ ) is the number of iron (hydrogen) atoms and  $\log(N_{\text{Fe}}/N_{\text{H}})_{\odot}$  is the solar abundance

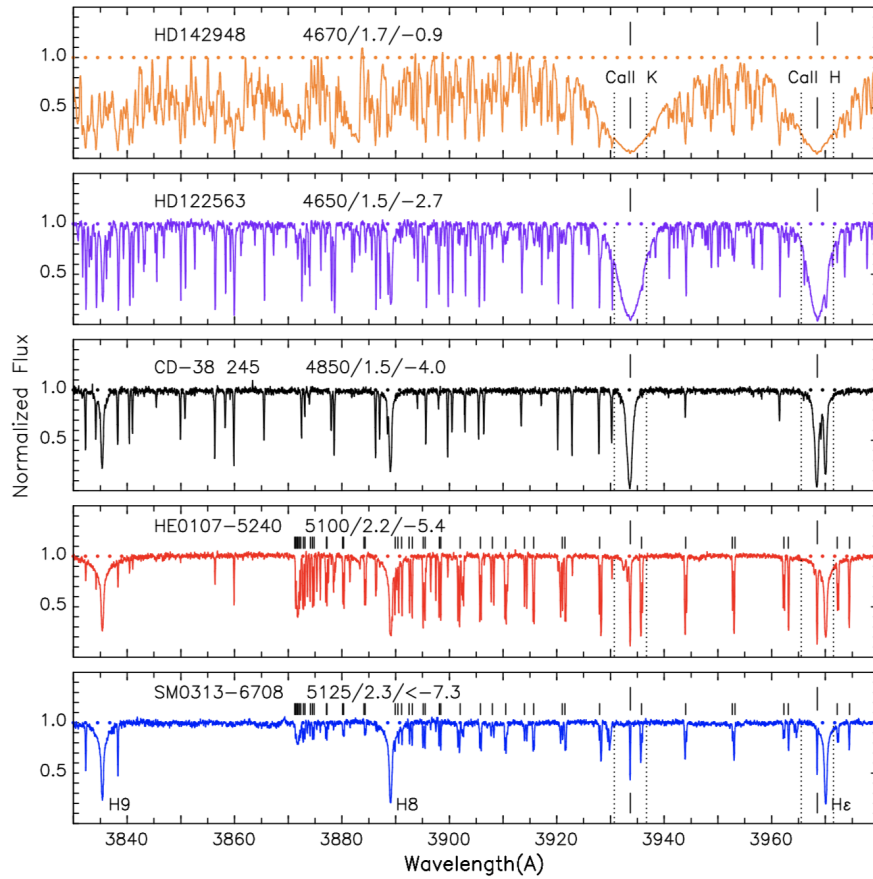


Figure 2.1: Spectra of metal-poor stars. The numbers in each panel to the right of the star’s identification represent the atmospheric parameters: temperature, logarithmic surface gravity value and  $[\text{Fe}/\text{H}]$  (Frebel & Norris 2015).

photometric or low-resolution spectroscopic surveys are used to give first estimate of the stellar metallicity and to select candidate metal-poor stars; (b) moderate-resolution spectroscopic follow-up observations of the candidates to validate the metal-poor stars among them; finally, (c) high-resolution spectroscopy of the most interesting candidates. The first step can be carried out in many different ways, for example, with proper-motion surveys or colorimetric surveys. The HK survey (Beers et al. 1985) and the Hamburg/ESO survey (HES, Wisotzki et al. 2000; Christlieb et al. 2004), select and collect large samples of such a stellar population. Here, as a preliminary step, simultaneously large numbers of low-resolution spectra (resolving power  $R = \lambda/\Delta\lambda \sim 400$ ) are obtained through the examination of the strength of the CaII K line, which is the strongest resonance line in the optical spectra of stars. The HK and HES projects each covered more than 7500 square degrees of the Northern and Southern sky. The promising metal-poor candidates are then observed at intermediate/high resolution ( $R \sim 2000/20000$ ) to obtain their stellar metallicity. Since CaII K line is the strongest atomic feature in the spectra of metal-

Table 2.2: Ultra metal-poor star of the Galactic halo.

Name	[Fe/H]	[C/Fe]	References
SMSS 031300.36-670839.3	$< -7.30$	$> +4.90$	Keller et al. (2014)
SDSS J0023+0307	$< -6.6$	$\lesssim +2.0$ ;	Aguado et al. (2018a)
HE 1327-2326	-5.66	+4.26	Frebel et al. (2005), Aguado et al. (2018b)
HE 0107-5240	-5.39	+3.70	Christlieb et al. (2004)
SDSS J103556+064144	$< -5.1$	$> +3.5$	Bonifacio et al. (2015)
SDSS J092912.32+023817.0	-4.97	+3.91	Caffau et al. (2016)
SDSS J102915+172927	-4.89	$< +0.93$	Caffau et al. (2011b)
HE 0557-4840	-4.81	+1.65	Norris et al. (2012)
Pristine 221.8781+9.7844	-4.66	$\leq +1.76$	Starkenburger et al. (2018)
SDSS J174259+253135	-4.8	+3.6	Bonifacio et al. (2015)
HE 0233-0343	-4.68	+3.46	Hansen et al. (2015)
SDSS J131326.89-001941.4	$-4.3 \sim -5.0$	$+2.5 \sim +3.0$	Prieto et al. (2015), Frebel et al. (2015)
2MASS J18082002-5104378	-4.1	$\lesssim +0.5$	Meléndez et al. (2016)

poor stars typically it is used to derive the stellar iron abundance [Fe/H]. An example of metal-poor stars spectra is shown in Fig.2.1 which presents high-resolution, high-S/N spectra of five metal-poor red giant stars, all having approximately the same effective temperatures and surface gravities, but with very different heavy element abundances, decreasing as one moves from top to bottom in the Figure. We can see that the CaII H and K lines decrease markedly as one moves from the top ([Fe/H] = -0.9), to the middle ([Fe/H] = -4.0) panel. Note that the Ca II H and K lines become very weak in the two most iron-poor stars and many more lines have appeared. Hence observing these stars is very challenging.

### 2.2.2 Milky Way Metal-Poor stars

Metal-poor stars have been discovered in the ancient environments of Milky Way such as the bulge, the halo as well as in dwarf galaxy satellites of the Milky Way. The first surveys looking for metal-poor stars have been carried out in the Galactic stellar halo, which is expected to be the most metal-poor component. The investigation into metal-poor stars has uncovered a remarkable rarity: only 12 stars with [Fe/H]  $< -4$  have been found in Milky Way's halo listed in Table 2.2. As we can see, the most iron-poor star has been found by Keller et al. (2014) with only an upper limit on Iron, [Fe/H]  $\lesssim -7.3$ . We can have a global picture if we look at the halo metallicity distribution function (MDF), i.e. the number of stars as a function of their [Fe/H] (see Fig.2.2). On the left panel of Fig.2.2, Bonifacio et al. (2021) show the comparison between the MDF of spectroscopic sample (black) and the bias-corrected one (red line) (see Bonifacio et al. 2021 for



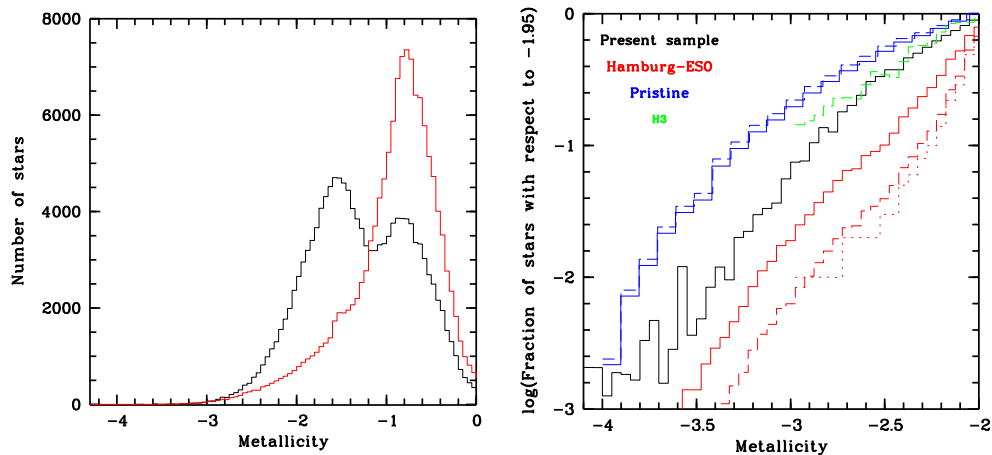


Figure 2.2: Raw metallicity distribution function (black line) and bias-corrected (red line) (Bonifacio et al. 2021) (left panel). Metal-weak tail of the corrected metallicity distribution function (black line), normalised at  $[\text{Fe}/\text{H}] = -1.95$ , compared with the corrected Hamburg/ESO (Schörck et al. 2009) (red) and the corrected Pristine (blue) MDFs (Youakim et al. 2020) (right panel).

details). From Fig.2.2 it is clear that the Galactic halo MDF is a rapidly declining function with decreasing  $[\text{Fe}/\text{H}]$ , implying that to find metal-poor stars is quite challenging. This is even more evident looking at the right panel of Fig.2.2 where the authors show metal-weak tail of the corrected MDF, normalised at  $[\text{Fe}/\text{H}] = -1.95$ , compared with the corrected Hamburg/ESO (Schörck et al. 2009) and the corrected Pristine (Youakim et al. 2020) MDFs. Yet, despite their rarity, metal-poor stars represent a unique observational opportunity to explore the early Universe and to provide constraints on the nature of the first stars and their initial mass function (e.g de Bressana et al. 2017).

### 2.2.3 Carbon-Enhanced Metal Poor (CEMP) stars

Among metal-poor stars at  $[\text{Fe}/\text{H}] < -2$ , the best-known type of chemically interesting stellar object is the *carbon-enhanced metal-poor* (CEMP) class (first noted by Beers et al. 1992), which has  $[\text{C}/\text{Fe}] > +0.7$  (Beers & Christlieb 2005; Aoki et al. 2007). This class can be divided into two main populations: (i) carbon-rich stars that also exhibit an excess in heavy elements formed by the slow neutron-capture processes, having  $[\text{Ba}/\text{Fe}] > 1$  and named CEMP-s stars, and (ii) carbon-rich stars with no excess of the heavy elements, having  $[\text{Ba}/\text{Fe}] < 0$  and known as CEMP-no stars. The CEMP-s stars are commonly assumed to be chemically enriched by mass transfer from a binary companion star that has gone through the Asymptotic Giant Branch (AGB) phase (Abate et al., 2015) and these objects are preferentially found in binary systems (Lucatello et al. 2005; Starkenburg et al. 2013; Hansen et al. 2016). On the other hand, CEMP-no stars are not primarily found in binary systems (Lucatello et al. 2005; Starkenburg et al. 2013; Hansen

et al. 2016) and even those that have a binary companion (Arentsen et al., 2020) show high values of  $^{12}\text{C}/^{13}\text{C}$ , which implies that the surface composition has not been altered by mass transfer (see Aguado et al. 2022, 2023). Hence the C-excess in CEMP-no stars is expected to be representative of the ISM out of which they formed, which was likely primarily polluted by the first stellar generations (Salvadori et al. 2015; de Bressan et al. 2017). Among metal-poor stars, CEMP stars are very frequent, this is particularly evident by inspecting Fig.2.3. In Fig.2.3, we present the main properties of Galactic halo sample (Cayrel et al. 2004; Christlieb et al. 2004; Norris et al. 2007; Caffau et al. 2011a; Yong et al. 2013a; Keller et al. 2014; Hansen et al. 2015; Frebel & Norris 2015; Bonifacio et al. 2015; Li et al. 2015; Bonifacio et al. 2018; François et al. 2018; Starkenburg et al. 2018; Aguado et al. 2019; Ezzeddine et al. 2019). The MDF peaks at  $[\text{Fe}/\text{H}] \sim -3$  and it extends down to  $[\text{Fe}/\text{H}] < -7$ . In the middle panel, we show  $[\text{C}/\text{Fe}]$  with respect to  $[\text{Fe}/\text{H}]$ , with observational errors or upper/lower limits, distinguishing between C-normal ( $[\text{C}/\text{Fe}] \leq +0.7$ ) and CEMP-no stars ( $[\text{C}/\text{Fe}] > +0.7$ ). The  $[\text{C}/\text{Fe}]$  abundance ratios increase as  $[\text{Fe}/\text{H}]$  decreases, and all stars at  $[\text{C}/\text{Fe}] \lesssim -5$  are C-enhanced. Finally, in the bottom panel of Fig. 2.3 we present the CEMP fraction, with the poissonian error computed as  $\sqrt{N_{\text{CEMP}}}/N$ , where  $N$  is the total number of stars and  $N_{\text{CEMP}}$  the number of CEMP-no stars in each  $[\text{Fe}/\text{H}]$  bin. As it is evident, the CEMP fraction increases strongly with decreasing  $[\text{Fe}/\text{H}]$ : it is around 1 for  $[\text{Fe}/\text{H}] \lesssim -5$ , 0.7 for  $[\text{Fe}/\text{H}] \sim -4$ , and 0.3 for  $[\text{Fe}/\text{H}] \sim -3$ , which is consistent with other studies (Placco et al. 2014; Arentsen et al. 2022).

## 2.2.4 Stellar chemical abundances

The study of the measured chemical abundance ratios of metal-poor stars can insight on their origin and on their possible connections with the first generation of stars. In Fig. 2.4, the mean chemical abundance ratios with respect to iron,  $[\text{X}/\text{Fe}]^2$ , for the CEMP-no (red) and C-normal (grey) stars of literature sample have been shown, distinguishing between  $[\text{Fe}/\text{H}] \leq -4$  (left) and  $[\text{Fe}/\text{H}] \in (-4; -2]$  (right). In the case of  $[\text{Fe}/\text{H}] \leq -4$ , both abundance averages excluding (filled points, error bars) and including (open symbols, arrows) upper/lower limits on  $[\text{X}/\text{Fe}]$  have been included. When  $[\text{X}/\text{Fe}]$  has more upper than lower limits an arrow pointing down (or vice versa) has been put. Moreover, measurements that only have upper limits in both  $[\text{Fe}/\text{H}]$  and  $[\text{X}/\text{H}]$  have been included.

The first thing to note from Fig. 2.4 is that CEMP-no stars have mean C, N and O abundance ratios that are typically much higher than those of C-normal stars.

However, it should point out that more than 60% of the measured  $[\text{N}/\text{Fe}]$  and  $[\text{O}/\text{Fe}]$  for  $^2 [\text{X}/\text{Fe}] = \log(N_{\text{X}}/N_{\text{Fe}}) - \log(N_{\text{X},\odot}/N_{\text{Fe},\odot})$ , where  $N_{\text{X}}$  and  $N_{\text{Fe}}$  are the abundances of elements X and iron and  $N_{\text{X},\odot}$  and  $N_{\text{Fe},\odot}$  are the solar abundances of these elements (Asplund et al. 2009).

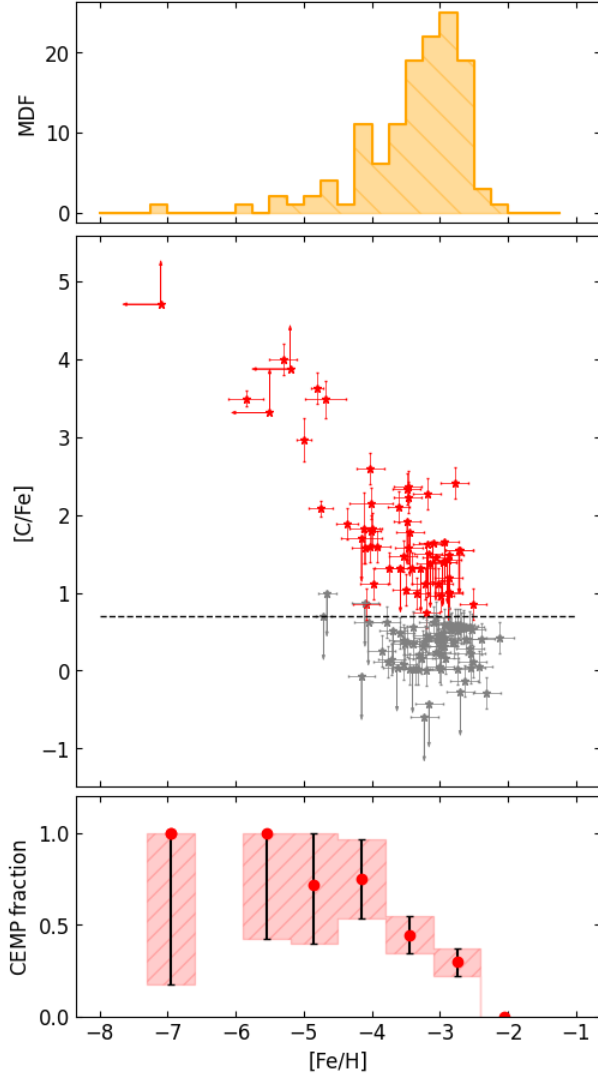


Figure 2.3: Properties of literature Galactic halo sample Yong et al. 2013a; Cayrel et al. 2004; Christlieb et al. 2004; Norris et al. 2007; Caffau et al. 2011a; Hansen et al. 2015; Keller et al. 2014; Frebel & Norris 2015; Bonifacio et al. 2015; Li et al. 2015; Bonifacio et al. 2018; François et al. 2018; Starkenburg et al. 2018; Aguado et al. 2019; Ezzeddine et al. 2019 . *Top panel:* Metallicity Distribution Function (MDF). *Middle panel:*  $[C/Fe]$  vs  $[Fe/H]$  for CEMP-no (red) and C-normal (grey) stars, corrected for the evolutionary status (Placco et al., 2014). The observational errors are shown, and the upper/lower limits are presented with arrows. *Bottom panel:* CEMP-no fraction, with the poissonian errors. From Vanni et al. 2023 (submitted MNRAS).

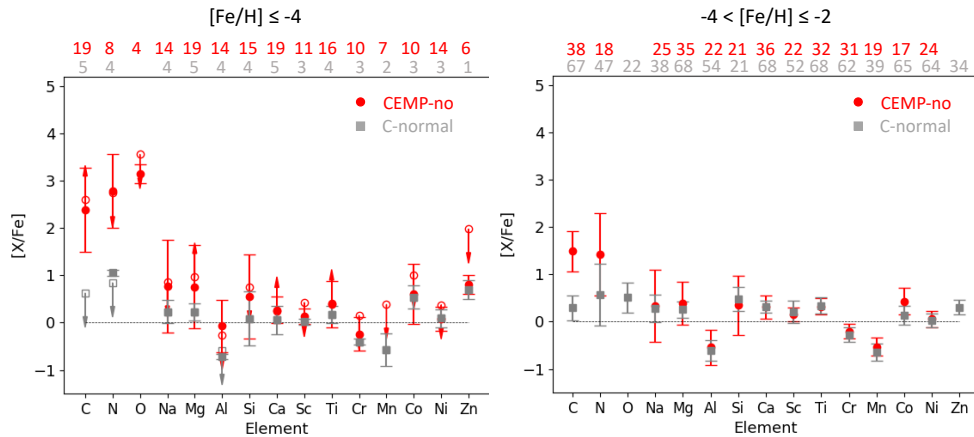


Figure 2.4: Mean abundance patterns for the stars in literature literature sample (see Sec.2.2.3) for CEMP-no (red points) and C-normal (grey points) stars, for  $[Fe/H] \leq -4$  (left), and  $\in (-4; -2]$  (right). On top are written the number of CEMP-no (red) and C-normal (grey) stars included for each chemical element. Filled points exclude limits, while open points include upper/lower limits. The error bar is the standard deviation of measurements, when there is only one observation we use the observational error. Measurements that present upper limits in both  $[Fe/H]$  and  $[X/H]$  are not included. The arrows point down if  $[X/Fe]$  has more upper than lower limits, and vice versa.

the CEMP-no stars are upper limits, hence their real values can be considerably lower than the ones represented here. Furthermore, at  $[Fe/H] < -4$ , the mean abundance ratios of many alpha-elements (e.g. Mg, Al, Si) over iron is higher in CEMP-no stars than in C-normal stars, while heavier elements (Co, Ni, Zn) are comparable between CEMP-no and C-normal stars. Finally, at  $-4 < [Fe/H] < -2$ , the mean abundance ratios of CEMP-no and C-normal stars are consistent among each other, with the only exception of C and N. Notably, CEMP-no stars typically have larger star-to-star scatter<sup>3</sup> than C-normal stars, even when the number of observed stars is similar or of the same order of magnitude (e.g. Na, Mg, Si, Al). In conclusion, the star-to-star scatter in the chemical abundance ratios of CEMP-no stars is large at  $-4 < [Fe/H] < -2$  and huge for  $[Fe/H] < -4$ . Conversely, C-normal stars show a small dispersion in their abundance ratios as already pointed out by Cayrel et al. (2004). For this reason, the star-to-star scatter can be used as a new path to understand which stars polluted the birth environment of metal-poor halo stars. Indeed, a group of stars which show a small scatter in the abundance ratios, same as the C-normal stars, might have formed in an environment chemically enriched by multiple stellar populations. On the contrary, the stars that exhibit, one from each other, different chemical abundances might have been enriched by one or few SNe.

<sup>3</sup> Here the star-to-star scatter is quantified with the standard deviation among different measurements

The increased fraction of CEMP-no stars with decreasing  $[\text{Fe}/\text{H}]$  further supports such a link with Pop III star pollution (de Bressan et al. 2017). Yet, the observed chemical abundance patterns of the most Fe-poor,  $[\text{Fe}/\text{H}] < -4$ , CEMP-no stars are indeed consistent with the yields of Pop III stars exploding as a faint supernovae and experiencing mixing and fallback (Iwamoto et al. 2005; Marassi et al. 2014). Furthermore, the high values of  $^{12}\text{C}/^{13}\text{C}$  recently observed in CEMP-no stars are consistent with an imprint from low-energy Pop III SNe (Aguado et al. 2023) and rule out the so-called “spinstars” (e.g. Meynet et al. 2006) as main pollutants. The CEMP-no halo stars at higher  $[\text{Fe}/\text{H}]$ , instead, appear to be consistent with being polluted either by only Pop III stars exploding with different energies (see Welsh et al. 2021) or by a combination of Pop III SNe and normal Pop II stars (see de Bressan et al. 2017; Koutsouridou et al. 2023). The imprints of a single very energetic Pop III SNe, the so-called hypernovae ( $E_{\text{SN}} > 5 \cdot 10^{51}$  erg), have been detected in C-normal metal-poor stars residing in the Galactic halo (Placco et al. 2021) and in the dwarf galaxy Sculptor (Skúladóttir et al. 2021, 2023a). In addition, stars with signs of an enrichment by an extremely energetic Pair Instability Supernova (PISN,  $E_{\text{SN}} > 10^{52}$  erg) combined with normal Pop II SNe have been found in the Galactic halo (Aoki et al. 2014; Salvadori et al. 2019). Finally, extremely recently, Xing et al. (2023) find the imprint of massive PISN of  $m_{\star} = 260 M_{\odot}$  for a very metal-poor star discovered in the LAMOST survey.

### 2.3 Primordial IMF from Stellar Archaeology

As we discussed in Chapter 1 our understanding of the IMF of primordial stars is still quite limited; current theoretical models propose a wide range of Pop III stellar masses, suggesting values from the sub-stellar regime to several hundred times the mass of our Sun. As a result, the precise values for the minimum and maximum masses allowed for the first stars, along with their characteristic mass, remain uncertain. The most stringent constraints on the properties and mass distribution of Pop III stars are likely to come from the study of extremely metal-poor stars in the Local Group. The newly discovered Galactic halo star LAMOST J1010+2358 (Xing et al. 2023) reveals great insight on the nature of Pop III stars since its abundance pattern is consistent with nucleosynthesis products from a very massive first-generation star. Yet, the discovery of a true PISN descendant not only confirms the existence of energetic Pop III SNe but also it proves the existence of very massive Pop III stars. Consequently, it enables us to indirectly put a lower limit on the maximum mass,  $m_{\text{max}}$ , allowed for zero metallicity stars, leading us to conclude that it exceeds 260 solar masses, i.e.  $m_{\text{max}} \geq 260 M_{\odot}$ . Furthermore, by exploiting the stellar chemical abundances measured in the oldest and most metal-poor

components of our Milky Way and its dwarf galaxies satellites (Skúladóttir et al. 2015; Frebel et al. 2015; Ji et al. 2016; Bonifacio et al. 2018; Li et al. 2018; Aguado et al. 2019; Bonifacio et al. 2019; Sestito et al. 2019; Reichert et al. 2020; Chiti et al. 2021) various different works have interpreted these results as the evidence of the existence of Pop III star with masses  $\sim [10 - 60] M_{\odot}$  (e.g. Aoki et al. 2014; de Bannassuti et al. 2017; Ishigaki et al. 2018; Tarumi et al. 2020). Finally, even non-detection of long-lived Pop III stars can be an instrument to constrain the lower mass limit of the Pop III IMF (Oey 2003; Tumlinson 2006; Salvadori et al. 2010). For example, Hartwig et al. (2015) have recently shown that to exclude the existence of any Pop III stars survivors and set the minimum mass of Pop III stars,  $m_{min} \geq 0.8 M_{\odot}$  a large observed stellar sample is required. The future surveys need to include at least  $\sim 2 \times 10^7$  halo stars and  $10^{10}$  for the Milky Way’s bulge. However these numbers are much larger than what can be expected in the largest spectroscopic surveys in the next decade (e.g. 4MOST de Jong et al. 2019). In conclusion, despite significant progress have been made into the comprehension of the nature the first stars and of their IMF, a complete understanding of their properties remains challenging.

## 2.4 Dwarf Galaxies

As already discussed, studies of individual metal-poor and ancient stars allow us to trace the properties of the first stars and thus the chemical enrichment of the ISM out of which they formed. Many of these studies has been performed in the Local Group. The Local Group is the galaxy group that includes the Milky Way and it has a total diameter of roughly 3 Mpc. It consists of two groups of galaxies: the Milky Way and its satellites on the one hand, the Andromeda galaxy and its satellites on the other. These nearby dwarf galaxy satellites, which have simple, small and predominantly old stellar populations are one of the best systems to look for metal-poor stars. In the last decade, many new dwarf galaxies have been discovered in the Local Group. Typically dwarf galaxies can be classified morphologically and through their luminosity. The most common dwarf galaxies in the Local Group are the so called “*Dwarf Spheroidal*” (dSph) galaxies. Their name indicates a simple morphology and it is applied to small, low-luminosity galaxies with an old stellar population, which are typically devoid of gas (McConnachie 2012). Furthermore, dSphs are also classified through their total luminosity,  $L_{tot}$ . “*Classical*” dSph galaxies are those with  $L_{tot} > 10^5 L_{\odot}$ , which are known since more than two decades (e.g. Tolstoy et al. 2009). “*Ultra-Faint*” dSph galaxies (UFD) are the faintest systems,  $L_{tot} \leq 10^5 L_{\odot}$ , first discovered by the Sloan Digital Sky Survey (SDSS) (e.g. Belokurov et al. 2006).

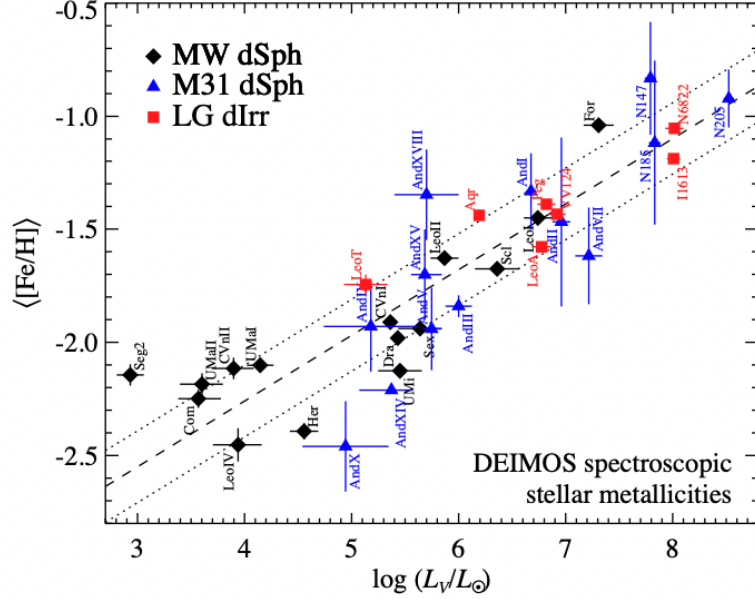


Figure 2.5: The luminosity–stellar metallicity relation for Local Group dwarf galaxies. The black diamonds (MW dSphs) and red squares Irregular dwarf galaxies are the average stellar iron abundances from spectroscopy of individual stars. The blue triangles (M31 dSphs) are the average stellar iron abundances from spectroscopy of groups of similar stars within each dwarf galaxy (Kirby et al. 2013).

In Fig.2.5 we show the Iron-Luminosity relation of Local Group dwarf galaxies derived by Kirby et al. (2013). As we can see, ultra-faint dwarf galaxies not only represent the least luminous systems in the Local group but also the most metal-poor ones. This key feature of UFDs is even more evident by inspecting MDFs of best studied dSph galaxies derived by several authors (e.g Battaglia et al. 2006; Starkenburg et al. 2010; Kirby et al. 2013; Suda et al. 2017). In Fig.2.6 we show the MDFs of “Classical” dwarf galaxies (Suda et al. 2017) while in Fig.2.7 the ones for all studied UFD galaxies (Brown et al. 2014). From Fig.2.6 it is evident that the distribution for dSph galaxies cover a range from  $[Fe/H] \approx -3$  to  $[Fe/H] \approx 0$ , with the peak of MDFs at  $[Fe/H] \sim [-1.5, -1]$ . MDFs of UFDs are dominated by metal-poor stars. All the distributions extend in the range between  $[Fe/H] = -1$  and  $[Fe/H] = -4$ , and the peak of each one is always below  $[Fe/H] = -2$ . On average,  $\sim 25\%$  of their stars have  $[Fe/H] \leq -3$ , and  $\sim 80\%$  have  $[Fe/H] \leq -2$ . UFD galaxies have a larger fraction of these Iron-poor stars with respect the “Classical” dwarf galaxies ( $< 5\%$ ). Therefore, UFD galaxies are the best systems to look for the most metal-poor stars and to eventually find long-living Pop III stars.

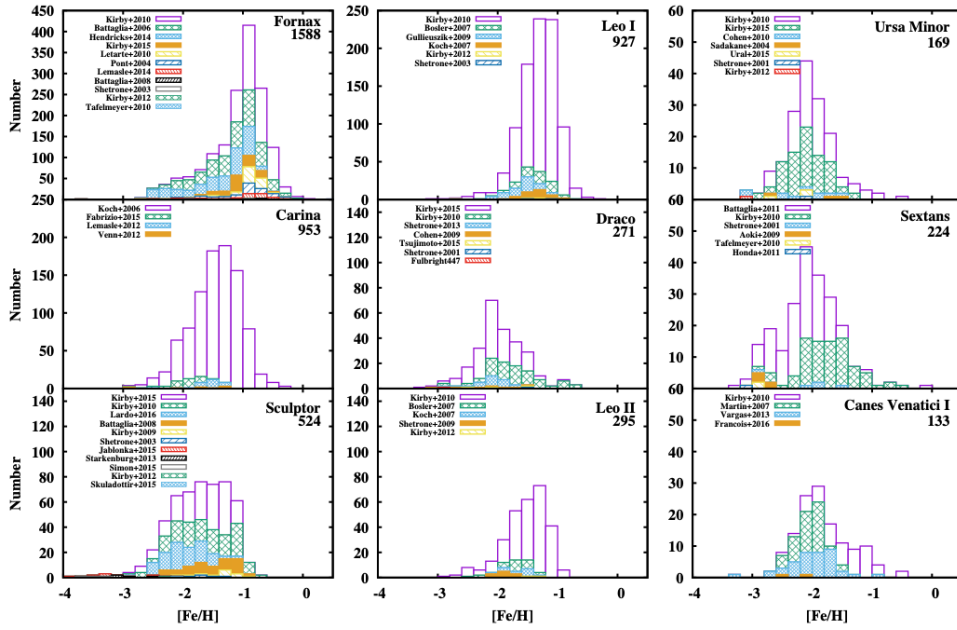


Figure 2.6: Metallicity distribution function for each galaxy. The data are separated by different source as denoted by the reference in the top left corner. The galaxy name and the number of data are shown in the top right corner. From Suda et al. (2017).

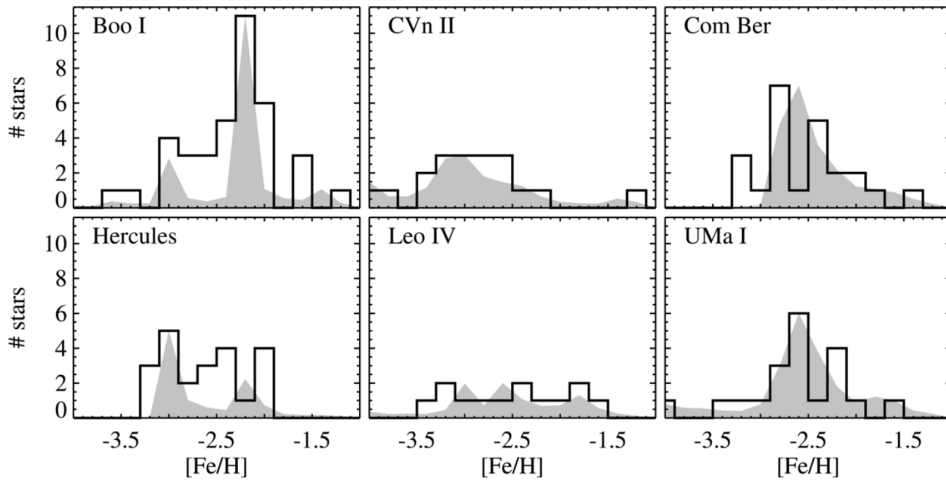


Figure 2.7: Metallicity distribution functions of six UFDs: Boötes I (Boo I), Coma Venatici II (CVn II), Coma Berenice (Com Ber), Hercules, Leo IV and Ursa Major I (UMA I). Histograms are the observed spectroscopic distributions, while the shaded areas are the simulated MDFs. From Brown et al. (2014).

Moreover, in Fig.2.8 is reported the dynamical mass,  $M_{\text{dym}}$  within the half-light radius of dwarf galaxies plotted against their total luminosity, for Milky Way satellites, M31 satellites, and for isolated dwarf galaxies. Also, the curves that correspond to a specific mass-to-light ratio are drawn. It is evident that with decreasing luminosity the mass-to-light ratio of dwarfs galaxies increases, from  $M/L \sim 1 - 10$  up to  $M/L \sim 10^3 - 10^4$ .



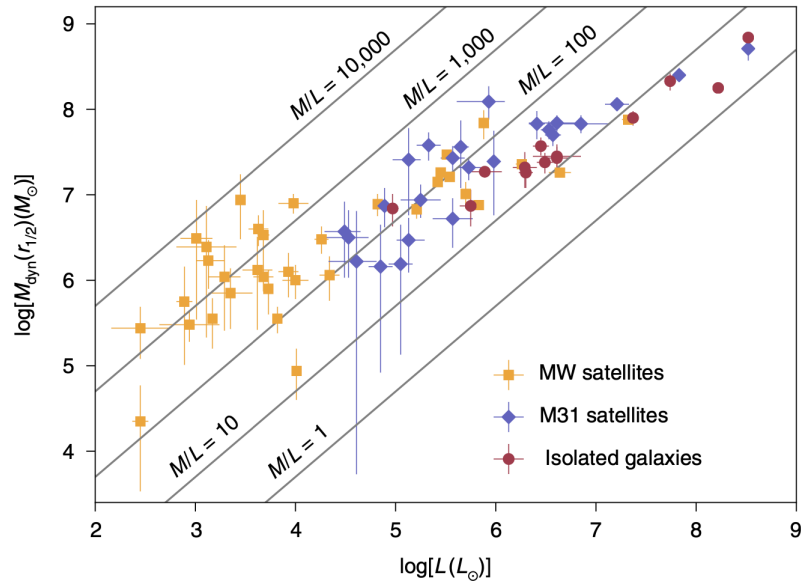


Figure 2.8: Dynamical mass  $M_{dyn}$  within the half radius  $r_{1/2}$  as a function of total V-band luminosity  $L$  for dwarf galaxies of the Local Group. The diagonal lines indicate constant mass-to-light ratios  $M/L = M_{dyn}(r_{1/2})/(L/2)$ , in units of  $M_{\odot}/L_{\odot}$ . From Battaglia & Nipoti (2022).

Considering only baryonic matter one would expect for these systems a mass-to-light ratio of the order of  $M/L \sim 1$ , while it is evident that dwarf galaxies, especially UFDs, are dark-matter dominated.

Moreover, since the dynamical mass is obtained by measuring the velocity dispersion of stars within the half-light radius of the dwarf, the values of  $M_{dym}$  in Fig.2.8 underestimate the mass of the hosting halo  $M_h$ . For example, UFD galaxies around the Milky Way have measured dynamical masses between  $10^4 M_{\odot}$  and  $10^7 M_{\odot}$ , and we expect their hosting halos to have masses  $M_h \gtrsim 10^6 - 10^7 M_{\odot}$ . Finally, the high mass-to-light ratio of UFDs is one of the characteristics that marks them as galaxies instead of star clusters, despite their similar luminosities.

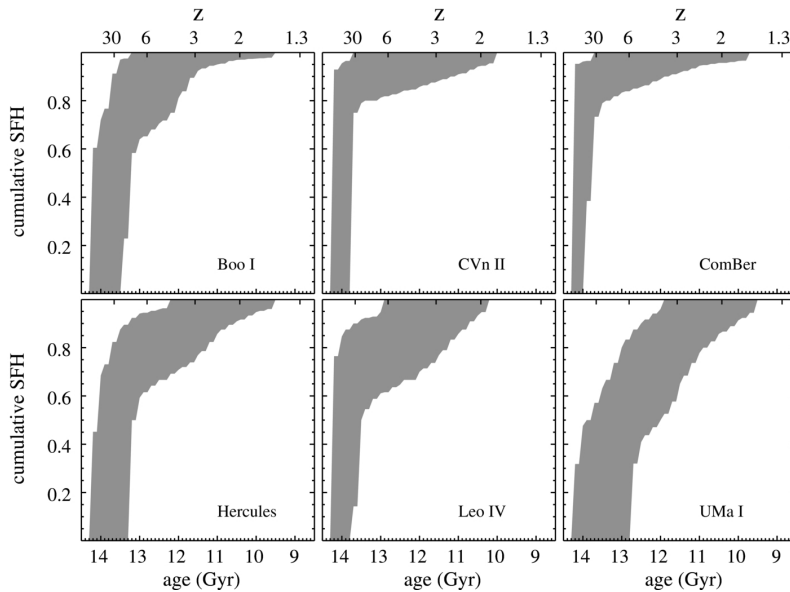


Figure 2.9: The cumulative SFH for each galaxy a function of stellar age and redshift, assuming two bursts. Within  $1\sigma$  uncertain, the SFH for each galaxy is consistent with a model that has at least 80% of the star formation completing by  $z \sim 6$ . Brown et al. (2014).

### 2.4.1 Ultra-Faint Dwarf Galaxies

UFD galaxies are the most common dwarf galaxies in the Local Group, representing more than 50% of the total number of dSph. They are the oldest, most dark matter-dominated, most metal-poor, and least chemically evolved stellar systems known (Simon 2019). Since they have the smallest dark matter halos they are more sensitive to feedback processes, representing an extreme limit of the galaxy formation processes. Several theoretical studies agree with the idea that UFDs are the living relics of the first star-forming *minihalos* that firstly hosted the Pop III stars (Bovill & Ricotti 2009; Salvadori & Ferrara 2009; Munoz et al. 2010; Salvadori et al. 2015). These theoretical predictions are also consistent with the observations of star formation histories (Brown et al. 2014; Gallart et al. 2021) which reveals that more than 75% of the stars in UFDs have ages  $> 10$  Gyr (see Fig.2.9) and that they experienced simply assembly histories with no major merger events. Moreover, spectroscopic studies show that CEMP stars have been found in a significant fraction in UFDs (e.g. Frebel 2010; Norris et al. 2010; Lai et al. 2011; Gilmore et al. 2013; Lai et al. 2011; Kirby et al. 2013; Yong et al. 2013a; Frebel et al. 2014; Yoon et al. 2019). Therefore, they are the compelling laboratories to search for the hints of Pop III SNe. Complementary, the metallicity of the observed stars in UFDs covers a broad range  $-4 < [\text{Fe}/\text{H}] < -1$ . Therefore UFDs can be also used to find the chemical imprint of energetic Pop III SNe.

### 2.4.2 Boötes I

Boötes I was the first UFD galaxy discovered since it is one of the most luminous,  $L_{\text{tot}} \sim 10^{4.5} L_{\odot}$  (Belokurov et al. 2006). Boötes I is located at  $66 \pm 2$  kpc from the Sun and, therefore it is one of closest Milky Way's satellite. It has been the subject of a number of investigations from both an observational (Frebel 2010; Norris et al. 2010; Lai et al. 2011; Gilmore et al. 2013; Frebel et al. 2016) and a theoretical point of view (Vincenzo et al. 2014; Romano et al. 2014). The color-magnitude diagrams of Boötes I reveal that its stellar population is old and metal-poor, with mean age  $\sim 13.3 \pm 0.3$  Gyr (Fig.2.9). The normalized MDF is shown in Fig.2.7 and it is the results of observations of 41 RGB stars (Lai et al. 2011; Norris et al. 2013; Gilmore et al. 2013). Note that the iron stellar abundance covers a range from  $-4.5 \lesssim [\text{Fe}/\text{H}] \lesssim -1$  and the MDF reaches the peak at  $[\text{Fe}/\text{H}] \sim -2.74$ . According to many theoretical studies (e.g. Vincenzo et al. 2014; Salvadori et al. 2015) Boötes I formed stars very inefficiently, i.e. with low star formation rate, which makes it consistent for being one of the living relics of the first star forming *minihalos*. All its characteristics make Boötes I an outstanding local benchmark to find the first stars and to investigate the nature of the first SNe. From an observational point of view furthermore, Boötes I is the best studied UFD. In this Thesis we select Boötes I as the primary subject for our studies.



---

---

# Modelling Ultra-Faint Dwarf Galaxies

In this Chapter we describe the main features of the semi-analytic code that we developed from scratch in order to follow the star formation and the chemical enrichment history of an UFD galaxy, from the epoch of its virialization until the present day.

## 3.1 Model Description

We model the evolution and the chemical enrichment history of present-day UFD galaxies by assuming that they experienced a “quiet” assembling history, i.e. without major merger events. The evolution in isolation is a good approximation for these tiny systems, as has been shown by cosmological models and simulations for the Local Group formation (e.g. Salvadori & Ferrara 2009; Salvadori et al. 2015; Safarzadeh et al. 2018), as well as recent observations (Gallart et al. 2021). To obtain a complete description of the evolution of a single isolated UFD galaxy it is necessary to take into account the most relevant physical processes driving the early galaxy formation such as the infall of pristine gas, the star formation, the stellar evolution, and the SNe explosions that reduce the gas in the galaxy that are described in next paragraphs.

### 3.1.1 Initial Conditions:

The nature of UFD galaxies is in ongoing debate. However, their observed properties suggest that they could be the living relics of the first star-forming minihalos that hosted Pop III stars. This scenario has been investigated, for example, by Salvadori & Ferrara (2009) that explored the origin of UFD galaxies using a cosmological model for the formation of the Milky Way and its dwarf satellites, including UFD galaxies. These authors selected Milky Way’s satellite candidates among star-forming halos that correspond to  $< 2 - \sigma$  density fluctuations<sup>1</sup> because these objects are the most likely to become satel-

<sup>1</sup>The quantity  $\sigma(M, z)$  represents the linear rms density fluctuation smoothed with a top-hat filter of mass  $M$  at redshift  $z$ .

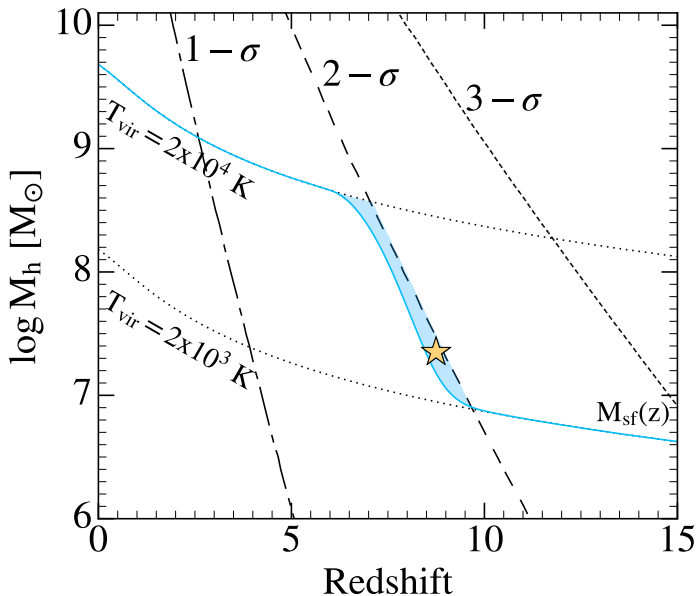


Figure 3.1: Evolution of the minimum halo mass to form stars,  $M_{\text{sf}}(z)$ , (solid blue line), of the halo mass corresponding to 1-, 2-, 3- $\sigma$  fluctuations of the density field (long-short, long, and short dashed lines), and of the halo mass with virial temperature  $T_{\text{vir}} = 2 \cdot 10^3 \text{K}$  and  $T_{\text{vir}} = 10^4 \text{K}$  (dotted lines) adapted from Salvadori & Ferrara (2009). The light blue shaded area shows the condition to form satellite dwarf galaxies,  $M_{\text{sf}}(z) < M_{\text{h}} < M_{2\sigma}$ . The yellow star represents our choice for the initial conditions:  $M_{\text{h}} = 10^{7.35} M_{\odot}$  and  $z_{\text{vir}} = 8.7$ .

lites (Diemand et al. 2005a). By comparing their model results with observations, they concluded that UFD galaxies are associated to minihalos formed prior to the end of reionization,  $z_{\text{rei}} > 6$ , which have not experienced mergers, i.e. they evolved in isolation (see also Salvadori et al. 2015). Following this approach we select the dark matter halos that correspond to  $< 2 - \sigma$  fluctuations of the density field<sup>2</sup> and that are able to form stars. The latter condition is described by the minimum halo mass required to allow star-formation,  $M_{\text{sf}}(z)$ , see Fig.3.1, whose evolution accounts for the increasing Lyman Werner and ionizing radiation (see Sec.2.1 Salvadori & Ferrara 2009). In Fig.3.1 our UFD galaxies candidates are those with dark matter halo mass  $M_{\text{sf}}(z) < M_{\text{h}} < M_{2\sigma}$  (indicated with the shaded light blue area). Following the results of Salvadori et al. (2015) the progenitor of Boötes I has dark matter halo  $M_{\text{h}} = 10^{7.35} M_{\odot}$  that virializes at  $z_{\text{vir}} = 8.7$  (yellow star in Fig.3.1), and adopt these values as the initial condition of our model.

We assume that at the epoch of virialization the dark matter halo contains a total amount of gas equal to  $\Omega_{\text{b}}/\Omega_{\text{m}} M_{\text{h}}$ . The star formation becomes possible when the gas begins to infall in the central part of the halo and to cool down. Considering the redshift of virialization, the infalling gas can be assumed to be metal-free (e.g. Salvadori & Ferrara 2012).

<sup>2</sup> We adopt  $\Lambda$  cold dark matter ( $\Lambda\text{CDM}$ ) with  $h = 0.669$ ,  $\Omega_{\text{m}} = 0.3103$ ,  $\Omega_{\Lambda} = 0.6897$ ,  $\Omega_{\text{b}} h^2 = 0.02234$ ,  $\sigma_8 = 0.8083$ ,  $n = 0.9671$ , according to the latest Planck results (Planck Collaboration et al. 2018)

### 3.1.2 Infall rate:

Following Salvadori et al. (2008, 2015) we exploit the results of simulations presented in Kereš et al. (2005) to compute the infall rate as:

$$\frac{dM_{inf}}{dt} = A \left( \frac{t}{t_{inf}} \right)^2 \exp \left( - \frac{t}{t_{inf}} \right) \quad (3.1)$$

where  $A$  is the normalization constant, which is set to be  $A = 2M_h \frac{\Omega_b}{\Omega_m} \frac{1}{t_{inf}}$  so that for  $t \mapsto \infty$  the accreted gas reaches the initial value,  $M_{inf}(\infty) = \Omega_b/\Omega_m M_h$ . In addition,  $t$  is the time since virialization and  $t_{inf}$  is the time-scale on which the gas cools, which is a free parameter of the model.

### 3.1.3 Star formation rate:

It has been assumed that star formation occurs in a free-fall time  $t_{ff} = (3\pi/32G\rho(z))^{1/2}$ , where  $G$  is the gravitational constant and  $\rho$  the total mass density inside the halo. Stars are assumed to form in a single burst at each time step,  $dt$ , and the star formation rate,  $\Psi$ , is given by:

$$\Psi = \frac{dM_\star}{dt} = \epsilon_\star \frac{M_{gas}}{t_{ff}(z)} \quad (3.2)$$

where  $M_\star$  is the total stellar mass formed,  $M_{gas}$  is the mass of the cold gas, and  $\epsilon_\star$  is the star formation efficiency, a second free parameter of our model.

### 3.1.4 Pop III and Pop II/I stars:

The metallicity of the cold gas of the interstellar medium (ISM),  $Z_{gas} = M_Z^{ISM}/M_{gas}$ , determines whether the stars forming are Pop III or Pop II/I stars. Pop III stars only form if the metallicity of the gas is lower than the critical metallicity,  $Z_{cr} = 10^{-4.5}Z_\odot$ , (de Bressan et al. 2017), instead Pop II/I stars form if  $Z_{gas} > Z_{cr}$ . At each time step we compute the stellar mass formed, and we assume that the star formation occurs only if a minimum value is reached, i.e. if  $M_\star(t_i) \geq M_\star^{min} = 100 M_\odot$  (Klessen et al. 2011).

### 3.1.5 Stellar initial mass function:

The stellar mass formed at each time step is distributed according to an Initial Mass Function (IMF). As a first approximation we assume that the stellar mass formed is

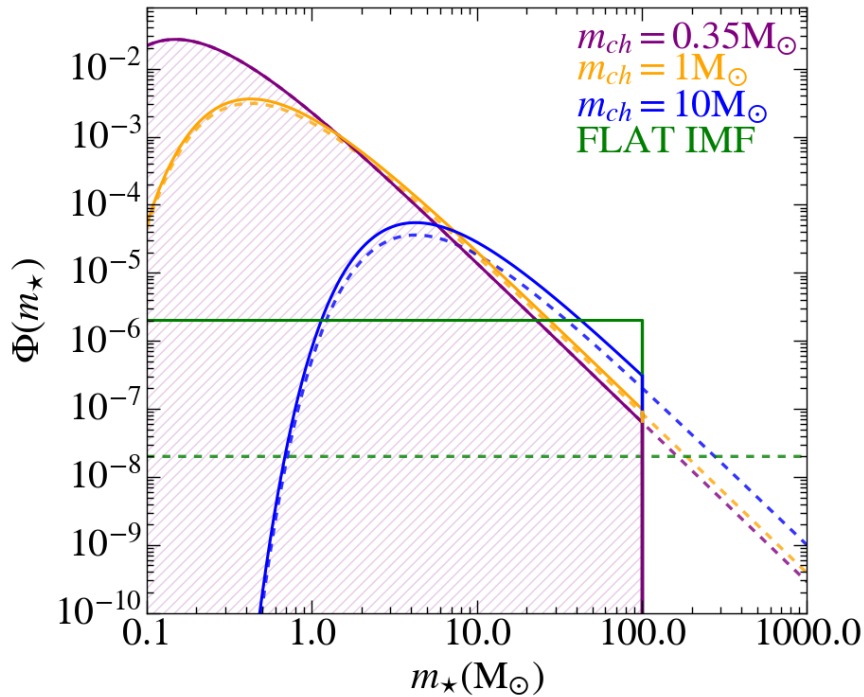


Figure 3.2: Normalized Pop III IMFs explored in our model (see labels). Solid lines represent IMFs in the mass range  $[0.1 - 100] M_{\odot}$ , while dashed lines have maximum mass,  $m_{max} = 1000 M_{\odot}$ . The hatched area highlights the IMF of present-day stars (Larson 1998).

enough to fully populate the IMF. In other words, the total mass of stars formed at each time-step is distributed throughout the overall stellar mass range. As stellar IMF for Pop II/I stars we choose a Larson-type (Larson 1998):

$$\phi(m_{\star}) = \frac{dN}{dm_{\star}} \propto m_{\star}^{-2.35} e^{-\frac{m_{ch}}{m_{\star}}} \quad (3.3)$$

where the stellar mass  $m_{\star}$  varies in the mass range  $[0.1 - 100] M_{\odot}$  and  $m_{ch} = 0.35 M_{\odot}$  is the characteristic mass. Since the Pop III IMF is unknown, we initially assume it to be equal to the IMF of present-day stars (Eq.3.3, see Fig.3.2) and we explore the impact of different minimum mass of Pop III stars,  $m_{min}$ . Then we vary both the maximum mass of Pop III stars,  $m_{max}$ , and the Pop III IMF shape by assuming three different  $m_{ch}$  along with a Flat IMF. All our explored Pop III IMFs are summarized in Fig.3.2.

### 3.1.6 Stellar evolution:

The model accounts for the finite stellar lifetimes, i.e. for the evolution of stars with different masses. We use the relation derived by Raiteri et al. (1996) in which the stellar lifetime depends not only on the stellar mass but also on the stellar metallicity,  $t_{\star}(m_{\star}, Z_{\star})$ , which is settled by the ISM out of which stars formed. All stars whose lifetime is greater than the difference between the age of the Universe at  $z = 0$  ( $\sim 13.8$  Gyr) and the age of



the Universe when they formed,  $t_\star > (t_{z=0} - t_{z_{form}})$ , can survive until today (see details in Salvadori et al. 2008). In particular, according to the adopted lifetime-mass-metallicity relations, all stars with  $m_\star \leq 0.8 M_\odot$  have a lifetime greater than the age of the Universe and can therefore survive until today independent on their formation redshift.

- *Returned fraction and metal yields:*

Stars return gas into the ISM, via supernova (SNe) explosions or via stellar winds in the Asymptotic Giant Branch (AGB) phase. This gas becomes thus newly available for star formation. We compute the rate at which the gas is returned into the ISM as:

$$\frac{dR(t)}{dt} = \int_{m_{turn}(z)}^{100 M_\odot} [(m_\star - w_m(m_\star))\Phi(m_\star)\Psi(t - t_\star)] dm_\star \quad (3.4)$$

where  $w_m(m_\star)$  is the remnant mass of a star with initial mass  $m_\star$ ,  $\Psi$  the star formation rate, and  $t_\star = t_\star(m_\star, Z_\star)$  is the stellar lifetime.

The gas that is returned to the ISM carries with it the products of nuclear burning, i.e metals (Z). The rate of heavy elements newly synthesised inside stars and re-ejected into ISM is:

$$\frac{dY_Z(t)}{dt} = \int_{m_{turn}(z)}^{100 M_\odot} [(m_\star - w_m(m_\star) - m_Z(m_\star, Z_\star))Z(t - t_\star) + m_Z(m_\star, Z_\star)]\Phi(m_\star)\Psi(t - t_\star) dm_\star \quad (3.5)$$

where  $m_Z(m_\star, Z_\star)$  is the mass of heavy elements produced by a star with initial mass  $m_\star$  and metallicity  $Z_\star$ , and  $Z(t - t_\star)$  is the abundance of metals in the ISM at the time  $(t - t_\star)$ . In our model we follow the evolution of the total amount of heavy elements (Z) and of iron (Fe). The values used in our model to compute the metal yields and returned fraction of gas are those derived by Woosley & Weaver (1995) for both Pop II/I and Pop III stars with masses  $< 100 M_\odot$ , while for Pop III stars with  $140 M_\odot \leq m_{PopIII} \leq 260 M_\odot$  we adopt the yields by Heger & Woosley (2002).

### 3.1.7 Mechanical feedback:

Stars with masses  $m_\star = [8 - 40]M_\odot$  end their life as SNe. SNe explosions power a blast wave which, if sufficiently energetic, may overcome the gravitational pull of the host halo leading to expulsion of gas and metals into the intergalactic medium (IGM). We assume the mass of gas ejected into the IGM due to SNe explosions to be regulated by the equation:

$$\frac{1}{2}M_{ej}v_{esc}^2 = E_{SN} \quad (3.6)$$

where  $E_{SN} = \epsilon_w N_{SN} \langle E_{SN} \rangle$  is the total kinetic energy injected by SN-driven winds,  $N_{SN}$  the number of SNe,  $\langle E_{SN} \rangle$  the average SNe explosion energy, and  $\epsilon_w$  is a free parameter, which controls the conversion efficiency of the explosion energy into kinetic form. Assuming the IMF described by Eq.3.3, we get that the number of SNe per unit of stellar mass formed  $\eta_{SN}$  is:

$$\eta_{SN} = \frac{\int_{8 M_{\odot}}^{40 M_{\odot}} m_{\star} \Phi(m_{\star}) dm_{\star}}{\int_{0.1 M_{\odot}}^{100 M_{\odot}} m_{\star} \Phi(m_{\star}) dm_{\star}} \approx 10^{-2} \quad (3.7)$$

For the average value of the SNe energy we assume  $\langle E_{SN} \rangle \sim 10^{51}$  erg for Pop II SNe, which is a typical value for a normal core-collapse SNe. For massive Pop III stars ( $[140 - 260] M_{\odot}$ ), i.e. Pair Instability SNe (PISN), we use the mass-energy relation of Heger & Woosley (2002), in which the energy increases with the mass of PISN. For less massive Pop III stars ( $[8 - 40] M_{\odot}$ ) we assume the same energy of Pop II SNe.

Following Salvadori et al. (2008) we differentiate Eq.3.6 to get the gas ejection rate:

$$\frac{dM_{ej}}{dt} = \frac{2 \epsilon_w \langle E_{SN} \rangle}{v_{esc}^2} \frac{dN_{SN}}{dt} \approx \frac{2 \epsilon_w \langle E_{SN} \rangle}{v_{esc}^2} 10^{-2} \frac{dM_{\star}}{dt} \quad (3.8)$$

and compute the escape velocity of the gas as a function of the halo virial radius,  $v_{esc}^2 = \frac{GM}{r_{vir}}$  (Barkana & Loeb 2001). In our model we assume that the metallicity of the ejected gas is the same as that of the ISM. This is an approximation, we are assuming that there is a complete mixing between the gas inside the halo and the heavy elements injected into the ISM by SNe explosions.

A limitation of this study is that only core-collapse SNe ( $m_{\star} = [8 - 40] M_{\odot}$ ) have been considered for Pop II/I stars and we have not included the contribution of SN Ia. The choice was guided by the fact that the evolutionary timescales associated with SN Ia are typically very long,  $> 1\text{Gyr}$ , compared to the evolution time-scale of our galaxy ( $\sim 500$  Myr). Although there are studies that have shown that the evolutionary scale times of SN Ia can be shorter (e.g. Matteucci et al. 2006), cosmological models for UFDs formation that also include prompt formation of SN Ia show that their influence on the chemical evolution is extremely limited, and is only relevant at the highest  $[\text{Fe}/\text{H}]$  (Salvadori et al. 2015). In fact, a detailed chemical abundance study of Boötes I did not reveal significant

SN Ia contribution (Gilmore et al. 2013). Therefore their contribution will only be considered in future work. Finally, we considered the evolution of an isolated UFD galaxy, however to obtain a more accurate and realistic model the cosmological context should be considered.

### 3.1.8 Galaxy evolution:

To follow the evolution of an UFD galaxy we solve Eq. 3.2 along with the subsequent system of differential equations:

$$\frac{dM_{gas}}{dt} = -\Psi + \frac{dR}{dt} + \frac{dM_{inf}}{dt} - \frac{dM_{ej}}{dt} \quad (3.9)$$

$$\frac{dM_Z}{dt} = -Z^{ISM} \Psi + \frac{dY_Z}{dt} + Z^{inf} \frac{dM_{inf}}{dt} - Z^{ISM} \frac{dM_{ej}}{dt} \quad (3.10)$$

where  $M_{gas}$  in Eq.3.9 is the mass of cold gas inside the halo, which increases due to the infall rate (Eq.3.1) and to the amount of gas released by massive and AGB stars (Eq.3.4), and it decreases due to star formation (Eq.3.2) and gas ejection caused by SNe explosions (Eq.3.8). The second equation, Eq.3.10, describes the variation of the total mass of metals ( $M_Z$ ) in gas where  $Z^{ISM}$ ,  $Z^{inf}$  and  $Z^{ej}$  are respectively the metallicity in the ISM, in the infalling gas, and in the ejected gas. In our model we assume  $Z^{inf} = 0$ , i.e. the infalling gas is considered metal (and iron free) and  $Z^{ej} = Z^{ISM}$  (see previous paragraph). Thus, we can write the fourth equation that describes the evolution of the iron mass in the ISM as:

$$\frac{dM_{Fe}}{dt} = -\frac{M_{Fe}^{ISM}}{M_{gas}} \Psi + \frac{dY_{Fe}}{dt} - \frac{M_{Fe}^{ISM}}{M_{gas}} \frac{dM_{ej}}{dt} \quad (3.11)$$

where  $M_{Fe}^{ISM}$  is the total iron mass in the ISM.

## 3.2 Model Calibration

The model includes three free parameters: the infall time,  $t_{inf}$ , the star formation efficiency,  $\epsilon_*$ , and the SNe wind efficiency,  $\epsilon_w$ . We calibrate our model by comparing with observations, using a statistical approach. In particular, we fix the free parameters of the model to reproduce the following observed properties of Boötes I:

- The total luminosity of the galaxy,  $\log(L_*/L_\odot) = 4.5 \pm 0.1$  (Kirby et al. 2013);
- The average iron abundance of stars,  $\langle [Fe/H] \rangle = -2.58 \pm 0.43$  (Lai et al. 2011; Norris et al. 2010);

- The time interval, counted starting from the first star formation event, needed to form at least the 50% of the total stellar mass (*Cumulative SFH* = 0.5,  $t_{50} \approx (600 \pm 400)$  Myr, Brown et al. 2014);
- The observed metallicity distribution function (MDF)<sup>3</sup> (Norris et al. 2010; Lai et al. 2011; Gilmore et al. 2013).

Since Pop III stars have not been observed so far, we calibrated our model by assuming that there are no zero-metallicity stars survivors. Therefore, we set the minimum mass of Pop III stars to  $m_{min} = 0.9 M_{\odot}$ .

By varying  $t_{inf}$ ,  $\epsilon_{\star}$ ,  $\epsilon_w$  we find the combination that minimises the reduced  $\chi^2$ . The  $\chi^2$  distribution presents a minimum for  $(t_{inf}, \epsilon_{\star}, \epsilon_w) = (14.5 \text{ Myr}, 0.07, 0.03)$  for which we get  $\chi^2 = 0.33$ . In the top panel of Fig.3.3 we show the  $\chi^2$  confidence levels in the parameter space of  $\epsilon_{\star}$  and  $\epsilon_w$  at fixed  $t_{inf} = 14.5$  Myr. We note that degeneracy exists between the parameters, however the minimum of  $\chi^2$  is unique.

From each combination of  $(\epsilon_{\star}, \epsilon_w)$ , we derive  $\langle[\text{Fe}/\text{H}]\rangle$ , and the total luminosity,  $L_{\star}$ . The corresponding Fe –  $L_{\star}$  relation is shown in the middle panel of Fig.3.3, where we compare our model results with the observed  $\langle[\text{Fe}/\text{H}]\rangle - L_{\star}$  relation for Boötes I and other Local Group UFDs (Kirby et al. 2011, McConnachie 2012; Kirby et al. 2013; Simon 2019; Gallart et al. 2021). As we can see, the  $\chi^2$  99% confidence level contour contains three other UFD galaxies: Hercules, Leo IV and Eridanus II. This means that we expect these galaxies to have experienced an evolution similar to that of Boötes I and hence to have similar best values of the free parameter  $(\epsilon_{\star}, \epsilon_w)$ . To check this, we re-calibrate the model to fit the observed properties of each one of these three additional UFDs (see Tab.3.1 for their physical properties). The  $(\epsilon_{\star}, \epsilon_w)$  values obtained for these UFDs are shown in Fig.3.3 (top panel). We see that in all cases the combinations of  $(\epsilon_{\star}, \epsilon_w)$  are enclosed in the 99%  $\chi^2$  confidence level contours of Boötes I. Finally, the bottom panel of Fig.3.3 shows the comparison between the observed MDF of Boötes I and the simulated one, which are in good agreement, while in Fig.3.4 the same comparison for Hercules, Leo IV and Eridanus II. We can see that in all cases we find a good agreement between model results and observations.

<sup>3</sup> we use 8 points in the observed MDF

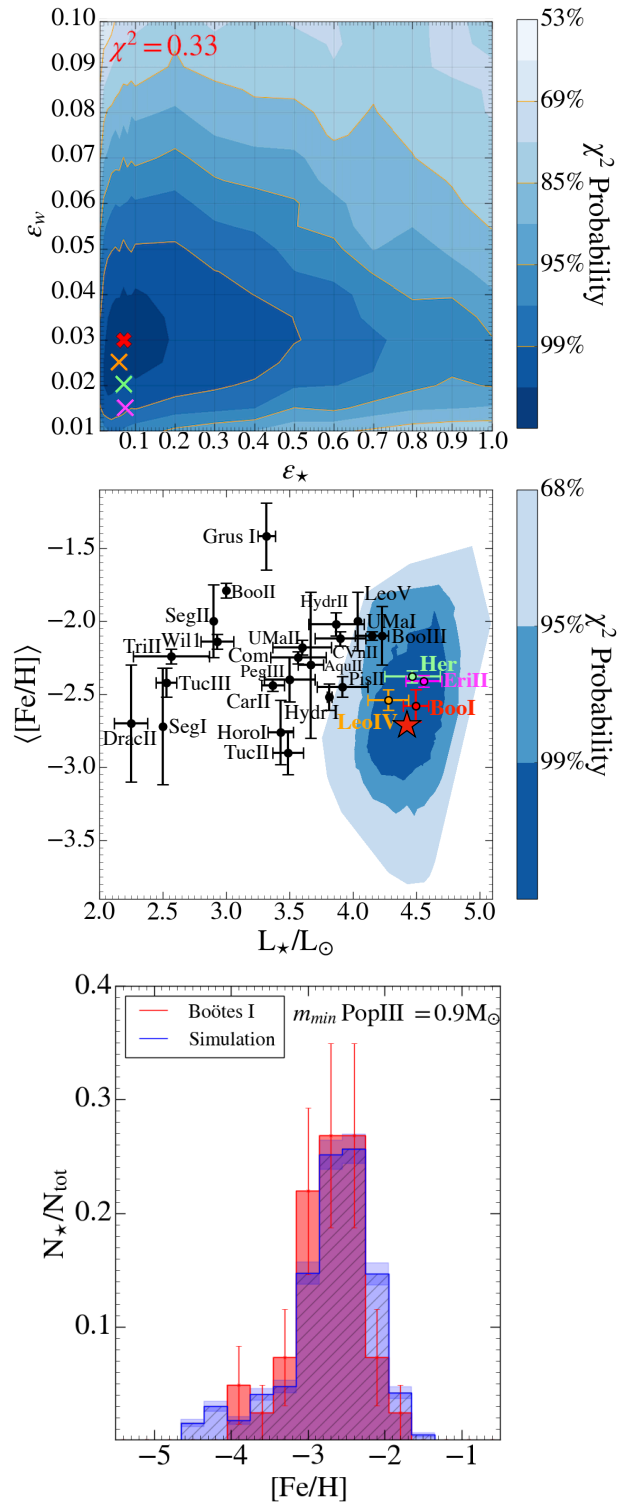


Figure 3.3: Top panel:  $\chi^2$  confidence level contours in the parameter space ( $\epsilon_\star, \epsilon_w$ ). Red, orange, light green and magenta crosses indicate the minimum of the reduced  $\chi^2$  for Boötes I, Leo IV, Hercules and Eridanus II, respectively. Middle panel: Iron-Luminosity relation, colours trace the  $\chi^2$  confidence level contours. Bottom panel: comparison between the simulated (blue), and the observed (red) MDF of Boötes I.

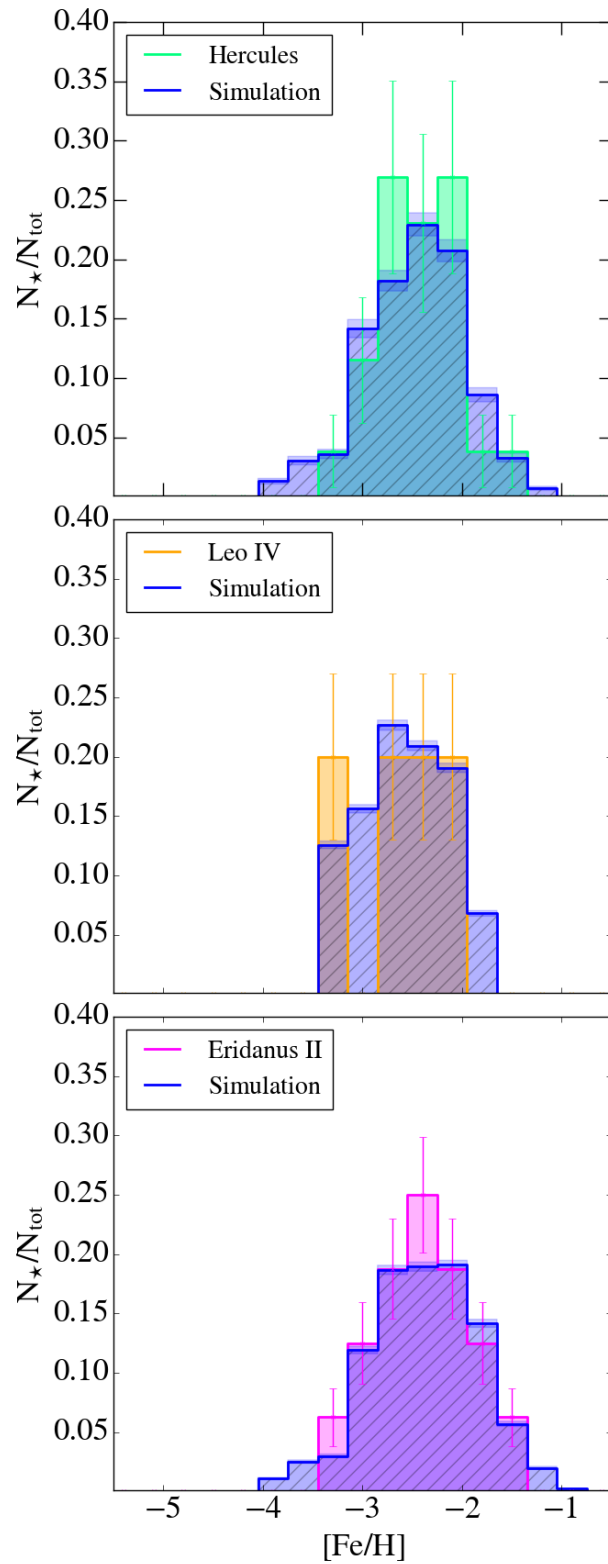


Figure 3.4: The comparison between the observed and the simulated (blue) MDFs for UDFs in the 99% of confidence level  $\chi^2$  contour of Boötes I: Hercules (lightgreen), Leo IV (orange) and Eridanus II (magenta).

Galaxy	$\log(L_*/L_\odot)$	$\langle[\text{Fe}/\text{H}]\rangle$	$t_{50}(\text{Myr})$
Boötes I	$4.5 \pm 0.1$	$-2.58 \pm 0.43$	$(600 \pm 400)$
Hercules	$4.46 \pm 0.14$	$-2.41 \pm 0.04$	$(600 \pm 500)$
Leo IV	$4.28 \pm 0.16$	$-2.54 \pm 0.07$	$(400 \pm 300)$
Eridanus II	$4.70 \pm 0.22$	$-2.38 \pm 0.04$	$(100 \pm \dots)$

Table 3.1: Observed properties of UFDs in the  $\chi^2$  99% confidence level contour of Boötes I. The observed MDFs are shown in Fig. 3.4.

### 3.3 Modelling the IMF random sampling

The data-calibrated model was obtained by assuming to fully populate the IMF (Sec. 3.1). It is customary to treat the stellar mass distribution, i.e the IMF, like a continuous function where the stellar mass formed is distributed over the whole range of masses. When dealing with a large galaxy, or a high star-formation rate in general, it is justified to think of the IMF as a densely sampled probabilistic function. However, when dealing with poorly star-forming systems, the hypothesis of a fully populated IMF breaks down (Kroupa & Weidner 2003; Weidner & Kroupa 2006; Carigi & Hernandez 2008; Kroupa et al. 2011; Leaman 2012; Weidner et al. 2013; de Bressana et al. 2017; Applebaum et al. 2018). It is therefore important to understand how the incomplete sampling of the IMF influences the chemical evolution of poorly star-forming UFDs.

Therefore, in this section we first study how the IMF is populated in UFD galaxies that form stars at a very low rate, and then we explore its consequences on the chemical evolution of Boötes I. Finally, we investigate the effect of the IMF random sampling on the expected number of long-living first stars in our fiducial model.

#### 3.3.1 Stochastic IMF sampling procedure

The Monte Carlo procedure that is used to determine the masses of stars formed in a single burst,  $M_*$ , can be described as follows: we choose a normalized IMF (e.g. Larson, Eq.3.3), and then we build up the probability function, i.e. the cumulative IMF that ranges between 0 and 1. For each randomly extracted number between 0 and 1, we determine the corresponding mass through the probability function. When the extracted random number falls in the mass interval between  $m_*^i$  and  $m_*^{i+1}$  we assume to form a star with mass  $m_*^i = (m_*^i + m_*^{i+1})/2$ . Random numbers are generated until the total mass of stars equals the stellar mass formed,  $M_* = \sum_i m_*^i N_*^i$ , where  $N_*^i$  is the number of stars with mass  $m_*^i$ . Thus at each time step, we obtain the *effective IMF* that can be compared with the theoretical one.

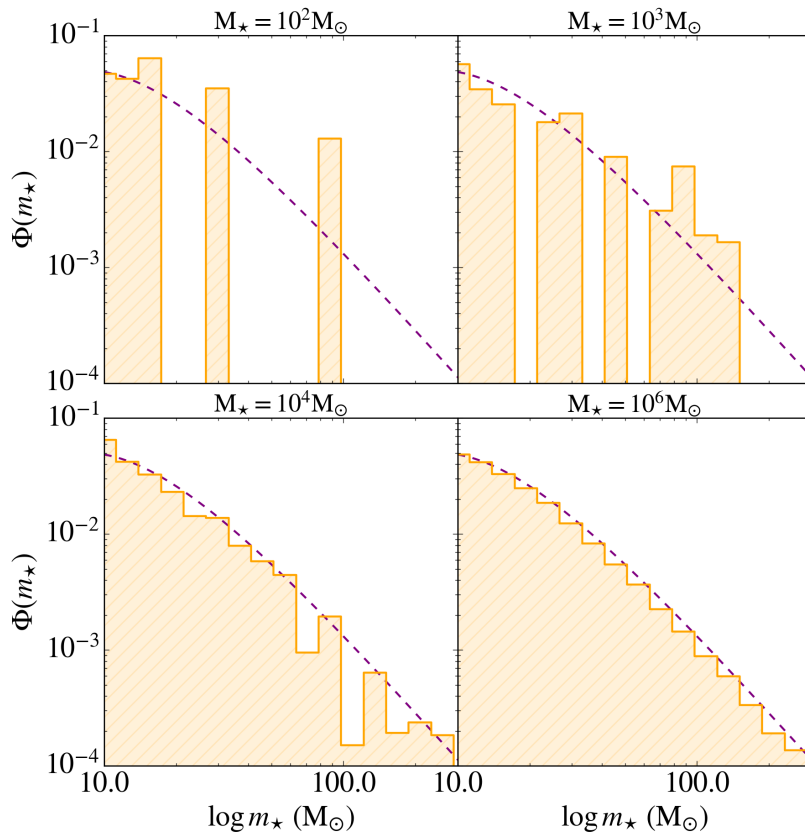


Figure 3.5: Comparison between the theoretical IMF (purple dashed lines) and the effective mass distribution resulting from the random sampling procedure (orange histograms).

### 3.3.2 Model validation

To validate the method adopted to stochastically populate the IMF, first we try to reproduce the results presented in the paper by de Bressan et al. (2017) who assumed a Larson-type IMF (see Chapter 3, Sec. 3.1.5) with  $m_{ch} = 20 M_{\odot}$  in the mass range  $m_{\star} = [10 - 300] M_{\odot}$ . Fig. 3.5 shows the comparison between the theoretical IMF and the one obtained with the random sampling procedure by assuming different total stellar masses. The effective IMF appears like a collection of histograms while the dashed line gives the theoretical IMF. It is illustrative to see how the discrete sampled IMFs converge to the theoretical ones as the total stellar mass increases. Therefore, the sampling of the IMF strongly depends on the stellar mass  $M_{\star}$ . In particular for values of  $M_{\star}$  lower than  $10^4 M_{\odot}$  the theoretical IMF is not well reproduced. So the lower is the stellar mass formed, the worse is the match between the sampled and the theoretical IMF. Instead, when  $M_{\star} \gtrsim 10^5 M_{\odot}$  the overall mass range can be fully sampled and the theoretical IMF is well reproduced. This is in perfect agreement to what has been found by de Bressan et al. (2017) (see their Fig. 2).



### 3.4 The evolution of UFDs with IMF random sampling

To follow the evolution of poorly star-forming UFD galaxies, we implemented the model so that giving in input the total stellar mass formed at each time step  $M_*$ , we simulate the stellar population having a total masses  $M_*$  by sampling directly the theoretical IMF. This produce a discrete collection of stars, which is then used as input for the chemical evolution code.

In Fig.3.6 we illustrate how this random IMF sampling affects poorly star-forming UFDs when a normal Larson IMF is assumed for both Pop III and Pop II/I stars. The top panel shows the predicted SFH of Boötes I, which illustrates that UFDs have extremely low star-formation rates across their whole evolution ( $\Psi < 3 \cdot 10^{-3} M_\odot \text{yr}^{-1}$ ). The bottom panels show the comparison between the theoretical IMF and the effective one, resulting from the Monte Carlo procedure, for three different evolutionary phases. The lower is  $\Psi$ , the worse is the sampling of the theoretical IMF, in particular at the high-mass end. Furthermore, the overall star-formation rate is so low in these small systems, that when the IMF is shifted towards higher masses,  $m_{ch} \geq 1 M_\odot$ , we can only form a few stars around the peak. In those cases, the IMF is poorly populated both at high and low masses. As we will see in Sec.4.1 this effect is extremely important for the surviving Pop III fraction.

Moreover, since we will test different Pop III IMF in Fig.3.7 shows the comparison between the theoretical Pop III IMF (see Fig.3.2) and the effective one obtained with the random sampling procedure, when we assume to form a total stellar mass of  $\approx 200 M_\odot$ . This the typical mass formed in a single burst during the early evolutionary phases of Boötes I, i.e. when  $\Psi \approx 2 \cdot 10^{-4} M_\odot \text{yr}^{-1}$  (Fig. 3.6). We see that the theoretical Pop III IMF is poorly sampled independent of its shape, the  $m_{ch}$ , and the  $m_{max}$ . Furthermore, while for  $m_{ch} = 1 M_\odot$  we still have a good sampling of the Pop III IMF at the lowest mass-end,  $m_* < 1 M_\odot$ , when the peak of the IMF is shifted towards higher masses ( $m_{ch} = 10 M_\odot$ ) or there is not a preferential mass scale, i.e. the IMF is flat, the lowest mass-end becomes less and less populated with respect to the theoretical IMF. This implies that the number of surviving Pop III stars is much lower than expected. These results are even more extreme for  $m_{max} = 1000 M_\odot$  (bottom panels).

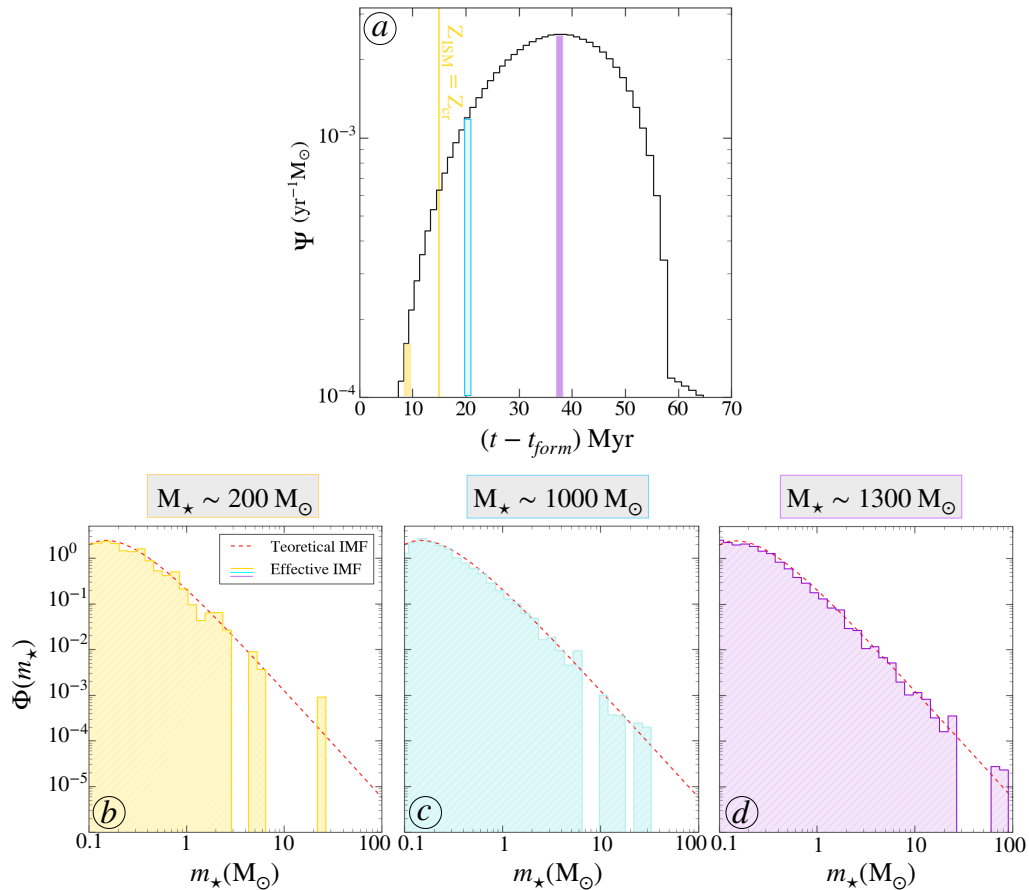


Figure 3.6: *Panel a*: star formation history of Boötes I according to our fiducial model. The vertical yellow line shows the transition between PopIII and PopII stars. The coloured shaded histogram bins underline the star-formation rate in three different evolutionary phases: the early star formation,  $(t - t_{form}) \approx 10$  Myr, when PopIII stars form at a very inefficient rate ( $\Psi \approx 2 \cdot 10^{-4} M_{\odot} \text{yr}^{-1}$ , yellow); and two other stages,  $(t - t_{form}) \approx 20 - 40$  Myr, when PopII stars form and the star formation rate is at the average ( $\Psi \approx 10^{-3} M_{\odot} \text{yr}^{-1}$ , blue) and the maximum ( $\Psi \approx 2.5 \cdot 10^{-3} M_{\odot} \text{yr}^{-1}$ , purple) value. Panels *b*-*c*-*d*): for the three evolutionary phases highlighted in *panel a*) we compare the normalized theoretical IMF (dashed line) and the effective IMF (histograms) resulting from our Monte Carlo procedure (Sec.3.3.1). Note that the IMFs have been normalized to one.

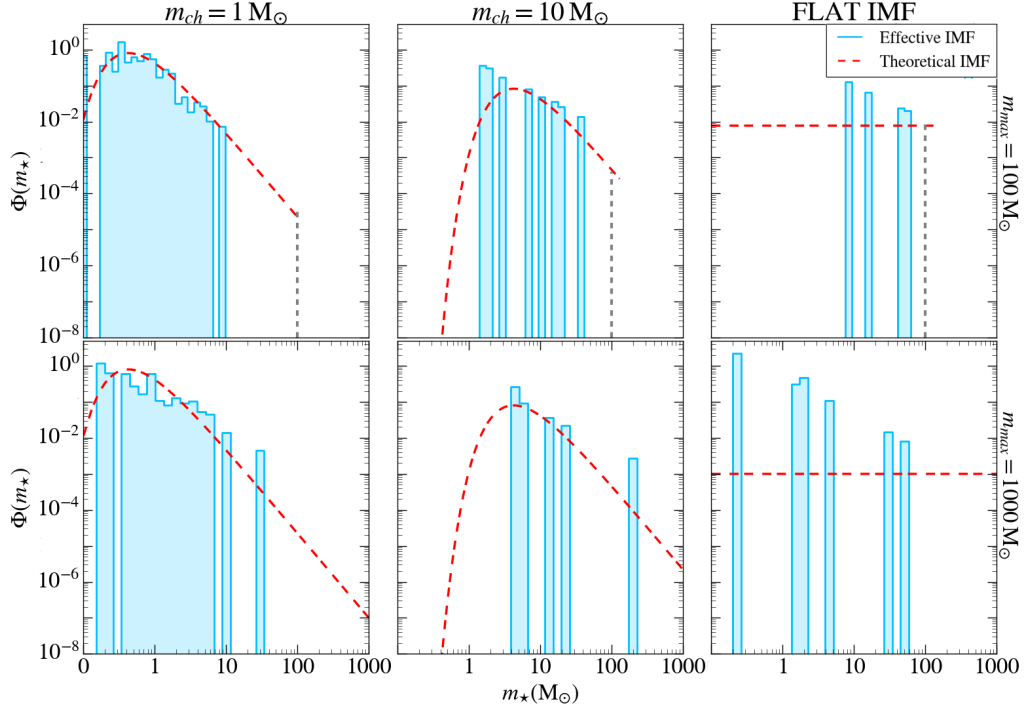


Figure 3.7: The comparison between the theoretical IMF (red dashed line) and the effective one (blue histograms) for different shapes and maximum mass,  $m_{max}$ , of the Pop III IMF. We show a Larson IMF with  $m_{ch} = 1 M_{\odot}$  (left panels),  $m_{ch} = 10 M_{\odot}$  (middle panels), and a flat IMF (right panels). The top (bottom) panels show results for  $m_{max} = 100 M_{\odot}$  ( $m_{max} = 1000 M_{\odot}$ ).

It should be noted that these results might be affected by the choice of  $\Delta t$ , since the IMF random sampling strongly depends on the total stellar mass formed in a single time-step. However, we are limited in choosing the time-step resolution: if we want to adequately follow the stellar evolution we need to have  $\Delta t < 4$  Myr. On the other hand, the typical time scales for star formation are  $\Delta t \geq 0.1$  Myr. We investigated how different choices of  $\Delta t$ , in the allowed range  $[0.1 - 4]$  Myr, affect the chemical evolution of the galaxy. In order to match the global properties of Boötes I for larger (smaller) time-steps we are obliged to choose lower (higher) star formation efficiencies, so the resulting  $\Psi$  and fraction of Pop III stars are exactly the same. In other words, the system is “self-regulated” by feedback processes, and the results of the IMF random sampling are robust.

In conclusion, our results show that, even at the peak of the star formation in Boötes I (Fig.3.6), there is not a complete convergence between the effective IMF and the theoretical one. In general, we find that the overall mass range can be fully sampled only when  $\Psi \gtrsim 10^{-1} M_{\odot} \text{yr}^{-1}$ , which is never the case in UFDs. Thus, our findings demonstrate that to study UFDs it is fundamental to model the incomplete IMF sampling, which not only affects Pop III star formation but also the formation of “normal” Pop II/I stars.

### 3.4.1 Impact of the IMF random sampling

Accounting for the random sampling of the IMF produces two main differences with respect to a fully populated stellar mass distribution. The statistical sampling of the IMF produces a more realistic, discrete number of stars for each mass bin. Secondly, when the star formation rate is small ( $\lesssim 10^{-3} \text{ M}_\odot \text{ yr}^{-1}$ ), the effective IMF is only populated with a few stars beyond  $8 \text{ M}_\odot$  (see Fig.3.6). Since stars with  $8 \text{ M}_\odot \leq m_\star \leq 40 \text{ M}_\odot$  are those that explode as SNe and are responsible for outflows and enrich the ISM with metals, the chemical enrichment history of the UFDs with and without IMF random sampling could be very different.

Due to the stochastic nature of the IMF sampling, every time that a star formation event occurs the effective stellar mass distributions can be differently populated, especially at the higher masses. For this reason we exploit a statistical approach and derive the main properties of Boötes I (see Sec.3.2) by averaging among the results of 50 runs of the code and quantifying the scatter among them.

In Fig.3.8 we compare the MDF obtained by assuming a fully populated IMF to that achieved with stochastic IMF sampling. In both cases we assume the same free parameters (Sec. 3.2). The most important difference between the two MDFs is the number of surviving zero-metallicity stars, which is more than three times higher in the random IMF sampling case, i.e.  $\approx 10\%$  of the total number of stars instead of  $2.7\%$ . As we can see in Fig.3.8, the resulting MDFs are also different in the position and amplitude of the peak. In fact, the MDF obtained with the random IMF sampling has a less pronounced peak that is shifted towards higher iron abundance,  $[\text{Fe}/\text{H}] \approx -2$ . As a consequence the observed properties ( $L_\star$ , and average  $[\text{Fe}/\text{H}]$ ) are not well reproduced in the random IMF sampling model due to the lower star formation rate.

We can therefore conclude that, when we account for the IMF random sampling in the modelling of poorly star-forming UFD galaxies, their evolution and global properties change. Hence, the model needs to be re-calibrated, using the procedure described in Sec.3.2. The new free parameters that minimise the reduced  $\chi^2$  are  $(t_{inf}, \epsilon_\star, \epsilon_w) = (14.5 \text{ Myr}, 0.9, 0.03)$ . Note that  $\epsilon_\star$  is much larger in this case<sup>4</sup>. Because of the poor IMF sampling at high masses, the effect of mechanical feedback driven by SNe is not continuous but intermittent. The impact of SNe explosions is therefore stronger since it is produced by a finite number of SNe instead of fractional numbers indeed, following the

<sup>4</sup>The fraction of gas that at each time-step is converted in stars is given by the ratio between star-formation efficiency and the free-fall time, i.e.  $\epsilon_\star \cdot dt/t_{ff}(z)$  (see Sec.3.2)

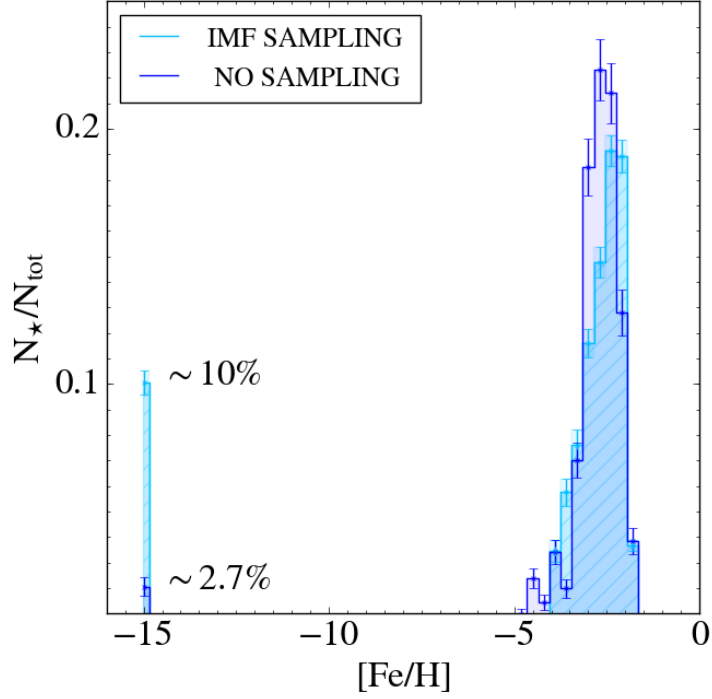


Figure 3.8: Comparison between the MDFs obtained with (light blue) and without (blue, same as Fig.3.3) IMF random sampling for which we respectively get:  $\log(L_*/L_\odot) = 4.1$ ,  $\langle[\text{Fe}/\text{H}]\rangle = -2.6$ , and  $\log(L_*/L_\odot) = 4.4$ ,  $\langle[\text{Fe}/\text{H}]\rangle = -2.7$ . The MDF obtained by stochastically sampling the IMF has been derived by averaging over 50 runs. The error bars represent the  $\pm\sigma$  dispersion among different runs. For the case without the random sampling we show the Poissonian errors.

chemical evolution of the galaxy it emerged that the explosion of one, at most two SNe, is enough for the ISM metallicity to exceed  $Z^{\text{ISM}} = 10^{-3.5}Z_\odot$ . As a consequence, the star formation rate is more easily damped. Thus, to reproduce the the total luminosity of Boötes I, a higher star-formation efficiency,  $\epsilon_*$ , is required. Finally, with the re-calibrated model, using these new parameters, we get that the fraction of zero-metallicity stars is  $\sim 12\%$  with respect to the total survivor stars. To better understand the impact of IMF random sampling in Fig. 3.9 we show the evolution of the ISM iron abundance,  $[\text{Fe}/\text{H}]$ , the star formation rate,  $\Psi$ , and the ejected gas mass,  $M_{\text{ej}}$ , of Boötes I when we consider models with and without the random sampling of the IMF. In the bottom panel of Fig.3.9 we see that  $[\text{Fe}/\text{H}]$  in the random sampling model starts with a time-delay of  $\sim 2\text{Myr}$ . This is because the more massive SNe,  $m_* = 40 M_\odot$ , that explode first are not produced in this early burst of star formation, which has  $\Psi \approx 10^{-4} M_\odot\text{yr}^{-1}$  (middle panel). Still, as soon as low-mass SNe stars to explode, the  $[\text{Fe}/\text{H}]$  in the IMF sampling model rapidly grows, exceeding the value of the model without sampling (top) in spite of the equal rate of star formation (middle panel). This is because the random sampling of the IMF provide us with a finite number of SNe instead of a fraction. Although delayed, the effect of feedback from SNe is stronger on both the ISM enrichment (top) and the mass of gas

ejected (bottom panel). When  $(t - t_{form}) \approx 25$  Myr, i.e. at the peak of the star formation for the IMF sampling model, we find that  $[\text{Fe}/\text{H}] \approx -2.6$ , which corresponds to the peak of the MDF (Fig. 3.8). In the model without IMF sampling the star formation rate reaches higher values but this maximum appears at later times,  $(t - t_{form}) \approx 35$  Myr. Yet, because of the lower metal enrichment,  $[\text{Fe}/\text{H}] \approx -2.7$ . This explains why the MDF is higher but shifted towards lower  $[\text{Fe}/\text{H}]$  values in the model without IMF sampling (Fig. 3.8).

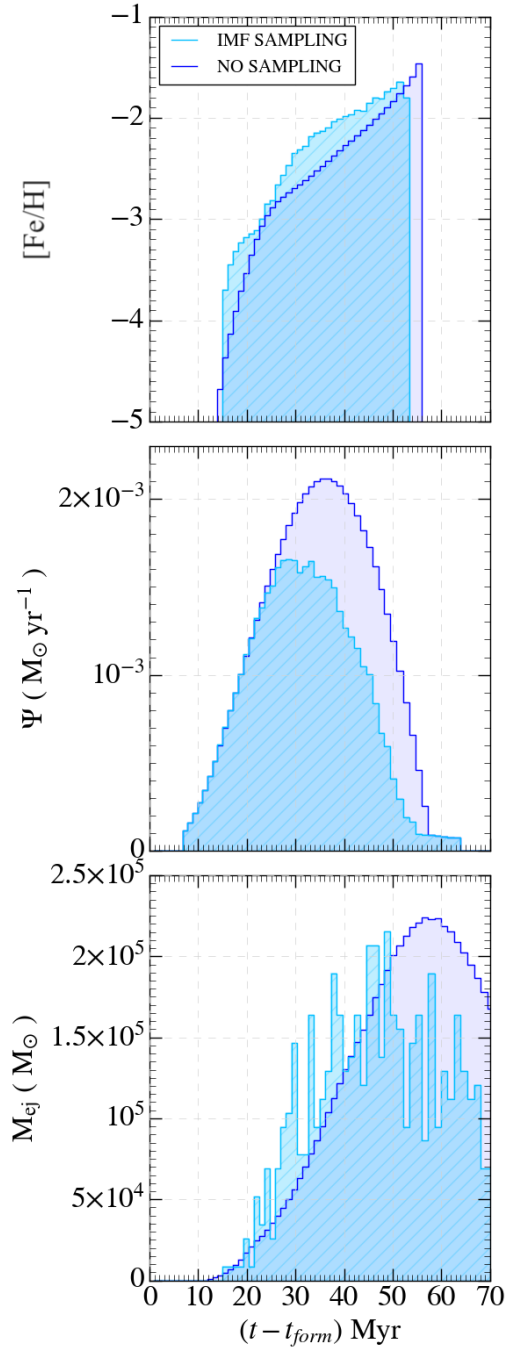


Figure 3.9: The evolution of iron abundance (top panel), star-formation rate (medium panel) and the ejected gas mass (bottom panel) for the model with (light blue) and without (dark blue) IMF random sampling.





---



---

## Unveiling the minimum mass of the first stars

The IMF of the first stars is one of the most puzzling topics in modern Cosmology. Since there are no direct observations of metal-free stars, which could provide constraints on their mass, the IMF of Pop III stars is still completely uncertain and giving constraints on it remains elusive. As we discussed in Chapter 1 and Chapter 2 theoretical studies on the formation of the first stars suggest that Pop III stars were predominantly very massive with characteristic mass  $[10 - 20] M_{\odot}$  (Omukai & Palla 2001; Abel et al. 2002; Bromm et al. 2002; Tan & McKee 2004; Hirano et al. 2014). This was confirmed by the studies of Stellar Archaeology that *indirectly* proved the existence of massive Pop III stars ( $[10 - 60] M_{\odot}$ ), as well the proof of existence of pair-instability supernovae,  $m_{\star} = [140 - 260] M_{\odot}$  (Aoki et al. 2014; Salvadori et al. 2019; Tarumi et al. 2020). However, 3D simulations that study the cooling of primordial gas reveal that less massive Pop III stars, with mass  $m_{\star} \leq 0.8 M_{\odot}$ , can form. (e.g. Machida et al. 2008; Turk 2009; Smith et al. 2010; Clark et al. 2011; Greif et al. 2011; Stacy et al. 2013; Dopcke et al. 2013; Stacy & Bromm 2014; Stacy et al. 2016; Susa 2019; Wollenberg et al. 2020). Therefore it cannot be excluded that Pop III stars with  $m_{\star} \leq 0.8 M_{\odot}$  might be able to form and survive until present-days. Hence, the precise value of the lower-mass limit to Pop III stars is important in predicting whether any truly metal-free stars could have survived until the present-day. At the moment, we have only a few observational-driven constraints on the IMF of the Pop III stars, and we are not even able to exclude that it was equal to the present-day stellar IMF. *How can we further constrain the Pop III IMF?*

The non-detection of zero-metallicity stars in ultra-faint dwarf galaxies can be used to constrain IMF of the first stars by means of a statistical comparison between available data and predictions from chemical evolution models. To this end, in this Chapter we investigate the frequency of Pop III star survivors in UDF galaxies and we explore the impact of different shape and lower mass-limits of the Pop III IMF on the expected number of long-living first stars in Boötes I. By comparing our model results with the

current number of observed stars in Boötes I, and other UFDs, we give constraints on the shape (characteristic mass,  $m_{ch}$ ) and low-mass end (the minimum mass,  $m_{min}$ ) of the first stars. The results presented in this Chapter are mainly based on the paper Rossi et al. (2021).

## 4.1 Impact of the Pop III IMF

As we see in the previous Chapter 3 (Sec. 3.4), our study has revealed that it is crucial to take into account the incomplete sampling of the IMF in poorly star-forming systems, like UFDs, to realistically represent their stellar populations. This is especially relevant for the earliest star formation, where Pop III stars formed very inefficiently for a limited time. So far we have assumed that Pop III stars form according to the present-day stellar IMF (see Eq. 3.3). With this assumption we estimated that the expected fraction of long-lived Pop III stars in Boötes I is  $\sim 12\%$  of the total. Now we explore how this result changes by varying the Pop III IMF shape, minimum, and maximum mass. As illustrated in Fig.3.2, we here consider three Larson IMF with different characteristic masses,  $m_{ch}$ , along with a Flat IMF case (see also Sec.3.1.5).

### 4.1.1 Pop III star survivors

Our results show that the observed global properties of Boötes I are almost entirely determined by Pop II/I stars, and that the Pop III IMF has negligible effect on the average  $[\text{Fe}/\text{H}]$  and  $L_*$  of the galaxy. Pop III stars form during the first evolutionary phase of Boötes I, ( $t - t_{form}$ )  $\sim 15$  Myr, when the star formation rate is low,  $\Psi \lesssim 10^{-3.5} \text{yr}^{-1} M_\odot$  (see Fig.3.6). Their contribution to the total stellar mass formed in Boötes I, and therefore to the total  $L_*$ , is only  $\approx 10\%$ . Consequently, very few Pop III SNe are formed, both due to their low star formation rate, and the incomplete sampling of the IMF. The overall ISM metal enrichment is therefore dominated by Pop II/I stars. Similarly, changing the Pop III IMF only slightly affects the MDF of Boötes I. This is illustrated in Fig.4.1, where we show the MDFs obtained by varying both the shape and lower mass limit of the Pop III IMF. All the simulated MDFs are in good agreement with that of Boötes I and consistent among each other (i.e. within the dispersion of different runs). This is because the shape of the MDF between  $-4 < [\text{Fe}/\text{H}] < 1$  is driven by the Pop II/I stars whose IMF has not been changed.

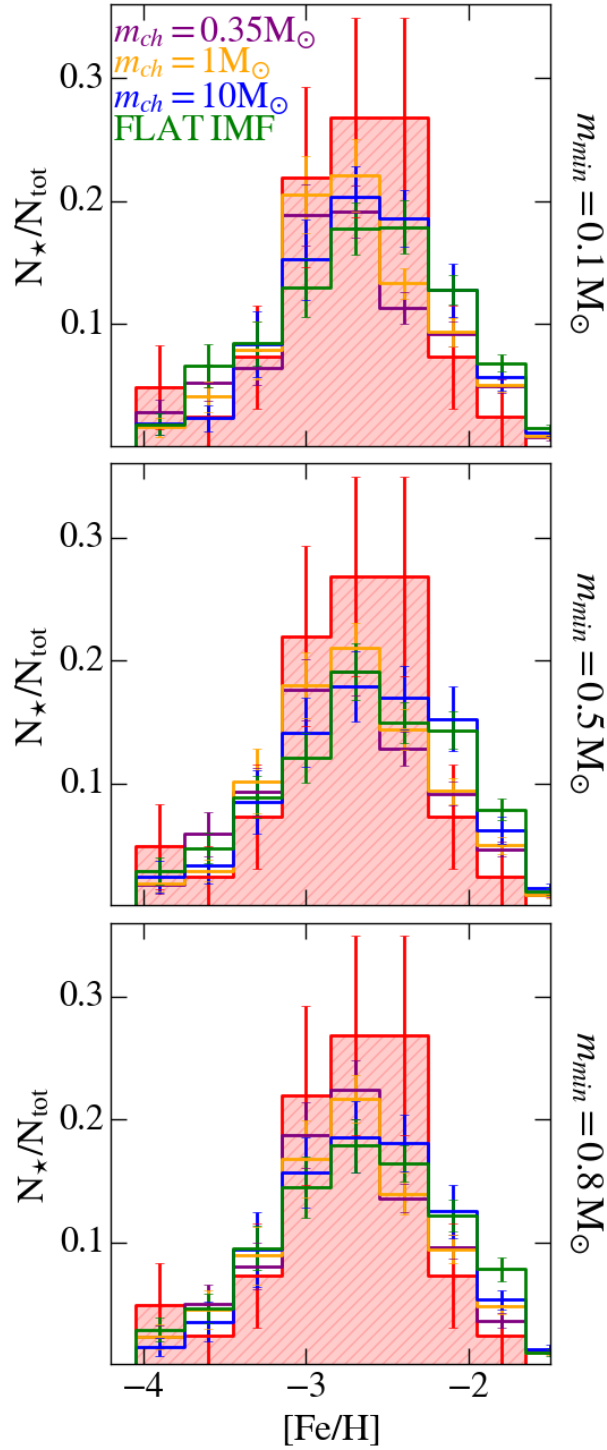


Figure 4.1: The simulated MDFs, obtained by varying the PopIII IMF, in comparison with that of Boötes I (red histogram). In the column we show MDFs obtained by varying the minimum mass,  $m_{\text{min}}$ , of the PopIII stars, while the different colours identify different IMF shapes, i.e. the different characteristic mass,  $m_{\text{ch}}$ .

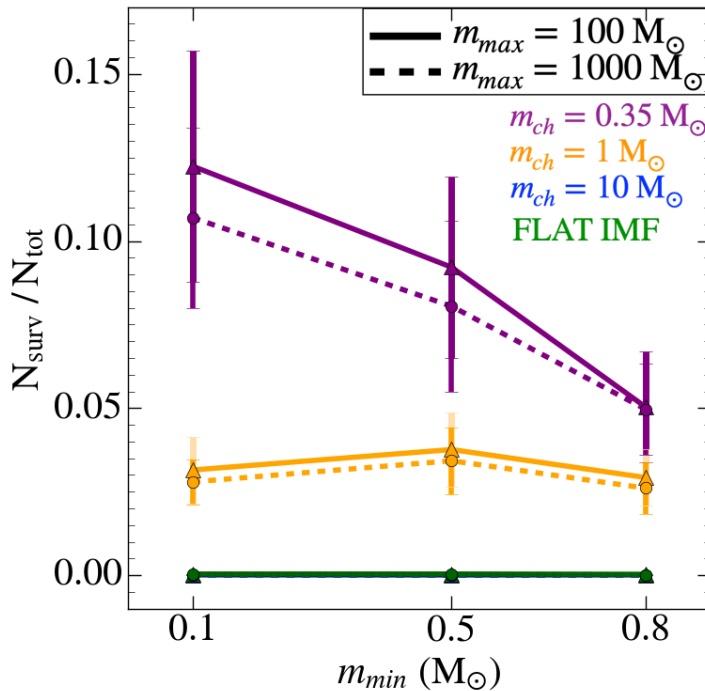


Figure 4.2: The number of Pop III survivors,  $N_{surv}$  ( $Z_{\star} \leq Z_{cr}$ ), with respect to the total,  $N_{tot}$ , as a function of the minimum mass of Pop III stars,  $m_{min}$ , assuming a maximum mass of  $m_{max} = 100, 1000 M_{\odot}$  (solid, dashed lines). The colours represent the different choices of the Pop III IMFs (see Fig.3.2).

Conversely, the expected number of Pop III stars changes considerably by varying the Pop III IMF. This is illustrated in Fig.4.2, where we show the number of surviving Pop III stars,  $N_{surv}$ , with respect to the total number of stars in Boötes I,  $N_{tot}$ , for different  $m_{min}$ ,  $m_{max}$ , and shape of the Pop III IMF. At fixed  $m_{min}$ , we can see that  $N_{surv}/N_{tot}$  decreases as  $m_{ch}$  increases. This is expected since when  $m_{ch}$  increases it becomes less likely to form stars with  $m_{\star} \leq 0.8 M_{\odot}$ , especially when the star formation rate is low ( $\Psi \lesssim 10^{-3} M_{\odot} \text{ yr}^{-1}$ ). For this reason, both the Flat Pop III IMF and a Larson Pop III IMF with  $m_{ch} = 10 M_{\odot}$  give very low  $N_{surv}/N_{tot} < 0.0001$ .

By varying  $m_{min}$  at fixed  $m_{ch}$ , we can identify two different trends: for  $m_{ch} = 0.35 M_{\odot}$ ,  $N_{surv}/N_{tot}$  decreases with increasing  $m_{min}$ , while for all the others IMFs the increase of  $m_{min}$  has essentially no effect on the fraction of long-lived Pop III stars. These trends can be explained as a combination of two effects: the shape of the theoretical IMF, i.e. the higher is the characteristic mass, the more unlikely it is to form low-mass stars; and the incomplete IMF sampling.

For  $m_{ch} = 0.35 M_{\odot}$  the low-mass end of the Pop III IMF, i.e. where the maximum resides, is well-populated even when the star formation rate is very low (see Fig.3.6). So when we increase  $m_{min}$  we are automatically decreasing the number of low-mass Pop III

stars that can form and survive until the present day. Increasing  $m_{min}$  therefore leads to a decrease in the percentage of survivor Pop III stars. Instead for  $m_{ch} > 1 M_{\odot}$  and a Flat IMF, when  $\Psi \lesssim 10^{-3} M_{\odot} \text{yr}^{-1}$  it is unlikely to form stars with  $m_{\star} \leq 0.8 M_{\odot}$ . Hence, by increasing  $m_{min}$  the probability to form low-mass stars does not change significantly, and therefore the percentage of long-lived Pop III stars is roughly constant.

In Fig.4.2 we also explore how the fraction of Pop III stars changes if we extend the maximum mass of Pop III stars,  $m_{max}$ , up to  $1000 M_{\odot}$ . As we can see,  $N_{surv} / N_{tot}$  is roughly independent of  $m_{max}$ . In fact, as we have previously discussed, Pop III stars formed in the first evolutionary phases of the galaxy, when  $\Psi \lesssim 10^{-3} M_{\odot} \text{yr}^{-1}$ . It follows that the Pop III IMF is badly populated, especially for  $m_{\star} \geq 10 M_{\odot}$ , whatever IMF is chosen (Fig.3.6 panel a). Hence the probability to form low-mass stars does not change. In conclusion, extending  $m_{max}$  up to  $1000 M_{\odot}$  has very little effect on the fraction of Pop III stars that we expect to find in Boötes I.

Finally, we made the same analysis for the other UFDs that have global properties consistent with our model (Fig.3.3). The fractions of Pop III star survivors that we expect to find in Hercules, Leo IV and Eridanus II are all consistent with those of Boötes I, within the error bars.

## 4.2 Constraining the low-mass end of Pop III stars

We can now exploit the non-detections of metal-free stars in Boötes I to put constraints on the minimum mass of Pop III stars. The key question is: how many stars do we need to observe to have a probability<sup>1</sup> of 68%, 95% and 99% to catch Pop III stars for a given IMF?

Following the statistical approach of Hartwig et al. (2015), we estimate the minimum stellar sample ( $N_o$ ) needed to be observed in Boötes I as a function of  $m_{min}$  for different Pop III IMFs to constrain  $m_{min}$  (Fig.4.3). Since no Pop III stars have been discovered so far, all models that predict a  $N_o$  smaller than the total number of stars observed in Boötes I, can be used to constrain  $m_{min}$ .

For  $m_{ch} = 0.35 M_{\odot}$ ,  $N_o$  increases with  $m_{min}$  (Fig.4.3). As discussed in the previous Sec.4.1.1 (Fig.4.2), the fraction of Pop III survivors,  $N_{surv}$ , decreases with increasing  $m_{min}$  and so a larger stellar sample is needed to exclude their existence. Instead,  $N_o$  is roughly constant for  $m_{ch} = 1 M_{\odot}$  (Fig.4.3), and this reflects the roughly constant trend of

<sup>1</sup> Assuming that all stars have the same probability of being observed, the probability of not having detected any Pop III survivor stars in the observed sample is:  $p_0 = \frac{(N_{tot} - N_{surv})!(N_{tot} - N_o)!}{N_{tot}!(N_{tot} - N_{surv} - N_o)!}$ , where  $N_{tot}$  is the total number of stars in the galaxy at  $z = 0$ ,  $N_{surv}$  the expected number of survivor Pop III stars, and  $N_o$  is the number of observed stars.  $1 - p_0$  is therefore the probability to observe Pop III stars.

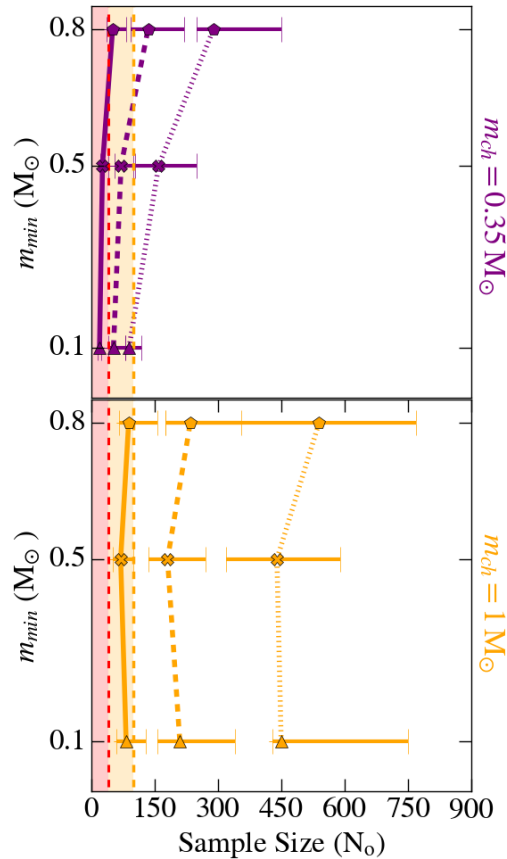


Figure 4.3: The sample size,  $N_o$ , needed to constrain the Pop III IMF as a function of  $m_{min}$  of the Pop III IMF. The different colours represent the Pop III characteristic mass, purple  $m_{ch} = 0.35 M_\odot$ , and orange  $m_{ch} = 1 M_\odot$ . The lines mark the different confident levels: 68% (solid), 95% (dashed), and 99% (dotted).

$N_{\text{surv}}$  with  $m_{min}$  (Fig.4.2). In Fig.4.3 we only show our findings for  $m_{ch} \leq 1 M_\odot$  because in the case  $m_{ch} = 10 M_\odot$  and the Flat IMF the sample size required to put constraints is  $\sim 10^4$ , independently of  $m_{min}$  and  $m_{max}$ . We can now try to get some observationally driven limits on  $m_{min}$  for different Pop III IMFs. So far there are only 41 stars in Boötes I with measured iron abundances. By using these stars (red area in Fig.4.3) we can already exclude that Pop III stars formed according to a present-day stellar Larson-type IMF at the 68% confidence level. In other words, either  $m_{ch} > 0.35 M_\odot$  or  $m_{min} > 0.8 M_\odot$ . We recall that our model is also able to reproduce the properties of the UFD galaxies Hercules, Leo IV, and Eridanus II (Fig.3.3). If we also consider stars that have been observed in these UFD galaxies, the actual sample size goes up to  $N_o = 96$  (orange area in Fig.4.3). Using these additional data we get even tighter constraints, and the present-day stellar IMF is excluded at the 95% of confidence level. Furthermore we can assert that  $m_{min} > 0.8 M_\odot$  or  $m_{ch} > 1 M_\odot$  at the 68% of confidence level.

### 4.2.1 Stronger Pop III IMF constraints

By using the non-detection of zero-metallicity stars in Boötes I, we have constrained the shape and minimum mass of the Pop III IMF (Sec.4.1). However, even if Pop III stars with  $m_{\star} \leq 0.8 M_{\odot}$  were able to form and survive until today, it does not necessarily imply that they are readily identifiable. Currently, we can obtain the spectra necessary for iron abundance determination, only for the most luminous red giant branch stars in UFD galaxies. Therefore, to quantify and identify Pop III stars that are on the red giant branch, color-magnitude diagrams (CMD) are required. This will allow us to determine how many Pop III stars are bright enough to be observed with current telescopes, but also to make testable predictions for the new-generation telescopes and instruments (MOSAIC/ELT, Hammer et al. 2014; Evans et al. 2015).

## 4.3 Simulating the Boötes I CMD

To simulate the CMD of Boötes I we used the PARSEC isochrones (Bressan et al. 2012) and CMD generator<sup>2</sup> adopting the SDSS ugriz photometric system. For the evolutionary tracks we use PARSEC version 1.2S plus COLIBRI S35 (Pastorelli et al. 2019) that add the TP-AGB evolution. For dust we assumed the scaling relations from Marigo et al. (2008), the extinction curve of Cardelli et al. (1989) plus O'Donnell (1994), and we applied extinction coefficients computed star-by-star. Finally, we selected the Kroupa IMF that, especially in the low-mass end, is the most similar to the Larson IMF assumed in our model (see Sec. 3.1.5). Note that PARSEC is limited in metallicity, therefore we assign to metal-free stars the minimum available metallicity of  $Z_{\star} = 10^{-7} Z_{\odot}$ . The synthetic CMD is shown in Fig.4.4, where i magnitude has been corrected, taking into account the distance of Boötes I (McConnachie 2012). For each star in the CMD we assign a random error in magnitude and color<sup>3</sup> in order to simulate real observations.

---

<sup>2</sup> available at <http://stev.oapd.inaf.it/cmd>

<sup>3</sup> We adopt the errors estimated in: <http://classic.sdss.org/dr4/algorithms/sdssUBVRITransform.html>

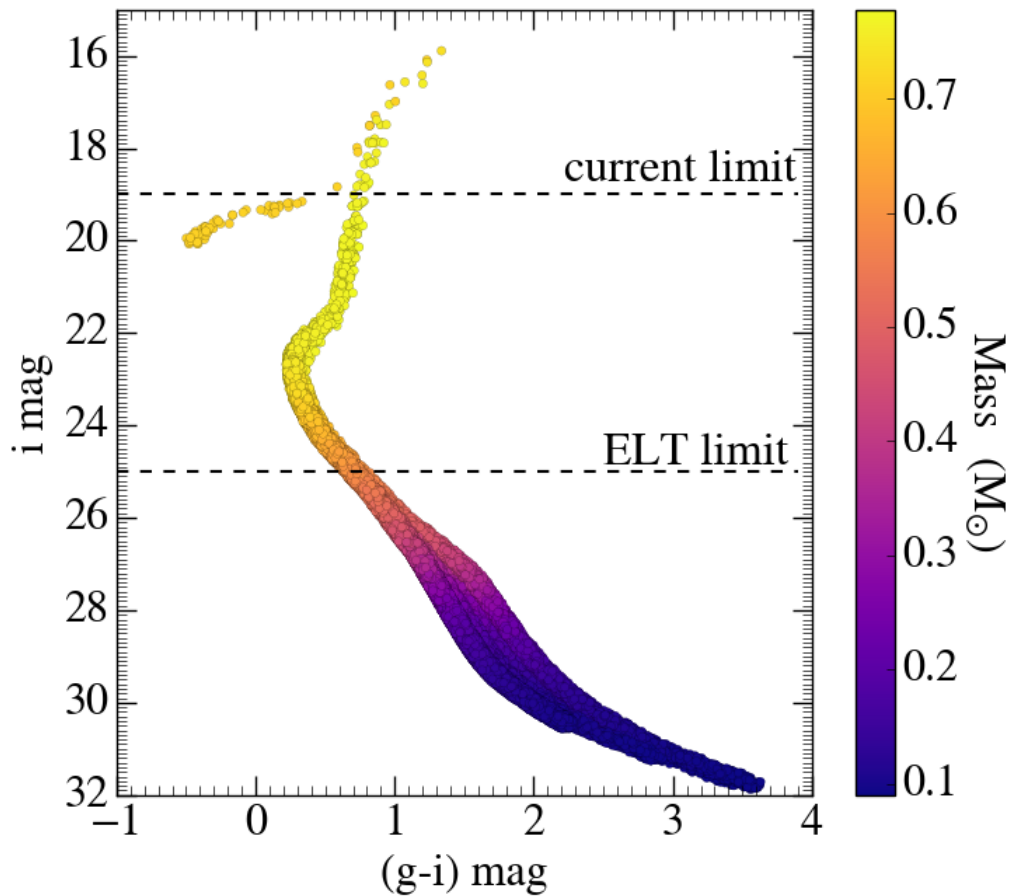


Figure 4.4: The Boötes I simulated CMD, derived using PARSEC CMD generator with SDSS photometric bands. The color bar represents the mass of the stars in the CMD, while the two dashed horizontal lines indicate respectively the limit magnitude of the current observations of Boötes I,  $i = 19$ , and the limit given for MOSAIC on ESO ELT,  $i = 25$ .

#### 4.3.1 Can we really catch zero-metallicity stars?

The synthetic CMD in Fig.4.4 shows a clear general trend of stellar mass and luminosity, i.e. the smaller is  $m_*$ , the fainter is the star. The spectroscopic data, currently available for Boötes I, reach a magnitude  $i \sim 19$ , for which 41 stars have measured  $[\text{Fe}/\text{H}]$ . At the moment we are thus only able to measure iron and other chemical elements in the more massive, and therefore more luminous,  $m_* \geq 0.7 M_\odot$ . However, to catch potential zero-metallicity stars with  $m_* = 0.1 M_\odot$ , observations should reach extremely deep magnitude,  $i = 32$ . Indeed, as show in Fig.4.4, the planned MOSAIC instrument on the ESO ELT will be able to reach  $V \approx 25$  at  $R \approx 15\,000 - 20\,000$  (Evans et al. 2015). This means that most of these very low-mass Pop III stars, if they ever existed, will be invisible even for future generation telescopes.



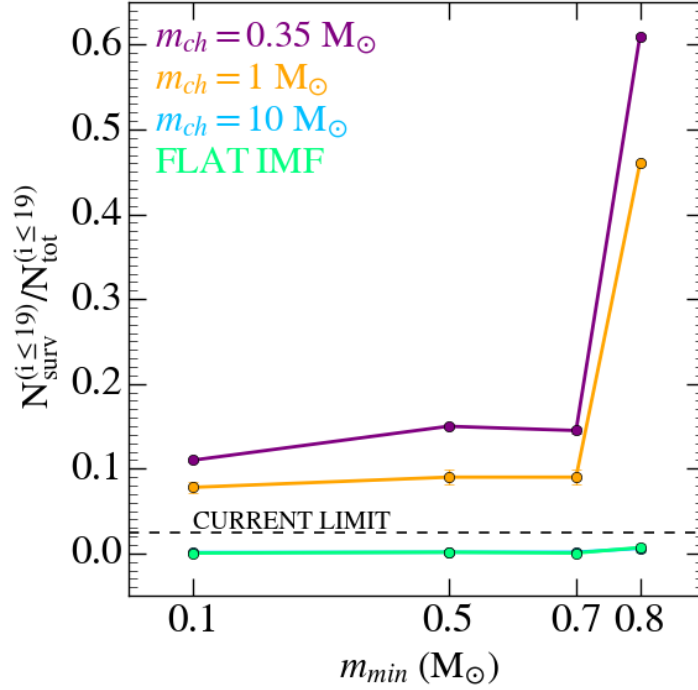


Figure 4.5: The fraction of zero-metallicity stars with respect the truly observable sample of stars as a function of the Pop III minimum mass. Colours identify the different Pop III IMFs, where  $m_{max} = 100 M_{\odot}$  in all cases.

### 4.3.2 How to get tighter Pop III IMF constraints

In Sec.4.2 we estimated the fraction of Pop III stars that survive until  $z = 0$  with respect to the total number of surviving stars in Boötes I, i.e. all the stars present in the CMD (Fig.4.4). What happens if we compute the number of Pop III star survivors within the sample of stars that are realistically observable?

In Fig.4.5, we show the fraction of Pop III survivors in Boötes I, as a function of  $m_{min}$ , for the current magnitude limit,  $i \leq 19$ , i.e.  $N_{surv}^{(i \leq 19)} / N_{tot}^{(i \leq 19)}$ . For the two cases,  $m_{ch} = 0.35 M_{\odot}$  and  $1 M_{\odot}$ , the new fractions of zero-metallicity stars increase with  $m_{min}$ , i.e. the trend is inverted with respect to what was found in Fig.4.2. Furthermore, at  $m_{min} = 0.8 M_{\odot}$ , the fractions for  $m_{ch} = 0.35 M_{\odot}$  ( $m_{ch} = 1 M_{\odot}$ ) are one order of magnitude higher than in Fig.4.2, reaching 60% (45%) of the total, instead of 5% (3%).

The reason for these significant differences has to be found in the stellar mass-magnitude relationship, shown in Fig.4.4. In the case of  $m_{min} = 0.1 M_{\odot}$  and  $m_{ch} = 0.35 M_{\odot}$ , long-lived Pop III stars are distributed over all magnitudes according to their masses, in the same way as Pop II/I stars. The fraction of Pop III survivors at  $i < 19$  is thus comparable to the total fraction (e.g. 12% for  $m_{ch} = 0.35 M_{\odot}$  in both Fig.4.2 and Fig.4.5).

However, as  $m_{min}$  increases, a higher number of Pop III star survivors is more massive and thus more luminous. This results in a higher fraction of long-lived Pop III stars in the observable region, i.e.  $i \leq 19$  (corresponding to  $m_{\star} \gtrsim 0.7 M_{\odot}$ ). Going to deeper magnitudes, in this case, will thus only result in a higher contamination by Pop II stars and thus a lower  $N_{surv}/N_{tot}$ . On the other hand, if  $m_{ch} = 10 M_{\odot}$  or if the IMF is flat, the fractions of Pop III star survivors do not vary significantly with respect to Fig.4.2 since the probability to form long-lived  $m_{\star} < 0.8 M_{\odot}$  Pop III stars is always very low, independently on  $m_{min}$  (see Fig.3.2).

Among the 41 stars spectroscopically observed in Boötes I, no long-lived Pop III stars ( $Z_{\star} < Z_{cr} = 10^{-4.5} Z_{\odot}$ ) have been identified. We can thus assert that, according to current observations, the probability to have long-lived Pop III stars in Boötes I should be  $P_{obs} < 1/N_{tot} = 1/41 \sim 2\%$ . Since  $P_{obs}$  represents the upper limit of the probability to detect Pop III stars, all models that predict a probability larger than  $P_{obs}$  can be discarded. This current (upper) limit is shown in Fig.4.5, where we can appreciate the power of this simple approach: models with  $m_{\star} \leq 0.8 M_{\odot}$  or  $m_{ch} \leq 1 M_{\odot}$  can be already excluded, which implies that we can put even tighter constraints on the Pop III IMF.

In Fig.4.6 we show the sample size,  $N_o$ , needed to constrain the low-mass end of Pop III IMF at different confidence levels, using the approach from Sec.4.2, but now only focusing on stars with  $i \leq 19$ . First, we notice that the required stellar sample size is smaller ( $N_o \leq 100$ ) with respect to the previous case ( $N_o \sim 800$ , Fig.4.3). In fact,  $N_o$  strongly depends on both  $N_{surv}^{(i \leq 19)}$  and  $N_{tot}^{(i \leq 19)}$ ; the higher is the fraction of zero-metallicity stars the lower is  $N_o$ . By using the current sample of stars observed in Boötes I, we are able to exclude  $m_{min} = 0.8 M_{\odot}$  at 99% of confidence level for  $m_{ch} = 0.35 M_{\odot}$  and  $m_{ch} = 1 M_{\odot}$ . Furthermore, by including the data for Hercules, Leo IV and Eridanus II, we can conclude that Pop III stars should have  $m_{min} > 0.8 M_{\odot}$  or  $m_{ch} > 1 M_{\odot}$  at 99% of confidence level. Note that we are not showing models with  $m_{ch} = 10 M_{\odot}$  and a Flat IMF since  $N_{surv}^{(i \leq 19)}/N_{tot}^{(i \leq 19)} \approx 0.2\%$  (see Fig. 4.5), hence even by observing all stars with  $i \leq 19$  in Boötes I ( $N_{tot}^{(i \leq 19)} \approx 100$ ) we are unable to constrain  $m_{min}$ .

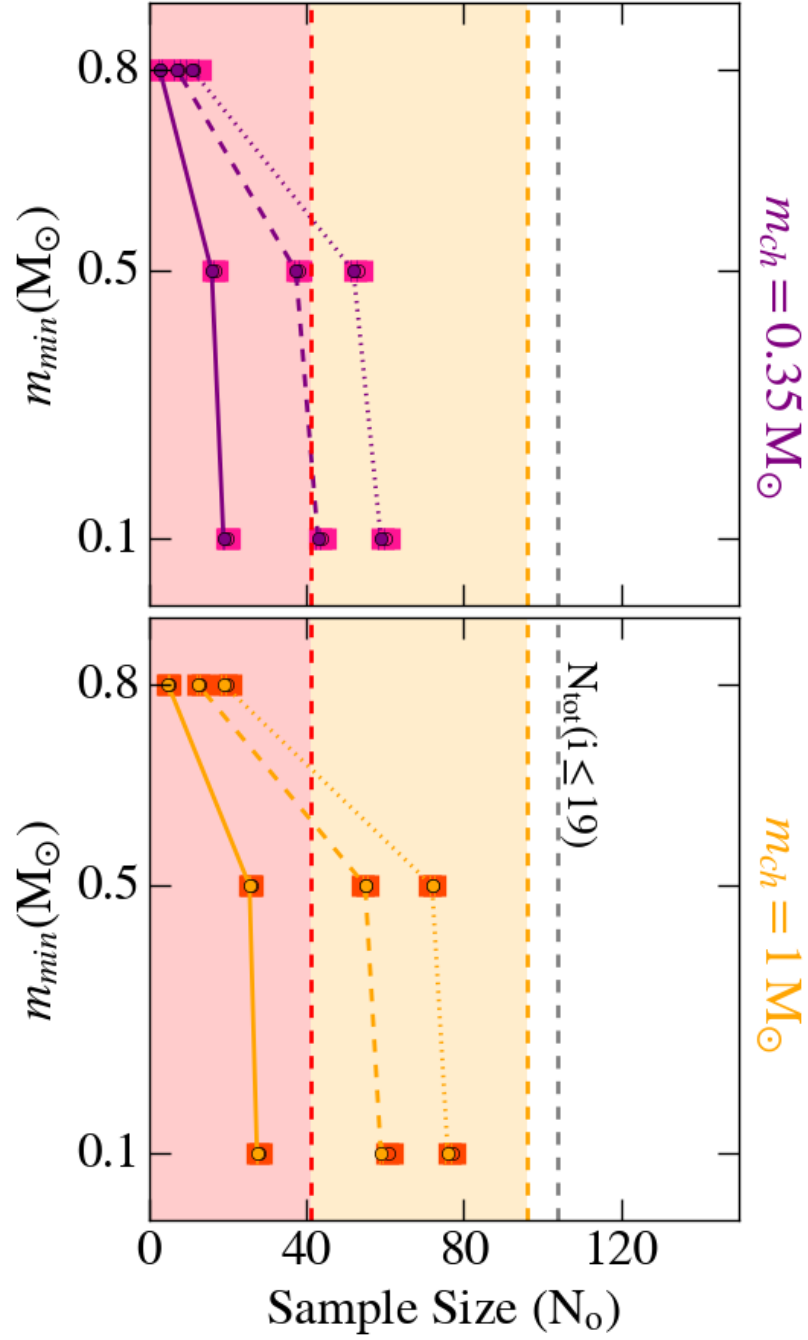


Figure 4.6: The sample sizes,  $N_o$ , needed to constrain the minimum mass,  $m_{min}$ , of Pop III stars, for  $m_{max} = 0.35 M_{\odot}$  (purple) and  $m_{max} = 1 M_{\odot}$  (orange), at different confidence levels, for stars with  $i \leq 19$ . The shaded areas display the currently observed stars in Boötes I (red) and Boötes I+Hercules+Leo IV+Eridanus II (orange). The vertical dashed line in grey delineates the total number of stars with  $i \leq 19$  in Boötes I. The filled circles represent the results assuming  $m_{max} = 100 M_{\odot}$  for Pop III stars, while squares correspond to  $m_{max} = 1000 M_{\odot}$ .

### 4.3.3 How deep should we go?

Fig.4.7 shows how the fraction of Pop III stars changes as a function of the observed magnitude. In most cases we see, somewhat counterintuitively, that the fraction of Pop III survivor stars *decreases as we reach fainter magnitudes*. This is because most of the Pop III IMFs tested here are more top-heavy compared to the adopted Pop II/I IMF. This means that, as we go to fainter magnitudes (and thus reach lower-mass stars), the stellar sample becomes more and more dominated by the normal low-mass Pop II/I stars. An exception is when the Pop II/I and Pop III IMF is assumed to be the same ( $m_{ch} = 0.35$  and  $m_{min} = 0.1$ ). In that case the trend with limiting magnitude is flat (Fig.4.7) since both populations are equally distributed in mass (and thus magnitude).

In conclusion, a higher limiting magnitude does not imply a higher fraction of Pop III survivors. So why should we go deeper in magnitude? The key point is that for  $m_{ch} > 1 M_{\odot}$  the predicted fraction of Pop III star survivors is so low ( $< 0.5\%$ ), that if we want to constrain  $m_{min}$  to at least the 68% of confidence level, we need larger stellar samples, which can only be obtained with deeper observations.

We use the simulated CMD (Fig.4.4) to count the number of stars at a given magnitude in Boötes I. The results are illustrated in Fig.4.8, where we show the limiting magnitude (sample size) required to constrain  $m_{min}$  at the 68% confidence level for different  $m_{ch}$ . Future instruments and telescopes and dedicated surveys, such as MOSAIC on the ELT and 4MOST survey (Skúladóttir et al. 2023, ESO Messenger), will allow us to measure the metallicity of  $10^4$  stars in Boötes I (see Fig.4.8) and thus either discover a bona fide zero-metallicity star or convert the persisting non-detection into even stronger Pop III IMF constraints:  $m_{min} > 0.8 M_{\odot}$  or  $m_{ch} > 5 M_{\odot}$  at the 68% confidence level. To get constraints for  $m_{ch} = 10 M_{\odot}$  (or a Flat IMF) we need  $N_o \approx 10^{4.3}$  stars, which implies to observe  $\sim 90\%$  of the stars in Boötes I, and thus to reach extremely deep magnitudes,  $i = 26$ . Finally, after simulating the theoretical CMDs for Hercules, Leo IV and Eridanus II, thereby accounting for the different distances, we find that with MOSAIC on the ELT we can collect a sample size of  $10^{4.2}$  stars at  $i \leq 25$ , and therefore constrain the Pop III minimum mass,  $m_{min} > 0.8 M_{\odot}$ , for  $m_{ch} = 7 M_{\odot}$  at the 68% of confidence level. In conclusion, by targeting UFDs with next generation instruments and telescopes we will be able to tightly constrain the minimum mass of Pop III stars,  $m_{min} > 0.8 M_{\odot}$ , independent of the shape of their IMF.

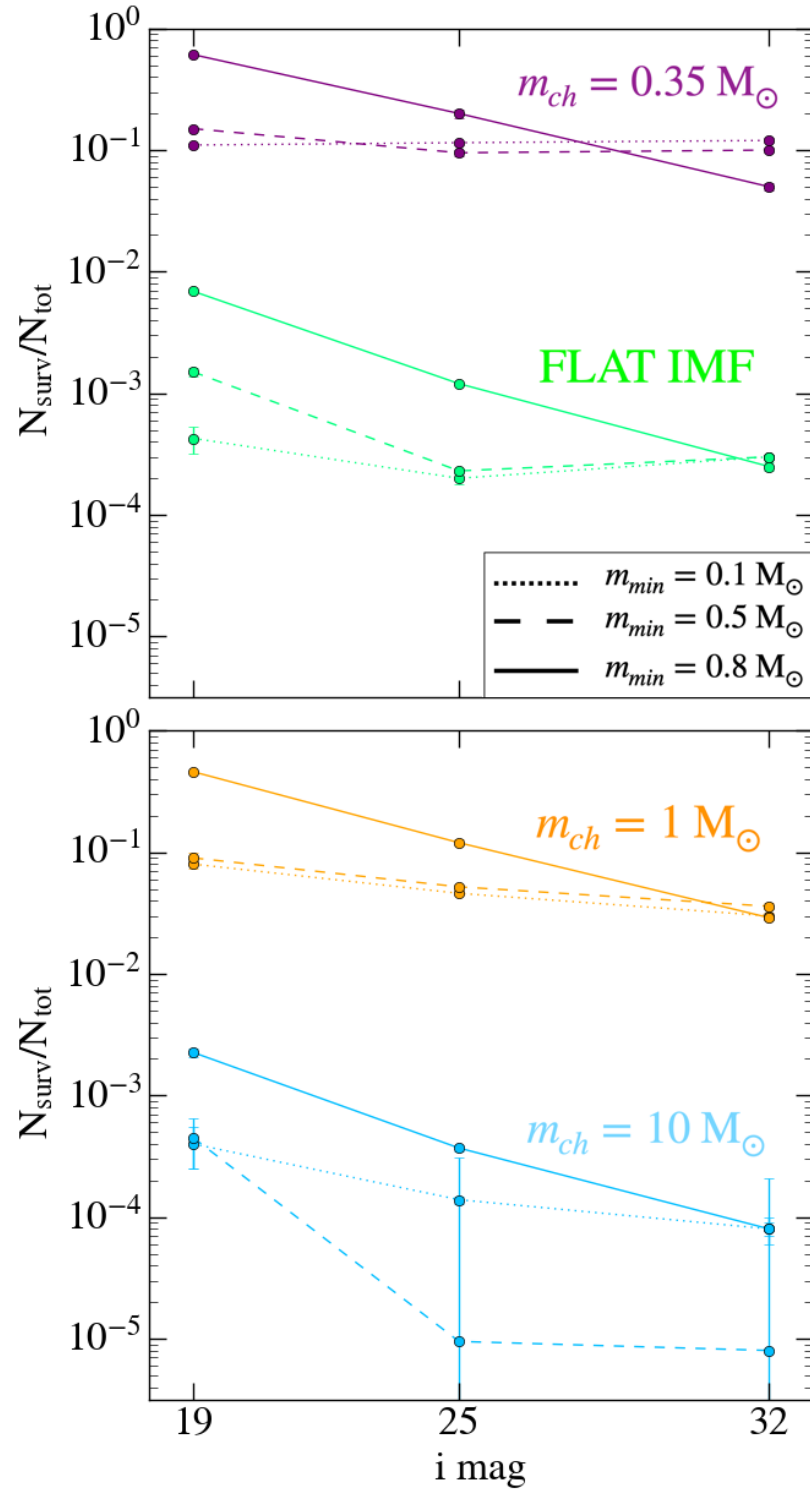


Figure 4.7: Fractions of Pop III survivor stars in Boötes I as a function of the  $i$  magnitude for Pop III IMFs with different shapes and  $m_{min}$ , assuming  $m_{max} = 100 M_{\odot}$ .

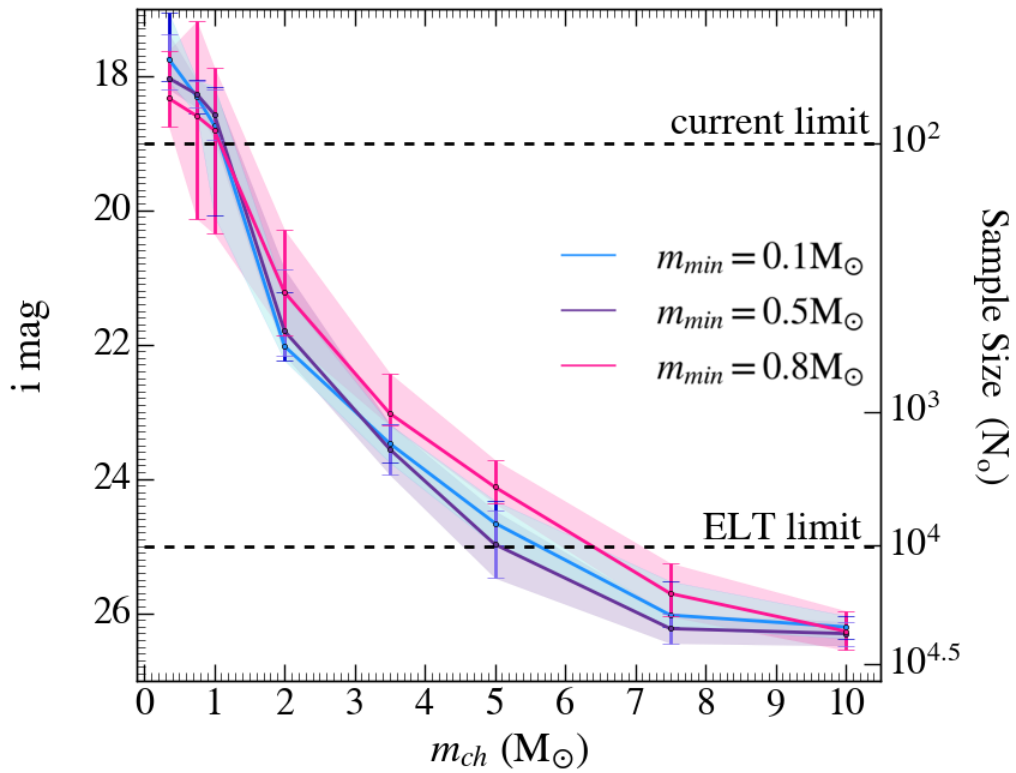


Figure 4.8: The magnitude or equivalently the total number of observed stars in Boötes I required to constrain the minimum mass of PopIII stars,  $m_{min}$ , at 68% of confidence level, as a function of  $m_{ch}$ . Colours delineate models with different  $m_{min}$ , while the shaded areas represent the  $\pm\sigma$  errors.

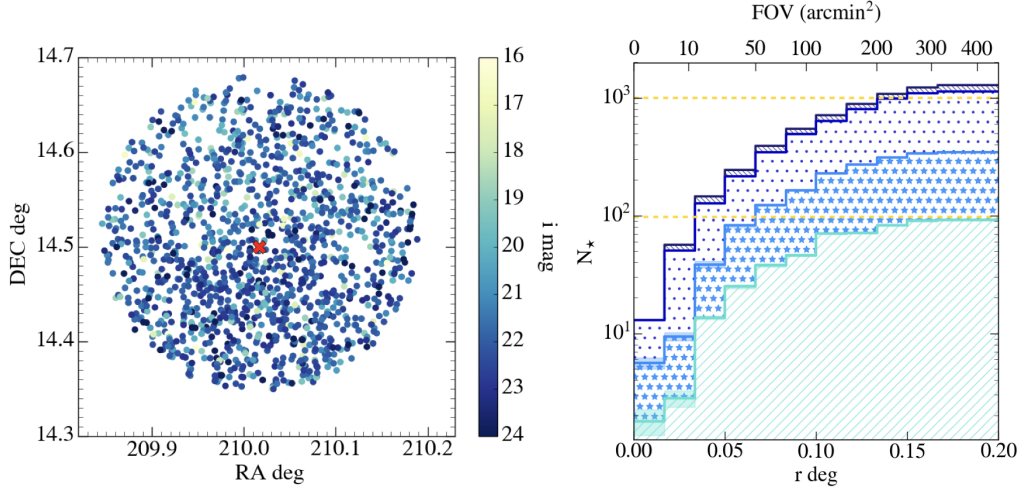


Figure 4.9: Left: the Boötes I spatial distribution of stars from the simulated CMD. The color bar highlights the different magnitudes, while the red cross identifies the center of mass,  $x_{cm} = 210.017$  deg, and  $y_{cm} = 14.5$  deg. Right: the number of stars enclosed in a circumference of radius  $r$  (bottom) and the corresponding FOV (top), for different limiting magnitudes. These trends were obtained by averaging over 50 realisations of the Boötes I simulated CMD and the corresponding spatial distributions, and the shaded areas represent the  $\pm\sigma$  Poisson errors.

#### 4.3.4 Deeper or wider?

Combining observations and theoretical predictions for Boötes I allows us to derive the galaxy’s *real* stellar spatial distribution.

To achieve this goal, we take advantage of the SDSS archive to obtain the observed CMD of Boötes I. By comparing the simulated Boötes I CMD to a real one, we can select member stars from the observed one, and assign RA and Dec to the stars of the simulated CMD.

For each star in the observed CMD we identify the best “*twin*” in the simulated one, i.e. we look for the simulated star with color and magnitude closest to the observed one by minimising the distance in the  $g-i$  and  $i$  magnitude space.<sup>4</sup> We then assign the positions of the observed stars (RA, Dec.) to the simulated ones (Fig.4.9, left). Since the errors assigned to the stars in the simulated CMD are random (Sec.4.3), in every run the simulated stars move around their positions in the CMD. Therefore we identify the best twins for each run and then obtain the final results by averaging over 50 runs. The Boötes I SDSS data are limited in magnitude,  $i = 24$ , above which the observed CMD is not well populated. Therefore the spatial distribution of the simulated stars, shown in Fig.4.9, is limited to  $i \leq 24$ .

Starting from the center of Boötes I, we count the number of stars with different limiting

<sup>4</sup>  $d = \sqrt{((g-i)_{\text{obs}} - (g-i)_{\text{sim}})^2 + (i_{\text{obs}} - i_{\text{sim}})^2}$

magnitudes as a function of the radius and field-of-view (FOV) of the targeted area, see Fig.4.9 (right). Currently we have spectroscopic data of 41 Boötes I stars with a limiting magnitude  $i \sim 19$ . By covering an area  $\sim 400 \text{ arcmin}^2$ , it is possible to observe up to  $\approx 100$  stars at  $i \leq 19$ . However, we can obtain the same sample size by going deeper in magnitude. For example, to reach 100 stars at  $i = 21$  (23), the FOV should be  $\approx 50 \text{ arcmin}^2$  ( $10 \text{ arcmin}^2$ ). Finally, by reaching limiting magnitude  $i = 24$ , and covering the entire FOV of Boötes I, we can obtain a sample of  $> 10^3$  observed stars, which implies that we can constrain  $m_{min}$  for  $m_{ch} > 2 M_{\odot}$  at 68% of confidence level (see Fig.4.8).

## 4.4 Discussion and conclusions

The aim of this work is to give observationally driven constraints on the Initial Mass Function (IMF) of the first (Pop III) stars, and to understand if zero-metallicity low-mass stars ( $m < 0.8 M_{\odot}$ ) are able to form. We use the semi-analytical model (described in Chapter 3) that describes the evolution of an isolated ultra faint dwarf (UFD) galaxy, from the epoch of its formation until the present day. To set the initial conditions of our model we used the results of cosmological simulations (Salvadori & Ferrara 2009; Salvadori et al. 2015), and we follow their findings by assuming that UFD evolve in isolation, i.e. that they did not experience major merger events. The model is data-calibrated, using a statistical approach based on  $\chi^2$  analysis. The free parameters of our model have been fixed in order to reproduce the global observed properties of Boötes I, i.e. the total luminosity,  $L_{\star}$ , the average stellar iron abundance,  $[\text{Fe}/\text{H}]$ , the Metallicity Distribution Function (MDF) and the star formation history.

Our key results and the main implications arising from them are:

- Our analysis of the random sampling of the stellar IMF for  $m_{\star} = [0.1-100/1000]M_{\odot}$  showed that in poorly star-forming systems like UFD galaxies,  $\langle \Psi \rangle \approx 10^{-3} M_{\odot} \text{yr}^{-1}$ , the assumption of a fully populated IMF breaks down (Sec.3.3.1).
- Including the IMF random sampling has a strong impact on the fraction of long-lived Pop III stars in Boötes I: it increases by a factor of  $\sim 3$  with respect to the model in which we assumed to fully populate the IMF (Sec.3.4.1).
- We explored how the number of surviving Pop III stars depends on the underlying Pop III IMF, where we tested three Larson-type IMFs ( $m_{ch} = [0.35, 1, 10] M_{\odot}$ ) and a Flat IMF, with different low/high-mass limits (Sec.4.1.1). Our results showed





$>10\,000$  stars. If the non-detection of metal-free stars will be persistent, we will limit  $m_{min} > 0.8 M_{\odot}$  independent of the Pop III IMF at 68% confidence level (Sec.4.3.3).

In addition, we explored how our results are affected by the choice of critical metallicity value,  $Z_{cr}$  that established the transition between Pop III-to-Pop II/I stars. The exact value of  $Z_{cr}$  is largely uncertain, it is estimated that it can vary between  $Z_{cr} = (10^{-4.5 \pm 1}) Z_{\odot}$  (Bromm et al. 2001, Schneider et al. 2003, Omukai et al. 2005). However we have not found any dependence of the fractions of zero-metallicity stars on the critical metallicity. In fact, following the chemical evolution of the galaxy it emerged that the explosion of one, at most two SNe, is enough for the metallicity to exceed  $10^{-3.5} Z_{\odot}$ . Therefore we move from a metal-free environment with  $Z_{ISM} = 0$ , to one with  $Z_{ISM} > 10^{-3.5} Z_{\odot}$ . Hence our results are not affected by the choice of the  $Z_{cr}$  value.

There have been several theoretical works (e.g. Vincenzo et al. 2014; Romano et al. 2014) that model the evolution of Boötes I since it is one of the observationally best studied UFD galaxy. However none of these models take into account the stochastic sampling of the IMF. Furthermore, none of these works have investigated the expected fraction of Pop III star survivors in Boötes I. In agreement with our findings, Vincenzo et al. (2014) concluded that the star formation efficiency of Boötes I was very small. This is also consistent with studies of Boötes I in cosmological context (e.g. Salvadori & Ferrara 2009; Bovill & Ricotti 2009; Romano et al. 2014; Bland-Hawthorn et al. 2015; Salvadori et al. 2015).

One of the key points in this work was to estimate the fraction of Pop III star survivors in UFD galaxies. The same was done by Magg et al. (2018), who derived the percentage of surviving Pop III that are expected to be found in our Milky Way and its satellites. Unfortunately we cannot make a direct comparison, since they used a logarithmically Flat IMF. However, our results for  $m_{ch} = 10 M_{\odot}$  and the case of Flat IMF predict a Pop III fraction consistent with their findings.

Our methods allow us to estimate the minimum stellar sample size required to put observationally driven constraints on the Pop III IMF. This approach was used by Hartwig et al. (2015) for halo/bulge stars of our Milky Way. They found that the expected number of Pop III star survivors decreases as  $m_{min}$  increases, assuming a logarithmically Flat Pop III IMF. Our findings have the same trend for IMF with  $m_{ch} = 0.35 M_{\odot}$ . However, for the other IMFs ( $m_{ch} = 10 M_{\odot}$  and Flat IMF) the fraction of Pop III survivors is extremely low ( $< 0.01\%$ ) regardless of the minimum mass. The reason is twofold: i) the

IMF shape, which makes it very unlikely to form low-mass stars (Fig.3.2); ii) the random sampling of the IMF which strongly affects the population of the lower mass-end (see Fig.3.7), i.e. the number of stars with  $m_{\star} \leq 0.8 M_{\odot}$ . In fact, for  $m_{ch} \geq 1 M_{\odot}$  and for Flat IMF it is unlikely to form long-lived Pop III stars independently of the minimum mass. Furthermore, Hartwig et al. (2015) found that to conclude that Pop III stars should have  $m_{\star} \geq 0.8 M_{\odot}$  at a 68% confidence level, we need to observe  $N_o \approx 10^6$  stars in the Milky Way stellar halo. However, with our method, even tighter constraints can be put on the Pop III IMF by only using  $N_o \approx 10^2$  stars.

For the first time, we have performed an in-depth analyses of four UFDs, Boötes I, Hercules, Leo IV and Eridanus II with the goal to constrain the IMF of Pop III stars. By developing a chemical evolution model of isolated UFDs, and combining observational constraints with a statistical approach we have shown that old and pristine UFDs are the ideal systems to understand the physical properties of the first stars. Our study has revealed that it is crucial to take into account the incomplete sampling of the IMF in these poorly star-forming systems, to realistically represent their stellar populations. This is especially relevant for the earliest star formation, where Pop III stars formed very inefficiently for a limited time. Our novel approach of connecting our models with real data through synthesizing the CMD of Boötes I, has revealed that taking the mass distribution of the observed stars into account, allows us to put even stronger constraints on the  $m_{min}$  and the shape of the Pop III IMF. In this work, with only 96 observed stars in Boötes I, Hercules, Leo IV, and Eridanus II, we can derive at a 99% confidence level that  $m_{min} > 0.8 M_{\odot}$  or  $m_{ch} > 1 M_{\odot}$ . Thus, we conclude that Pop III stars were typically more massive than those that form today, and the mass distribution of the first stars was fundamentally different from stars at later times. Finally, we showed that future telescopes will be able to get much larger samples ( $>10^4$  stars), which will provide even better understanding of the nature of the very first stars in the Universe.



---



---

# Understanding the origin of CEMP-no stars through UFDs

Among ancient and very metal-poor stars ( $[\text{Fe}/\text{H}] < -2$ ) CEMP stars are expected to be the direct descendants of the first stars. However the origin of their carbon excess and their possible connections with the chemical elements released by first SNe is not fully understood. In this Chapter we investigate the nature of CEMP stars to unveil the true Pop III star descendants in Ultra Faint Dwarf galaxies. The following results are based on the paper Rossi et al. (2023).

## 5.1 The debate origin of CEMP stars

The origin of Carbon-Enhanced Metal-Poor (CEMP-no) stars with low abundances of neutron-capture elements is still unclear. These stars are ubiquitous, found primarily in the Milky Way halo and ultra-faint dwarf galaxies.

Spectroscopic studies in the Galactic halo and in the Ultra-Faint Dwarf galaxies have revealed that a large fraction of very metal-poor stars,  $[\text{Fe}/\text{H}] < -2$ , show an enhancement of carbon (see Chapter 2, Sec.2.4),  $[\text{C}/\text{Fe}]^1 > +0.7$ , i.e. the so-called *Carbon-Enhanced Metal-Poor* (CEMP) stars (Beers & Christlieb 2005; Aoki et al. 2014; Yong et al. 2013b; Norris et al. 2013). However, the origin of CEMP stars and their possible connection with the chemical elements produced by the first generation of stars is far from being fully understood.

As we discussed in Chapter 2 (Sec.2.2.3), CEMP stars are usually divided into two classes: CEMP-*s* (*r*) stars that show an enhancement in the slow (rapid) neutron-capture elements, and CEMP-no stars that do not show an excess in heavy elements ( $[\text{Ba}/\text{Fe}] < 0$ ). The observed differences in the chemical signatures of these two classes seem to reflect the different origin of the carbon enhancement (see Chapter 2, Sec.2.2.3).

<sup>1</sup>  $[\text{X}/\text{Y}] = \log 10(m_{\text{X}}/m_{\text{Y}}) - \log 10(m_{\text{X},\odot}/m_{\text{Y},\odot})$ , where  $m_{\text{X}}$  and  $m_{\text{Y}}$  are the abundances of elements X and Y and  $m_{\text{X},\odot}$ , and  $m_{\text{Y},\odot}$ , are the solar abundances of these elements (Asplund et al., 2009).

Observationally, CEMP-no stars can be distinguished from CEMP-*s* based on the absolute carbon abundance<sup>2</sup>,  $A(\text{C})$  (Bonifacio et al. 2015). The CEMP-*s* stars belong to the ‘*high carbon band*’ with  $A(\text{C}) > 7.4$ , while CEMP-no stars are characterized by  $A(\text{C}) \leq 7.4$ , i.e. they belong to the ‘*low carbon band*’. More recently, Yoon et al. (2016) showed that CEMP-no stars can be further subdivided into two groups: Group II, which shows a correlation of  $A(\text{C})$  with iron abundance  $[\text{Fe}/\text{H}]$ , and Group III, with nearly constant  $A(\text{C})$  with  $[\text{Fe}/\text{H}]$ .

*But what is the origin of CEMP-no stars and the different nature of Group II & III?*

## 5.2 New Features of the model

To understand the origin of the carbon abundances measured in CEMP-no stars, we have expanded the model from described in Chapter 3 to track and to follow the evolution of all chemical elements from carbon to zinc, taking into account contributions from AGB stars and SNe. AGB stars in the mass range  $[2-8]M_{\odot}$  enrich the ISM only through stellar winds (C, N, and O), and we adopt the stellar yields from van den Hoek & Groenewegen (1997) for both Pop III and Pop II/I AGB stars. On the other hand, SNe can enrich the ISM with all the chemical elements from C to Zn. For Pop II SNe in the mass range  $[8-40]M_{\odot}$  we use the updated metal yields of Limongi & Chieffi (2018) (model R, without rotation velocity) and an explosion energy,  $E_{\text{SN}} = 10^{51}$  erg. We assume that Pop III SNe in the mass range  $[10-100]M_{\odot}$  can explode with different  $E_{\text{SN}}$  from  $0.3 \times 10^{51}$  erg up to  $10^{52}$  erg and different mixing efficiency  $\eta = [0-0.25]$ , and we adopt the corresponding yields provided by Heger & Woosley (2010). Every time that a Pop III SNe forms we randomly assign to it an energy and a mixing efficiency. The energies allowed for Pop III SNe are equiprobable and they determine the Pop III SNe types: *faint* SNe with  $E_{\text{SN}} = 0.3-0.6 \times 10^{51}$  erg, *core-collapse* SNe with  $E_{\text{SN}} = 0.9-1.5 \times 10^{51}$  erg, *high-energy* SNe with  $E_{\text{SN}} = 1.8-3.0 \times 10^{51}$  erg, and *hypernovae* with  $E_{\text{SN}} = 5.0-10.0 \times 10^{51}$  erg. For massive Pop III SNe in the mass range  $[140-260]M_{\odot}$ , the so-called *Pair Instability* SNe (PISN), we maintain the same assumptions of the previous work, i.e. an explosion energy proportional to the stellar mass, and we adopt the stellar yields of Heger & Woosley (2002).

## 5.3 The Carbon Enrichment in Boötes I

In the top panel of Fig.5.1 we show a comparison between the observed MDF of Boötes I and the simulated one, which are in good agreement, and the same is true for other

<sup>2</sup>  $A(\text{C}) = \log(N_{\text{C}}/N_{\text{H}}) + 12$  where  $N_{\text{C}}$  and  $N_{\text{H}}$  represent the number density fraction of carbon element and hydrogen, respectively.

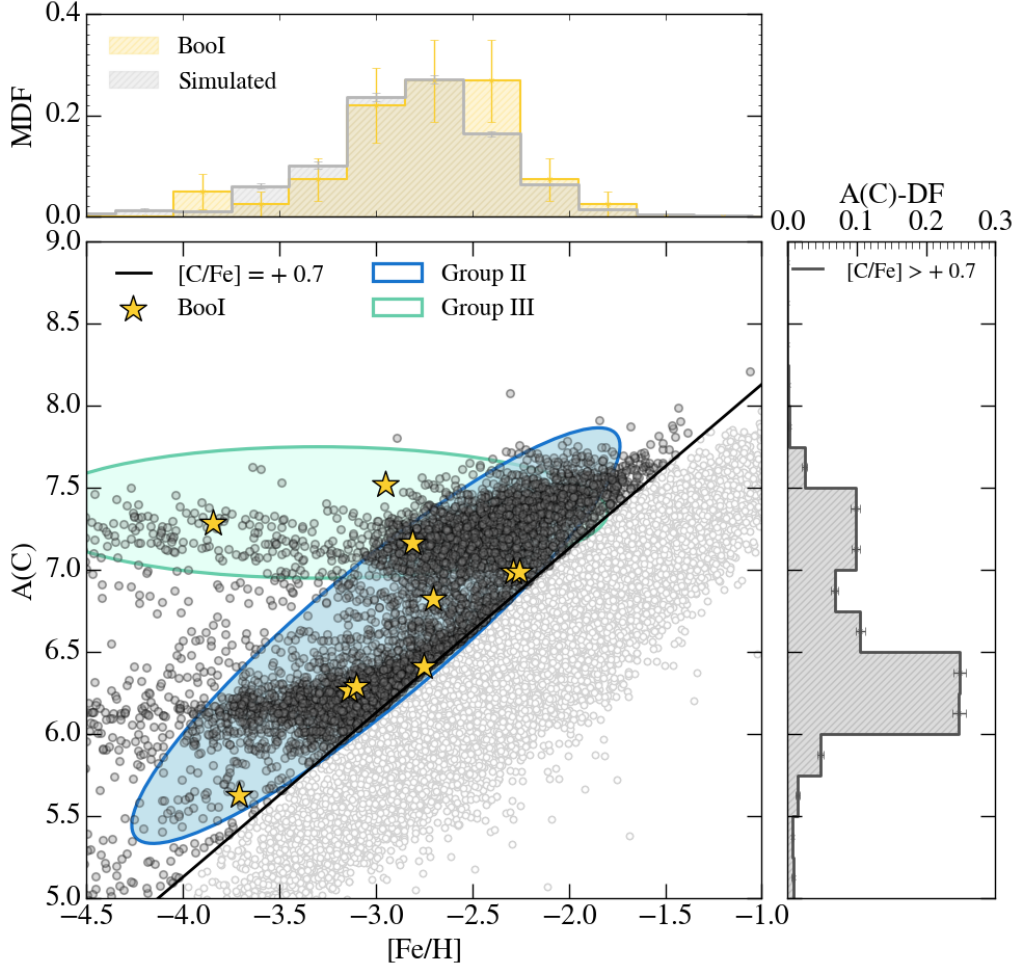


Figure 5.1: The A(C)-[Fe/H] diagram of our simulated stellar populations (1000 realisations) of Boötes I. The black line corresponds to  $[C/Fe] = +0.7$ . Yellow star symbols identify the observed CEMP-no stars in Boötes I, while the green and blue ellipses correspond to the CEMP-no groups by (Yoon et al., 2019). The top plot shows the comparison between the observed (yellow; data from Norris et al. 2010; Lai et al. 2011; Gilmore et al. 2013) and simulated (grey) MDF. The right marginal plot shows the simulated A(C)-DF of CEMP-no stars.

observed properties (i.e. the total luminosity, the average stellar iron abundance and the star formation history). In fact, changing the properties of Pop III stars (e.g. yields, IMF) has very limited effects on the MDF, since the general stellar population is dominantly enriched by normal Pop II/I stars. The central plot of Fig.5.1 shows the A(C) distribution with [Fe/H], for the simulated stellar populations of Boötes I, where the CEMP-no stars ( $[C/Fe] > +0.7$ ) are highlighted (black symbols above solid line). In agreement with observational studies (e.g. Yoon et al. 2019), we find the existence of two distinct groups (II & III) which clearly show different behaviors in the A(C)-[Fe/H] diagram: Group II exhibits a strong correlation with [Fe/H] while Group III is constant with [Fe/H]. The bimodal trend of A(C) is even more evident if we look at the right marginal plot of

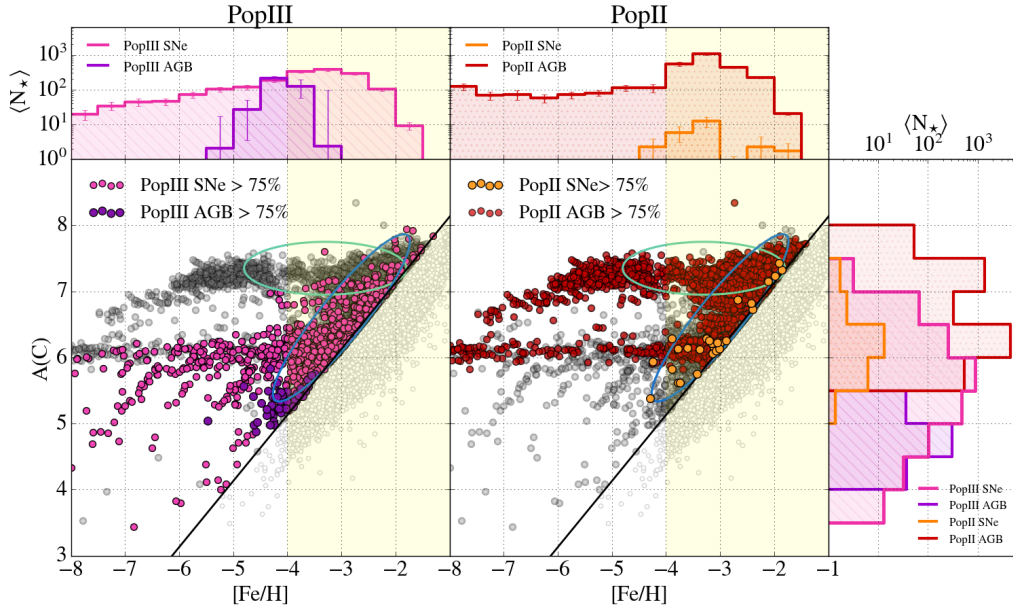


Figure 5.2: The  $A(C)$  versus  $[Fe/H]$  diagram for different CEMP-no stellar populations. Colors highlight CEMP-no stars enriched to a level higher than 75% by different stellar populations: in the columns we distinguish between Pop III (left) and Pop II stars (right) and in each panel we differentiate between SNe and AGB stars. In the marginal plots we show the number of stars averaged over the different runs,  $\langle N_{\star} \rangle$  as a function of  $[Fe/H]$  (top) and  $A(C)$  (right). The yellow shaded area represents the  $[Fe/H]$  range in which the currently available Boötes I data are located. Note that all stellar populations have total metallicity  $Z_{\star} > Z_{crit}$ .

Fig.5.1, in which we show the  $A(C)$ -Distribution Function<sup>3</sup> ( $A(C)$ -DF). As we can see the distribution is bimodal with two peaks at  $A(C) \sim 7.2$  and  $A(C) \sim 6.2$  that roughly correspond to Group III and II, respectively.

## 5.4 The different CEMP-no populations

Following the evolution of single stars with different metallicity (Pop III - Pop II) and with different timescales (SNe - AGB) we can determine the main drivers of carbon enrichment in any given stellar population in Boötes I. Fig.5.2 shows the  $A(C)$ - $[Fe/H]$  diagram for CEMP-no stars, where colors highlight what stellar population is the main driver of carbon enrichment: Pop III or Pop II stellar populations (left/right panels), SNe or AGB stars. The first thing to note is that CEMP-no stellar populations cover all the iron range  $-8 < [Fe/H] < -1$  regardless of which stellar population is the main driver of enrichment (Pop III/Pop II). It is also evident that two separate branches exist, both showing roughly constant  $A(C)$  values in the  $[Fe/H]$  range. The first branch, at  $A(C) \sim 7$ , is populated by CEMP-no stars mainly enriched by Pop II stars while, in the

<sup>3</sup>  $A(C)$ -DF: the number of CEMP-no stars in bin of  $A(C)$  normalized with respect to the total number of CEMP-no stars



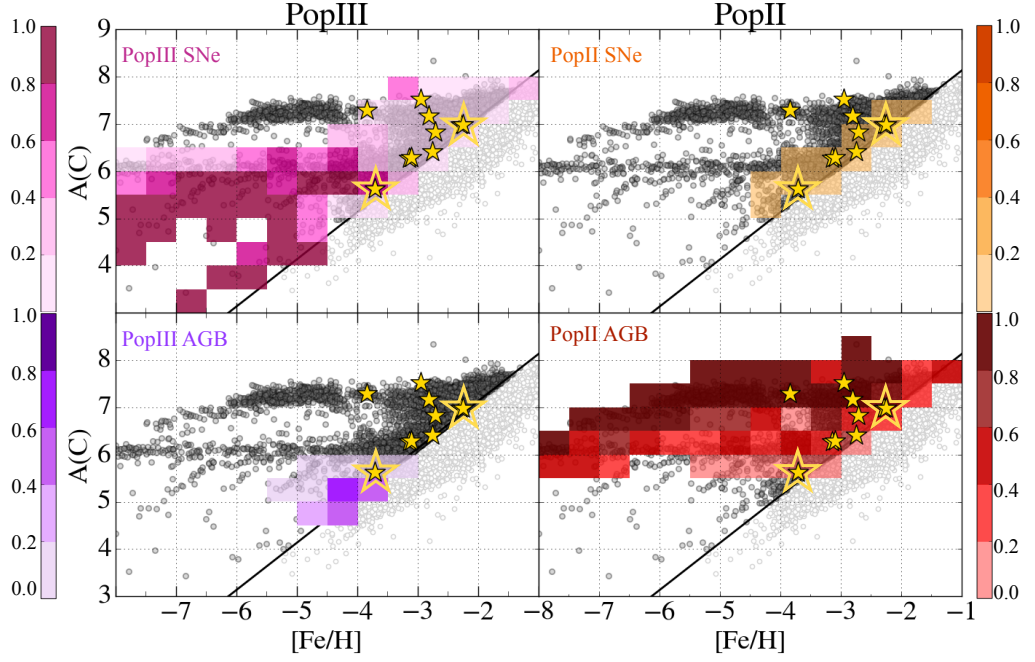


Figure 5.3: The  $A(C)$  versus  $[Fe/H]$  diagram for CEMP-no stellar populations. The colored squares identify the probability to find, at fixed  $[Fe/H]$  and  $A(C)$ , CEMP-no stars predominantly enriched by Pop III or by Pop II stars (columns), while in the rows we distinguish between SNe and AGB stars. Yellow stars represent the Boötes I data, while double marked points identify stars for which Mg abundance is available in the literature.

second branch, at  $A(C) \sim 6$ , the enrichment is driven by Pop III stars.

In the range where data are available,  $[Fe/H] > -4$ , the number of CEMP-no stars enriched by Pop II stars, both Pop II SNe (rapid timescale) and AGB stars (longer timescale), is  $\sim 2$  times greater than those enriched by Pop III stars (top marginal plot of Fig.5.2), in good agreement with Sharma et al. (2019). It should be noted that almost all PopII-enriched CEMP stars have been polluted by AGB stars, while only a few ( $\lesssim 1\%$ ) are PopII SNe enriched. The latter formed in birth cloud mainly enriched by *normal* PopII SNe but pre-polluted by PopIII SNe, allowing to reach  $[C/Fe] > +0.7$ . On the other hand, at  $[Fe/H] \leq -4$  the number of CEMP-no stars predominantly enriched by Pop III stars is  $\sim 1.5$  times greater than those enriched by Pop II stars. We find that these Pop III star *descendants* formed out of an ISM enriched by low-energy SNe ( $\leq 10^{51}$ erg). The branch-like behavior of Pop III enriched CEMP-no stars at  $A(C) \sim 6$  can be explained as follows. In our model for isolated UFDs the gas gradually accumulates and when the first Pop III stars form typically  $M_{\text{gas}} \gtrsim 10^3 M_{\odot}$  (Rossi et al. 2021). A single (or a few) low-energy Pop III SNe produce a mass of carbon  $M_C \sim 1 M_{\odot}$ , which is diluted in  $M_{\text{gas}} \sim 10^5 M_{\odot}$  thus leading to  $A(C) \sim 6$ . Although the majority ( $\sim 60\%$ ) of CEMP-no stars at  $[Fe/H] \leq -4$  have been enriched by the Pop III SNe,  $\sim 40\%$  formed from an ISM mainly imprinted by Pop II AGB stars. These stars are rare, and form when most

of the gas and metals have been ejected through previous SNe explosions and thus AGB stars can substantially contribute to the ISM enrichment. Fortunately, they can be easily distinguished from Pop III enriched CEMP-no stars, thanks to their higher  $A(C)$  value. From the right marginal plot in Fig.5.2, we clearly see that the distribution for CEMP-no stars enriched by Pop II populations (SNe+AGB) covers the range  $5.0 \leq A(C) < 8.0$ , with a peak at  $A(C) \sim 6.5$ , at which the enrichment is dominated by Pop II AGB stars. On the other hand, the distribution for Pop III (SNe+AGB) enriched CEMP-no stars covers the range  $3.5 < A(C) < 7.5$  with the peak at  $A(C) \sim 6$ . Pop III stars *descendants* are therefore characterized by  $A(C) \lesssim 6$  (and  $[Fe/H] \leq -3.5$ ) and they are distinguishable from those mainly imprinted by Pop II stellar populations identified by  $A(C) > 6$  for all  $[Fe/H]$ .

To unveil the origins of different CEMP-no stars, we derived the probability (at fixed  $[Fe/H]$  and  $A(C)$ ) that CEMP-no stars have been imprinted by a given stellar population. From Fig.5.3 it is evident that the probability to find Pop III star *descendants* increases as the  $[Fe/H]$  decreases and it is maximum for  $A(C) < 6$  and  $[Fe/H] < -3.5$ , where most of observational data for Boötes I are not yet available, except for one star. For  $A(C) > 6$  at all  $[Fe/H]$ , the majority of CEMP-no stars are mainly enriched by Pop II stars. Furthermore, we see that for  $A(C) > 7$  and  $-4 < [Fe/H] < -1$ , the probability to find CEMP-no stars mainly enriched by Pop II AGB is  $> 80\%$  while by Pop II SNe it is  $\lesssim 20\%$ . Finally, by comparing our predictions with the available data in Boötes I (Fig.5.3) we can see that most of the observed CEMP-no stars are found at  $[Fe/H] > -4$  and  $A(C) > 6$ , i.e. in the region where stars are more likely to have been imprinted by Pop II stellar populations. However, one star ( $[Fe/H] = -3.71$ ,  $A(C) = 5.62$ ; Norris et al. 2010) is found in a region where the probability that it has been Pop III enriched is  $\gtrsim 60\%$ .

#### 5.4.1 Moderate CEMP-s stars

Since our model does not account for binary transfer, our results do not predict classical CEMP-s stars. However, it is evident from Fig.5.2 that for  $6.5 < A(C) < 8$  there exists a class of CEMP stars forming from an ISM imprinted by Pop II AGB stars, which represent about  $\gtrsim 90\%$  of the Pop II-enriched CEMP stars at  $[Fe/H] > -4$ . These stars have different PopII AGB progenitors: stars with  $A(C) \sim 6.5$  have been enriched on average by massive Pop II AGB ( $m_* \gtrsim 5M_\odot$ ), while the ones with  $A(C) \gtrsim 7$  by low-massive Pop II AGB ( $m_* < 5M_\odot$ ). The C-excess is *moderate* with respect to CEMP-s stars ( $A(C) \sim 8$ ), but it originates from the same source. Thus, we dub them *moderate CEMP-s stars*. These moderate CEMP-s stars are expected to have intermediate characteristics compared to CEMP-no ( $[Ba/Fe] < 0$ ) and CEMP-s stars ( $[Ba/Fe] > +1$ ), because their

chemical enrichment is not powered by mass transfer through a binary AGB companion. Our adopted AGB yields (van den Hoek & Groenewegen 1997) do not include s-process production, but by using observational constraints on the [Ba/C] ratio (Masseron et al. 2010) in combination with our predicted [C/Fe], we estimate these stars to have  $0 \lesssim [\text{Ba}/\text{Fe}] \lesssim +1$ , filling the gap of unexplained CEMP stars. Our model is thus able to explain for the first time this neglected population of stars as *moderate CEMP-s* stars, formed from the products of Pop II AGB stars.

#### 5.4.2 Testing our predictions: [C/Mg]

The [C/Mg] ratio represents an additional key diagnostic on the origin of CEMP-no stars. In Fig.5.4 we identify two different [C/Mg] trends. The Pop III enriched CEMP-no stars show an approximately constant [C/Mg] value over the entire [Fe/H] range. These stars formed in an environment predominantly enriched by Pop III SNe, which produce both C and Mg giving  $[\text{C}/\text{Mg}] \sim \text{constant}$ , while their [Fe/H] depends on both the mass and explosion energy of Pop III SNe (Rossi et al. in prep.). On the contrary, Pop II enriched CEMP-no stars exhibit a strong correlation where [C/Mg] increases towards lower [Fe/H]. The position of these Pop II enriched CEMP-no stars in [C/Mg]-[Fe/H] space therefore depends on the level of enrichment from PopII AGB stars: stars with  $[\text{Fe}/\text{H}] \leq -4$  are ‘purely’ Pop II AGB imprinted ( $\gtrsim 95\%$ ). They are therefore C-rich and Mg-poor giving high [C/Mg] values. As [Fe/H] increases, CEMP-no stars form in environments mainly enriched by PopII AGB but with a significant contribution to the enrichment from PopII SNe ( $\sim 25\%$ ). The latter mainly produce Mg, Fe giving a decrease of the [C/Mg] ratio.

In Fig. 5.4 we compare the predicted [C/Mg] ratio for these two different stellar populations with the values measured in two CEMP-no stars in Boötes I (double marked stars in Fig.5.3, Fig.5.4). These two stars separate very nicely into the two different stellar populations in our model: the star at the lowest value of [Fe/H] is consistent with an enrichment dominated by Pop III stellar populations, while the other is compatible with Pop II stellar populations enrichment. Finally, comparing our model predictions with Galactic halo data (squares in Fig.5.4) we are able to probe the existence of the two branches in the A(C)-[Fe/H] diagram. This suggests that low-Fe ( $[\text{Fe}/\text{H}] < -4$ ) Pop III imprinted CEMP-no stars could exist also in UFDs, unless they form in pre-enriched environments (e.g. Salvadori & Ferrara, 2012). Furthermore, this comparison demonstrates that [C/Mg] is a key diagnostic tool to distinguish the origin of CEMP-no stars (see bottom panel of Fig.5.4).

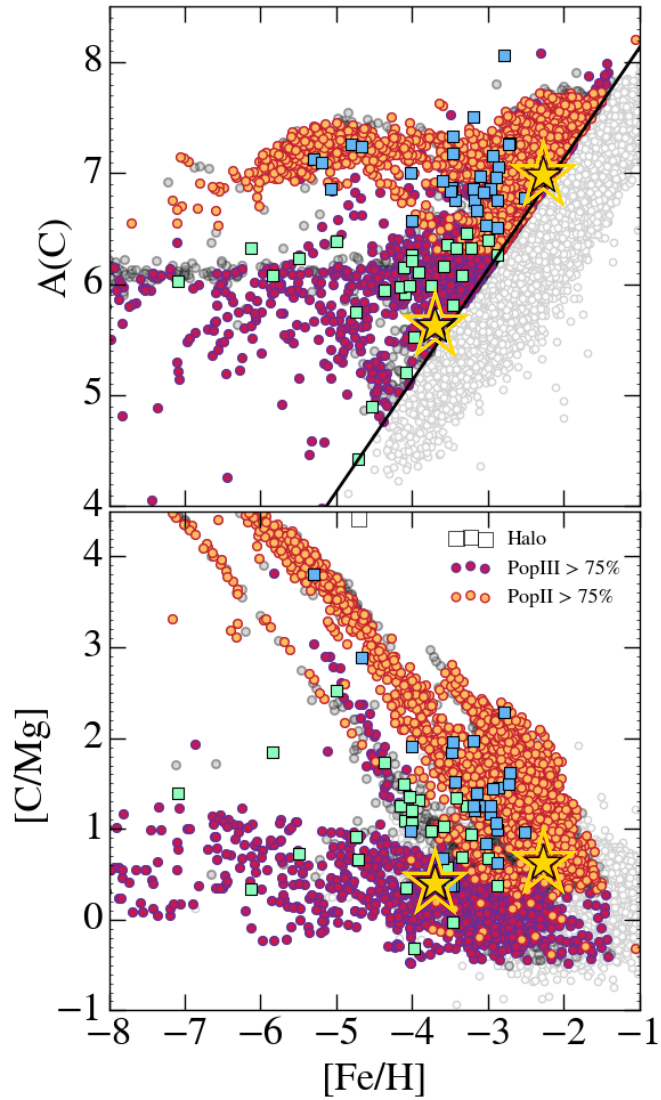


Figure 5.4: The CEMP stars in Boötes I, enriched to a level higher than 75% by PopIII (magenta) or by PopII (orange). Double marked yellow stars represent Boötes I stars for which there is available  $[Mg/Fe]$  (Norris et al. 2010; Chiti et al. 2018). Squares represent the Milky Way halo:  $A(C) > 6$  (light blue), and  $A(C) < 6$  (green), from the compilation of Yoon et al. (2016).

## 5.5 Discussion and conclusions

For the first time, we unveil the origin of CEMP-no stars by exploiting a self-consistent model (Rossi et al. 2021), data-calibrated on Boötes I, that simultaneously accounts for the different enrichment sources of CEMP stars. We present a unique way of distinguishing between the primary sources of their enrichment (SNe or AGB stars) as well as the type of stellar populations (Pop III or Pop II) that polluted their natal clouds. Our model predicts where in the A(C)-[Fe/H] diagram present day stars should be located, depending on their main source of C- enrichment. The majority of CEMP stars at  $A(C) \gtrsim 6$  are predominantly polluted Pop II stars. In particular, we predict a population of CEMP stars, which get their C-enhancement from AGB stellar winds, without binary transfer. These *moderate CEMP-s stars* are expected to cover the range  $0 < [Ba/Fe] < +1$ . Our model is thus able to explain these stars that fall in between the classical categories of CEMP-no and CEMP-s stars. On the other hand, CEMP-no stars with  $A(C) \lesssim 6$  are predominantly true Pop III *descendants*. These Pop III only-enriched CEMP-no stars, have roughly constant [C/Mg] with [Fe/H], in stark contrast with CEMP stars mainly enriched by Pop II stars. Thus, [C/Mg] is a key diagnostic to distinguish between different populations. Furthermore, PopIII descendants are characterized by  $-0.5 < [C/Mg] < +1$ , in agreement with findings of Hartwig et al. (2018), despite different approaches. Most of these Pop III descendants lie at  $[Fe/H] < -4$ , therefore representing a still hidden population in UFDs. However, observations of hyper iron-poor stars in the Milky Way strongly support our findings. This indicates a close connection of UFDs with the Milky Way halo at the lowest [Fe/H]. In the present and upcoming era of large spectroscopic surveys (e.g. 4DWARFS) and new instrumentation (e.g. ELT), we can expect find these rare populations, predicted by our model. Only with dedicated models able to reproduce full abundance patterns (e.g. Rossi+23 in prep) will we be able to exploit this large influx of data to understand the properties of the first stars and the earliest galaxies.



---



---

## Deciphering the signatures of first Pop III SNe

In the previous Chapter, we show that CEMP-no stars observed in UFDs (and in the Galactic stellar halo) are likely connected with the chemical products of Pop III stars exploding as low energy “faint-SNe” of tens of solar masses. However, in the mass range  $m_{\star} = [10 - 100] M_{\odot}$ , models predict that SNe can explode with a variety of possible energies ( $E_{\text{SN}}$ ). Recent observations studies have identified the chemical signatures of energetic Pop III SNe with  $E_{\text{SN}} > 10^{51}$  erg. The chemical signature of these energetic pristine SNe can be found both among CEMP-no stars and Carbon-normal stars. Ezzeddine et al. (2019) identified the fingerprints of asymmetric hypernova with  $E_{\text{SN}} = 5 \times 10^{51}$  erg in CEMP-no star HE 1327-2326, and more recently, Skúladóttir et al. (2021, 2023a) and Placco et al. (2021) discovered two C-normal metal-poor stars ( $[\text{Fe}/\text{H}] < -4$ ) in Sculptor dwarf galaxy and in the Galactic halo, respectively, whose abundance patterns are compatible with an enrichment from Pop III hypernova with  $E_{\text{SN}} = 10 \times 10^{51}$  erg. In this Chapter, which is based on Rossi, Salvadori, Skúladóttir et al. (2023) (to be submitted) we investigate the chemical signature of Pop III SNe with different energies in UFDs, especially focusing on the best studied system, Boötes I.

### 6.1 The energy distribution function of Pop III SNe

The energy of Pop III stars that end their life as SNe, as well as their Energy Distribution Function (EDF) of the first stars are far to be constrained. The yield models by Heger & Woosley (2010) predict that Pop III stars with masses  $[10 - 100] M_{\odot}$  can explode a SNe with a variety of energies:

- *faint* SNe, with  $E_{\text{SN}} = 0.3 - 0.6 \times 10^{51}$  erg;
- *core-collapse (cc)* SNe, with  $E_{\text{SN}} = 0.9 - 1.5 \times 10^{51}$  erg;
- *high-energy* SNe, with  $E_{\text{SN}} = 1.8 - 3.0 \times 10^{51}$  erg;
- *hypernovae* with  $E_{\text{SN}} = 5.0 - 10.0 \times 10^{51}$  erg;

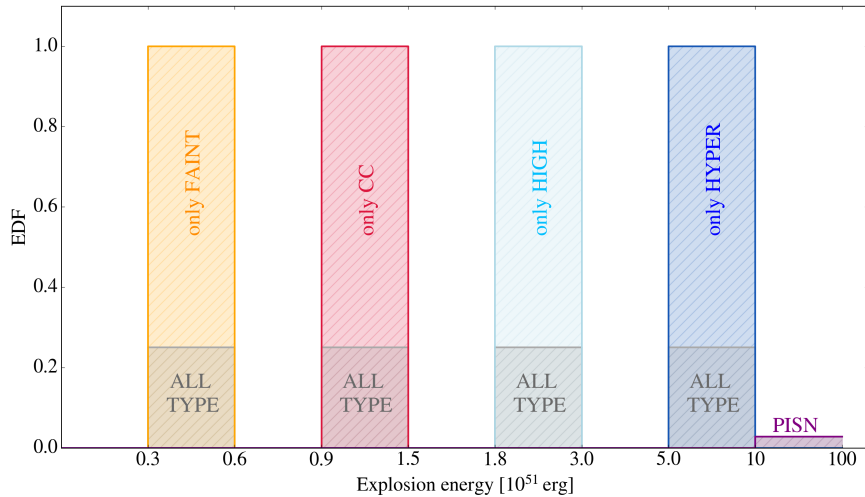


Figure 6.1: The different EDF assumed: four cases in which the EDF is a top-hat function centered in each type on SNe (100% of probability), and the last case in which the EDF is spread among the different SNe explosion energies. This equivalent to assume that each SNe type as the 25% of probability to be selected. The purple histogram represent the probability to form PISN which depends on the assumed Pop III IMF.

The EDF of these Pop III SNe is unknown, so here we consider five different scenarios that are shown in Fig.6.1. In the first four cases we assume extreme scenarios in which Pop III SNe are all of a single type, respectively *only faint* (orange), or *only cc* (red), or *only high*(lightblue), or *only hyper* (dark blue). This correspond to assume four top-hat EDFs in which the probability to form each type of SNe is 100% (see Fig.6.1). In the last case we assume an EDF spread among all different explosion energies (grey histograms in Fig.6.1), that coincides to assume that each type of SNe has 25% of probability to be selected. Finally, regardless of the EDF assumed, every time that a Pop III SNe forms we randomly assign to it an explosion energy. Finally, each time we have a SNe we randomly select an internal stellar "mixing efficiency" (see Heger & Woosley 2002) in between  $f_{mix} = [0.039 - 0.063 - 0.100 - 0.158]$ .

Note that the probability to form very massive PISN is independent on the EDF (only regulating SNe with  $[10 - 100] M_{\odot}$ ) and it depends on the assumed Pop III IMF. As shown in Fig.6.1 this probability is very low ( $\sim 0.2\%$ ) for the assumed Larson PopIII IMF with  $m_{ch} = 10 M_{\odot}$ .



Model	$\log(L_*/L_\odot)_{\text{sim}}$	$\langle[\text{Fe}/\text{H}]\rangle_{\text{sim}}$	$\chi^2$
FAINT	$4.60 \pm 0.01$	$-3.00 \pm 0.01$	1.5
CC	$4.59 \pm 0.02$	$-2.60 \pm 0.01$	0.9
HIGH	$4.60 \pm 0.01$	$-2.68 \pm 0.03$	0.4
HYPHER	$4.40 \pm 0.01$	$-3.20 \pm 0.01$	4.8
all TYPE	$4.54 \pm 0.04$	$-2.70 \pm 0.01$	0.5

Table 6.1: The simulated properties of Boötes I (second and third column) obtained assuming different EDF for Pop III SNe and  $\chi^2$  value.

## 6.2 Testing different Pop III SNe energies

In Fig.6.2 we analyze the impact of different of the different EDFs of Pop III SNe on the MDF of Boötes I. From the top to the bottom we show the comparison between the observed MDF of Boötes I (black histogram) and the ones obtained by assuming the EDFs shown in Fig.6.1. As we can see at first sight, all the model reproduce quite well the observed MDF of Boötes I except for the models “only hyper” and “only faint”. Since faint SNe produce large amount of C and small of Fe (e.g. see Chapter 5, Rossi et al. 2021, Vanni et. al. 2023) they produce a long low-Fe tail in the MDF that, at the moment, it is not observed in Boötes I. On the other hand, the model “only hyper” produces a MDF shifted towards low values of  $[\text{Fe}/\text{H}]$ . Indeed assuming that all SNe explode as hypernovae has the effect that it became difficult to enrich the ISM with metals: because of the low binding energy of Boötes I, the chemical products of these energetic Pop III SNe are easily evacuated out of the galaxy, making the metal enrichment difficult. To evaluate which model is able to best reproduce all the observed properties of Boötes I (Luminosity,  $\langle[\text{Fe}/\text{H}]\rangle$ , MDF) we use a statistical approach based on  $\chi^2$ , whose values are listed in the Table 6.1. The model “only faint”, and “only hyper” produced a  $\chi^2$  value greater than one, while the other models give a  $\chi^2 < 1$ . Among these model the ones that minimize the  $\chi^2$  are “only high ” and “all type ” for which we obtain  $\chi^2 = 0.4$ ,  $\chi^2 = 0.5$  respectively. However, the discrepancy between the two  $\chi^2$  values is too small to put constraints on the model to be used. Indeed, we need to employ other observables of Boötes I to discern the most suitable model to utilize.

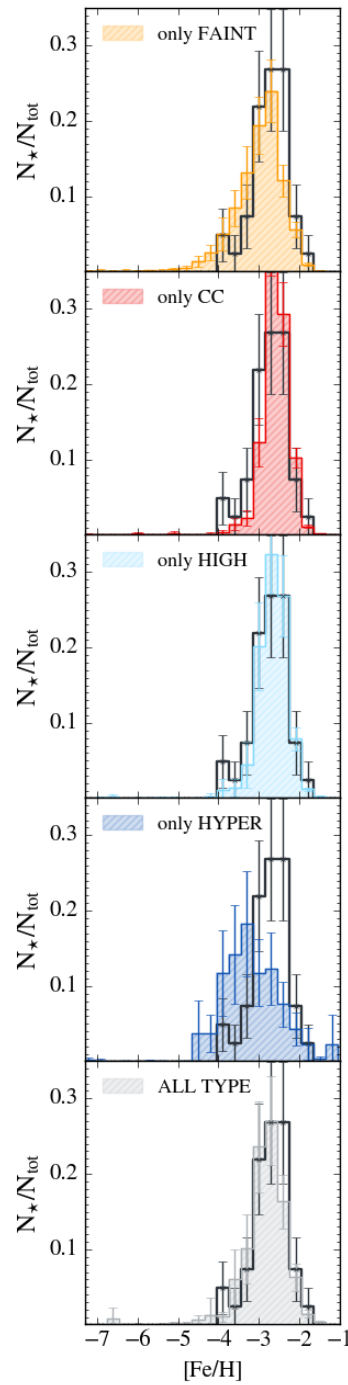


Figure 6.2: Comparison between the observed (black histograms) and the simulated MDFs of Boötes I. From the top, first four simulated MDFs are obtained assuming that Pop III SNe are all of a single type, faint (orange), core-collapse (CC) (red), high (light blue) or hyper (dark blue) respectively. In the bottom panel we show the simulated MDF obtained assuming a flat EDF spread among all energies (grey).

To make a step forward, we analyze the impact of Pop III SNe with different energies on some abundance ratios<sup>1</sup>  $[X/Fe]$ , measured in Boötes I stars. In Fig.6.3 we show the  $[C/Fe]$  and  $[Zn/Fe]$  abundance ratio measured in 39 and 9 Boötes I stars, respectively, as a function of their  $[Fe/H]$ . For each model, the contours delineate the stellar populations that have been enriched by a level higher than 75% by a unique type of SNe. By inspecting Fig.6.3, the first thing to note is that the descendants of Pop III SNe with different energy, occupy different regions in  $[X/Fe]$  versus  $[Fe/H]$  space. The location of these Pop III stars descendants in  $[X/Fe]$ - $[Fe/H]$  space depends on both the energy and on the mass of the SNe that enriched the birth cloud in which the descendants formed out (see Vanni et al. (2023)). The descendants of low-energy Pop III SNe (faint, cc) cover a wide range in both  $[Fe/H]$  and  $[C/Fe]$ ,  $-7.5 \lesssim [Fe/H] \lesssim 0$ , and,  $-1 \lesssim [C/Fe] \lesssim 6$ , and they are characterized by  $[Zn/Fe] \lesssim 0$ . On the other hand, Pop III star descendants predominantly enriched by energetic SNe (high and hypernovae) exhibit a narrower range in  $-1 \lesssim [C/Fe] \lesssim 3$  and  $-4 < [Fe/H] < 0$ . Note that only stars imprinted by high-energy SNe and hypernovae can reach super-solar  $[Zn/Fe]$  values, up to  $\approx 1.5$ . Finally, in Fig.6.3 we also show the regions covered by stars enriched by *normal* Pop II SNe, which typically have  $[C/Fe] \lesssim 1$  and they can reach high values of  $[Zn/Fe] \gtrsim 0$ , comparable with those obtained with hypernovae enrichment.

*What do we need to reproduce the observed abundance ratio of Boötes I stars?* Combining our model results with Boötes I observational data it is evident (Fig.6.3), that none of the individual models (only faint, only cc, only high, only hyper) is able to reproduce, at the same time, the observed distributions of  $[C/Fe]$  and  $[Zn/Fe]$ . In fact assuming that all pristine SNe evolve as low-energy SNe allows to reproduce the high values of  $[C/Fe]$  observed in Boötes I stars but not the high  $[Zn/Fe]$  values. On the other hand, energetic SNe (high and hypernovae) can reproduce the measured values of  $[Zn/Fe]$ , but fail to reproduce the values of  $[C/Fe]$ . Finally, even taking into account the contribution of Pop II SNe, it is not possible to reproduce the data. In conclusion, to reproduce the chemical some of the abundance ratios in Boötes I stars we need the contribution of Pop III SNe with different energies. Thus, we choose as the “*fiducial model*” the “all type” model (see Fig.6.1) in which the theoretical EDF is spread among different equiprobable energies.

<sup>1</sup>  $[X/Fe] = \log(N_X/N_{Fe}) - \log(N_{X,\odot}/N_{Fe,\odot})$ , where  $N_X$  and  $N_{Fe}$  are the abundances of elements X and iron and  $N_{X,\odot}$  and  $N_{Fe,\odot}$  are the solar abundances of these elements (Asplund et al., 2009)

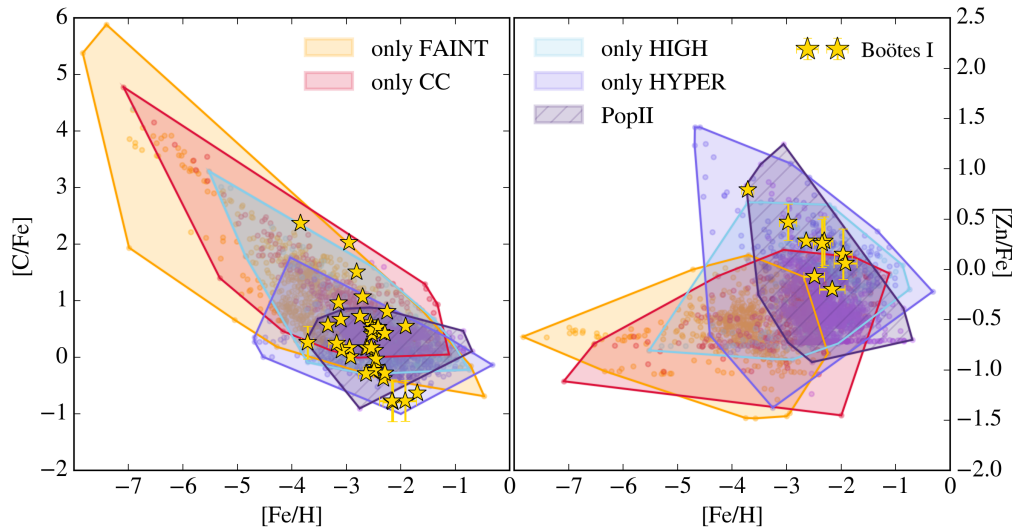


Figure 6.3: The  $[C/Fe]$  (left panel) and  $[Zn/Fe]$  (right panel) abundance ratio of Boötes I stars (yellow stars) as a function of their  $[Fe/H]$ . Colored contours identify the stellar populations enriched to a level higher than 75% by Pop III SNe with different energies, *faint* (orange), *cc* (red), *high* (lightblue), *hyper* (dark blue). For comparison we also show the expected chemical abundance ratios of stellar population mainly enriched by *normal* Pop II SNe (dark purple shaded area)

### 6.3 The chemical signatures of Pop III SNe

Before investigating what are the key chemical signature of different Pop III SNe we need to verify that using our fiducial model we are able to reproduce all the observed abundance ratios measured in Boötes I stars. In Fig.6.4 we show the  $[X/Fe]$  versus  $[Fe/H]$  density maps for the stellar populations at  $z = 0$  in Boötes I. The first thing to note is that all the simulated  $[X/Fe]$  density maps effectively reproduce the observed data. Moreover, the peaks of the simulated density distributions for each chemical element perfectly match the corresponding observed distributions. It is worth mentioning that the simulated density maps cover a broader range in  $[X/Fe]$ - $[Fe/H]$  space compared to the observations. Indeed, our model predicts regions of low density (Density  $< 20\%$ ), representing rare stellar populations that are particularly intriguing for investigating the signatures of the first stars.

Thanks to our semi-analytical model we are able to follow the evolution of single stars with different metallicity (Pop III or Pop II). Thus, we can determine if the main drivers of the enrichment of any stellar population of Boötes I are Pop III or Pop II/I stars. Let's now investigate, if they exist, regions in  $[X/Fe]$  - $[Fe/H]$  space in which it is possible to uniquely identify the fingerprints of first supernovae. In the top marginal plots we show the comparison between the observed (yellow histograms) and the simulated (grey) MDF of Boötes I. In each top panel we also show the MDFs of stars predominantly enriched (at

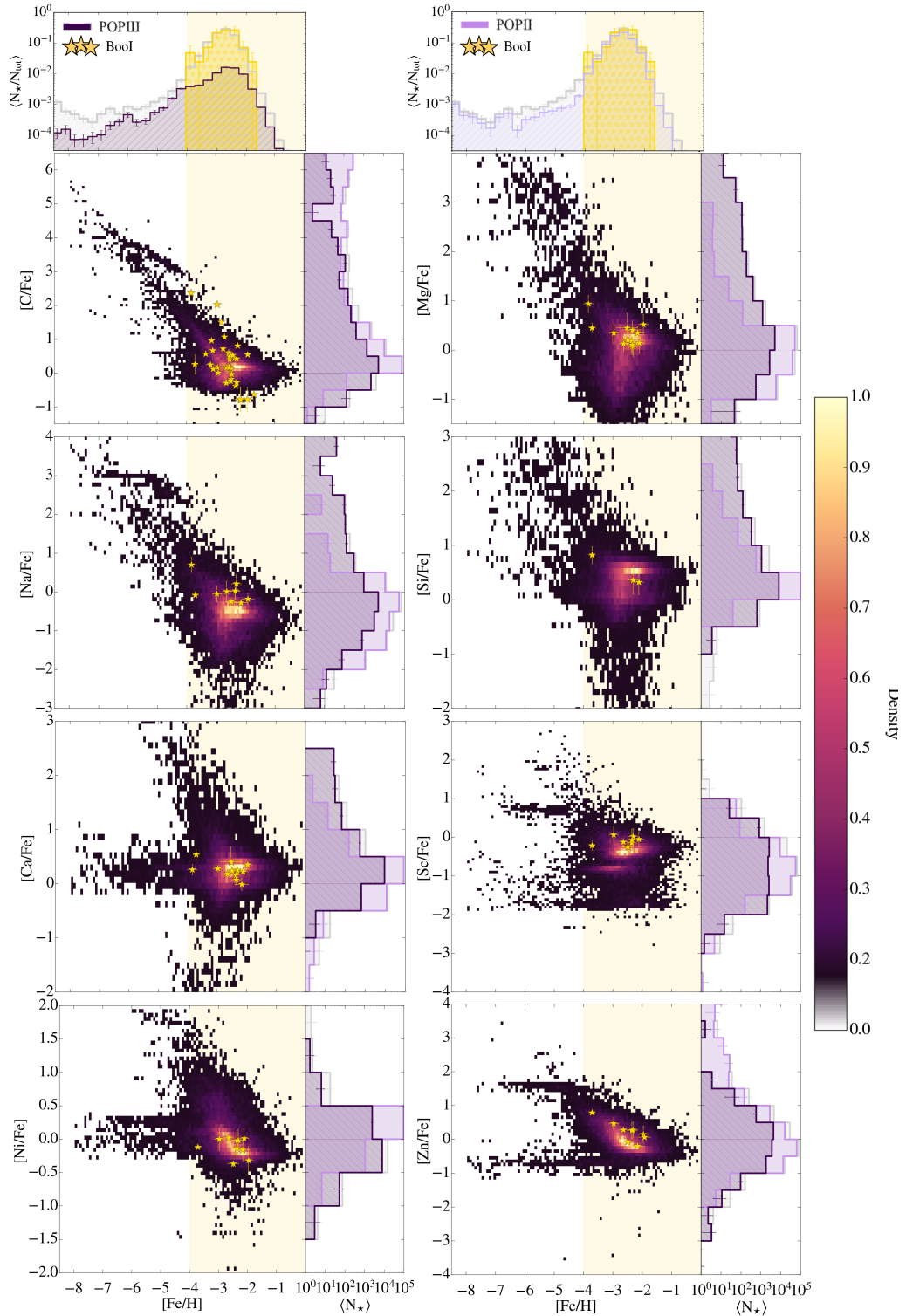


Figure 6.4: Density maps,  $[X/Fe]$  vs.  $[Fe/H]$ , of the simulated stellar populations at  $z = 0$ . Yellow star symbols are observed chemical abundances of Boötes I stars.

level higher than 75%) by Pop III (on the right, dark purple) and by Pop II (on the left, light purple) stars. As we already show in Fig.6.2 (bottom panel), in the range where data are available,  $[\text{Fe}/\text{H}] > -4$  (yellow shaded area) the simulated MDF nicely reproduce the one of Boötes I. In this range the MDF is dominated by stars predominantly enriched by normal Pop II stars which represent  $> 80\%$  of the total stars while Pop III enriched stars are extremely rare at  $[\text{Fe}/\text{H}] > -4$  consisting in  $\approx 1\%$  of the total number of stars. In the low-metallicity tails of the MDF ( $[\text{Fe}/\text{H}] < -4$ ), we find the imprint of both Pop II/I and Pop III stars and the number of stars mainly enriched by Pop III SNe is of the same order of magnitude as those enriched by Pop II stars. Fortunately, first stars *descendants* can be easily distinguished from Pop II enriched stars thanks to their  $[\text{X}/\text{Fe}]$  abundance ratio.

To identify the chemical signatures of the first supernovae in the right marginal plots of Fig.6.4 we show the number of stars averaged over different runs,  $\langle N_{\star} \rangle$ , as a function of  $[\text{X}/\text{Fe}]$  abundance ratio, i.e. we derive the X-Distribution Function<sup>2</sup> (XDF). In the marginal plot we show the comparison between the total XDF (light grey) and the ones obtained selecting the stars predominantly enriched by Pop III (dark purple) or normal Pop II/I stars (light purple).

First of all we can note that independently from the chemical abundance ratio, the peak of XDFs corresponds to the density peak and it is dominated by stellar populations mainly enriched by normal Pop II/I stars. On the other hand, in the low-density regions, the fingerprints of the first supernova arise, i.e. the XDFs are dominated by Pop III enriched stars. In particular, the precious *descendants* of the first supernovae appear at  $[\text{Fe}/\text{H}] < -4$ , and they are characterized by  $[\text{C}/\text{Fe}] \gtrsim +1$  and  $[\text{C}/\text{Fe}] \lesssim 0$ ,  $[\text{Mg}/\text{Fe}] \gtrsim +0.5$ ,  $[\text{Na}/\text{Fe}] \gtrsim +0.5$ ,  $[\text{Si}/\text{Fe}] \gtrsim +1$ ,  $[\text{Ca}/\text{Fe}] \gtrsim +0.5$ ,  $[\text{Ni}/\text{Fe}] \gtrsim +0.5$  and  $[\text{Zn}/\text{Fe}] \lesssim -1$ .

## 6.4 Looking for first stars descendants

The  $[\text{C}/\text{Fe}]$  ratio is commonly used as a diagnostic tool for identifying metal-poor stars enriched by Pop III sources. A significant fraction of metal-poor stars exhibit an enrichment of carbon, resulting in the so-called CEMP stars (see Chapter 2, Sec.2.2.3). Among these, the carbon excess measured in CEMP-no stars has been interpreted as the fingerprint low-energy Pop III supernovae (see Chapter 2, Sec.2.3). Additionally, the  $A(\text{C})$  value is employed to discern the origins of distinct CEMP stellar populations: in Chapter 5 (from Rossi et al. 2023) we show that, among CEMP-no stars, true Pop III stars *descendants* appear for  $A(\text{C}) \lesssim 6$  and  $[\text{Fe}/\text{H}] \lesssim -3.5$ .

<sup>2</sup> XDF: the number of stars in bin of  $[\text{X}/\text{Fe}]$  averaged over different runs

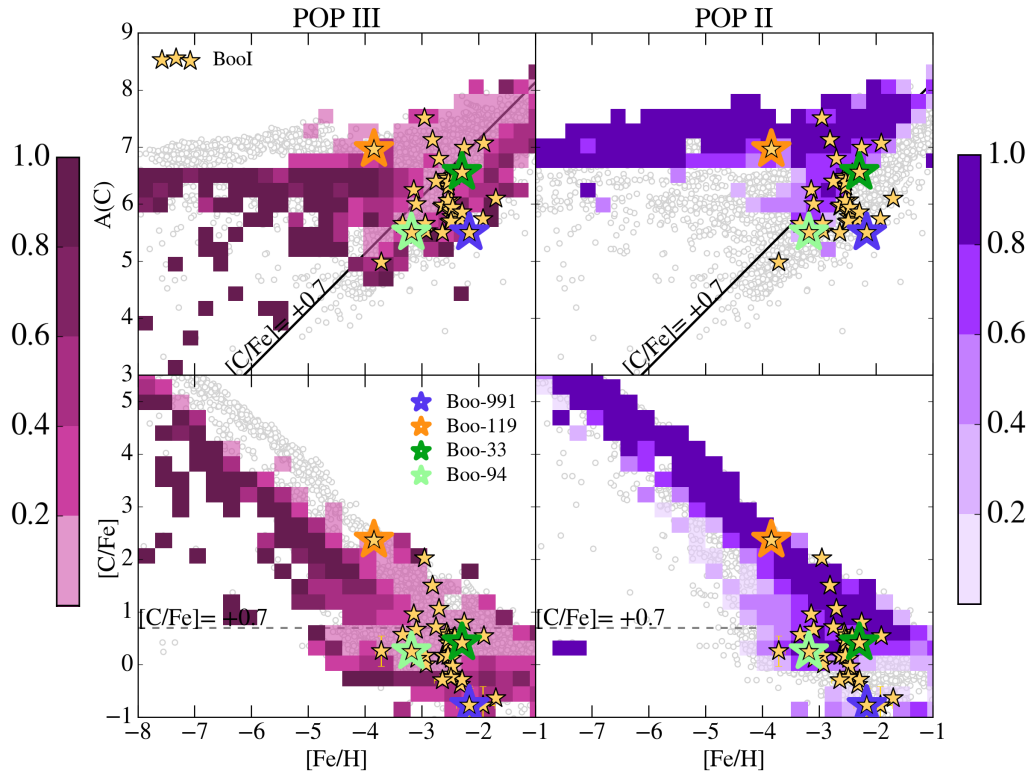


Figure 6.5: The  $A(C)$  (top panel) and  $[C/Fe]$  (bottom panel) versus  $[Fe/H]$  diagram for Boötes I stellar populations. The colored squares identify the probability to find, at fixed  $[Fe/H]$  and  $A(C)$  (of  $[C/Fe]$ ), stars predominantly enriched by Pop III or by Pop II stars (columns). Yellow stars represent the Boötes I data, while double marked points identify stars for which the abundance ratio of different chemical elements is available in the literature.

To unveil what are the key abundance ratios to unveil the chemical signature of Pop III SNe among CEMP-no and C-normal stars in Boötes I, we derived the probability that a given stellar population has been imprinted by Pop III and Pop II SNe for different  $[Fe/H]$  and  $[C/Fe]$  (or  $A(C)$ ) values. The results are displayed in Fig.6.5. By inspecting the  $A(C)$ - $[Fe/H]$  diagram in Fig.6.5 it is evident that two separate branches exist, both showing roughly constant  $A(C)$  values in the  $[Fe/H]$  range. The first branch, at  $A(C) \approx 7$  is dominated by stars predominantly enriched by Pop II stars. Complementary in the second branch,  $A(C) \lesssim 6$ , the enrichment is driven by Pop III SNe. The two different branches are also evident in  $[C/Fe]$ - $[Fe/H]$  space where we can note that Pop III and Pop II enriched stars are located in two parallel branches that exhibit a strong correlation with  $[Fe/H]$ .

As we already discussed in Chapter 5 Pop II enriched stars can be divided into two different groups with different chemical enrichment sources: stellar populations with  $[C/Fe] > +0.7$  and  $[Fe/H] \lesssim -4$ , located in the branch at  $A(C) \gtrsim 7$ , are the so called *moderate CEMP-s* stars, which formed from an ISM mainly enriched by Pop II AGB stars. C-normal stars with  $[C/Fe] \lesssim +0.7$  and  $-4 \lesssim [Fe/H] \lesssim -1$  form in birth clouds predominantly enriched by Pop II SNe. Indeed, Pop II SNe stellar yields adopted (Limongi & Chieffi 2018), do not allow to form stellar populations enhanced in carbon, i.e. with  $[C/Fe] > +0.7$ . Finally, carbon-enhanced stars with  $-3.5 \lesssim [Fe/H] \lesssim -1$  formed out from gas enriched by both AGB and SNe Pop II stars.

Pop III enriched stars are located in the low-branch at  $A(C) \lesssim 6$  of the  $A(C)$ - $[Fe/H]$  diagram or equivalently in the bottom branch of the  $[C/Fe]$ - $[Fe/H]$  diagram. The majority of Pop III stars descendants are CEMP-no stars and the probability to find them increases as  $[Fe/H]$  decreases and it is maximum for  $A(C) \lesssim 6$  and  $[Fe/H] \lesssim -3.5$ . Furthermore, it is predicted that Pop III star descendants can be found among C-normal stars. In particular, at  $[C/Fe] < 0$  and  $-4 \lesssim [Fe/H] \lesssim -1$ , the probability is to find the chemical signatures of pristine SNe exceeds  $\gtrsim 50\%$ .

In conclusion, exploiting both  $[C/Fe]$  and  $A(C)$  as diagnostics we can successfully predict promising descendants among both CEMP and C-normal stars: carbon-enhanced Pop III stars descendants are predicted to have  $A(C) \lesssim 6$  and  $[Fe/H] \lesssim -3.5$  while C-normal stars imprinted by Pop III SNe have  $[C/Fe] < 0$ . and  $[Fe/H] \gtrsim -3.5$ .

Now we go deep into understanding the origin of Pop III star descendants, exploring the *type* of SNe that enriched their birth cloud. In Fig.6.6 we show the  $[C/Fe]$ - $[Fe/H]$  diagram for Boötes I stellar populations predominantly enriched by different Pop III SNe type: low-energy (faint, cc, left column) vs high-energy Pop III SNe (high, hyper, right column). The first thing to emphasize is that the descendants of the first stars can be characterized by a broad range of both  $-7 < [Fe/H] < -1$  and  $-1 \lesssim [C/Fe] \lesssim 4$ . A significant fraction ( $\gtrsim 95\%$ ) of stars with  $[Fe/H] < -4$  are CEMP stars, with approximately 20% originating from environments enriched by Pop III SNe (i.e. faint, cc, high). Conversely, direct descendants of hypernovae are uncommon within this range. As  $[Fe/H]$  values increase, the population of CEMP stars enriched by low-energy Pop III SNe decreases, while the population of C-normal stars enriched by energetic (high and hyper) Pop III SNe increases. This can be seen by looking at the top marginal plots in Fig.6.6 in which we show the average number of stars,  $\langle N_{\star} \rangle$ , enriched at a level higher than 75% by Pop III SNe with different energy, distinguishing between CEMP and C-normal stars. At  $[Fe/H] \lesssim -3.5$  we can find the chemical imprint of Pop III SNe with  $E_{SN} < 3 \times 10^{51}$  erg among both CEMP and C-normal stars while for  $[Fe/H] \gtrsim -3$ , the chemical traces of



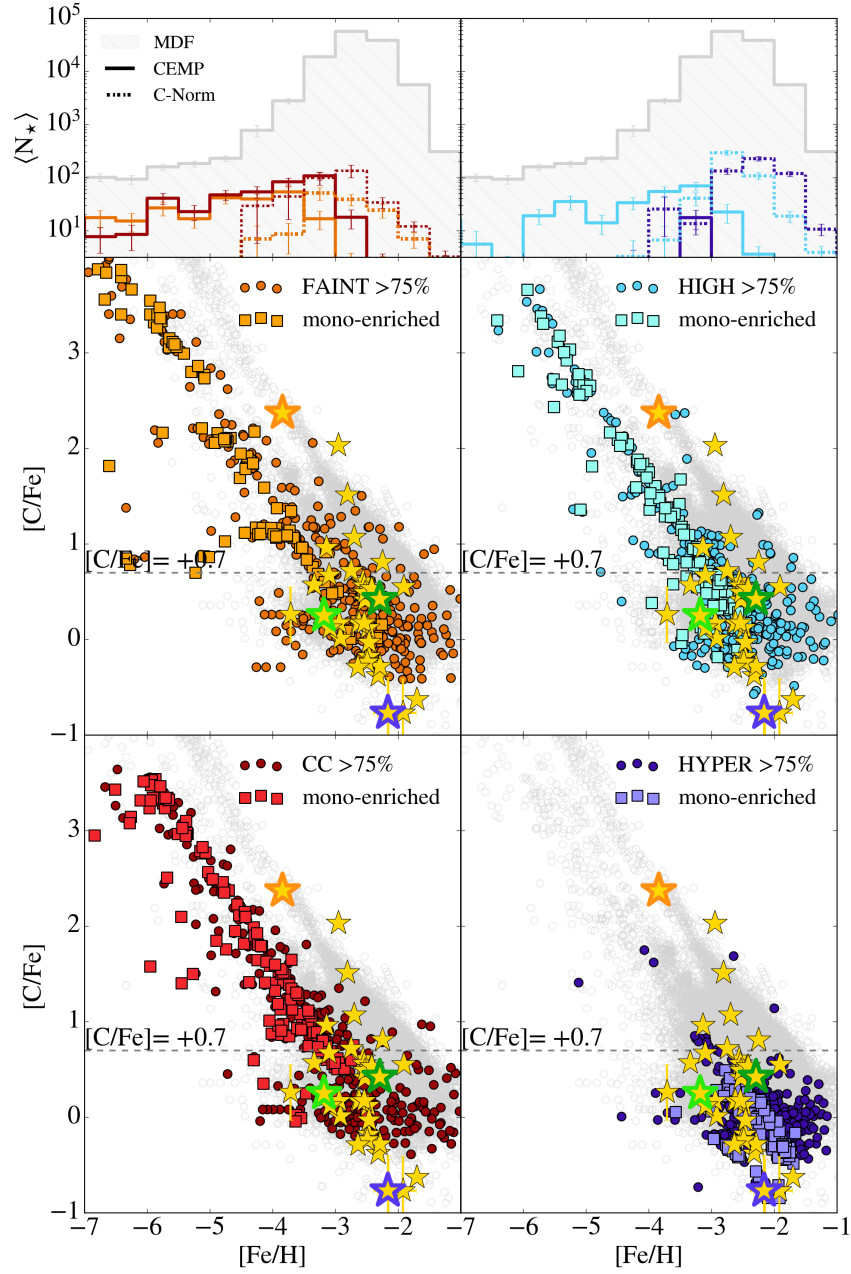


Figure 6.6: The  $[C/Fe]$  vs  $[Fe/H]$  diagram of Boötes I stellar populations mainly enriched by Pop III SNe with different energy: low-energy (first column), high-energy (second column). marginal plots show the average number of stars,  $\langle N_{\star} \rangle$ , as a function of their  $[Fe/H]$  of CEMP (solid) and C-normal (dashed) stars enriched at level higher than 75% by different Pop III SNe types, as well as the distribution of overall stars in Boötes I. Yellow stars represent the Boötes I data, while double marked points identify stars for which the abundance pattern is available in the literature.

more energetic Pop III SNe become noticeable within the C-normal stars. Although the chemical imprint of the first SNe is present across the entire range of  $[\text{Fe}/\text{H}]$ , Pop III stars descendants are rare, representing 2% of total stars in Boötes I. Therefore, how can we identify them?

#### 6.4.1 CEMP stars

In Fig.6.7 we present the  $A(\text{C})$ - $[\text{Fe}/\text{H}]$  diagram for CEMP stars where colors highlight the different Pop III SNe types that predominantly (a level higher than 75%) contributed to the enrichment of their birth clouds. To provide a comparison, we additionally show the stellar population in Boötes I mainly enriched by Pop II stars. At  $[\text{Fe}/\text{H}] < -4$ , the fraction CEMP star enriched by faint, cc, high Pop III SNe are roughly comparable. On the other hand, CEMP stars predominantly enriched by Pop III hypernovae are rare since they only reveal themselves for  $[\text{Fe}/\text{H}] \gtrsim -4$ . Indeed, hypernovae not only contribute with a significant amount of carbon injected into the ISM, but they also enrich the medium with a substantial quantity of iron (over ten times greater than other types of Pop III SNe), resulting in higher  $[\text{Fe}/\text{H}]$  values and  $[\text{C}/\text{Fe}] \lesssim +0.7$ . As previously mentioned, CEMP stars predominantly enriched by very first supernovae can be well-identified among metal-poor stars through their  $A(\text{C})$  value:  $A(\text{C}) \lesssim 6$ . This distinction becomes especially clear looking at the  $A(\text{C})$ -DFs in the right marginal plot, where we separate the contribution of different Pop III SNe and Pop II stars. From Fig.6.7 it is evident that CEMP stars with  $A(\text{C}) \lesssim 6$  have a variety of Pop III progenitors: from low to energetic Pop III SNe. These Pop III star descendants have been enriched by a single (or few) Pop III SNe that release a mass of carbon  $M_{\text{C}} \lesssim 1 M_{\odot}$  which is diluted in a total mass of gas  $M_{\text{gas}} \sim 10^4/10^5 M_{\odot}$ , thus leading to  $A(\text{C}) \sim 6$ . Pop III stars descendants with  $A(\text{C}) \lesssim 5$  have low-mass SNe progenitors,  $m_{\star} \lesssim 40 M_{\odot}$  and high mixing value ( $f_{\text{mix}} = [0.100, 0.158]$ ), which eject, on average, a total mass of carbon  $M_{\text{C}} \approx 10^{-2} M_{\odot}$ . On the other hand, CEMP stars with  $A(\text{C}) \approx 6$  have been imprinted on average by more massive Pop III SNe with  $m_{\star} > 50 M_{\odot}$ , which release into the ISM  $M_{\text{C}} \sim 1 M_{\odot}$  independently from the  $f_{\text{mix}}$ . In conclusion, the distinctive fingerprints of Pop III SNe appear at  $[\text{Fe}/\text{H}] \lesssim -4$  and  $A(\text{C}) \lesssim 6$ , where we can discover the chemical signatures of both low-energy supernovae, faint and cc, and high-energy Pop III SNe.

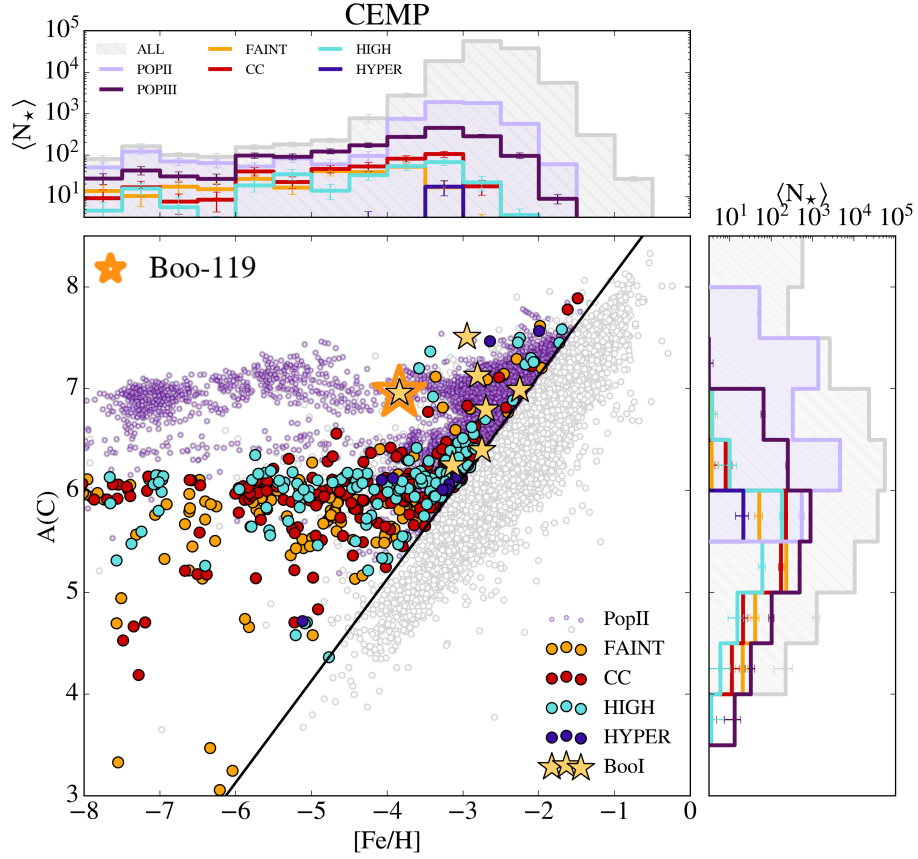


Figure 6.7: The A(C) versus [Fe/H] diagram for CEMP-no stellar populations. Colors highlight CEMP-no stars enriched to a level higher than 75% by different stellar populations: Pop II (light purple) and Pop III SNe with different energies, faint (orange), cc (red), high (light blue) and hypernovae (blue), respectively. In the marginal plots we show the number of stars averaged over the different runs,  $\langle N_{\star} \rangle$  as a function of [Fe/H] (top) and A(C) (right). The different color in the marginal plot represent the distributions of CEMP star predominantly enriched by Pop II (light purple) and Pop III (purple) stellar populations as well as by Pop III SNe with different energies. Yellow stars represent the Boötes I data, while double marked points identify stars for which abundance pattern is available in the literature.

### 6.4.2 C-normal stars

The chemical signature of pristine SNe can be also found among C-normal stars. In Fig.6.8 we show the A(C)-[Fe/H] diagram for C-normal stellar populations in Boötes I enriched by different Pop III SNe types. The first thing to note is that C-normal stars are preferentially found at  $[\text{Fe}/\text{H}] > -4$ , where the the chemical enrichment is dominated by Pop II stars (see top right marginal plot of Fig.6.4). This is particularly obvious inspecting the top marginal plot of Fig.6.8: at  $[\text{Fe}/\text{H}] > -4$  C-normal stars predominantly enriched by Pop II stars represent  $\approx 70\%$  of the total stars, while Pop III star descendants are only 6%. In this range, we can detect the chemical signatures of all Pop III SNe types, including hypernovae, even if catching their imprint is challenging because they

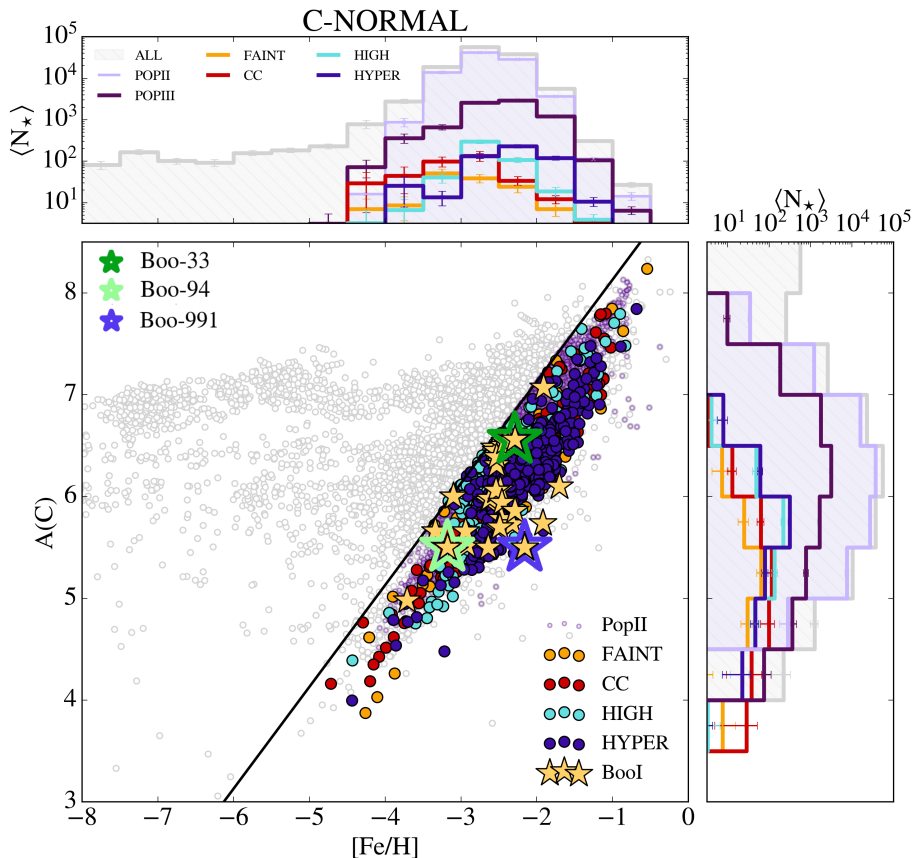


Figure 6.8: Same as Fig.6.7 but for C-normal stellar populations.

are hidden by C-normal stars enriched by Pop II stars. Fortunately, C-normal Pop III enriched stars can be identified due to their  $A(C)$  value. As we can see in the right marginal plot C-normal Pop III star descendants are predicted to have  $A(C) < 5$ , where 82% of C-normal stars have been enriched by Pop III SNe. Furthermore, pure descendants of hypernovae, become recognisable, representing  $\approx 6\%$  of C-normal stars.

### 6.4.3 Testing our predictions

Based on the predictions of our model, CEMP stars with  $[Fe/H] \lesssim -3.5$  and  $A(C) \lesssim 6$  are expected to be progeny of Pop III SNe with  $E_{SN} \leq 3 \times 10^{51}$  erg. Towards high  $[Fe/H]$  values, the probability to find direct descendants of Pop III stars declines due to the chemical pollution caused by subsequent Pop II stellar populations. Therefore, we expect that the majority of stars with  $[Fe/H] \gtrsim -3.5$  have originated from gas that has been enriched by multiple generations of Pop II stars. In particular, C-normal stars with  $-3.5 \lesssim [Fe/H] < -1$  and  $[C/Fe] \gtrsim 0.0$  are predicted to be normal Pop II stars descendants. Nevertheless, among C-normal stars with  $[C/Fe] \lesssim 0$  and  $A(C) \lesssim 5$  we expect to find the imprint of Pop III SNe of different energies, including hypernovae.

To test our predictions, we select four Boötes I stars that exhibit distinct  $[C/Fe]$  values (double marked point in Fig.6.6) and for which the abundant pattern is present in the literature.

In Fig.6.9 we show the comparison between the observed abundance patterns of Boötes I stars and our “best-fit models”. To find the best model that is able to reproduce the observed stellar abundance pattern, we use a statistical approach based on  $\chi^2$ : our initial step involves choosing stellar populations, among our predicted stars in Boötes I, with  $[Mg/Fe]$  and  $[Fe/H]$  consistent with the measured values. From these selected models, the one that minimizes the chi-square value is considered the best-fit model. The decision to use  $[Mg/Fe]$  as a constraint for the model instead of  $[C/Fe]$  is influenced by the fact that the published abundances of C and Fe have not been corrected for non-LTE and 3D effects, which can have a significant impact on the  $[C/Fe]$  value which can vary by -1 to +1 dex (Nissen et al. 2014; Skúladóttir et al. 2015; Amarsi et al. 2021). Similarly, the 3D and non-LTE corrections also affect the Mg abundance, resulting in a potential variation of  $\pm 0.27$  dex in  $[Mg/Fe]$ . However, this correction is smaller than the measured observational error, which justifies the use of  $[Mg/Fe]$  to identify the best-fit model.

From top to bottom in Fig.6.9 we present the abundance patterns of one CEMP star, two C-normal star and a C-low star. The “star”symbols indicate the measured abundance ratio, while the colored square points correspond to our best-fit model. For comparison, the abundance pattern of a star with  $[Mg/Fe]$  and  $[Fe/H]$  consistent with those observed but enriched by 100% Pop II stars is also shown in the figure (top and bottom panel, grey squared point). Additionally, the red data point represents the carbon abundances that have been corrected using the online tool<sup>3</sup> introduced in Placco et al. (2014).

- **CEMP star: Boo-119** - Based on our findings, the measured abundance pattern of the CEMP star Boo-119 (Gilmore et al. 2013), is consistent with 100% *faint* Pop III SNe enrichment. As we can see, our best fit nicely reproduces that observed except for  $[C/Fe]$  and  $[Ti/Fe]$ . It is important to note that the observed values have not undergone non-LTE corrections, which would enhance the agreement between the model and observations. As already said, accounting for 3D non-LTE effect would decrease  $[C/Fe]$ . As can be seen, the abundance pattern arising from an enrichment only produced by Pop II stars is well distinguishable from the one of Pop III SNe. Moreover, by comparing the predicted abundance patterns for 100% faint Pop III SNe and 100% Pop II SNe enrichments, we can identify the key abundance ratios that enable us to differentiate between the two

<sup>3</sup> <http://vplacco.pythonanywhere.com/>

types of enrichment. Specifically, the ratios  $[N/Fe]$ ,  $[O/Fe]$ ,  $[Na/Fe]$ , and  $[Al/Fe]$  exhibit differences exceeding 1 dex. Lastly, it is important to note that when we refer to a 100% enrichment by faint Pop III SNe, we are indicating that the star formed in an environment enriched solely by faint supernovae. However, this does not imply that the star has been enriched by a single supernova, i.e. that is a mono-enriched Pop III star descendant. In fact, according to our predictions, Boo-119 was enriched by two faint SNe: the first one with  $E_{SN} = 3 \times 10^{50}$  erg,  $m_{\star} = 55 M_{\odot}$ , and the second one with  $E_{SN} = 6 \times 10^{50}$  erg,  $m_{\star} = 58 M_{\odot}$ .

- **C-normal stars: Boo-94 and Boo-33** - Towards lower  $[C/Fe]$  values, we analysed the abundance pattern of Boo-94 (Ishigaki et al. 2014) and Boo-33 (Gilmore et al. 2013) abundance patterns (middle panel Fig.6.9). The first thing to note is that the abundance patterns measured for these stars are very similar. Furthermore, they are in agreement with an enrichment predominantly driven by Pop II SNe, accounting for 62% in the case of Boo-94 and 82% for Boo-33, respectively. It is worth noting that both of these stars experienced some level of enrichment from Pop III SNe hypernovae and core-collapse SNe, which, however, did not leave particularly distinct signatures in their abundance patterns.
- **C-low star: Boo-991**- Among the stars exhibiting  $[C/Fe] < 0$ , the star Boo-991 (Ishigaki et al. 2014) was found to reside in a region of  $[C/Fe]$  vs  $[Fe/H]$  where it is highly probable to have been enriched by Pop III SNe. Indeed, the abundance pattern of Boo-991 is consistent with 95% enrichment by Pop III stars, in particular  $\sim 84\%$  by Pop III hypernovae and  $\sim 13\%$  by high-energy Pop III SNe (bottom panel Fig.6.9). Again, we have included the abundance pattern of a star enriched by 100% Pop II SNe for comparison. As is evident, it fails to accurately reproduce several  $[X/Fe]$  ratios.

In conclusion, by combining our model with the observed data, we can not only identify the promising regions where the descendants of the first stars are more likely to be found, but also we are able to reveal which Pop III SNe *type* has predominantly contributed to their chemical enrichment.

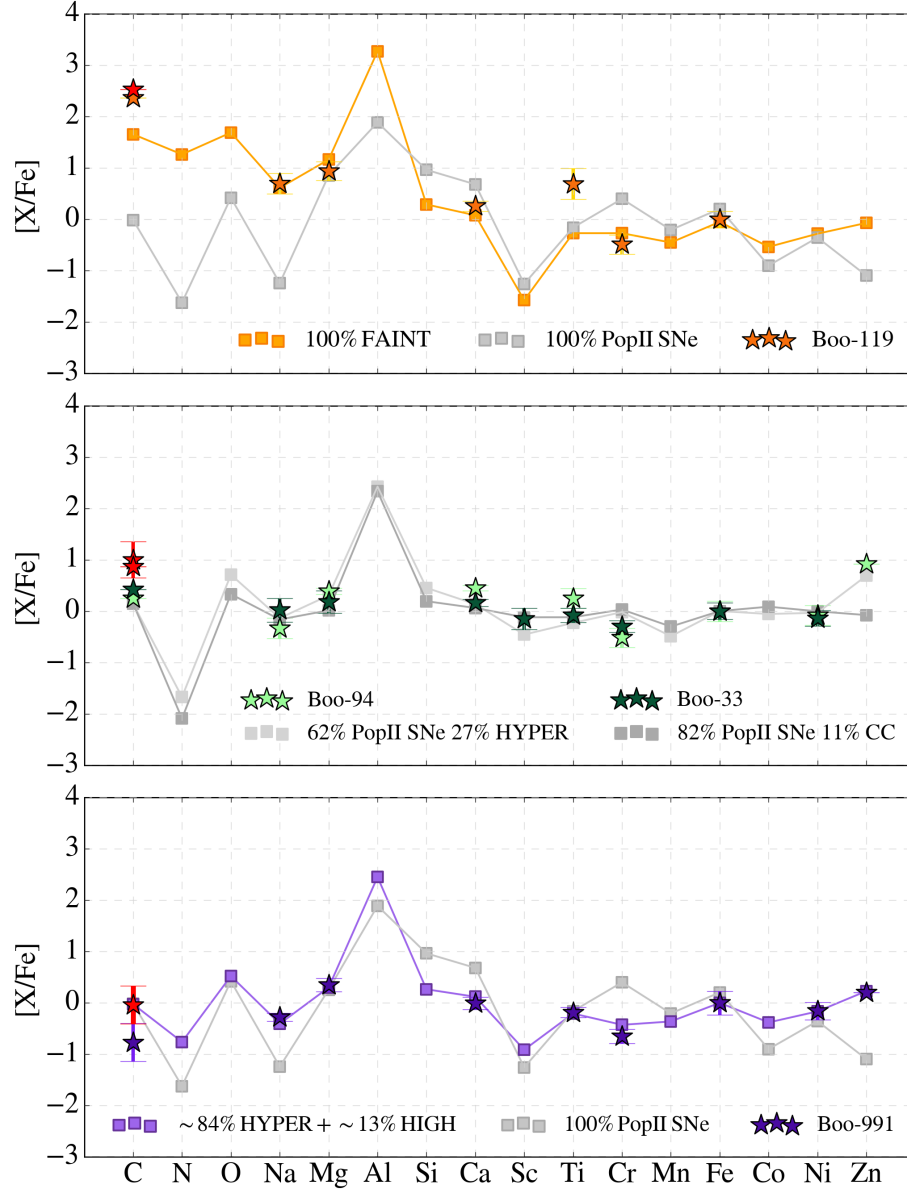


Figure 6.9: The comparison between the measured abundance patterns of Bootes I stars (colored star symbols) and our best-fit model (squared symbols). From top to bottom panel we show the data of CEMP Boo-119 star (Gilmore et al. 2013), two C-normal stars Boo-94 (Ishigaki et al. 2014) and Boo-33 (Gilmore et al. 2013) and C-low star Boo-991 (Ishigaki et al. 2014). Red points represent the Placco et al. (2014) corrections for  $[C/Fe]$  ratio.

#### 6.4.4 Mono-enriched stars

In the previous sections, we have seen that  $[C/Fe]$  and  $A(C)$  are the key diagnostic to identify the direct descendants of the first supernovae with different energies. However, to make further progress and effectively constrain the properties of Pop III supernovae, such as their energy and mass, it becomes essential to detect the mono-enriched descendants of Pop III stars. Here, we define “mono-enriched” stars as those that have originated from gas enriched by exactly one Pop III supernova. *Where can mono-enriched stars be found in Boötes I?*

Let’s inspect again Fig.6.6, where the squared symbols correspond to stellar populations that have been enriched by a single Pop III SNe. We see that in Boötes I we can find mono-enriched stars by different type of Pop III SNe which cover wide ranges of  $[Fe/H]$  and  $[C/Fe]$ . In line to what we discussed already, for  $[C/Fe] > +0.7$  and  $[Fe/H] \lesssim -4$ , we find predominantly mono-enriched stars imprinted by faint, cc and high, while mono-enriched stars by hypernovae are found at  $[C/Fe] < +0.7$  and  $[Fe/H] \gtrsim -4$ .

*How many are these peculiar stars with respect to the overall stars in Boötes I? And how can we individually identify them?* To determine the frequency of mono-enriched stars, in the first two panels of Fig.6.10 we show, the average number of stars,  $\langle N_{\star} \rangle$ , as a function of their  $[Fe/H]$  of stars solely (100%) enriched by Pop III SNe (top panel) and mono-enriched stars (middle panel). It is important to recall that a star 100% enriched by a unique Pop III SNe type is not necessarily a mono-enriched star. From the top panel we can clearly see that 100% of the low-energy Pop III-enriched stars can be found in overall  $[Fe/H]$  range, with a peak between  $-4 \lesssim [Fe/H] \lesssim -3$ . On the other hand, high-energy and hypernovae Pop III-enriched stars are predominantly located at higher  $[Fe/H]$  values ( $[Fe/H] > -4$ ), with the distribution peak around  $[Fe/H] \approx -2.5$ . Among 100% Pop III SNe enriched stars, a fraction are mono-enriched stars. In the middle panel of Fig.6.10 we present the comparison between the distribution of 100% Pop III SNe enriched (dashed histograms) and mono-enriched stars (solid histograms). The distribution of the mono-enriched stars follows that of the one of 100% Pop III enriched stars, but mono-enriched stars are obviously fewer in number. Finally, in the bottom panel, we show the fraction of mono-enriched stars,  $f_{mono}$ , with respect to the total number of stars Boötes I in each iron bin, as a function of  $[Fe/H]$ . As can be seen, mono-enriched stars are very rare and their fraction reaches a maximum of  $\approx 20\%$  at  $[Fe/H] < -4$ . In this range 3% of the total stars are predicted to be mono-enriched by faint, 4% by cc, 2% by high-energy and 0.01% by hypernovae. As  $[Fe/H]$  values increase, the fraction of mono-enriched stars exhibits a rapid decline, paralleling the rise in the total number of stars in the metallicity distribution function. At  $[Fe/H] > -4$  the fraction of mono-enriched by hypernovae grows up to reach  $\approx 1\%$  at  $[Fe/H] \approx -2.5$  where the peak of Boötes I resides.



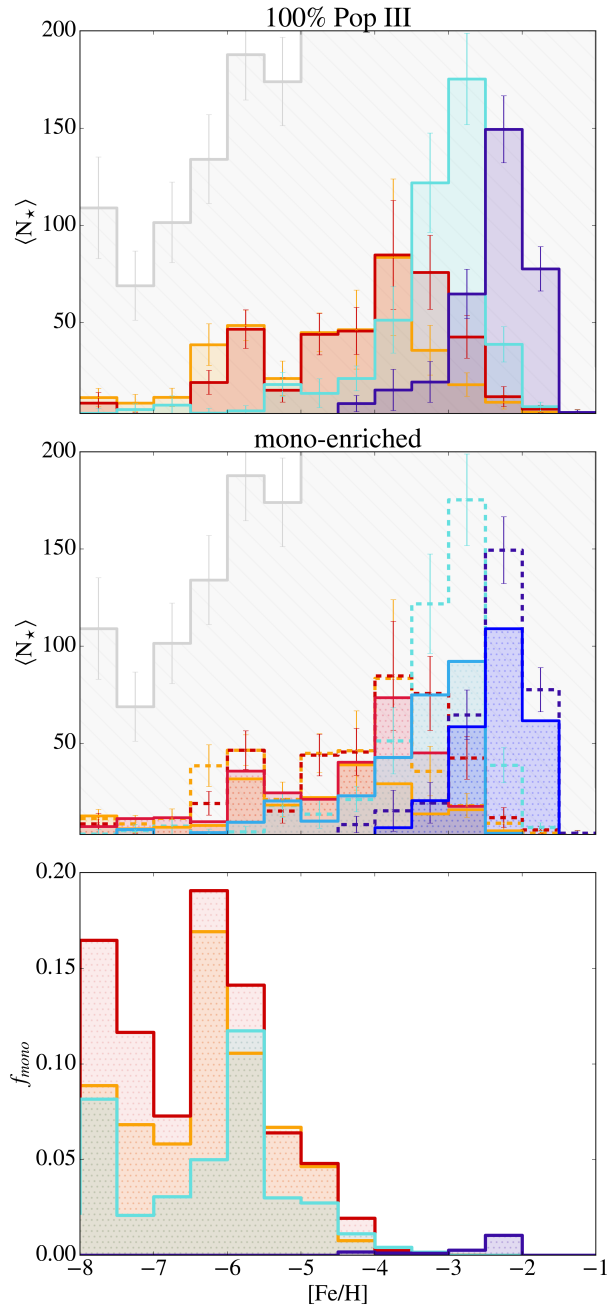


Figure 6.10: The average number of stars,  $\langle N_{\star} \rangle$ , as a function of their  $[\text{Fe}/\text{H}]$  of 100% enriched (top panel) and mono-enriched stars (middle panel), by Pop III SNe with different energies: *faint* (orange), *cc* (red), *high* (lightblue), *hypernovae* (blue). In the bottom panel, we show the fraction of mono-enriched stars compared to the total number of stars in Boötes I, as a function of  $[\text{Fe}/\text{H}]$ .

Although mono-enriched stars are very rare, finding them would allow us to make progress in understanding the nature of the first stars and to constraints the Pop III IMF. How can we detect them?

By exploiting the new diagnostic proposed by Hartwig et al. (2018) to identify stars mono-

enriched by a single Pop III SNe, in Fig.6.11 we show the  $[\text{Mg}/\text{C}]$  vs  $[\text{Fe}/\text{H}]$  diagram for Boötes I mono-enriched stars. In each panel of Fig.6.11, mono-enriched stars are color-coded according to their progenitors properties: SNe energy, (top), stellar mass  $m_*$  (bottom). Consistent with the findings of Hartwig et al. (2018), our predictions indicate that mono-enriched stars are located within the range of  $[\text{Mg}/\text{C}] \approx -1.5$  to  $[\text{Mg}/\text{C}] \approx 0.7$ . Let's stars inspecting the properties of the Pop III star progenitors of mono-enriched stars. Examining the top panel of Fig. 6.11 reveals that there is a correlation with energy. Particularly, hypernovae mono-enriched stars appears at  $[\text{Fe}/\text{H}] > -2.5$ , and they are precisely located within the  $[\text{Mg}/\text{C}]$  diagram:  $-0.5 \lesssim [\text{Mg}/\text{C}] \lesssim 0.5$ . With decreasing iron abundance,  $-3.5 \lesssim [\text{Fe}/\text{H}] \lesssim -2.5$ , we observe a predominance of mono-enriched stars originating from high-energy supernovae, characterized by  $-1 < [\text{Mg}/\text{Fe}] < 0.5$ . Finally, at  $[\text{Fe}/\text{H}] < -3.5$  and  $-1.5 < [\text{Mg}/\text{C}] \lesssim 0$ , we find mono-enriched stars imprinted by both faint and cc Pop III SNe.

The  $[\text{Mg}/\text{C}]$  diagnostic also correlates with the mass of Pop III SNe progenitors. This is evident by analysing the bottom panel of Fig.6.11: as can be seen, there are three main branches in which  $[\text{Mg}/\text{C}]$  correlates with  $[\text{Fe}/\text{H}]$  that are characterized by fixed progenitor mass range. Pop III descendants with  $[\text{Mg}/\text{C}] \gtrsim 0$  are predominantly enriched by massive SNe with  $m_* > 75 M_\odot$ . Those with  $-0.5 \lesssim [\text{Mg}/\text{C}] \lesssim 0$  originate from progenitors with masses between  $50 M_\odot < m_* < 75 M_\odot$ , while mono-enriched stars, imprinted by Pop III supernovae with  $25 M_\odot < m_* < 50 M_\odot$  exhibit  $-1.5 \lesssim [\text{Mg}/\text{C}] \lesssim 0.5$ . Finally, mono-enriched stars imprinted by low-mass Pop III are found in  $-4 \lesssim [\text{Fe}/\text{H}] \lesssim -2$  and  $-1 \lesssim [\text{Mg}/\text{C}] \lesssim 0.5$ .

Finally, comparing our results with Boötes I data, we can note that that our predicted multi-enriched Pop III star descendants Boo-119 (orange), and Boo-991 (dark purple) (see Sec.6.2) actually reside in regions where there are no mono-enriched Pop III stars. It should be noted that in Fig.6.11, we specifically focus on illustrating mono-enriched stars by Pop III supernovae, and we have not included the regions occupied by stars enriched by normal Pop II stars nor predominantly Pop III star descendants. So even if Boo-119 and Boo-991 are not consistent in being mono-enriched, they are located in a region of the  $[\text{Mg}/\text{C}]$ - $[\text{Fe}/\text{H}]$  diagram where they are likely to have been enriched by Pop III stars. Similarly, Boo-94 and Boo-33 seems to be located in regions where there are mono-enriched stars, in reality at the same  $[\text{Fe}/\text{H}]$  and  $[\text{Mg}/\text{C}]$  Pop II-enriched stars can also be found.

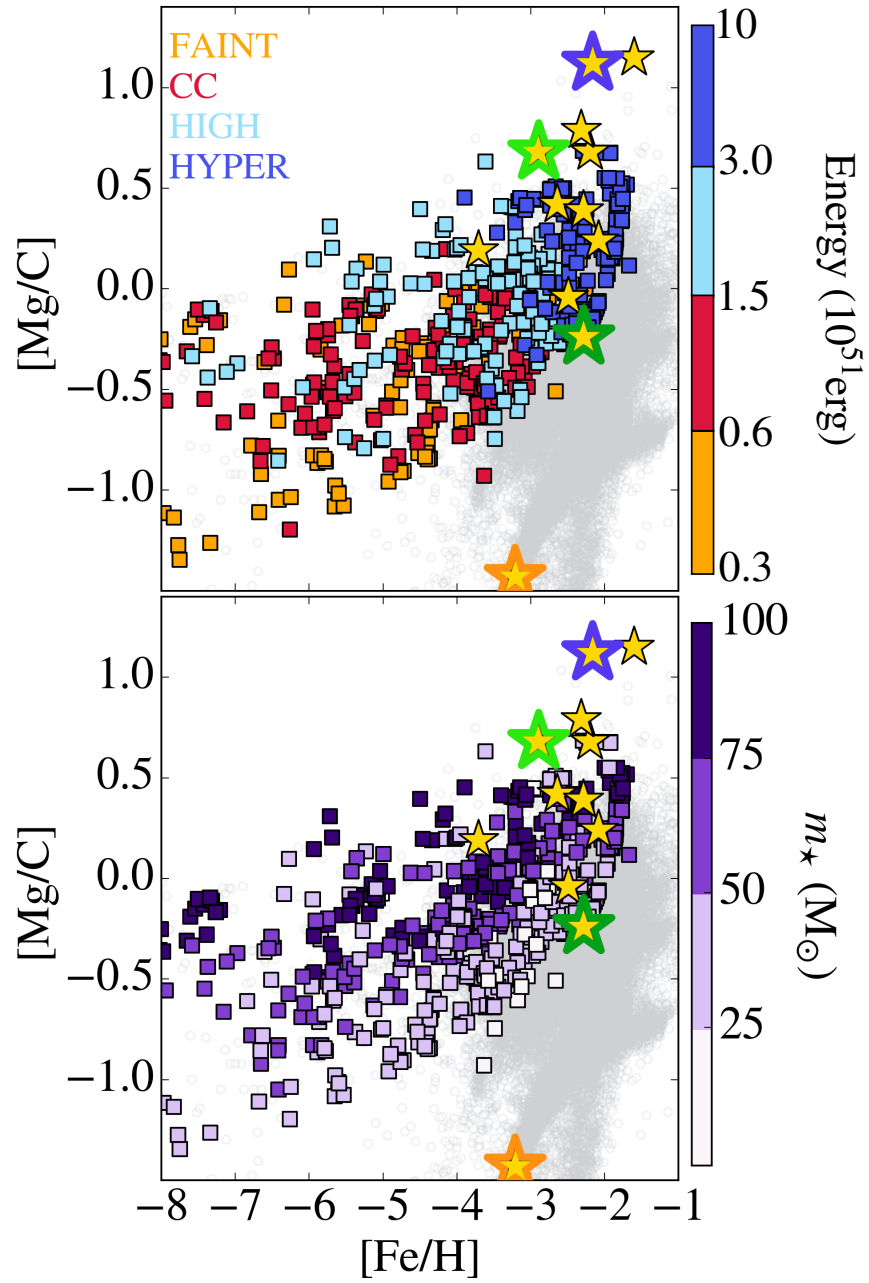


Figure 6.11: Predicted abundance ratios  $[Mg/C]$  vs.  $[Fe/H]$  for mono-enriched Pop III star descendants. In each panel mono-enriched stars are color-coded according to their progenitors properties: SNe energy, (top), stellar mass  $m_*$  (bottom).

## 6.5 Discussion and conclusions

In this work we investigate the chemical signature of Pop III SNe with different energies in UFDs, by exploiting our semi-analytical model capable to follow the chemical enrichment star-by-star. Our key results are:

- Through analysis of the different Energy Distribution Functions (EDFs) of Pop III SNe, we show that to reproduce the measured chemical of the abundance ratios in Boötes I stars we need the contribution of Pop III SNe with different energies, from low to high energies;
- The *descendants* of the first supernovae are predicted to be have  $[\text{Fe}/\text{H}] < -4$ , and they characterized by key abundance ratios:  $[\text{C}/\text{Fe}] \gtrsim +1$  and  $[\text{C}/\text{Fe}] \lesssim 0$ ,  $[\text{Mg}/\text{Fe}] \gtrsim +0.5$ ,  $[\text{Na}/\text{Fe}] \gtrsim +0.5$ ,  $[\text{Si}/\text{Fe}] \gtrsim +1$ ,  $[\text{Ca}/\text{Fe}] \gtrsim +0.5$ ,  $[\text{Ni}/\text{Fe}] \gtrsim +0.5$  and  $[\text{Zn}/\text{Fe}] \lesssim -1$ ;
- Exploiting  $A(\text{C})$  and  $[\text{C}/\text{Fe}]$  as key diagnostics, we find that the probability to find true Pop III star descendants increases toward lower value of  $[\text{Fe}/\text{H}]$ , and it is maximum for  $A(\text{C}) \leq 6$  and  $[\text{Fe}/\text{H}] \lesssim -3.5$ ;
- Our results show that Boötes I is an ideal environment to find the chemical fingerprints of Pop III SNe with progenitors masses  $[10 - 100] M_{\odot}$ . These peculiar signatures arises among both *Carbon-Enhanced Metal Poor (CEMP)* stars and *C-normal* stars;
- We proved that CEMP stars imprinted by the first stars have Pop III progenitors with different energy: *faint*, *core-collapse*, and *high-energy* SNe, and we identified a star purely imprinted by *faint* Pop III (100% of metals from its birth cloud) in Boötes I;
- At  $[\text{C}/\text{Fe}] \lesssim 0$  and  $[\text{Fe}/\text{H}] > -4$ , the chemical signatures of hypernovae became visible and we identified a star Boo-991 (Ishigaki et al. 2014) whose measured abundance pattern is consistence with a 95% enrichment by the first stars, in particular  $\sim 84\%$  by Pop III hypernovae and  $\sim 13\%$  by high-energy Pop III SNe;
- We show that mono-enriched stars are very rare and their fraction reaches a maximum of  $\approx 20\%$  at  $[\text{Fe}/\text{H}] < -4$ , where the chemical imprint of *faint*, *core-collapse* and *high-energy* Pop III SNe can be found. As  $[\text{Fe}/\text{H}]$  values increase, the fraction of mono-enriched stars exhibits a rapid decline, paralleling the rise in the total number of stars in the metallicity distribution function. Finally, at  $[\text{Fe}/\text{H}] > -4$  the fraction of mono-enriched by *hypernovae* grows up to reach  $\approx 1\%$  at  $[\text{Fe}/\text{H}] \approx -2.5$ , where the peak of Boötes I MDF resides.

- By exploiting the new [Mg/C] diagnostic proposed by Hartwig et al. (2018), we find that mono-enriched stars are located within the range of  $[\text{Mg}/\text{C}] \approx -1.5$  to  $[\text{Mg}/\text{C}] \approx 0.7$ , and they show a clear relation with the energy and masses of Pop III progenitors: *hypernovae* mono-enriched stars appears at  $[\text{Fe}/\text{H}] > -2.5$  and  $[\text{Mg}/\text{C}] -0.5 \lesssim [\text{Mg}/\text{C}] \lesssim 0.5$ . With decreasing iron abundance,  $-3.5 \lesssim [\text{Fe}/\text{H}] \lesssim -2.5$ , we observe a predominance of mono-enriched stars originating from *high-energy* supernovae, characterized by  $-1 < [\text{Mg}/\text{Fe}] < 0.5$ . Finally, at  $[\text{Fe}/\text{H}] < -3.5$  and  $-1.5 < [\text{Mg}/\text{C}] \lesssim 0$  we find mono-enriched stars imprinted by *faint* and *core-collapse* Pop III SNe. Moreover, Pop III stars descendants with  $[\text{Mg}/\text{C}] \gtrsim 0.0$  are predominantly enriched by massive SNe with  $m_{\star} > 75 M_{\odot}$ . Those with  $-0.5 \lesssim [\text{Mg}/\text{C}] \lesssim 0$  originate from progenitors with masses between  $50 M_{\odot} < m_{\star} < 75 M_{\odot}$ , while mono-enriched stars, imprinted by Pop III supernovae with  $25 M_{\odot} < m_{\star} < 50 M_{\odot}$  exhibit  $-1.5 \lesssim [\text{Mg}/\text{C}] \lesssim 0.5$ . Finally, mono-enriched stars imprinted by low-mass Pop III are found in  $-4 \lesssim [\text{Fe}/\text{H}] \lesssim -2$  and  $-1 \lesssim [\text{Mg}/\text{C}] \lesssim 0.5$ .



---

---

## Beyond Ultra-Faint Dwarfs: the Galactic Bulge

In the previous Chapters, we have seen how to derive constraints on the properties of the first stars through the ultra-faint dwarf galaxies. Now we extend our investigation to include ancient region within the Milky Way, i.e. the Galactic bulge with the aim of further understanding the nature of Pop III stars. The following contents are based on the paper by Pagnini, Salvadori, **Rossi** et al. (2023).

### 7.1 The Galactic Bulge

In the previous Chapters, we demonstrated that CEMP stars are, among the oldest stars, the direct descendants of the first SNe. Ultra-Faint Dwarf galaxies and the Milky Way's halo have been discovered to host a significant fraction of CEMP stars. Conversely, CEMP stars appear to be relatively uncommon in more luminous classical dwarfs (dSph) and in the Galactic bulge. According to the  $\Lambda$ CDM model and numerical simulations of Milky Way formation (White & Springel 2000; Diemand et al. 2005b; Tumlinson 2009; Salvadori et al. 2010; Starkenburg et al. 2017) the Galactic bulge is expected to contain the oldest stars, making it a promising environment to search for the descendants of Pop III stars. However, the Galactic bulge presents difficulties due to its dusty and densely populated environment, which is predominantly populated by stars rich in metals. As a result, detecting metal-poor objects in this area becomes a challenging task. Dedicated surveys such as the EMBLA Survey (Extremely Metal-poor bulge stars with AA $\Omega$ ) (Howes et al. 2014; Howes 2016) and more recently the Pristine Inner Galaxy Survey (PIGS) (e.g. Arentsen et al. 2020) attempt to discover candidate metal-poor stars in this inner region, however both surveys seems to confirm a *dearth* of CEMP-no stars with high [C/Fe] values in this region. In EMBLA sample in fact, only one CEMP-no star was found, having [Fe/H] =  $-3.48$  and [C/Fe] =  $+0.98$ . On the other hand PIGS, identified 24 new CEMP-no candidate stars in the Galactic bulge, with moderated C-enhancement,  $+0.7 < [\text{C}/\text{Fe}] < +1.2$ . Still, the overall fraction of CEMP-no stars obtained by PIGS

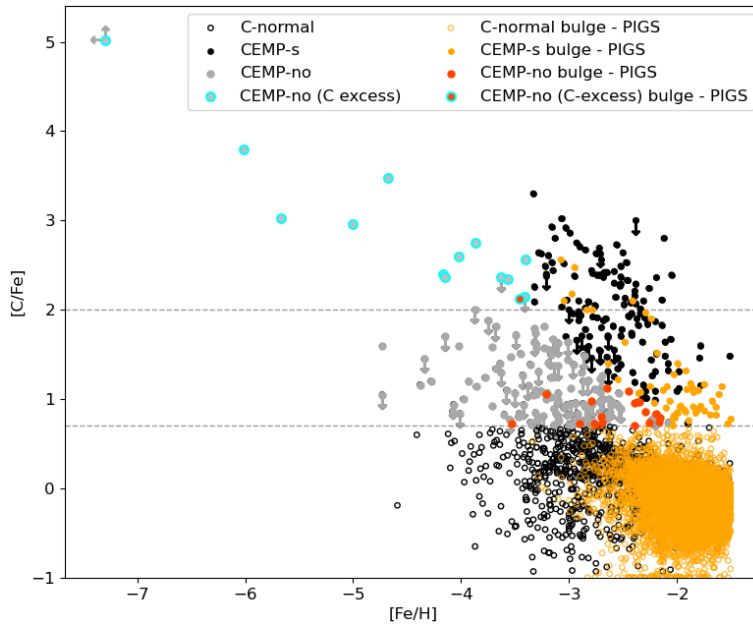


Figure 7.1: Measured  $[C/Fe]$  vs  $[Fe/H]$  for stars in the Galactic halo (black and grey points; JINAbase) and the bulge PIGS sample (orange and red points; Arentsen et al. 2021).

is only  $\lesssim 6\%$  at  $[Fe/H] < -2$ , i.e. much lower than what is found in the Galactic halo ( $\approx 20\%$ , see Arentsen et al. 2021).

To get a clear overview, Fig.7.1 shows the measured  $[C/Fe]$  vs  $[Fe/H]$  for a sample of 984 halo stars with carbon measurements from JINAbase<sup>1</sup> (Abohalima & Frebel 2018) and the bulge PIGS sample. Fig. 7.1 clearly shows how the  $[C/Fe]$  values in Galactic halo stars are higher at  $[Fe/H] < -3$  compared to stars in the bulge, and how in general CEMP-no stars are more frequent in the halo, although we cannot exclude that this can be due to a statistical effect, given the rarity of extremely metal-poor stars in the Galactic bulge. *What is the reason behind the apparent scarcity of CEMP-no stars within the Galactic bulge?* One possible explanation for the absence of stars exhibiting high  $[C/Fe]$  values in the Galactic bulge is that this ancient region underwent distinct formation and evolutionary processes compared to other environments. Our study aims to explore the underlying physical factors responsible for the observed dearth of CEMP-no stars within the Galactic Bulge. We specifically investigate whether there are any processes that actively reduce the fraction of CEMP-no stars in this region. By doing so, we aim to constrain the primordial IMF of the first stars.

<sup>1</sup> <https://jinabase.pythonanywhere.com/>



## 7.2 Model

To investigate the nature of the first stars in different environments, such as the Galactic bulge and the Milky Way's halo, it is essential to use cosmological simulations, which can trace the formation and evolution of the various component of the MW. Therefore, in this section, we provide an overview of the cosmological model utilized for our analysis in Pagnini et al. (2023).

We employ a model that integrates a  $N$ -body simulation that follows the hierarchical assembly of a Milky Way - like galaxy (used also in Salvadori et al., 2010; Pacucci et al., 2017) with a semi-analytical model (**GAMETE**, Salvadori et al., 2007, 2015) that trace the evolution of baryons, from the formation of the first stars to the present day. The semi-analytical model allows us to follow the star formation and metal enrichment history of the Milky Way from early times ( $z \sim 20$ ) until now ( $z = 0$ ), and thus to link the chemical abundances of present-day stars with the properties of the first stellar generations.

- **N-body simulation:** The  $N$ -body simulation used to study the hierarchical formation of the MW has a low-resolution region corresponding to a sphere of radius  $10h^{-1}$  Mpc (see Scannapieco et al., 2006). The region of the highest resolution is a sphere of radius  $1h^{-1}$  Mpc, i.e. four times the virial radius of the MW at  $z = 0$  ( $r_{vir} = 239$  kpc). A low-resolution simulation including gas physics and star formation has been used to confirm that the initial conditions will lead to a disk galaxy like the Milky Way. The system consists on about  $10^6$  dark matter (DM) particles within  $r_{vir}$  with masses of  $7.8 \times 10^5 M_{\odot}$ ; its virial mass and radius are respectively  $M_{vir} = 7.7 \times 10^{11} M_{\odot}$  and  $r_{vir} = 239$  kpc, roughly consistent with the observational estimates of the MW,  $M_{vir} \approx 10^{12} M_{\odot}$  (e.g. McMillan, 2011). The softening length is 540 pc. The simulation data is output every 22 Myr between  $z = 8 - 17$  and every 110 Myr for  $z < 8$ . At each output, the virialized DM halos have been identified using a *friend-of-friend* group finder with a *linking parameter*  $b = 0.15$ , and a threshold number of particles constituting virialized halos equal to 50. The  $N$ -body simulation enables to reconstruct a hierarchical history of the MW that proceeds through the consecutive merging of DM halos maintaining the information about the spatial distribution of DM particles belonging to them.
- **Star formation:** At the initial redshift of the simulation,  $z = 20$ , gas in DM halos is assumed to have a primordial composition, and only objects with virial temperatures  $T_{vir} \geq 10^4$  K are considered to be able to form stars. This choice,

which is equivalent to assuming that the star formation activity is rapidly quenched in mini-halos, is dictated by the limited DM resolution of the  $N$ -body simulation (Graziani et al. 2015). At each time-step, stars form in a single burst, proportional to the available cold gas mass,  $M_{\text{gas}}$ . The constant of proportionality is a redshift-dependent star-formation efficiency  $f_*(z) = \epsilon_* \frac{\Delta t(z)}{t_{\text{ff}}(z)}$ , where  $t_{\text{ff}}$  is the free-fall time,  $\Delta t(z)$  the  $N$ -body time-step and  $\epsilon_*$  a free parameter of the model, physically corresponding to a “local” star formation efficiency.

- Pop III stars:** Pop III stars form according to a *Larson IMF*:  $\Phi(m) = dN/dm \propto m^{-2.35} \exp(-m_{\text{ch}}/m)$ , biased towards more massive stars as it is expected for the first stellar generations. In particular, following the latest data-driven results from stellar archaeology (Rossi et al. 2021), we assume a minimum mass of Pop III stars equal to  $m_{\text{min}} = 0.8 M_{\odot}$ , a maximum mass  $m_{\text{max}} = 1000 M_{\odot}$ , and we explore different characteristic masses,  $m_{\text{ch}} \in \{1, 10, 100\} M_{\odot}$ . This allows us to account for the contribution to chemical enrichment of Pop III stars exploding as both faint SNe and PISN and to vary their relative proportions.
- Pop III-to-Pop II transition:** Following the critical metallicity scenario (Bromm et al. 2001; Schneider et al. 2003), we assume that the IMF of newly formed stars depends upon the initial metallicity of the star-forming clouds. Therefore, a star forming halo with a gas metallicity  $Z \leq Z_{\text{cr}}$  will form Pop III stars, otherwise, if  $Z > Z_{\text{cr}}$ , it will form Pop II/I stars. Exploiting the data driven constraints of de Bennassuti et al. (2017), we set  $Z_{\text{cr}} = 10^{-4.5} Z_{\odot}$ . Normal Pop II/I stars are assumed to have masses in the range  $[0.1, 100] M_{\odot}$  and to form according to a standard Larson IMF (Larson, 1998), which peaks at the characteristic mass  $m_{\text{ch}} = 0.35 M_{\odot}$  and rapidly declines with a Salpeter-like shape towards larger masses (Salpeter 1955).
- Metal enrichment:** The newly formed stars are assumed to instantaneously evolve at the following snapshot of the simulation (Instantaneous Recycling Approximation, IRA), since the time elapsed between two neighbouring steps is larger than the lifetime of the least massive stars evolving as SNe. For Pop III stars exploding as PISN we assume the yields of Heger & Woosley (2002), while for primordial faint SNe we assume those of Iwamoto et al. (2005). For Pop II/I stars we adopt the yields from Woosley & Weaver (1995). To not overestimate the contribution of carbon due to AGB stars that also produce slow neutron-capture process elements and, even if not in binary systems, can lead to the formation of “moder-

ate" CEMP-s stars (Rossi et al. 2023), we only considered the chemical products of Pop II/I that evolve as core-collapse SNe in short timescales (3 – 30 Myr). After SNe explosions the newly produced/injected metals are assumed to be instantaneously and homogeneously mixed within the ISM, eventually reaching the Inter Galactic Medium (IGM) via supernova driven outflows.

- Gas and metals dispersal:** Supernovae may release a high amount of energy, which may overcome the binding energy of the hosting halo leading to a partial gas and metals removal from the galaxy. The mass of gas ejected into the IGM,  $M_{\text{gas}}^{\text{ej}}$ , depends on the balance between the escape velocity of the halo,  $v_{\text{esc}}$ , and the kinetic energy released during the explosion, namely:  $M_{\text{gas}}^{\text{ej}} = (2E_{\text{SN}})/v_{\text{esc}}^2$ , where  $E_{\text{SN}} = \epsilon_w N_{\text{SN}} \langle E_{\text{SN}} \rangle$ , with  $N_{\text{SN}}$  number of SNe explosions and  $\langle E_{\text{SN}} \rangle$  the average explosion energy. For a typical PISN ( $\langle E_{200M_{\odot}}^{\text{PISN}} \rangle \sim 2.7 \times 10^{52}$  erg (Heger & Woosley, 2002), while a typical faint SNe provides ( $\langle E_{25M_{\odot}}^{\text{faint}} \rangle \sim 0.7 \times 10^{51}$  erg (Iwamoto et al. 2005; Marassi et al. 2014), which is lower than the energy released by a normal  $25 M_{\odot}$  core-collapse SN,  $E_{25M_{\odot}}^{\text{cc}} \approx 10^{51}$  erg. The quantity  $\epsilon_w$ , representing the second free parameter of the model, is the *wind efficiency*, that is the fraction of the explosion energy converted into kinetic form.
- Chemical evolution:** Due to mechanical feedback, the mass of gas and metals in a halo can decrease substantially. At each simulation time-step the gas mass reservoir in each halo,  $M_{\text{gas}}$ , is updated with respect to the initial gas mass,  $M_{\text{gas}}^{\text{in}}$ , to account for the mass of stars locked into newly formed stars,  $M_*$ , and the gas mass ejected out of the halo,  $M_{\text{gas}}^{\text{ej}}$ :  $M_{\text{gas}} = M_{\text{gas}}^{\text{in}} - (1 + R)M_* - M_{\text{gas}}^{\text{ej}}$ , where  $R$  is the returned fraction, which is equal to 1 only for PISN and lower than unity otherwise. Similarly, the mass of metals,  $M_Z$ , in each hosting halo is updated as follow:  $M_Z = M_Z^{\text{in}} + Y M_* - Z_{\text{ISM}}^{\text{in}} M_* - Z_{\text{ISM}}^{\text{in}} M_{\text{gas}}^{\text{ej}}$ , where  $M_Z^{\text{in}}$  is the initial mass of metals,  $Y_Z$  the metal yield, and  $Z_{\text{ISM}}^{\text{in}}$  the initial metallicity of the ISM.
- Model calibration:** To set the best values of the two model free parameters,  $\epsilon_*$  and  $\epsilon_w$ , the observed properties of the MW have been used as a benchmark. In particular, the results of the simulations at redshift  $z = 0$  have been compared with the gas/stellar mass and metallicity of the MW, the baryon-to-dark matter ratio, and the metallicity of high-velocity clouds (see for more details Salvadori et al. 2007; Salvadori et al. 2010).

### 7.2.1 The progenitor halos of the Bulge

Firstly, using the cosmological model (Sec.7.2) we reconstructed the hierarchical tree in the Milky Way analogue by combining the positions of the DM particles where star formation took place. Subsequently, we identified the halos that reside within the inner region of the Galaxy, i.e. the bulge, which exhibit the presence of the oldest Pop II/I stars. Figure 7.2 shows the present-day,  $z = 0$ , spatial distribution of DM particles, color-coded with their star-formation rate (SFR) during the first  $\approx 800$  Myr, i.e. averaged over the cosmic time between  $z = 15$  and  $z = 8$ , which corresponds to the lowest redshift for which we have Pop III star formation. Then, we computed the final  $\langle \text{SFR} \rangle$  by averaging among the results of all DM particles in the considered pixel. This results in a wide range of average star formation rates (Fig. 7.2),  $\langle \text{SFR} \rangle \approx (10^{-4} - 1.4) M_{\odot}/\text{yr}$ . The spatially resolved region with the highest mean SFR at  $z > 8$  is the innermost one, i.e. the Galactic bulge. This result, which is in agreement with previous theoretical (e.g. Cescutti & Matteucci, 2011) and observational (e.g. Lucertini et al., 2022) findings, suggests that the progenitors of the Galactic bulge experience, on average, a more intense star formation at early times with respect to the progenitors of the Galactic halo. Finally, we select pristine and star-forming halos for which more than 80% of particles are predicted to dwell in the Galactic bulge at the present time (8 halos). Their halo mass and redshift of formation range between  $M_{\text{h}} = (5.5 \times 10^7 - 1.7 \times 10^8) M_{\odot}$ , and  $11.4 < z < 16.3$ . The predicted star-formation rate for these first star-forming halos is  $\text{SFR} < 1.8 \times 10^{-2} M_{\odot}\text{yr}^{-1}$ , which in all cases is less than the threshold value for a fully populated Pop III IMF,  $\text{SFR}_{\text{min}} \sim 10^{-1} M_{\odot}\text{yr}^{-1}$  (Rossi et al. 2021). Thus, it is fundamental to include incomplete sampling of the adopted Pop III IMFs.

### 7.2.2 Pop III enrichment

To evaluate the Pop III star enrichment within the first star forming halos, we assume that Pop III stars form according to the Larson IMF (see Chapter 3 Eq.3.3), and we explore different characteristic mass,  $m_{\text{ch}} = [1, 10, 100] M_{\odot}$ . For each of our selected first star-forming halo, we derived the *effective* Pop III IMF associated to each burst of primordial star formation to account for the stochastic and incomplete IMF sampling. Figure 7.3 shows, for different  $m_{\text{ch}}$ , the comparison between the theoretical Pop III IMFs and effective ones, which have been obtained in one run of the random sampling. The mass range covered by faint SNe,  $[8 - 40] M_{\odot}$ ; PISN,  $[140 - 260] M_{\odot}$ ; and other stars that do not end their lives as supernovae are identified using different colours. Note that the average mass fraction of stars exploding as faint SNe (and PISN) strongly varies, not only with  $m_{\text{ch}}$  but also as a consequence of the incomplete IMF sampling. In the

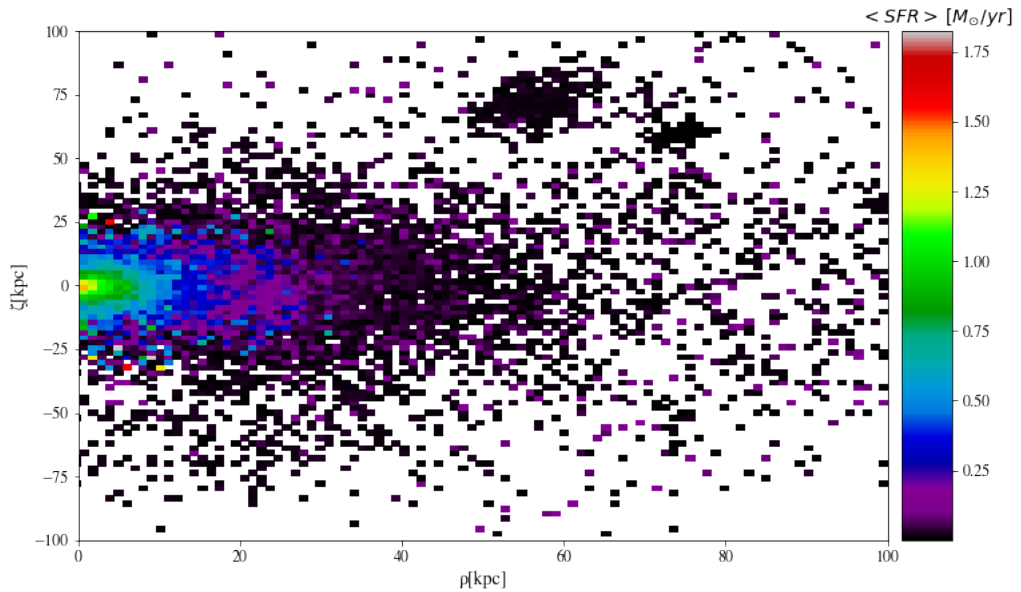


Figure 7.2: Present-day spatial distribution of DM particles in the cylindrical coordinate plane of the simulated galaxy, color-coded with their SFR averaged over the cosmic time between  $z = 15$  and  $z = 8$ .

mass range of faint SNe, the Pop III IMFs are almost completely sampled, except in the extreme case  $m_{ch} = 100 M_{\odot}$ . On the contrary, in the typical mass range of PISN the Pop III IMF is only partially populated. As expected, however, the mass range of PISN becomes more densely populated as the characteristic mass increases.

Now, let's analyze how different IMFs impact the chemical enrichment of the bulge. In Fig. 7.4 we show the  $[\text{Fe}/\text{H}]$  and  $[\text{C}/\text{Fe}]$  of the ISM in the 8 first star-forming halos currently dwelling in the Galactic bulge as obtained with our incomplete IMF sampling procedure (see Chapter 3), and as a function of the five different Pop III IMFs assumed. The abundance ratios for the different halos are colour-coded according to the halo mass and, for comparison, we also show the results obtained considering the fully sampled IMFs as solid grey lines. For each  $m_{ch}$  the average abundances over all halos are shown as empty black symbols together with their errors. The observed ranges of  $[\text{C}/\text{Fe}]$  within the Galactic halo and bulge are highlighted as well in Fig. 7.4 (respectively as grey and orange shaded areas).

First, we note that for all IMFs, the total gas metallicity after the Pop III star enrichment is  $Z_{\text{ISM}} > Z_{\text{cr}} = 10^{-4.5} Z_{\odot}$ , which implies that normal low-mass long-lived stars will be able to form in such environments. Furthermore, when we only account for the contribution of faint SNe, we get a very low value of  $[\text{Fe}/\text{H}] \simeq -5.6$  and an extremely high  $[\text{C}/\text{Fe}] \simeq +4$ , which is close to the maximum value observed in the Milky Way halo (Keller et al., 2014). As soon as the chemical contribution of PISN is also considered,

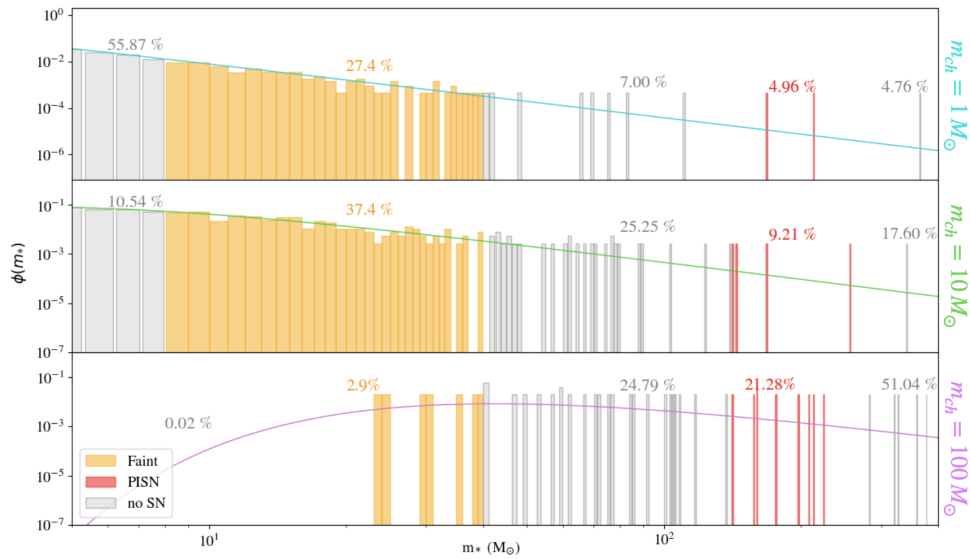


Figure 7.3: Theoretical (solid lines) and effective (coloured histogram) Larson IMFs of Pop III stars with increasing characteristic masses, from top to bottom ( $m_{ch} = 1, 10, 100 M_{\odot}$ ), obtained from one run of the random sampling. In each panel, the mass range covered by faint SNe, ( $8 - 40 M_{\odot}$ ) (orange); PISN, ( $140 - 260 M_{\odot}$ ) (red); and other stars that do not end their lives as supernovae (grey), are specified. The total mass fractions are also listed for each mass range. The total mass of the burst of Pop III is  $7.7 \times 10^3 M_{\odot}$ .

namely for  $m_{ch} = 1 M_{\odot}$ , the  $[C/Fe]$  value drops dramatically by at least 2 orders of magnitude. As we can see at fixed  $m_{ch}$ , as the halo mass increases, the abundances approach the fully sampled case, that is,  $[Fe/H]$  increases and  $[C/Fe]$  decreases. This result can easily be explained as a consequence of the Pop III IMF sampling: in the lower-mass halos, which have lower star formation rates, on average only one PISN explodes, thus only partially lowering the  $[C/Fe]$  value obtained in the case of faint SNe only. Still, even a single PISN is able to inject into the ISM 50% of its total stellar mass in form of heavy elements, thus strongly affecting the final  $[C/Fe]$  value of the ISM. In the most massive halo more PISN can actually form and explode, thus further lowering the expected  $[C/Fe]$  value. For increasing  $m_{ch}$ , the mean  $[C/Fe]$  values become even lower, since PISN production starts to dominate the chemical enrichment. When only PISN explode, no CEMP stars are able to form, regardless of the halo mass.

In conclusion, the measured  $[C/Fe]$  values in the Galactic bulge suggest that massive Pop III stars exploding as PISN have likely formed in this environment, washing out the high  $[C/Fe]$  signature left by low-energy primordial SNe. Furthermore, by comparing our predicted  $[C/Fe]$  with the values observed in the bulge (Fig. 7.4), we can exclude the two extreme IMF cases, where Pop III stars explode either only as faint SNe or only as PISN, and suggest that the IMF that best reproduces the observations is a Larson type with a characteristic mass possibly  $1 M_{\odot} \lesssim m_{ch} \lesssim 10 M_{\odot}$ .

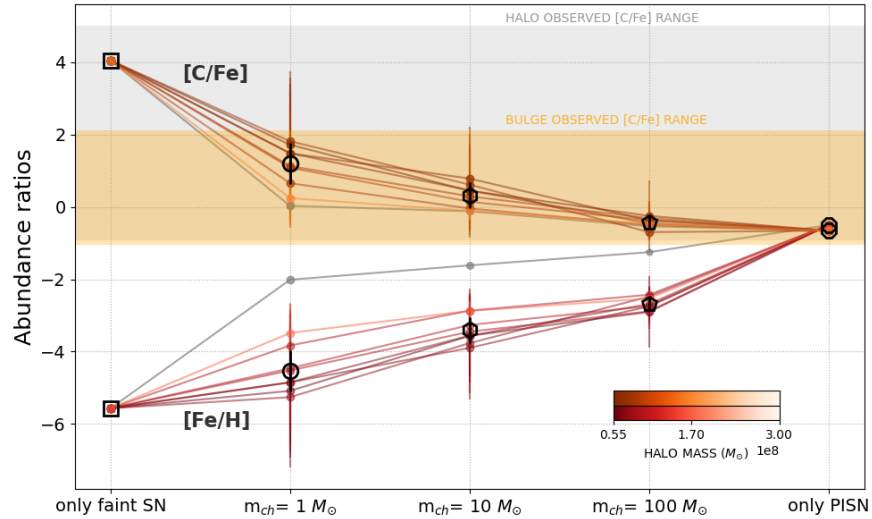


Figure 7.4: Average  $[\text{Fe}/\text{H}]$  and  $[\text{C}/\text{Fe}]$  of the ISM in 8 first star-forming halos (colour-coded according to the halo mass), obtained through the random sampling of different Pop III IMFs. The characteristic masses ( $m_{ch}$ ) are in solar masses ( $M_{\odot}$ ) and error bars are  $1\sigma$  confidence intervals. The values are computed assuming a time step  $\Delta t = 1$  Myr of star formation, consistent with Rossi et al. (2021). For comparison, the grey solid lines are related to the fully sampled IMFs. For each  $m_{ch}$  the average abundances over all halos are shown as empty black symbols together with their errors. Observed ranges of  $[\text{C}/\text{Fe}]$  within the Galactic halo (grey) and bulge (orange) are shown as shaded areas.

### 7.2.3 Discussion and conclusions

The aim of this work is to investigate the apparent dearth of carbon-enhanced metal-poor stars with high  $[\text{C}/\text{Fe}]$  values in the Galactic bulge with respect to other environments, such as the Galactic halo and ultra-faint dwarf galaxies (e.g. Howes et al. 2015; Howes 2016; Arentsen et al. 2021). This lack is particularly puzzling since the bulge is supposed to be the oldest Galactic stellar component (White & Springel 2000; Diemand et al. 2005b; Tumlinson 2009; Salvadori et al. 2010; Starkenburg et al. 2017) and CEMP stars are predicted to be among the most ancient observable stars, most likely being the direct descendants of first stars with intermediate masses that exploded as low-energy faint supernovae (e.g. Iwamoto et al. 2005; Bonifacio et al. 2015; de Bressana et al. 2017). A reason for the dearth of CEMP stars in the Galactic bulge could be linked to a bias introduced by the photometric selection performed by the surveys that have targeted metal-poor stars in this environment (Howes et al. 2015; Howes 2016; Arentsen et al. 2021). Despite these caveats, this issue still persists even though progress has been achieved over the years in detecting these types of stars leading to an actual increase in the number of their observations. Therefore, we asked ourselves: could this scarcity of CEMP stars be a consequence of the low statistics of metal-poor stars in the more metal-rich and dusty bulge? Could it suggest an intrinsically different formation mechanism of

this region compared to the other environments?

The key results can be summarised as follows:

- We investigate whether the lower  $[C/Fe]$  values of CEMP stars in the Galactic bulge reflects the different formation and evolution of this ancient environment. To address this question, we focused on the predictions derived from the  $\Lambda$ CDM cosmological model, through the use of a  $N$ -body simulation that follows the hierarchical formation of a MW-like galaxy combined with the semi-analytical model GAMETE (Salvadori et al. 2007; Salvadori et al. 2010; Salvadori et al. 2015; Graziani et al. 2015; Pacucci et al. 2017). If we assume that *all* Pop III stars explode as faint SNe, we find that the mass fraction of CEMP stars with  $[C/Fe] > +2$  increases at decreasing Galacto-centric radii and it is maximum in the Galactic bulge, which is the region of the simulation containing the most ancient stars, which is at odd with observations. However, the  $N$ -body simulations reveal that the stars dwelling into the present-day bulge form in halos that experienced the *highest mean star-formation rate* at high-redshifts ( $z > 8$ ).
- We inferred that the dearth of CEMP stars with  $[C/Fe] > +2$  in the Galactic bulge might be linked with the higher star-formation rate of its early progenitor halos, which hosted the first stars. Indeed, star-formation rates  $> 10^{-2}M_{\odot}/\text{yr}$  in primordial environments might allow the formation of rare very massive Pop III stars (Rossi et al. 2021), which evolve as energetic PISN.
- We thus explored how the chemical enrichment of the bulge progenitors depends upon the properties of rare Pop III stars that can *effectively form* in these highly star-forming systems. To this aim, we performed analytical calculations and computed the chemical properties of the ISM in the bulge progenitors after the contribution of Pop III stars. More specifically, we investigated how different Pop III IMFs affect the  $[C/Fe]$  and  $[Fe/H]$  values of the ISM by assuming various characteristic masses ( $m_{ch} = 1, 10, 100 M_{\odot}$ ), by including the contribution of Pop III stars exploding as PISN, and by accounting for the incomplete sampling of the Pop III IMF (Rossi et al. 2021). Our results show that very massive Pop III stars can effectively form in the bulge progenitors, and that their contribution to the chemical enrichment as energetic PISN can partially wash out the distinctive signature of faint SNe, lowering the carbon overabundance down to  $[C/Fe] < +2$ . In particular, we show that the higher the probability to form very massive Pop III



stars, i.e. the larger the  $m_{ch}$ , the lower is the  $[C/Fe]$  value of the ISM after the contribution of Pop III stars. By exploiting the available data we thus tentatively infer  $1 M_{\odot} \lesssim m_{ch} \lesssim 10 M_{\odot}$ , consistent with the constraints found by Rossi et al. (2021) based on ultra-faint dwarfs.

- We conclude that the modest  $[C/Fe]$  values of CEMP stars identified in the bulge,  $[C/Fe] \approx +0.8$ , along with the dearth of CEMP stars with  $[C/Fe] > +2$  could be an indirect probe of very massive first stars exploding as PISN, which are extremely rare and hence can only form in highly star-forming progenitors of the MW bulge.

Through careful analysis of observational data and theoretical simulations, we thus suggest that the dearth of CEMP stars in the bulge might be intrinsic, and not only a consequence of systematic observational effects. Furthermore we have shown that the first star forming halos that end up in the bulge have typically significantly higher star-formation rates than those in the outskirts of the galaxy. This means that the Pop III IMF is better sampled in these systems, enabling the formation of rare populations such as very massive first stars that explode as PISN. Ultimately, our analysis showed this to be a very plausible explanation for the dearth of CEMP stars in the bulge, as added PISN contribution will lower the observed  $[C/Fe]$ . Furthermore we suggested a new promising method that exploits the lack of CEMP stars to constrain the characteristic mass of the first stars.



---

## Beyond Ultra Faint Dwarfs: Galactic Halo

The presence of metal-poor stars in the halo of the Milky Way offers valuable insights into the properties of Pop III stars. In this Chapter, we undertake an extensive analysis of the properties exhibited by metal-poor stars within the Galactic halo, with the aim of unveiling the nature of the first stars. The following contents are based on the paper by Koutsouridou I., Salvadori S., Skúladóttir A., **Rossi, M.** et al. (2023) and Vanni I., Salvadori S., Skúladóttir A., **Rossi, M.** et al. (2023).

### 8.1 Milky Way’s Halo

Within our Galaxy, the halo of the Milky Way stands out as the most ancient and metal-poor environment, and for this reason it has been the subject of extensive surveys over the past two decades, which led to the discovery of a multitude of metal-poor stars (Beers & Christlieb 2005; Caffau et al. 2011b; Yong et al. 2013a; Bonifacio et al. 2021, see Chapter 2 ). The ancient stars, characterized by exceptionally low metallicities, provide crucial insights into the early stages of our galaxy’s formation and the nature of the Universe itself. As remnants of the earliest stellar generations, they offer a unique window into the conditions prevailing during the formation of the Milky Way and the early Universe. For these reasons the Galactic halo is an ideal place to study the chemical signatures left by Pop III stars, and thus constrain their properties. In this Chapter, we undertake an extensive exploration into the nature of the first supernovae. We demonstrate how we can constrain the properties of primordial SNe by comparing our model predictions with observations of very metal-poor stars in the Galactic halo.

### 8.2 Model implementations

The model described in Chapter 7, Sec.7.2 has been further implemented (for a complete description see Koutsouridou et al. 2023). Here, we provide an overview of the key implementations:

- *Relaxing the Instantaneous Recycling Approximation:* in all the previous work in which was employed the N-body simulation coupled with GAMETE, the chemical evolution was computed assuming the IRA, i.e., that all stars that do not survive until  $z = 0$ , die and return gas and metals into the ISM *instantaneously*. Here we relax the IRA approximation and we follow the evolution of each individual star, depending on its initial mass and metallicity. We adopt the stellar lifetimes of Raiteri et al. (1996) for Pop II/I stars and the stellar lifetimes of Schaerer (2002) for Pop III stars.
- *The energy distribution of Pop III SNe:* Currently, there is no theoretical constraint on the explosion energies of Pop III SNe with  $m_\star = [10 - 100] M_\odot$ , and while observations suggest that they could have spanned almost two orders of magnitude, their distribution remains completely unknown. We assume a mass-independent energy distribution function (EDF) of the form,  $dN/dE_\star \propto E_\star^{-\alpha_e}$ , where  $E_\star$  is the explosion energy and  $\alpha_e$  is a free parameter of the model. Based on the distribution, we assign randomly an energy to each Pop III SNe which then determines the supernovae types from the following options: faint SNe( $E_{51}^1 = [0.3, 0.6]$ ), a core-collapse SNe(ccSN;  $E_{51} = [0.9, 1.2, 1.5]$ ), high energy SNe( $E_{51} = [1.8, 2.4, 3]$ ) or hypernova ( $E_{51} = [5, 10]$ ).
- *Metal enrichment:* The chemical enrichment of the ISM is influenced by both Pop III and Pop II/I stellar populations. The metal yields and remnant masses of Pop III stars are adopted from Heger & Woosley (2002) for PISN ( $140 \leq m_\star / M_\odot \leq 260$ ) and from Heger & Woosley (2010) for less massive Pop III SNe ( $10 \leq m_\star / M_\odot \leq 100$ ). For Pop II/I stars we adopt the yields Limongi & Chieffi (2018) for massive stars evolving as core-collapse SNe (ccSNe) and the van den Hoek & Groenewegen (1997) yields for low and intermediate mass ( $m_\star < 8 M_\odot$ ) Asymptotic Giant Branch (AGB) stars.

### 8.3 Results

We investigate how the Metallicity Distribution Function (MDF), the Carbonicity Distribution Function (CDF), and the fraction of CEMP-no stars in the Galactic halo depends on the unknown energy distribution function (EDF) of the first Pop III supernovae. We examine, respectively, the degeneracy between the EDF and the other unknowns related to Pop III stars, especially the primordial IMF.

<sup>1</sup>  $E_{51} = E_\star / 10^{51} \text{erg}$

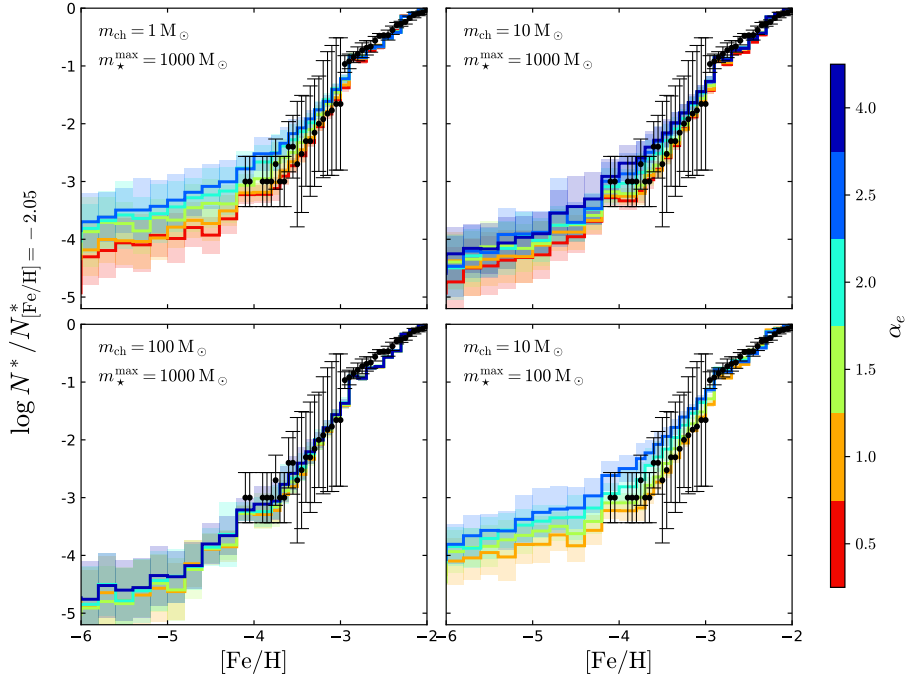


Figure 8.1: Mean metallicity distribution functions of very metal-poor, inner halo stars, normalized at  $[\text{Fe}/\text{H}] = -2.05$ , in comparison to the observations by Bonifacio et al. (2021) for the four Larson-type Pop III IMFs considered. For each IMF, results are shown for different values of the Pop III EDF exponent,  $\alpha_e$ , as denoted by the color. All mixing values of the Heger & Woosley (2010) yields are assumed to be equally probable.

### 8.3.1 Pop III stars: Energy Distribution Function vs IMF

This Section explores how the properties of the surviving halo stars in our model change when we vary the EDF of the first SNe. We assume that all different Pop III mixing parameters given by Heger & Woosley (2010) are equally probable and assign them randomly to each Pop III SNe. We consider four Larson-type IMFs: (i) with characteristic mass  $m_{ch} = 1 M_{\odot}$  and maximum mass for Pop III stars  $m_{max} = 1000 M_{\odot}$ , (ii) with  $m_{ch} = 10 M_{\odot}$  and  $m_{max} = 1000 M_{\odot}$ , (iii) with  $m_{ch} = 100 M_{\odot}$  and  $m_{max} = 1000 M_{\odot}$ , and (iv) with  $m_{ch} = 10 M_{\odot}$  and  $m_{max} = 100 M_{\odot}$ .

Figures 8.1 and 8.2 show the predicted MDFs for the four cases assuming different EDFs as denoted by the color. We find that at  $[\text{Fe}/\text{H}] > -3$  the halo MDF is essentially independent of the assumed Pop III IMF and EDF and it is in almost perfect agreement with the one derived by Bonifacio et al. (2021). It is worth noting that the MDF is a genuine prediction of our model since no free parameter was tuned to reproduce it the assumed Pop III IMF and EDF. At lower metallicities  $[\text{Fe}/\text{H}] < -3$  there is a clear trend: the MDF steepens as we move both to a higher characteristic mass  $m_{ch}$  (or higher  $m_{max}$ ) at fixed EDF or to a lower  $\alpha_e$  at fixed IMF, i.e., as more Pop III stars with high

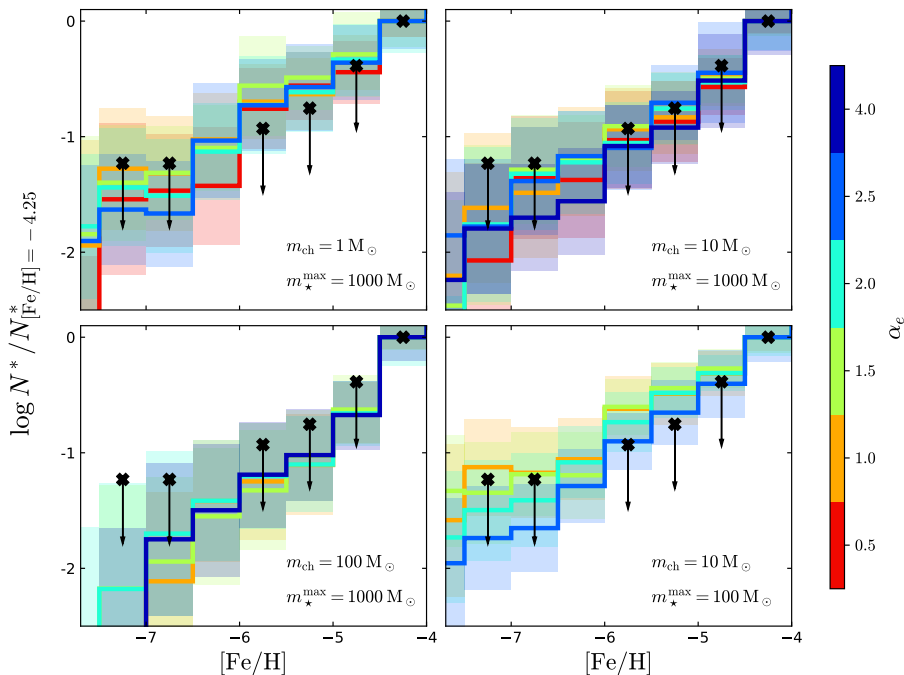


Figure 8.2: Same as Figure 8.1 but normalized to  $[\text{Fe}/\text{H}] = -4.25$  and compared to the ultra metal poor MDF from the SAGA database. The downwards pointing arrows indicate the possibility that the SAGA MDF might be biased towards the lowest metallicities.

masses and explosion energies are formed. This is to be expected, since high energy SNe, hypernovae and massive PISN yield more iron than faint and ccSNe and, thus, accelerate the chemical enrichment in their host halos resulting in a steeper MDF. Nevertheless, all MDFs are in agreement with the Bonifacio et al. (2021).

In addition, all model MDFs are in agreement with the SAGA MDF at  $[\text{Fe}/\text{H}] < -4$  within errors (Figure 8.2). Yet, the ones predicted by the  $[m_{ch}, m_{max}] = [1, 1000] M_{\odot}$  and the  $[m_{ch}, m_{max}] = [10, 100] M_{\odot}$  models, which result in less (or zero) PISN formed, lie above the observational data-points in most metallicity bins. Instead the others IMFs lie below the observations. It is probable that the number of stars at  $[\text{Fe}/\text{H}] < -4.5$  with respect to the number of stars at  $[\text{Fe}/\text{H}] \approx -4$  will decline in the future as more stars in the range  $-4.5 \leq [\text{Fe}/\text{H}] \leq -4$  will be followed up with high-resolution observations. Therefore, we could say that the latter two models are preferable here, or else that PISN are required to steepen the ultra metal-poor tail of the MDF. However, this could be a premature conclusion, given that only 14 stars with  $[\text{Fe}/\text{H}] < -4.5$  have been observed to date.

In Figure 8.3, we compare our predicted CEMP fractions to the observations. All halo stars with  $[\text{Fe}/\text{H}] < -5$  are predicted to be carbon enhanced,  $[\text{C}/\text{Fe}] > +0.7$ . At higher metallicities, and for a given Pop III IMF, we find that EDFs skewed towards high

explosion energies (i.e. with smaller  $\alpha_e$ ) result in lower CEMP fractions; naturally, since more energetic Pop III SNe yield less [C/Fe] at fixed mass and mixing level (e.g. see Vanni et al. (2023)).

The dependence of the yielded [C/Fe] on the Pop III stellar mass is not straightforward. At  $10 \leq m_*/M_\odot \leq 100$  and at a given explosion energy, the ejected [C/Fe] appears to increase with mass, especially at low mixing levels, but the relation is not monotonous and tends to reverse at the highest explosion energy  $E_* = 10 \times 10^{51}$  erg (Heger & Woosley, 2010). The opposite is true for PISN; the yielded [C/Fe] decreases dramatically with stellar mass from  $\sim 10^{13}$  at  $m_* = 140 M_\odot$  to  $\leq 10^{-1}$  at  $m_* = 260 M_\odot$  (Heger & Woosley, 2002). In addition, only the lowest explosion energies ( $E_* \leq 1.5 \times 10^{51}$  erg) and the lowest mixing levels produce [C/Fe] that exceed those of the least massive PISN ( $m_* \lesssim 170 M_\odot$ ). Yet, all non-PISN yield higher [C/Fe] than PISN with  $m_* \gtrsim 195 M_\odot$ . Nevertheless, Figure 8.3 reveals a clear trend. As we increase the characteristic mass from  $m_{ch} = 1 M_\odot$ , to  $m_{ch} = 10 M_\odot$ , and  $m_{ch} = 100 M_\odot$  (resulting in  $M_{\text{PISN}}/M_{\text{PopIII}} \approx 0.04, 0.11, \text{ and } 0.22$ , respectively) the predicted CEMP fraction for a given EDF decreases. For  $m_{ch} = 1 M_\odot$  we can reproduce the observed  $F_{\text{CEMP}}$  for  $\alpha_e > 1$  while for  $m_{ch} = 10 M_\odot$  we need a higher  $\alpha_e \gtrsim 1.5$ . That means that as the number of PISN increases, the number of hypernovae should drop (from  $< 22\%$  for  $m_{ch} = 1 M_\odot$  to  $< 8\%$  for  $m_{ch} = 10 M_\odot$ ). For  $m_{ch} = 100 M_\odot$  even the EDF with  $\alpha_e = 4$  (giving  $\sim 99\%$  faint SNe) cannot produce enough CEMP stars to meet the observations. This is because when  $m_{ch} = 100 M_\odot$  PISN dominate the ISM enrichment, thus washing out the high [C/Fe] yielded by faint SNe (Pagnini et al., 2023). Indeed, in the case where  $m_{max} = 100 M_\odot$ , i.e., when no PISN are allowed to form, our model fits the observations for  $\alpha_e \sim 1.5 - 2$ . Finally, in Figure 8.4, we compare the cumulative CDFs, for stars with  $[\text{Fe}/\text{H}] \leq -2$ , predicted by our models with observations from the SAGA database. We find that the CDFs become steeper as the  $m_{ch}$  of the Pop III IMF increases, or else as more PISN form. Models with  $m_{ch} = 100 M_\odot$  (bottom left panel) significantly underpredict the number of stars with  $[\text{C}/\text{Fe}] > +4$ , yet all other models are in agreement with the observations within errors. At fixed IMF, we see that when the model CDFs are normalized to  $[\text{C}/\text{Fe}] = +2$ , they show no clear dependence on the assumed EDF. That is not true, however, when we consider the CDFs extending down to lower [C/Fe]. There, our now-familiar trend is evident; the higher the energy of Pop III SNe (or else the lower the  $\alpha_e$ ), the lower the yielded [C/Fe] and, therefore, the steeper the resulting CDF.

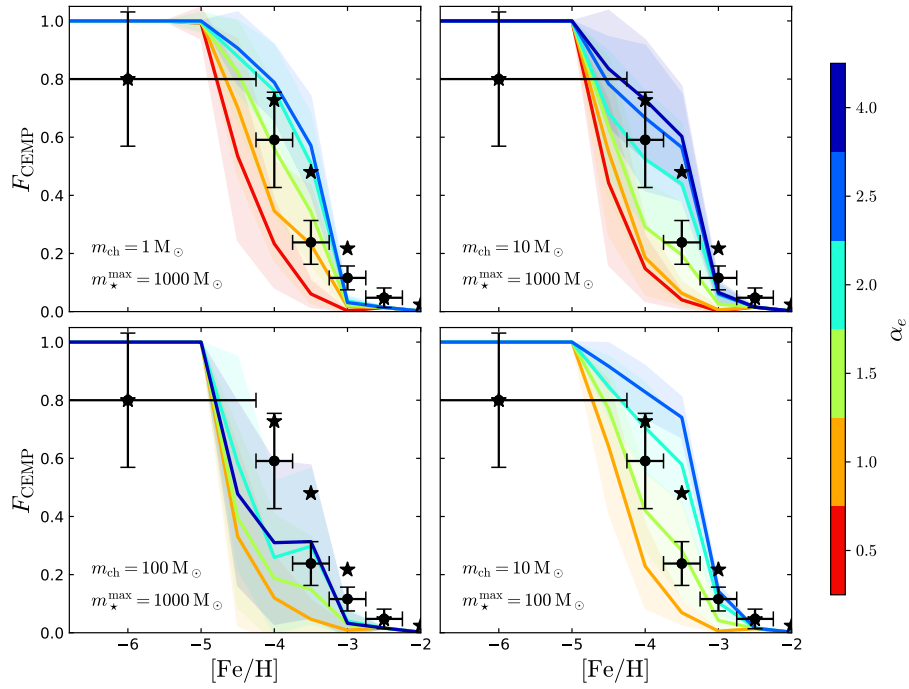


Figure 8.3: Differential CEMP fractions of very metal poor inner halo stars, for the four IMFs and different  $\alpha_e$  values considered. Data-points show the observational estimates of Yong et al. (2013a) and Placco et al. (2021).

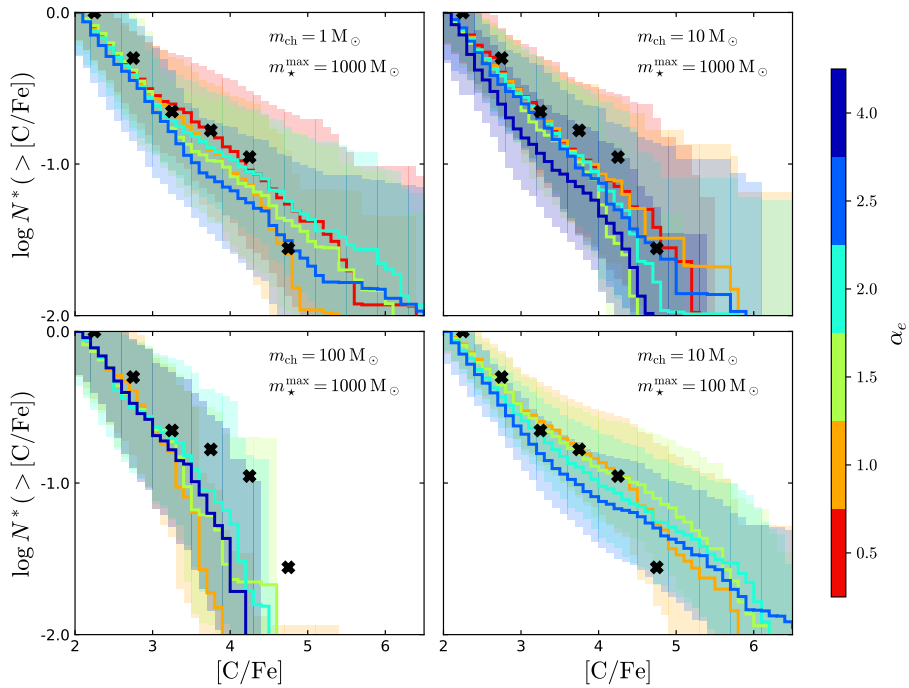


Figure 8.4: Cumulative  $[C/Fe]$  distribution functions of very metal poor, inner halo stars, normalized at  $[C/Fe]=+2$ , in comparison with observations from the SAGA database.



### 8.3.2 Metal contribution from Pop III stars

It became clear that there exist degeneracies between the EDF and the IMF of Pop III stars. Given the currently large errors in the observational data, it is hard to single out a preferred model. It is useful to examine the average behaviour of all our "successful" models, see Table 8.1, i.e., those that are in better agreement with the observed MDF, CDF and  $F_{\text{CEMP}}$ .

Table 8.1: Pop III stellar parameters for the models that successfully reproduce the observed MDF (Bonifacio et al. 2021), the CDF and the CEMP fractions (Yong et al. 2013a; Placco et al. 2014) of very metal-poor stars in the inner halo. In all models below, all values of stellar mixing given by Heger & Woosley (2010) are assumed to be equally probable.

		Model 1	Model 2	Model 3
IMF	$m_{\text{ch}}$	1 $M_{\odot}$	10 $M_{\odot}$	10 $M_{\odot}$
	$m_{\star}^{\text{max}}$	1000 $M_{\odot}$	1000 $M_{\odot}$	100 $M_{\odot}$
EDF	$\alpha_e$	1.0-2.0	1.5 - 2.5	1.5-2.0

Figure 8.5 (left) shows the present-day distribution of very metal-poor, inner halo stars in the [C/Fe]-[Fe/H] diagram. The main bulk of the observed C-normal population is in very good agreement with our model predictions, and coincides with the region predicted to have the highest density of stars. Furthermore, the CEMP-no stars are also well represented by our models. Similar to the observations, our models show a sharply decreasing [C/Fe] with increasing [Fe/H]. However, our [C/Fe]-[Fe/H] relation appears shifted towards lower [Fe/H] compared to the observed one. As a result the CEMP stars with the highest carbonicities in each [Fe/H] bin are not reproduced by our models. This is a problem faced by several other works (e.g. Cooke & Madau 2014; Komiya et al. 2020; Jeon et al. 2021). The right panel of Figure 8.5, depicts the *minimum* metal fraction contributed by Pop III stars, as a function of metallicity and carbon enhancement. In particular, the colors denote the minimum  $f_Z^{\text{Pop III}} \equiv m_Z^{\text{Pop III}}/m_Z^{\text{tot}}$  of all stars belonging to each [C/Fe]-[Fe/H] bin in our models (Table 8.1), where  $m_Z^{\text{tot}} = m_Z^{\text{Pop III}} + m_Z^{\text{Pop II}}$  is the total mass of metals in a star and  $m_Z^{\text{Pop III}}$  and  $m_Z^{\text{Pop II}}$  the metals' mass that it has inherited from Pop III and Pop II progenitors, respectively. We find that all C-enhanced stars at [Fe/H] < -3, are at least  $\sim 20\%$  enriched by Pop III progenitors.<sup>2</sup> As we go towards higher [C/Fe], this value increases rapidly, up to > 50% for stars with [C/Fe] > +1, and up to > 80% for stars with [C/Fe] > +1.5 (at the same [Fe/H] < -3).

<sup>2</sup> Note that our model does not include binary transfer, i.e., CEMP-s stars.

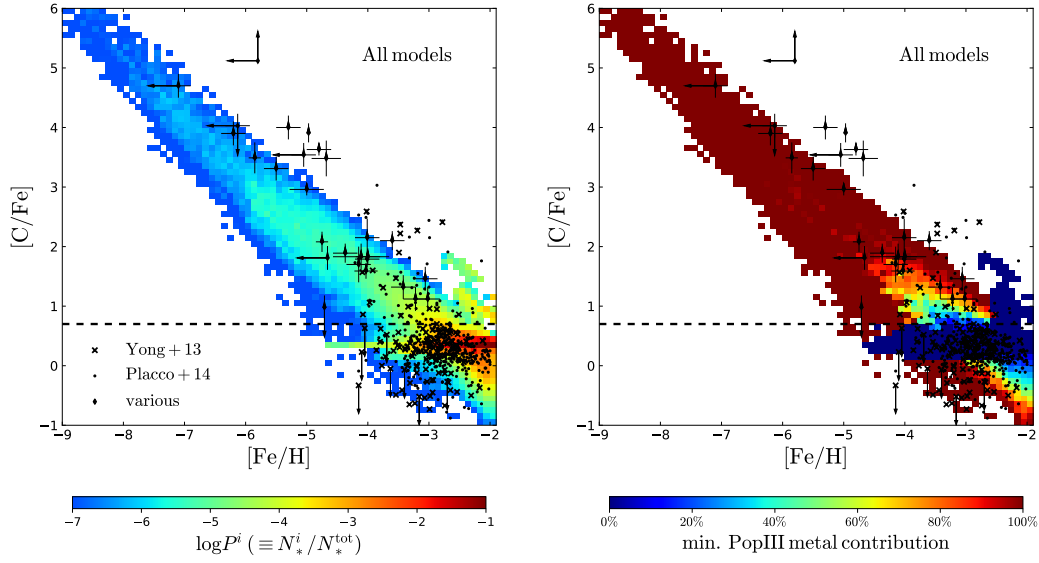


Figure 8.5: Left: Distribution of very metal-poor, inner-halo stars on the  $[\text{Fe}/\text{H}]$ – $[\text{C}/\text{Fe}]$  diagram. The color denotes the probability  $P_i \equiv N_*^i / N_*^{\text{tot}}$  of stars to belong in each bin  $i$ , where  $N_*^i$  is the number of stars in the bin and  $N_*^{\text{tot}}$  is the total number of  $[\text{Fe}/\text{H}] \leq -2$  stars. Right: Same as left panel only here the color denotes the *minimum* metal fraction inherited by Pop III ancestors for all the stars in each  $[\text{Fe}/\text{H}]$ – $[\text{C}/\text{Fe}]$  bin. Data points in both panels, show the C-normal and CEMP-no stars from the samples of Yong et al. (2013a;  $\times$  points), Placco et al. (2014; points), and various authors (diamonds; Christlieb et al. 2002; Norris et al. 2007; Caffau et al. 2011a; Keller et al. 2014; Hansen et al. 2015; Frebel & Norris 2015; Li et al. 2015; Bonifacio et al. 2015; Caffau et al. 2016; Bonifacio et al. 2018; François et al. 2018; Aguado et al. 2018c; Starkenburg et al. 2018; Aguado et al. 2019; Ezzeddine et al. 2019; Nordlander et al. 2019).

Moreover, all stars with  $[\text{C}/\text{Fe}] \gtrsim +2$  and/or  $[\text{Fe}/\text{H}] \lesssim -4.7$  are *pure* Pop III descendants; their abundance patterns are less than 5% contaminated by Pop II stars. In addition to the Pop III enriched CEMP stars, there is a group of C-enhanced stars that have been entirely enriched by Pop II stars, at  $[\text{Fe}/\text{H}] > -2.8$  and  $[\text{C}/\text{Fe}] < +2$  (dark blue area in Figure 8.5). Our adopted Pop II SNe yields (Limongi & Chieffi, 2018) have a maximum  $[\text{C}/\text{Fe}] = +0.69$  at  $[\text{Fe}/\text{H}] \leq -2$ , and are, therefore, not able to beget very metal-poor CEMP stars. Instead, we find that such Pop II CEMP stars are formed in minihalos enriched to high  $[\text{C}/\text{Fe}]$  by Pop II AGB stars, after SNe explosions have removed all gas from the halo and with it the iron rich signature of more massive Pop II stars (see also Rossi et al. 2023). The stars at  $0 < [\text{C}/\text{Fe}] < +0.7$  are predominantly enriched by Pop II progenitors. They correspond to the highest density region of Figure 8.5 (left), which implies that most of the observed C-normal stars are not Pop III star descendants. Yet, at low  $[\text{C}/\text{Fe}] < 0$ , the Pop III metal contribution starts dominating again. This is a natural consequence of the fact that Pop II stars yield a minimum  $[\text{C}/\text{Fe}] \approx 0.07$  at

$[\text{Fe}/\text{H}] \leq -2$  (Limongi & Chieffi, 2018), while energetic Pop III SNe can reach down to  $[\text{C}/\text{Fe}] \approx -1.3$  (Heger & Woosley 2002; Heger & Woosley 2010).

### 8.3.3 Discussion and conclusions

For the first time, we explore the energy distribution function, EDF, of the first SNe in the context of a cosmological galaxy formation model of a MW-analogue. Our model follows the formation and evolution of individual Pop III stars, which is uniquely determined by their initial mass, stellar mixing and explosion energy. Their contribution in the chemical enrichment of their host minihaloes is imprinted in the present-day properties of very metal-poor Galactic halo stars, such as their MDF, CDF, and CEMP fractions. We have demonstrated that the Pop III EDF can be equally important to their IMF in shaping the abundances of extremely metal poor halo stars. We find that only EDFs that are weighted towards low explosion energies combined with bottom heavy IMFs (even if they extend to  $1000 M_{\odot}$ ) can reproduce simultaneously the MDF, the CDF and the fraction of CEMP stars in the Galactic halo. However, this comparison alone does not allow a tighter constraint on the Pop III IMF. We draw the following main conclusions:

- *Pop III Energy Distribution Function.* The fraction of CEMP stars,  $F_{\text{CEMP}}$ , is highly sensitive to the primordial EDF, especially at  $[\text{Fe}/\text{H}] < -3$ . Assuming an EDF of the form:  $dE/dN \propto E^{-\alpha_e}$ , we find that we can reproduce the observed CEMP fractions for  $\alpha_e \sim 1 - 2.5$ , depending on the adopted IMF for Pop III stars (Figure 8.3). This value corresponds to a  $\sim 40 - 90\%$  probability for Pop III stars with  $m_{\star} = [10 - 100] M_{\odot}$  to explode as faint SNe, and a  $20 - 0.5\%$  probability for them to explode as hypernovae. The effect of the Pop III EDF (and of their IMF) on the halo MDF is only prominent at  $[\text{Fe}/\text{H}] \lesssim -3$ , but there the observational uncertainties are so large that they render any comparison inconclusive (Figures 8.1 and 8.2).
- *Pop III Initial Mass Function.* A top-heavy primordial IMF (with characteristic mass  $m_{ch} = 100 M_{\odot}$  in the range  $[0.1-1000] M_{\odot}$ ) is disfavoured, as it underestimates the CEMP fraction and results in a too steep CDF, even if all Pop III stars with  $m_{\star} = 10 - 100 M_{\odot}$  explode as faint SNe (Figures 8.3 and 8.4).
- *Pop II descendants.* The great majority of very metal-poor stars lie at  $0 < [\text{C}/\text{Fe}] < +0.7$ , i.e. they are C-normal. We predict that these stars have been predominantly polluted by normal Pop II SNe, in agreement with recent studies investigating the abundance patterns of C-normal stars and their small star-to-star scatter (Vanni et al. 2023). In addition, we find a population of CEMP stars at  $[\text{Fe}/\text{H}] \gtrsim -2.8$ , which were born from gas enriched by Pop II AGB stars.

- *Pop III descendants.* Regardless of the assumed model, all CEMP stars at  $[\text{Fe}/\text{H}] \lesssim -2.8$  have been enriched to  $> 20\%$  by Pop III progenitors. This value increases to  $> 95\%$  at  $[\text{C}/\text{Fe}] \gtrsim +2$  (Figure 8.5). At fixed  $[\text{C}/\text{Fe}]$ , CEMP stars with the lowest metallicities are faint SNe descendants, while as we move to higher  $[\text{Fe}/\text{H}]$  the contribution of higher energy Pop III SNe prevails. According to our results, very metal-poor stars with  $[\text{C}/\text{Fe}] \lesssim 0$  are predominantly imprinted by primordial hypernovae (at  $[\text{Fe}/\text{H}] \lesssim -2.5$ ) and PISN (at  $[\text{Fe}/\text{H}] \gtrsim -2.5$ )

## 8.4 A general parametric model

In previous Sections, we have seen how to infer the properties of Pop III stars by exploiting cosmological simulations of Milky Way formation. Here we present a novel parametric model which is suitable for applications on a broad range of topics related to early chemical enrichment. Indeed, it can interpret the chemical fingerprints left by the first SNe explosions in both long-living stellar descendants (e.g. Skúladóttir et al. 2023a) and in more distant gas clouds, which can be observed as absorption systems (Salvadori et al. 2023).

### 8.4.1 The model

We briefly summarize the simple and general parametric study presented by Salvadori et al. (2019) and further implemented by Vanni et al. (2023). The model aims to chemically characterize the descendants of Pop III stars: long-lived stars formed in environments predominantly polluted by Pop III SNe, i.e. where the metals from Pop III SNe account for  $\geq 50\%$  of metals in the ISM. The model assume that a single Pop III star can form in primordial star-forming halos. Then, we evaluate the chemical enrichment of the ISM after: (i) the injection of heavy elements by Pop III SNe with different explosion energies and progenitor masses; and (ii) the subsequent contribution of "normal" Pop II stars exploding as core-collapse SNe. We adopt the yields by Heger & Woosley (2002) for very-massive Pop III stars,  $m_{\star} = [140 - 260] M_{\odot}$ , that explode as Pair Instability SNe and by Heger & Woosley (2010) for intermediate-mass Pop III stars,  $m_{\star} = [10 - 100] M_{\odot}$ , exploding as faint, core-collapse, high-energy SNe and hypernovae, whose explosion energy is respectively equal to  $E_{\text{SN}} = (0.6, 1.2, 3.0, 10.0) \times 10^{51}$  erg. For Pop II stars we adopt the yields of Woosley & Weaver (1995) and Limongi & Chieffi (2018).

### 8.4.2 Birth environments of Pop III descendants

In Fig. 8.6 we show the  $[C/Fe]$  vs  $[Fe/H]$  density maps for Pop III descendants which have been only enriched by Pop III SNe and which have also been partially enriched by normal Pop II stars. First, let's start by inspecting the chemical abundances of an ISM solely imprinted by Pop III stars (first column of Fig. 8.6). The C element is particularly informative because it is sensitive to the mass and explosion energy of Pop III stars. In the first four rows of Fig. 8.6 we show the chemical enrichment of an ISM imprinted by Pop III stars in the mass range  $[10 - 100]M_{\odot}$  (faint SN, core-collapse or CC SN, high-energy or HE SN, and hypernovae) and in the bottom row by PISN, with  $[140 - 260]M_{\odot}$  and  $E_{SN} \in [10^{52}; 10^{53}]$  erg. By inspecting Fig. 8.6 we notice that high-energy SNe and hypernovae (rows 3 and 4) pollute the ISM with large quantities of Fe. The abundances of their descendants are, therefore, peaked at relatively high  $[Fe/H] > -4$  and  $[C/Fe] \in (-1, 0)$ . The descendants of high-energy SNe also have very small (but non-zero) chances for being C-enhanced. Thus, high-energy SNe and hypernovae alone cannot reproduce all the chemical abundances observed in metal-poor halo stars. On the other hand, the second generation stars formed from the ejecta of faint SNe, CC SNe, and PISN span  $-8 \lesssim [Fe/H] \lesssim -1$ , and can, therefore, reproduce the iron abundances of all the literature halo sample. Furthermore, they cover a wide range of  $-1 \lesssim [C/Fe] \lesssim +5$ . The peaks of the  $[Fe/H]$  and  $[C/Fe]$  distributions are, however, located at different values for different progenitors. The faint SNe descendants show a prominent peak at  $[Fe/H] \approx -7$  and  $[C/Fe] \approx +3.5$ ; the CC SNe descendants are more equally distributed in the whole  $[Fe/H]$  and  $[C/Fe]$  range, showing different peaks at both low and high  $[C/Fe]$ ; while PISN descendants have the strongest peak at  $[Fe/H] > -2$  and  $[C/Fe] < 0$ . The  $[C/Fe]$  values of the second generation stars strongly depend on the mass of the Pop III progenitor. For a fixed mixing parameter,  $f_{mix}$ , when the progenitor star explodes as a faint or CC SN, the descendants of the *most massive* Pop III stars show the *highest values* of  $[C/Fe]$  (and  $[O/Fe]$ ,  $[Mg/Fe]$  (see Fig.6 in Vanni et al. 2023)). If, on the other hand, it explodes as a PISN, this trend is the opposite; the more massive is the progenitor, the lower are the  $[C, O, Mg/Fe]$  values of the descendants. Yet, if we vary the mixing efficiency, this relation between the progenitor masses and the  $[C/Fe]$  values of the descendants is not straightforward. Indeed, depending on the mixing efficiency, we find that descendants of progenitors with different masses can have the same  $[C/Fe]$  values. We can therefore conclude that the metal-poor Milky Way halo stars with  $[C/Fe] > +2.5$  agree with the chemical abundances predicted for the descendants of Pop III low-energy SNe, which are also predicted to imprint the ISM with an over-abundance of other light elements:  $[O/Fe] > +2$ ,  $[Mg/Fe] > +1.8$ ,  $[Si/Fe] > +1.8$ . The carbon abundances of these CEMP-no halo stars also agree with the descendants of the least massive PISN,  $m_{*} = 140M_{\odot}$ .

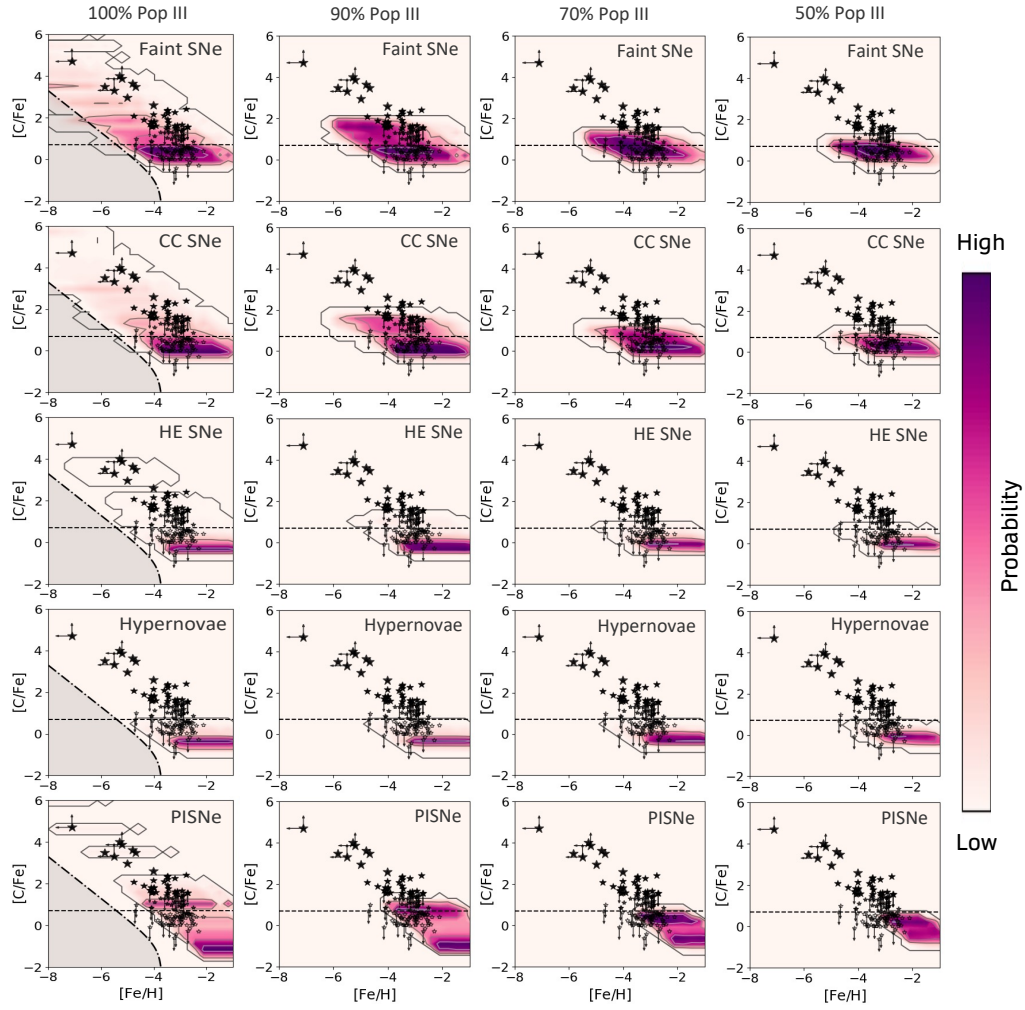


Figure 8.6: Density map of the predicted ISM  $[C/Fe]$  abundance ratios as a function of  $[Fe/H]$  with different Pop III enrichment level: 100%, 90% , 70%, 50%. Explosion energies of Pop III stars increase from top to bottom. The results obtained with the two sets of Pop II yields are shown together (Woosley & Weaver, 1995; Limongi & Chieffi, 2018). Star symbols are observed chemical abundances of CEMP-no (filled, the sizes are proportional to the  $[C/Fe]$  values) and C-normal (open) halo star. The dash-dotted line in the  $[C/Fe]$  diagrams is at  $Z_{ISM} = Z_{cr}$ .

However, this doesn't hold for the abundances of the other chemical elements.

At  $[C/Fe] < +2.5$ , the abundances of the metal-poor halo stars are also consistent with being the descendants of Pop III stars exploding as more energetic SNe  $[10 - 100] M_{\odot}$ , with  $E_{SN}$  up to  $10^{52}$  erg, but not of PISN. However, determining the progenitors of moderately C-enhanced and C-normal metal-poor halo stars is complicated by possible contribution of Pop II stars. From the first column of Fig. 8.6 it is evident that, independent of the explosion energy (and progenitor mass), the metals yielded by individual Pop III SNe typically enable the ISM to reach  $Z_{ISM} \geq Z_{cr}$ , which implies that long-lived Pop II second-generation stars can form in these environments but also that massive Pop II stars can start contributing to the ISM enrichment.

For increasing Pop II contribution to the chemical enrichment (columns from two to four in Fig.8.6),  $[Fe/H]$  increases while  $[C/Fe]$  decreases, moving towards the abundances of the C-normal stars. As shown in Fig. 8.6 (second column), a small relative enrichment of 10% from Pop II stars is enough to limit the maximum  $[C/Fe] \lesssim +2.5$ , even in environments predominantly imprinted by low-energy Pop III SNe. This strongly suggests that halo stars with  $[C/Fe] \gtrsim +2.5$  have been enriched *only* by low-energy Pop III stars, and are thus true second generation stars. Indeed, their extreme C-enhancement cannot be reproduced with any contribution ( $\geq 10\%$ ) of Pop II stars, or higher energy Pop III SN, the only exception being PISN with the lowest mass which however do not produce the other observed abundance ratios. On the other hand, we can reproduce the halo stars with  $[C/Fe] \lesssim +2.5$  with products of low-energy Pop III SNe and a  $\geq 10\%$  pollution from Pop II stars. In particular, from Fig. 8.6 it is evident that the probability of producing a C-enhanced ISM with the products of low-energy Pop III SNe decreases as the contribution of Pop II stars to the chemical pollution increases. We also see that high-energy Pop III SNe can, with small probability, imprint the ISM up to  $[C/Fe] \approx +1.5$  if the contribution of Pop II stars is  $\lesssim 10\%$ . The same is true for PISN enrichment but in this case it is limited to  $[Fe/H] \geq -4$ . Finally, we note that gaseous environments predominantly imprinted by Pop III hypernovae cover a broad iron range,  $[Fe/H] \geq -4.5$  but always have  $[C/Fe] < +0.7$ , regardless of the Pop II contribution.

Based on the  $[C/Fe]$  abundance ratio, we can only conclude that the most C-enhanced halo stars are true second generation stars. On the other hand, the CEMP-no stars with  $[C/Fe] < +2.5$  could be polluted by Pop III stars exploding with different energies and Pop II stars at different levels. Thus, we need to investigate the imprint of the first stars also with heavier chemical elements.

### 8.4.3 Other chemical elements

In Fig. 8.7 we show the predicted range of  $[X/Fe]$  vs  $[Fe/H]$  for the  $\alpha$ -elements O, Mg and Si, with varying Pop III contribution (from 100% down to 50%), and for increasing explosion energy of Pop III SNe (top to bottom rows). In general, the predicted abundance ratios for elements lighter than Ca follow a similar trend to  $[C/Fe]$ , i.e. the maximum  $[X/Fe]$  values decrease as the Pop II contribution increases, moving towards the abundances of C-normal stars. Most of the highly C-enhanced halo stars ( $[C/Fe] > +2.5$ , largest points in Figs. 8.7) also have high values of  $[O, Mg, Si/Fe]$  and these enhancements agree only with 100% enrichment from Pop III SNe, either faint, core-collapse or high-energy SNe. On the other hand, we predict too high  $[Al/Fe]$  values for the highly C-enhanced stars. The highly C-enhanced stars of our literature sample also show high  $[Zn/Fe]$  values ( $\gtrsim 0.8$ ), though there is only one star with a  $[Zn/Fe]$  measurement (Ezzeddine et al., 2019) while for the other there exist only upper limits. Our predictions for faint, core-collapse, and high-energy SNe descendants are therefore consistent with the  $[Zn/Fe]$  values of the highly C-enhanced halo stars. To conclude, the abundance ratios of the descendants shown in Figs. 8.7, confirm that the most C-enhanced and Fe-poor halo stars have been most likely imprinted by a single or few Pop III low-energy SNe ( $E_{SN} < 3 \times 10^{51}$  erg). The C-enhanced stars with  $[C/Fe] \leq +2.5$  have  $[O, Mg, Si, Al, Ca/Fe]$  values in agreement with the descendants of Pop III SNe, either faint, core-collapse or high-energy, with a contribution from Pop III stars down to 70%, for the ones with  $[C/Fe] > +1.5$ , and down to 50%, for the ones with  $[C/Fe] \leq +1.5$ . To conclude, while the progenitors of the most C-enhanced stars are likely single or few massive primordial SNe, the abundances of moderately C-enhanced ( $[C/Fe] \lesssim +2.5$ ) and C-normal stars are consistent with both the enrichment from primordial Pop III SNe and/or from a subsequent generation of Pop II stars.

### 8.4.4 The complete abundance pattern

In the previous Sections we investigated how a single Pop III star pollutes with its chemical products the ISM in which it explodes and how the resulting chemical abundances change with the Pop II contribution. Our results show that C-normal environments (or stars) can be either imprinted by single Pop III SNe or predominantly polluted by normal Pop II stars. Here we aim at discriminating among these two possibilities by exploiting all the different chemical elements measured. In Fig. 8.8, we show the mean chemical abundance patterns of all predicted Pop III 100% and 50% descendant stars, distinguishing between the CEMP-no ones with  $[Fe/H] \in [-7.5; -4]$  (top left) and  $\in (-4; -2]$  (top right) and the C-normal ones with  $[Fe/H] \in (-4; -2]$  (bottom right). For the CEMP-no



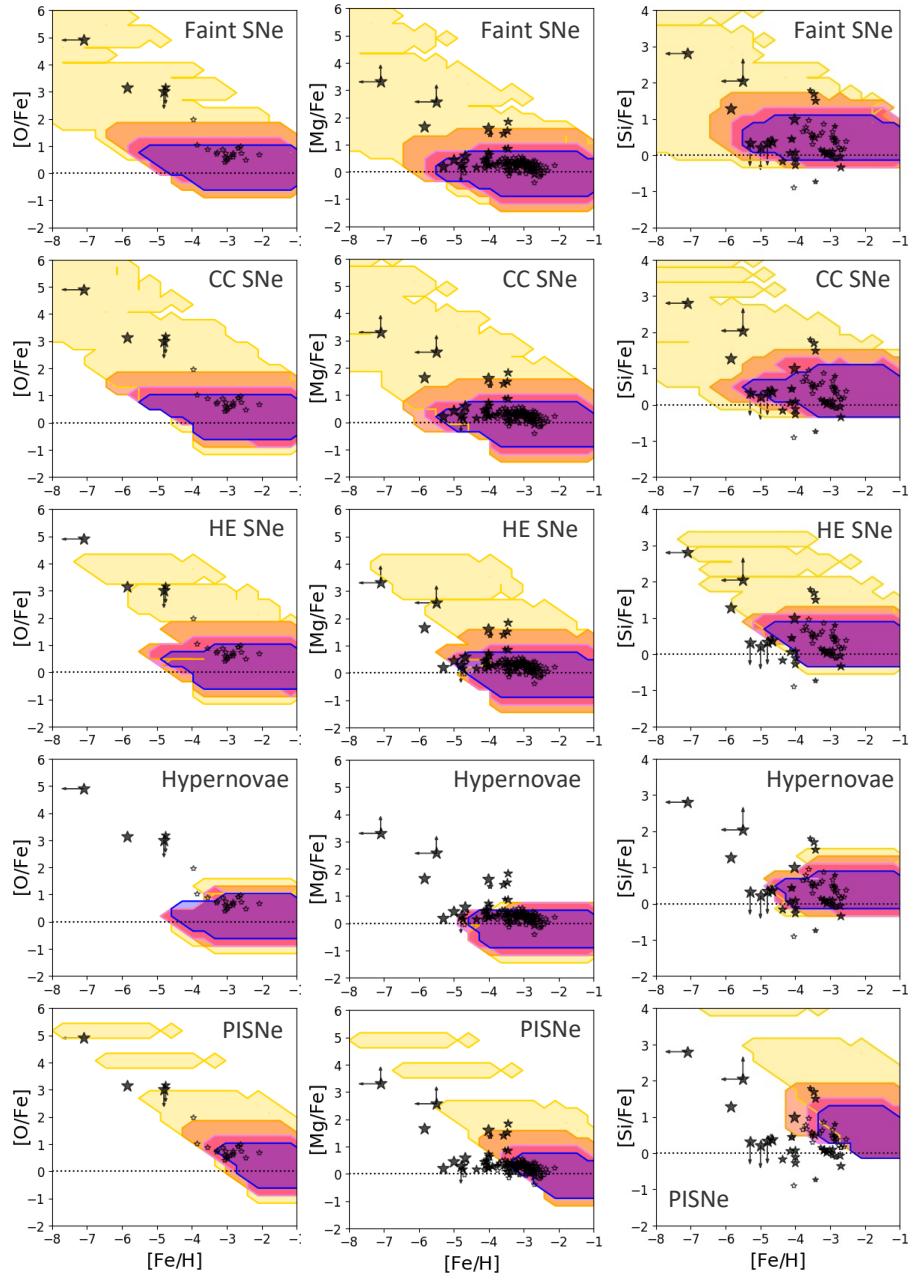


Figure 8.7: Predicted ISM abundance ratios  $[X/Fe]$  vs.  $[Fe/H]$ , for the elements O, Mg, and Si, after the explosion of Pop III and Pop II SNe. Colored areas show different Pop III contribution to the chemical enrichment: 100% (yellow), 90% (orange), 70% (magenta) and 50% (purple). The explosion energy of Pop III stars increases from top to bottom rows. Star symbols are observed chemical abundances of CEMP-no (filled, the sizes are proportional to the  $[C/Fe]$  values) and C-normal (open) halo star.

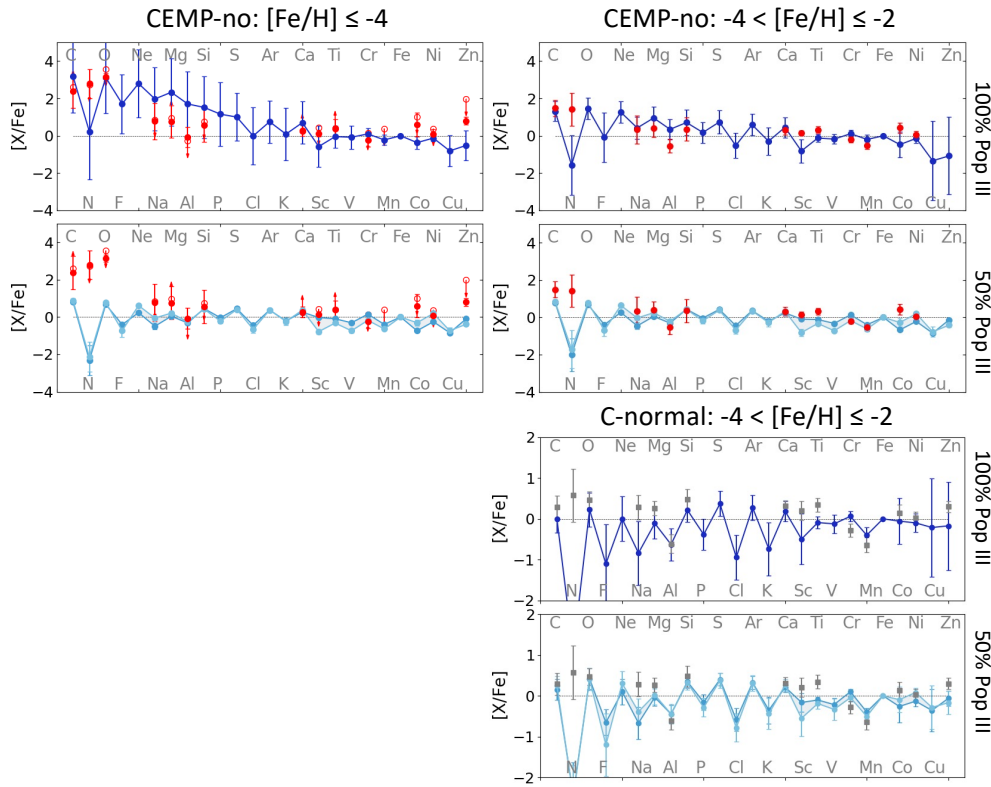


Figure 8.8: Mean chemical abundance patterns for our models (blue) with the 100% and 50% contribution from Pop III stars that predict: CEMP-no descendants with  $-7.5 \leq [\text{Fe}/\text{H}] \leq -4$  (top left); CEMP-no descendants with  $-4 < [\text{Fe}/\text{H}] \leq -2$  (top right); C-normal descendants with  $-4 < [\text{Fe}/\text{H}] \leq -2$  (bottom right); compared with the mean measured abundances of CEMP-no stars (red) and C-normal stars (grey). Blue error bars are the standard deviation between models. For  $f_{\text{PopIII}} = 50\%$  the abundance patterns are calculated using both PopII yields from Woosley & Weaver (1995) (darker blue) and Limongi & Chieffi (2018) (lighter blue). The coloured area between them represents an intrinsic uncertainty due to the choice of the Pop II yields.

stars in the top left of Fig. 8.8, the predicted abundance ratios,  $[X/\text{Fe}]$ , of elements lighter than Ca decrease with increasing Pop II contribution. The average  $[\text{Cu}/\text{Fe}]$  and  $[\text{Zn}/\text{Fe}]$  increase as the contribution from Pop II stars increase. This effect is mainly due to the fact that the most copper- and zinc-deficient descendants, which are the ones enriched by primordial PISN, become C-normal when we add the contribution from Pop II stars and do not contribute anymore to the average abundance pattern of CEMP-no descendants. On the contrary, the abundances of C-normal descendant stars (bottom panels of Fig. 8.8) do not change significantly with an increasing Pop II contribution. In all the cases depicted in Fig. 8.8, the standard deviation of the predicted chemical abundances is significantly reduced when the Pop II contribution increases. Note that our models always underestimate the  $[\text{N}/\text{Fe}]$  ratio. This is partly due to the fact that PISN ejecta present a strong odd-even effect, always producing  $[\text{N}/\text{Fe}] \leq 0$  in the ISM (see Salvadori

et al. 2019), and partly due to the difficulty of modeling the nucleosynthesis of N in the stars. At the lowest  $[\text{Fe}/\text{H}] \leq -4$ , the measured abundances of CEMP-no stars are only consistent with theoretical predictions of 100% Pop III contribution. CEMP-no stars with  $-4 < [\text{Fe}/\text{H}] < -2$ , on the other hand, have chemical abundances that are consistent with either being second generation stars, or having Pop III enrichment at a  $\gtrsim 70\%$  level, with a partial Pop II pollution. Our model overestimates the  $[\text{Mg}/\text{Fe}]$  and  $[\text{Al}/\text{Fe}]$  ratios, relative to observations, but when non-LTE corrections are applied, this discrepancy is expected to disappear. The predicted  $[\text{Zn}/\text{Fe}]$  average is lower than the observed one. Indeed, the yields of normal SNe are not able to reproduce the observed high  $[\text{Zn}/\text{Fe}]$  values and, moreover, the abundances of PISN descendants, which have  $[\text{Zn}/\text{Fe}] \ll 0$ , strongly lower the average  $[\text{Zn}/\text{Fe}]$ . However, the average observed  $[\text{Zn}/\text{Fe}]$ , is an upper limit and there is only one finite measurement, which is just at the edge of the values predicted by our model. The measured chemical abundances of the C-normal stars in the range  $[\text{Fe}/\text{H}] \in (-4; -2]$ , on the other hand, agree with our predictions for the descendants enriched by Pop III stars at a  $\gtrsim 50\%$  level. However, if the birth environments of C-normal descendants are predominantly ( $> 50\%$ ) polluted by Pop III stars, the predicted scatter is higher than what is observed in C-normal stars. Furthermore, the agreement between the average and the observed abundances is better for some elements, C, O, Sc, Co and Zn, with a contribution of Pop II stars at the  $\sim 50\%$  level. For C-normal descendants we predict a lower  $[\text{Na}/\text{Fe}]$  average, but the non-LTE corrections should lower the observed abundances. Finally, we predict a smaller  $[\text{Ti}/\text{Fe}]$  with respect to the observed one. Ti is lightly affected by non-LTE effects, and in general the stellar evolution models underestimate it.

#### 8.4.5 The star-to-star scatter

The last and most conclusive result of our work concerns how the maximum scatter in abundance ratios is dependent on the relative pollution from Pop III stars,  $f_{\text{PopIII}}$ . In Fig. 8.9 we show the predicted dispersion of  $[\text{C}/\text{Fe}]$  and  $[\text{Mg}/\text{Fe}]$  with respect to  $f_{\text{PopIII}}$ . The pure Pop III descendants,  $f_{\text{PopIII}} = 100\%$ , show a dispersion  $> 5$  dex in the abundance ratios  $[\text{C}/\text{Fe}]$  and  $[\text{Mg}/\text{Fe}]$ , as well as in the other chemical elements lighter than Ca. These abundance ratios are very dependent on the mass, SNe explosion energy, and mixing efficiency of the progenitor, and therefore vary over a wide range of values. As Pop II stars contribute more to the pollution of the ISM, they wash out the diverse chemical peculiarities of the different primordial progenitors and the dispersion between different descendants is reduced. Finally, when the contribution from Pop III stars is negligible (Pop II only case), the abundances of the descendants almost correspond to the solar values. To conclude, with our model, we predict that the scatter in  $[\text{C}/\text{Fe}]$  and

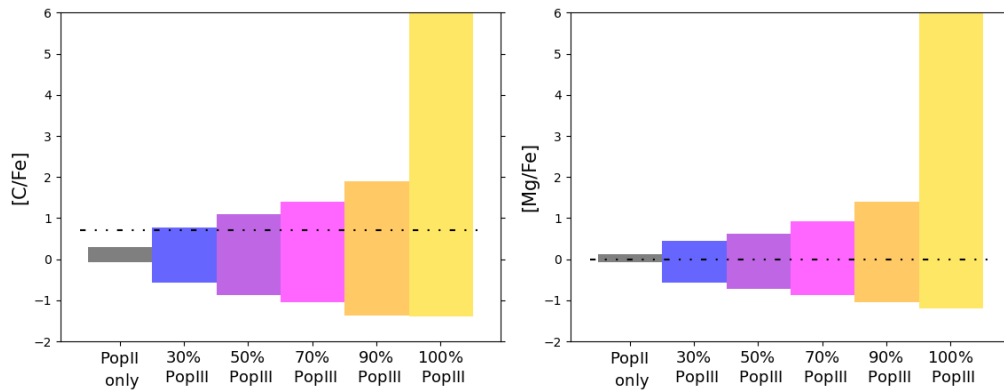


Figure 8.9: Maximum extent of the abundance ratios  $[C/Fe]$  (left) and  $[Mg/Fe]$  (right) for Pop III descendant stars as a function of relative Pop III pollution. Coloured areas represent different levels of enrichment from Pop III stars,  $f_{\text{PopIII}}$ : 100% (yellow), 90% (orange), 70% (magenta), 50% (purple), 30% (indigo), and only Pop II stars (grey). The dash-dotted lines correspond to  $[C/Fe] = +0.7$  (left) and  $[Mg/Fe] = 0$  (right).

$[Mg/Fe]$  ratios is maximum for Pop III only enriched environments and that it decreases as the contamination from Pop II stars increases.

#### 8.4.6 Conclusions

Here we aim at finding the peculiar chemical imprints left by the first stars and to determine the real descendants of Pop III stars, i.e. if 50% of their metals are produced by Pop III stars, by exploiting the parametric model developed by Salvadori et al. (2019), and further improved and extended by Vanni et al. (2023). Our main conclusions are:

- The most C-enhanced ( $[C/Fe] > +2.5$ ) halo stars have chemical abundances that agree with an imprint from only one primordial Pop III star exploding with low energy ( $< 2 \times 10^{51}$  erg).
- C-enhanced metal-poor halo stars with  $+0.7 < [C/Fe] < +2.5$  are likely born in environments polluted by both Pop III and Pop II stars where Pop III stars provided  $\geq 50\%$  of the total amount of metals.
- C-normal metal-poor halo stars have probably been imprinted mainly by Pop II SNe, which provided  $\geq 50\%$  of the total metals amount of their birth places. However, we might also find C-normal metal-poor stars which are pure descendants of the most energetic Pop III SNe (hypernovae and PISN) with peculiar and outlier abundance patterns.
- A key diagnostic employed to understand the origin of C-normal stars is the dispersion between the chemical abundances predicted by different models and its

variation with respect to the pollution level from Pop II stars. Indeed, the scatter between the abundances of different descendants decreases as the contribution of Pop II stars to the metal pollution increases.



---



---

## Conclusions

In this Thesis I have investigated how to unveil the nature of the first (Pop III) stars by exploiting the spectroscopic studies of ancient metal-poor stars in the Local Group, with a particular focus on Ultra-Faint Dwarf galaxies (UFDs). To this aim, I developed a novel theoretical model that follows the formation and chemical evolution (elements from carbon to zinc) of Boötes I, the best studied UFD galaxy. My physically driven model simultaneously accounts for the incomplete sampling of the IMF and the chemical enrichment of individual stars from different sources: supernovae (SNe) and asymptotic giant branch (AGB) stars, both from Pop III and subsequent normal Pop II stellar populations. With my innovative approach, I compared observations of UFDs with my model results, and provided new and vital constraints on the elusive properties of the first stars. By exploring different ancient and metal-poor environments such as the Galactic bulge and the halo, thereby even further constraints have been given on the unknown characteristics of the first stars. I will here go through the foremost results of the works I have carried out as leading author and co-author during my Ph.D. and their main implications.

### 9.1 Results of my work

#### IMF random sampling

The Initial Mass Function (IMF) describes the mass distribution of stars at birth. In my work I showed that the random sampling of the IMF plays a crucial role in driving the evolution of poorly star-forming,  $\langle \Psi \rangle \lesssim 10^{-3} \text{ M}_{\odot} \text{ yr}^{-1}$ , systems like UFD galaxies with star-formation rate, in which the assumption to fully populate the stellar IMF breaks down. By comparing the theoretical IMF and the effective one, resulting from the Monte Carlo procedure, I showed that the lower is  $\Psi$ , the worse is the sampling of the theoretical IMF, in particular at the high-mass end. Furthermore, the overall star-formation rate,  $\Psi$ , is so low in these small systems, that when the IMF is shifted towards higher

characteristic masses,  $m_{ch} \geq 1 M_{\odot}$ , only a few stars around the peak can form. In those cases, the IMF is poorly populated both at high and low masses. Thus, my findings clearly demonstrated that to study UFDs, it is fundamental to model the incomplete IMF sampling, which not only affects Pop III star formation but also “normal” Pop II/I stars. The IMF random sampling affects the global properties of Boötes I, however its impact is even more evident on *the fraction of Pop III star survivors*: for a Larson type Pop III IMF with  $m_{ch} = 0.35 M_{\odot}$  in the mass range  $[0.1 - 100] M_{\odot}$ , it increases by a factor of  $\sim 3$  with respect to the model in which we assumed to fully populate the IMF. Accounting for the random IMF sampling is therefore fundamental when studying the first stars in UFDs.

### The fraction of long-lived Pop III stars

Theoretical models predict the formation of low-mass long-lived Pop III stars. If Pop III stars with  $m_{\star} \leq 0.8 M_{\odot}$  were able to form, they should survive until today as living relics of the first star and they should be observable in the most ancient and metal-poor environments, such as UFDs. However truly zero-metallicity stars have so far escaped detection. The non-detection of Pop III stars in UFDs can be used to constrain the IMF of the first stars by means of a statistical comparison between the available data and predictions from chemical evolution models. First, I explored how my results depend on the assumed Pop III IMF and its lower-mass limit. My results show that the assumed Pop III IMF does not affect the global properties of Boötes I, since the bulk of its stellar populations has been predominantly imprinted by subsequent generations of Pop II stars. On the other hand, the expected number of surviving Pop III stars strongly depends on both the shape, the characteristic mass,  $m_{ch}$ , and the minimum mass,  $m_{min}$ , of the first stars IMF. The higher is the characteristic mass,  $m_{ch}$ , the lower is the number of expected Pop III star survivors. For  $m_{ch} = 0.35 M_{\odot}$ , the fraction of Pop III stars at  $z = 0$  strongly depends on  $m_{min}$ : it decreases from 12% ( $m_{min} = 0.1 M_{\odot}$ ) to 7% ( $m_{min} = 0.8 M_{\odot}$ ). On the other hand, for  $m_{ch} > 1 M_{\odot}$  and for a Flat IMF the number of expected Pop III star survivors is very low ( $< 0.5\%$ ) and roughly independent of  $m_{min}$ . Moreover, the fraction of zero-metallicity stars survivors is not significantly affected by the choice of Pop III maximum mass ( $m_{max} = [100/1000] M_{\odot}$ ).



## Color-Magnitude Diagram (CMD)

Even if Pop III stars with  $m_{\star} \leq 0.8 M_{\odot}$  were able to form and survive until now, that does not necessarily imply that they are bright enough to be observed in distant UFD satellites, therefore to quantify and identify Pop III stars that are bright enough to be detectable, *color-magnitude diagrams (CMD) are required*. The simulated Boötes I CMD shows a clear general trend of stellar mass and luminosity, i.e. the smaller is  $m_{\star}$ , the fainter is the star. Our results reveal that, at the moment, we are only able to measure chemical abundance in the more massive, and therefore more luminous stars,  $m_{\star} \geq 0.7 M_{\odot}$ . Moreover, to catch potential zero-metallicity stars with  $m_{\star} = 0.1 M_{\odot}$ , observations should reach an extremely deep magnitude,  $i = 32$ . Therefore, very low-mass Pop III stars, if they ever existed, will be invisible even for future generation telescopes such as ELT. Simulating the Boötes I CMD has proved to be essential to identify and quantify the Pop III star survivors that are truly observable.

## Constraining the low-mass end of the first stars

My novel approach of connecting model results with real data through synthesizing the CMD of Boötes I, allows me to put constraints on the minimum mass,  $m_{min}$ , and the shape,  $m_{ch}$ , of the Pop III IMF. By exploiting the 96 stars with measured metallicities ( $i < 19$ ) in the UFDs represented by my model (Boötes I, Hercules, LeoIV, Eridanus II), I demonstrated that:  $m_{ch} > 1 M_{\odot}$  or  $m_{min} > 0.8 M_{\odot}$  at 99% confidence level. Thus, I proved that Pop III stars were typically *more massive* than those that form today, and the mass distribution of the first stars was fundamentally different from stars at later times. Finally, I predicted that by targeting the four UFDs Boötes I, Hercules, Leo IV, and Eridanus II with future instruments (such as MOSAIC on the ELT), it will be possible to collect a sample of  $>10\,000$  stars. If the non-detection of metal-free stars will be persistent, I will be able to limit  $m_{min} > 0.8 M_{\odot}$  independent of the Pop III IMF at the 68% confidence level.

## Pop III descendants

Massive Pop III stars are expected to evolve as SNe, disappearing from the Universe only a few Myrs after their formation. The chemical signatures of Pop III SNe can be found in low-mass second generation stars, the so called Pop III “descendants”, that are still alive. I present a unique way to identify the true Pop III descendants, exploiting A(C) and [C/Fe] as key diagnostics. The probability to find stars imprinted by first Pop III SNe increases toward lower value of [Fe/H], and it is maximum for  $A(C) \leq 6$  and

$[\text{Fe}/\text{H}] \lesssim -3.5$ . My results show that Boötes I is an ideal environment to find the chemical fingerprints of Pop III SNe with progenitors masses  $[10 - 100] M_{\odot}$ . These peculiar signatures arise among both *Carbon-Enhanced Metal Poor (CEMP)* stars and *C-normal* stars: carbon-enhanced Pop III imprinted stars are predicted to have  $A(\text{C}) \lesssim 6$  and  $[\text{Fe}/\text{H}] \lesssim -3.5$  while C-normal stars imprinted by Pop III SNe have  $[\text{C}/\text{Fe}] < 0$ . and  $[\text{Fe}/\text{H}] \gtrsim -3.5$ .

### Carbon-Enhanced Metal Poor (CEMP) stars

The origin of CEMP stars and their connection with the chemical elements injected by Pop III SNe with different energies was explored. For the first time, I show that carbon-enhanced stars purely imprinted by Pop III SNe are located in a specific region of  $A(\text{C})$ - $[\text{Fe}/\text{H}]$  diagram:  $A(\text{C}) \lesssim 6$  and  $[\text{Fe}/\text{H}] \lesssim -3.5$ . I went deep into understanding the origin of Pop III star descendants, exploring the *type* of SNe that enriched their birth cloud. I proved that CEMP stars imprinted by the first stars have Pop III progenitors with different energy: *faint*, *core-collapse* and *high-energy* SNe. I identified a star in Boötes I purely imprinted by *faint* Pop III (100% of metals from its birth cloud).

### Carbon-normal stars

Towards higher  $[\text{Fe}/\text{H}]$  values, the detection of stars imprinted by Pop III SNe is challenging due to the increasing chemical contamination by normal Pop II stars. However, I demonstrated that the rare descendants of more energetic Pop III SNe, like *hypernovae*, can be preferentially found among C-normal stars with  $A(\text{C}) \lesssim 5$  and  $[\text{Fe}/\text{H}] > -4$ . In particular at  $[\text{C}/\text{Fe}] \lesssim 0$  and  $[\text{Fe}/\text{H}] > -4$ , the chemical signatures of hypernovae became visible and I identified a star, Boo-991 (Ishigaki et al. 2014), whose measured abundance pattern is consistent with a 95% enrichment by the first stars, in particular  $\sim 84\%$  by Pop III hypernovae and  $\sim 13\%$  by high-energy Pop III SNe.

### The missing PISN descendants in UFDs

The descendants of very massive,  $m_{\star} = [140 - 260] M_{\odot}$ , Pop III stars that end their lives as energetic Pair Instability Supernovae (PISN), are predicted to appear at high metallicities,  $-4 \leq [\text{Fe}/\text{H}] \leq -1$  (Karlsson et al. 2008; Salvadori et al. 2019). Pure PISN descendants are predicted to be uncommon, representing  $< 0.1\%$  of Milky Way stars (de Bressana et al., 2017). My results showed that the chemical signatures of massive PISN are even more rare in UFDs: among Pop III star descendants, only  $< 0.01\%$  of the total stars in Boötes I are predicted to be predominantly enriched (at level higher than

75%) by PISN. The “*missing PISN descendants problem*” can be explained by considering the intrinsic properties of UFDs: low star-formation rates and low binding energies. At low star formation rates,  $\langle \Psi \rangle \lesssim 10^{-3} \text{ M}_{\odot} \text{ yr}^{-1}$ , the stochastic Pop III IMF sampling produces an effective IMF poorly populated at high masses ( $m_{*} > 100 \text{ M}_{\odot}$ ), leading to the formation at most one Pop III star within the mass range of PISN. On the other hand, due to the low binding energy of UFDs, the chemical products of massive and energetic PISN ( $E_{\text{SN}} \geq 10^{52} \text{ erg}$ ) are easily evacuated out of the galaxy, making it challenging to form direct PISN descendants. These results suggest that pure PISN descendants should be searched for in more massive and therefore more luminous environments like classical dwarfs galaxies or the *Galactic bulge*.

### The Galactic bulge

The Galactic bulge is predicted to host the oldest stars, but it shows a striking dearth of CEMP stars with  $[\text{C}/\text{Fe}] \gtrsim +2.0$ , compared with the Galactic halo. We explored the possible reasons for this anomaly by performing a statistical analysis of the observations of metal-poor stars in combination with predictions of  $\Lambda$ CDM models. We showed that the dearth of CEMP stars with high  $[\text{C}/\text{Fe}]$  is the result of the different formation process of the bulge compared with the halo and UFDs.  $N$ -body simulations showed that the first star-forming halos which end up in the bulge are characterized by the highest star-formation rates. These rates enable the formation of rare massive first stars exploding as PISN, which wash out the signature of primordial faint supernovae. Furthermore, the higher binding energy of these progenitors enable to retain the chemical products of PISN. We demonstrated that the mean  $[\text{C}/\text{Fe}]$  in environments polluted by Pop III stars decreases with the increasing contribution of PISN. We concluded that the dearth of CEMP stars in the Galactic bulge indirectly probes the existence of elusive PISN, and propose a novel method which exploits this to constrain the mass distribution of the first stars.

### The Galactic halo

Within our Galaxy, the halo of the Milky Way stands out as the most ancient and metal-poor environment. It is therefore an ideal place to study the chemical signatures left by Pop III stars, and thus constrain their properties. By exploiting the new data-calibrated semi-analytic model based on a  $N$ -body simulation, NEFERTITI (Koutsouridou et al. 2023), that traces the formation and evolution of individual Pop III and Pop II/I stars, we explored the unknown properties of Pop III stars such as their Energy Distribution Function (EDF). By comparing our model predictions to observations of very metal poor stars in the Galactic halo we provided the first available constraints on the EDF,

$dN/dE_* \propto E_*^{-\alpha_e}$  with  $1 \leq \alpha_e \leq 2.5$ . Moreover, our results suggested that the characteristic mass of the Pop III IMF should be  $m_{\text{ch}} < 100 M_\odot$ . Independent of the assumed Pop III properties, we find that all stars with  $[\text{C}/\text{Fe}] > +0.7$  (at  $[\text{Fe}/\text{H}] < -2.8$ ) have been enriched by Pop III supernovae at a  $> 20\%$  level, and stars with  $[\text{C}/\text{Fe}] > +2$  at a  $> 95\%$  level. Finally, we showed that all very metal-poor stars with  $[\text{C}/\text{Fe}] < 0$  are predicted to be predominantly enriched by Pop III hypernovae and/or PISN.

## 9.2 A look to the future

The results of this Thesis show the progresses that has been made in understanding the nature of the first stars by exploiting the current spectroscopic observations of the metal-poor stars in our Galaxy and its dwarf satellite galaxies. Among ancient and most metal-poor environments, Ultra Faint Dwarf galaxies (UFDs) have been proven to be compelling laboratories to constrain the unknown properties of Pop III stars. In particular, I demonstrated that these living relics of the first star-forming mini-halos are the ideal environments to put limits on the low-mass end of the mass distribution of the first stars, and to discover the key chemical signatures of the first SNe. Moreover, UFDs allow to make testable predictions for future surveys to uniquely detect the direct descendants of Pop III stars and finally put constraints on their Initial Mass Function (IMF). Additional constraints on the first generation of stars can be obtained by exploring different ancient and metal-poor environments of our Milky Way, such as the Galactic bulge and the halo. Combining the constrains that arise from these different environments I showed how to further limit the shape of the Pop III IMF and the energy distribution of the first SNe. Currently, the limited observational data sample do not allow to give tighter constraints on the properties of the Pop III star. Therefore a global understanding on the IMF of the first stars and on the properties their SNe is still missing. Now we are entering an exciting era of deep spectroscopic surveys such as WEAVE and 4MOST, including 4DWARFS, (Skúladóttir et al. 2023b), of which I am one of the core co-investigators, and the new J-PLUS (Cenarro et al. 2019) and S-PLUS (de Oliveira et al. 2019) photometric surveys, that will very soon provide chemical information for 100s of millions of stars. These surveys will increase the number of stars with measured chemical abundances in the Local Group by orders of magnitude, and will shed light on the elusive signatures of the first stars. Using in synergy observational data and theoretical models, and by exploiting methods that I have developed during my Ph.D, we will finally be able to reveal the intriguing secrets of the first stars.

---

## Bibliography

- Abate C., Pols O. R., Izzard R. G., Karakas A. I., 2015, *VizieR Online Data Catalog*, pp J/A+A/581/A22
- Abel T., Bryan G. L., Norman M. L., 2001, *science*, 295, 93
- Abel T., Bryan G. L., Norman M. L., 2002, *Science*, 295, 93
- Abohalima A., Frebel A., 2018, *The Astrophysical Journal Supplement Series*, 238, 36
- Aguado D. S., Prieto C. A., Hernández J. I. G., Rebolo R., 2018a, *The Astrophysical Journal Letters*, 854, L34
- Aguado D. S., Prieto C. A., Hernández J. I. G., Rebolo R., 2018b, *The Astrophysical Journal Letters*, 854, L34
- Aguado D. S., Prieto C. A., Hernández J. I. G., Rebolo R., 2018c, *The Astrophysical Journal Letters*, 854, L34
- Aguado D. S., González Hernández J. I., Allende Prieto C., Rebolo R., 2019, *ApJL*, 874, L21
- Aguado D. S., et al., 2022, *A&A*, 668, A86
- Aguado D. S., et al., 2023, *A&A*, 669, L4
- Amarsi A. M., Grevesse N., Asplund M., Collet R., 2021, *A&A*, 656, A113
- Aoki W., Beers T. C., Christlieb N., Norris J. E., Ryan S. G., Tsangarides S., 2007, *The Astrophysical Journal*, 655, 492
- Aoki W., Tominaga N., Beers T., Honda S., Lee Y., 2014, *Science*, 345, 912
- Applebaum E., Brooks A. M., Quinn T. R., Christensen C. R., 2018, *arXiv preprint arXiv:1811.00022*
- Arentsen A., et al., 2020, *MNRAS*, 491, L11
- Arentsen A., et al., 2021, *Monthly Notices of the Royal Astronomical Society*, 505, 1239

- Arentsen A., Placco V. M., Lee Y. S., Aguado D. S., Martin N. F., Starkenburg E., Yoon J., 2022, *MNRAS*, 515, 4082
- Asplund M., Grevesse N., Sauval A. J., Scott P., 2009, *ARA&A*, 47, 481
- Barkana R., Loeb A., 2001, *Physics reports*, 349, 125
- Battaglia G., Nipoti C., 2022, *Nature Astronomy*, 6, 659
- Battaglia G., et al., 2006, *VizieR Online Data Catalog*, 345
- Beers T. C., Christlieb N., 2005, *Annu. Rev. Astron. Astrophys.*, 43, 531
- Beers T. C., Preston G. W., Shectman S. A., 1985, *AJ*, 90, 2089
- Beers T. C., Preston G. W., Shectman S. A., 1992, *AJ*, 103, 1987
- Belokurov V., et al., 2006, *The Astrophysical Journal Letters*, 647, L111
- Bland-Hawthorn J., Sutherland R., Webster D., 2015, *ApJ*, 807, 154
- Bond J., Cole S., Efstathiou G., Kaiser N., 1991, *The Astrophysical Journal*, 379, 440
- Bonifacio P., et al., 2015, *Astronomy & Astrophysics*, 579, A28
- Bonifacio P., et al., 2018, *A&A*, 612, A65
- Bonifacio P., et al., 2019, *MNRAS*, 487, 3797
- Bonifacio P., et al., 2021, *aap*, 651, A79
- Bovill M. S., Ricotti M., 2009, *The Astrophysical Journal*, 693, 1859
- Bressan A., Marigo P., Girardi L., Salasnich B., Dal Cero C., Rubele S., Nanni A., 2012, *MNRAS*, 427, 127
- Bromm V., 2000, PhD thesis, Yale University, Connecticut
- Bromm V., Ferrara A., Coppi P., Larson R., 2001, *Monthly Notices of the Royal Astronomical Society*, 328, 969
- Bromm V., Coppi P. S., Larson R. B., 2002, *ApJ*, 564, 23
- Brown T. M., et al., 2014, *The Astrophysical Journal*, 796, 91
- Caffau E., et al., 2011a, *Messenger*, 146, 28
- Caffau E., et al., 2011b, *nature*, 477, 67
- Caffau E., et al., 2016, *Astronomy & Astrophysics*, 595, L6

- Cardelli J. A., Clayton G. C., Mathis J. S., 1989, *The Astrophysical Journal*, 345, 245
- Carigi L., Hernandez X., 2008, *Monthly Notices of the Royal Astronomical Society*, 390, 582
- Carroll S. M., 2001, *Living reviews in relativity*, 4, 1
- Cayrel R., et al., 2004, *A&A*, 416, 1117
- Cenarro A. J., et al., 2019, *A&A*, 622, A176
- Cescutti G., Matteucci F., 2011, *Astronomy & Astrophysics*, 525, A126
- Chiaki G., Yoshida N., 2022, *MNRAS*, 510, 5199
- Chiaki G., Tominaga N., Nozawa T., 2017, *Monthly Notices of the Royal Astronomical Society: Letters*, 472, L115
- Chiti A., Frebel A., Ji A. P., Jerjen H., Kim D., Norris J. E., 2018, *ApJ*, 857, 74
- Chiti A., et al., 2021, *Nature Astronomy*, pp 1–9
- Christlieb N., et al., 2002, *Nature*, 419, 904
- Christlieb N., Gustafsson B., Korn A. J., Barklem P. S., Beers T. C., Bessell M. S., Karlsson T., Mizuno-Wiedner M., 2004, *ApJ*, 603, 708
- Ciardi B., Ferrara A., Marri S., Raimondo G., 2001, *Monthly Notices of the Royal Astronomical Society*, 324, 381
- Clark P. C., Glover S. C., Smith R. J., Greif T. H., Klessen R. S., Bromm V., 2011, *Science*, 331, 1040
- Cooke R. J., Madau P., 2014, *ApJ*, 791, 116
- Diemand J., Madau P., Moore B., 2005a, *Monthly Notices of the Royal Astronomical Society*, 364, 367
- Diemand J., Moore B., Stadel J., 2005b, *Nature*, 433, 389
- Dopcke G., Glover S. C. O., Clark P. C., Klessen R. S., 2013, *ApJ*, 766, 103
- Evans C., et al., 2015, arXiv preprint arXiv:1501.04726
- Ezzeddine R., et al., 2019, *ApJ*, 876, 97
- Farmer R., Renzo M., de Mink S. E., Marchant P., Justham S., 2019, *ApJ*, 887, 53
- François P., et al., 2018, *A&A*, 619, A10

- Frebel A., 2010, *Astronomische Nachrichten*, 331, 474
- Frebel A., Norris J. E., 2015, *Annual Review of Astronomy and Astrophysics*, 53, 631
- Frebel A., et al., 2005, *Nature*, 434, 871
- Frebel A., Simon J. D., Kirby E. N., 2014, *The Astrophysical Journal*, 786, 74
- Frebel A., Chiti A., Ji A. P., Jacobson H. R., Placco V. M., 2015, *The Astrophysical Journal Letters*, 810, L27
- Frebel A., Norris J. E., Gilmore G., Wyse R. F., 2016, *The Astrophysical Journal*, 826, 110
- Gallart C., et al., 2021, arXiv e-prints, p. arXiv:2101.04464
- Gilmore G., Norris J. E., Monaco L., Yong D., Wyse R. F., Geisler D., 2013, *The Astrophysical Journal*, 763, 61
- Graziani L., Salvadori S., Schneider R., Kawata D., de Bressan M., Maselli A., 2015, *Monthly Notices of the Royal Astronomical Society*, 449, 3137
- Greif T. H., 2015, *Computational Astrophysics and Cosmology*, 2, 3
- Greif T., Springel V., White S., Glover S., Clark P., Smith R., Klessen R., Bromm V., 2011, arXiv preprint arXiv:1101.5491
- Hammer F., et al., 2014, in Ramsay S. K., McLean I. S., Takami H., eds, *Society of Photo-Optical Instrumentation Engineers (SPIE) Conference Series Vol. 9147, Ground-based and Airborne Instrumentation for Astronomy V*. p. 914727, doi:10.1117/12.2055148
- Hansen T., Hansen C. J., Christlieb N., Yong D., Beers T., Andersen J., 2015, arXiv preprint arXiv:1503.01990
- Hansen T. T., Andersen J., Nordström B., Beers T. C., Placco V. M., Yoon J., Buchhave L. A., 2016, *A&A*, 588, A3
- Hartwig T., Bromm V., Klessen R. S., Glover S. C., 2015, *Monthly Notices of the Royal Astronomical Society*, 447, 3892
- Hartwig T., et al., 2018, *MNRAS*, 478, 1795
- Heger A., Woosley S. E., 2002, *The Astrophysical Journal*, 567, 532
- Heger A., Woosley S. E., 2004, in *American Astronomical Society Meeting Abstracts #204*. p. 34.01
- Heger A., Woosley S. E., 2010, *ApJ*, 724, 341



- Hirano S., Hosokawa T., Yoshida N., Umeda H., Omukai K., Chiaki G., Yorke H. W., 2014, *The Astrophysical Journal*, 781, 60
- Hirano S., Hosokawa T., Yoshida N., Omukai K., Yorke H. W., 2015, *MNRAS*, 448, 568
- Hosokawa T., Omukai K., Yoshida N., Yorke H. W., 2011, *Science*, 334, 1250
- Howes L. M., 2016, PhD thesis, Australian National University, Canberra
- Howes L. M., et al., 2014, *Monthly Notices of the Royal Astronomical Society*, 445, 4241
- Howes L. M., et al., 2015, *Nature*, 527, 484
- Ishigaki M. N., Aoki W., Arimoto N., Okamoto S., 2014, *A&A*, 562, A146
- Ishigaki M. N., Tominaga N., Kobayashi C., Nomoto K., 2018, *The Astrophysical Journal*, 857, 46
- Iwamoto N., Umeda H., Tominaga N., Nomoto K., Maeda K., 2005, *Science*, 309, 451
- Jeon M., Bromm V., Besla G., Yoon J., Choi Y., 2021, *MNRAS*, 502, 1
- Ji A. P., Frebel A., Ezzeddine R., Casey A. R., 2016, *ApJL*, 832, L3
- Johnson J. L., Greif T. H., Bromm V., 2007, in *American Astronomical Society Meeting Abstracts*. p. 91.15
- Karlsson T., Johnson J. L., Bromm V., 2008, *ApJ*, 679, 6
- Keller S. C., et al., 2007, *Publ. Astr. Soc. Australia*, 24, 1
- Keller S., et al., 2014, *Nature*, 506, 463
- Kereš D., Katz N., Weinberg D. H., Davé 2005, *Monthly Notices of the Royal Astronomical Society*, 363, 2
- Kirby E. N., Martin C. L., Finlator K., 2011, *The Astrophysical Journal*, 742, L25
- Kirby E. N., Cohen J. G., Guhathakurta P., Cheng L., Bullock J. S., Gallazzi A., 2013, *The Astrophysical Journal*, 779, 102
- Klessen R., 2019, in , *Formation of the first black holes*. World Scientific, pp 67–97
- Klessen R. S., Glover S. C. O., 2023, arXiv e-prints, p. arXiv:2303.12500
- Klessen R. S., Krumholz M. R., Heitsch F., 2011, *Advanced Science Letters*, 4, 258
- Komiya Y., Suda T., Yamada S., Fujimoto M. Y., 2020, *The Astrophysical Journal*, 890, 66

- Koutsouridou I., Salvadori S., Skúladóttir Á., Rossi M., Vanni I., Pagnini G., 2023, MNRAS, 525, 190
- Kroupa P., Weidner C., 2003, The Astrophysical Journal, 598, 1076
- Kroupa P., Weidner C., Pflamm-Altenburg J., Thies I., Dabringhausen J., Marks M., Maschberger T., 2011, arXiv preprint arXiv:1112.3340
- Kulkarni M., Visbal E., Bryan G. L., 2021, ApJ, 917, 40
- Lai D. K., Lee Y. S., Bolte M., Lucatello S., Beers T. C., Johnson J. A., Sivarani T., Rockosi C. M., 2011, The Astrophysical Journal, 738, 51
- Larson P. L., 1998, Gaia, 15, 389
- Latif M. A., Volonteri M., 2015, MNRAS, 452, 1026
- Leaman R., 2012, The Astronomical Journal, 144, 183
- Li H., Aoki W., Zhao G., Honda S., Christlieb N., Suda T., 2015, Pub. Astron. Soc. Japan, 67, 84
- Li H., Tan K., Zhao G., 2018, The Astrophysical Journal Supplement Series, 238, 16
- Limongi M., Chieffi A., 2018, VizieR Online Data Catalog, p. J/ApJS/237/13
- Longair M. S., 2004, Measuring and modeling the universe, 2
- Lucatello S., Tsangarides S., Beers T. C., Carretta E., Gratton R. G., Ryan S. G., 2005, ApJ, 625, 825
- Lucertini F., Monaco L., Caffau E., Bonifacio P., Mucciarelli A., 2022, A&A, 657, A29
- Machida M. N., Matsumoto T., Inutsuka S.-i., 2008, ApJ, 685, 690
- Magg M., Hartwig T., Agarwal B., Frebel A., Glover S. C. O., Griffen B. F., Klessen R. S., 2018, MNRAS, 473, 5308
- Magg M., Klessen R. S., Glover S. C. O., Li H., 2019, MNRAS, 487, 486
- Marassi S., Chiaki G., Schneider R., Limongi M., Omukai K., Nozawa T., Chieffi A., Yoshida N., 2014, ApJ, 794, 100
- Marigo P., Girardi L., Chiosi C., Wood P. R., 2001, Astronomy & Astrophysics, 371, 152
- Marigo P., Girardi L., Bressan A., Groenewegen M. A. T., Silva L., Granato G. L., 2008, A&A, 482, 883

## BIBLIOGRAPHY

---

- Masseron T., Johnson J. A., Plez B., van Eck S., Primas F., Goriely S., Jorissen A., 2010, *A&A*, 509, A93
- Matteucci F., Panagia N., Pipino A., Mannucci F., Recchi S., Della Valle M., 2006, *Monthly Notices of the Royal Astronomical Society*, 372, 265
- McConnachie A. W., 2012, *The Astronomical Journal*, 144, 4
- McKee C. F., Chakrabarti S., Tan J. C., 2003, *IAU Symposium*, 221, P78
- McMillan P. J., 2011, *mnras*, 414, 2446
- Meléndez J., Placco V. M., Tucci-Maia M., Ramírez I., Li T. S., Perez G., 2016, *Astronomy & Astrophysics*, 585, L5
- Meynet G., Ekström S., Maeder A., 2006, *A&A*, 447, 623
- Mo H., White S., 2002, *Monthly Notices of the Royal Astronomical Society*, 336, 112
- Mo H., Van den Bosch F., White S., 2010, *Galaxy formation and evolution*. Cambridge University Press
- Munoz R. R., Geha M., Willman B., 2010, *The Astronomical Journal*, 140, 138
- Nissen P. E., Chen Y. Q., Carigi L., Schuster W. J., Zhao G., 2014, *A&A*, 568, A25
- Nomoto K., Maeda K., Mazzali P. A., Umeda H., Deng J., Iwamoto K., 2004, in , *Stellar Collapse*. Springer, pp 277–325
- Nordlander T., et al., 2019, *MNRAS*, 488, L109
- Norris J. E., Christlieb N., Korn A. J., Eriksson K., Bessell M., Beers T. C., Wisotzki L., Reimers D., 2007, *The Astrophysical Journal*, 670, 774
- Norris J. E., Yong D., Gilmore G., Wyse R. F., 2010, *The Astrophysical Journal*, 711, 350
- Norris J. E., Christlieb N., Bessell M., Asplund M., Eriksson K., Korn A. J., 2012, *The Astrophysical Journal*, 753, 150
- Norris J. E., et al., 2013, *ApJ*, 762, 28
- O'Donnell J. E., 1994, *The Astrophysical Journal*, 422, 158
- Oey M. S., 2003, *MNRAS*, 339, 849
- Oh S. P., Haiman Z., 2002, *ApJ*, 569, 558
- Oh S. P., Haiman Z., Rees M. J., 2001, *ApJ*, 553, 73

- Omukai K., Palla F., 2001, *ApJL*, 561, L55
- Omukai K., Tsuribe T., Schneider R., Ferrara A., 2005, *The Astrophysical Journal*, 626, 627
- Pacucci F., Loeb A., Salvadori S., 2017, *Monthly Notices of the Royal Astronomical Society: Letters*, 471, L72
- Padmanabhan T., 1993, *Structure formation in the universe*. Cambridge university press
- Pagnini G., Salvadori S., Rossi M., Aguado D., Koutsouridou I., Skúladóttir Á., 2023, *MNRAS*,
- Pastorelli G., et al., 2019, *Monthly Notices of the Royal Astronomical Society*, 485, 5666
- Peebles P. J. E., 1993, *Principles of physical cosmology*. Princeton University Press
- Placco V. M., Frebel A., Beers T. C., Stancliffe R. J., 2014, *ApJ*, 797, 21
- Placco V. M., et al., 2021, *ApJL*, 912, L32
- Planck Collaboration et al., 2018, arXiv e-prints, p. arXiv:1807.06209
- Press W. H., Schechter P., 1974, *The Astrophysical Journal*, 187, 425
- Prieto C. A., et al., 2015, *Astronomy & Astrophysics*, 579, A98
- Prole L. R., Clark P. C., Klessen R. S., Glover S. C. O., Pakmor R., 2022, *MNRAS*, 516, 2223
- Raiteri C., Villata M., Navarro J., 1996, *Astronomy and Astrophysics*, 315, 105
- Regan J. A., Downes T. P., 2018, *MNRAS*, 478, 5037
- Reichert M., Hansen C. J., Hanke M., Skúladóttir Á., Arcones A., Grebel E. K., 2020, *Astronomy & Astrophysics*, 641, A127
- Riaz S., Hartwig T., Latif M. A., 2022, *ApJL*, 937, L6
- Riaz R., Schleicher D. R. G., Bovino S., Vanaverbeke S., Klessen R. S., 2023, *MNRAS*, 518, 4895
- Romano D., Bellazzini M., Starkeburg E., Leaman R., 2014, *Monthly Notices of the Royal Astronomical Society*, 446, 4220
- Rossi M., Salvadori S., Skúladóttir Á., 2021, *MNRAS*, 503, 6026
- Rossi M., Salvadori S., Skúladóttir Á., Vanni I., 2023, *MNRAS*, 522, L1

- Safarzadeh M., Ji A. P., Dooley G. A., Frebel A., Scannapieco E., Gómez F. A., O'Shea B. W., 2018, *MNRAS*, 476, 5006
- Salpeter E. E., 1955, *The Astrophysical Journal*, 121, 161
- Salvadori S., Ferrara A., 2009, *Monthly Notices of the Royal Astronomical Society: Letters*, 395, L6
- Salvadori S., Ferrara A., 2012, *MNRAS*, 421, L29
- Salvadori S., Schneider R., Ferrara A., 2007, *Monthly Notices of the Royal Astronomical Society*, 381, 647
- Salvadori S., Ferrara A., Schneider R., 2008, *Monthly Notices of the Royal Astronomical Society*, 386, 348
- Salvadori S., Ferrara A., Schneider R., Scannapieco E., Kawata D., 2010, *MNRAS*, 401, L5
- Salvadori S., Skuladottir A., Tolstoy E., 2015, *Monthly Notices of the Royal Astronomical Society*, 454, 1320
- Salvadori S., Bonifacio P., Caffau E., Korotin S., Andreevsky S., Spite M., Skúladóttir Á., 2019, *Monthly Notices of the Royal Astronomical Society*, 487, 4261
- Salvadori S., D'Odorico V., Saccardi A., Skuladottir A., Vanni I., 2023, *arXiv e-prints*, p. arXiv:2305.07706
- Scannapieco E., Schneider R., Ferrara A., 2003, *ApJ*, 589, 35
- Scannapieco E., Kawata D., Brook C. B., Schneider R., Ferrara A., Gibson B. K., 2006, *ApJ*, 653, 285
- Schaerer D., 2002, *A&A*, 382, 28
- Schneider R., Ferrara A., Salvaterra R., Omukai K., Bromm V., 2003, *Nature*, 422, 869
- Schörck T., et al., 2009, *Astronomy & Astrophysics*, 507, 817
- Sestito F., et al., 2019, *MNRAS*, 484, 2166
- Sharda P., Federrath C., Krumholz M. R., Schleicher D. R. G., 2021, *MNRAS*, 503, 2014
- Sharma M., Theuns T., Frenk C., 2019, *MNRAS*, 482, L145
- Shu F. H., 1977, *The Astrophysical Journal*, 214, 488
- Simon J. D., 2019, *Monthly Notices of the Royal Astronomical Society*

- Skinner D., Wise J. H., 2020, MNRAS, 492, 4386
- Skúladóttir Á., Tolstoy E., Salvadori S., Hill V., Pettini M., Shetrone M. D., Starkenburg E., 2015, A&A, 574, A129
- Skúladóttir Á., et al., 2021, ApJL, 915, L30
- Skúladóttir Á., Vanni I., Salvadori S., Lucchesi R., 2023a, arXiv e-prints, p. arXiv:2305.02829
- Skúladóttir Á., et al., 2023b, The Messenger, 190, 19
- Smith R. J., Clark P. C., Glover S., Klessen R. S., 2010, in Whalen D. J., Bromm V., Yoshida N., eds, American Institute of Physics Conference Series Vol. 1294, First Stars and Galaxies: Challenges for the Next Decade. pp 285–286, doi:10.1063/1.3518879
- Stacy A., Bromm V., 2014, ApJ, 785, 73
- Stacy A., Greif T. H., Klessen R. S., Bromm V., Loeb A., 2013, Monthly Notices of the Royal Astronomical Society, 431, 1470
- Stacy A., Bromm V., Lee A. T., 2016, MNRAS, 462, 1307
- Starkenburg E., et al., 2010, Astronomy & Astrophysics, 513, A34
- Starkenburg E., et al., 2013, Monthly Notices of the Royal Astronomical Society, 429, 725
- Starkenburg E., Oman K. A., Navarro J. F., Crain R. A., Fattahi A., Frenk C. S., Sawala T., Schaye J., 2017, MNRAS, 465, 2212
- Starkenburg E., et al., 2018, MNRAS, 481, 3838
- Suda T., et al., 2017, Pub. Astron. Soc. Japan, 69, 76
- Susa H., 2019, The Astrophysical Journal, 877, 99
- Tan J. C., McKee C. F., 2004, ApJ, 603, 383
- Tarumi Y., Hartwig T., Magg M., 2020, ApJ, 897, 58
- Tegmark M., Silk J., Rees M. J., Blanchard A., Abel T., Palla F., 1997, The Astrophysical Journal, 474, 1
- Tolstoy E., Hill V., Tosi M., 2009, Annual Review of Astronomy and Astrophysics, 47, 371
- Tumlinson J., 2006, The Astrophysical Journal

- Tumlinson J., 2009, *The Astrophysical Journal*, 708, 1398
- Turk M. J., 2009, PhD thesis, Stanford University
- Vincenzo F., Matteucci F., Vattakunnel S., Lanfranchi G. A., 2014, *Monthly Notices of the Royal Astronomical Society*, 441, 2815
- Weidner C., Kroupa P., 2006, *Monthly Notices of the Royal Astronomical Society*, 365, 1333
- Weidner C., Kroupa P., Pflamm-Altenburg J., Vazdekis A., 2013, *Monthly Notices of the Royal Astronomical Society*, 436, 3309
- Welsh L., Cooke R., Fumagalli M., 2021, *MNRAS*, 500, 5214
- White S. D. M., Springel V., 2000, in Weiss A., Abel T. G., Hill V., eds, *The First Stars*. p. 327
- Wisotzki L., Christlieb N., Bade N., Beckmann V., Köhler T., Vanelle C., Reimers D., 2000, *A&A*, 358, 77
- Wollenberg K. M., Glover S. C., Clark P. C., Klessen R. S., 2020, *Monthly Notices of the Royal Astronomical Society*, 494, 1871
- Woosley S. E., 2017, *ApJ*, 836, 244
- Woosley S. E., Weaver T. A., 1995, *ApJS*, 101, 181
- Woosley S. E., Heger A., Weaver T. A., 2002, *Reviews of modern physics*, 74, 1015
- Xing Q.-F., et al., 2023, *Nature*,
- Yong D., et al., 2013a, *ApJ*, 762, 26
- Yong D., et al., 2013b, *ApJ*, 762, 26
- Yoon J., et al., 2016, *ApJ*, 833, 20
- Yoon J., Beers T. C., Tian D., Whitten D. D., 2019, *ApJ*, 878, 97
- Youakim K., et al., 2020, *MNRAS*, 492, 4986
- de Bressan M., Salvadori S., Schneider R., Valiante R., Omukai K., 2017, *Monthly Notices of the Royal Astronomical Society*, pp 926–940
- de Jong R. S., et al., 2019, arXiv preprint arXiv:1903.02464
- de Oliveira C. M., et al., 2019, *Monthly Notices of the Royal Astronomical Society*, 489, 241
- van den Hoek L. B., Groenewegen M. A. T., 1997, *A&A Supp.*, 123, 305